SOLID CATALYSTS WITH MODIFIED REDOX PROPERTIES FOR DEVELOPING GREEN PROCESSES FOR FRAGRANCE CHEMICALS

A THESIS SUBMITTED TO
UNIVERSITY OF PUNE

FOR THE DEGREE OF
DOCTOR OF PHILOSOPHY
(IN CHEMISTRY)

BY
Mr. Vivek R. Mate

Research Guide
Dr. Chandrashekhar V. Rode
Chief Scientist

CHEMICAL ENGINEERING AND PROCESS DEVELOPMENT DIVISION

CSIR-NATIONAL CHEMICAL LABORATORY

PUNE- 411 008, INDIA

May-2013

सीएसआयआर–राष्ट्रीय रासायनिक प्रयोगशाला
(वैज्ञानिक तथा औद्योगिक अनुसंधान परिषद)
डॉ. होमी भाभा मार्ग, पुणे – 411 008. भारत
CSIR-NATIONAL CHEMICAL LABORATORY
(Council of Scientific & Industrial Research)
Dr. Homi Bhabha Road, Pune - 411008. India

Certificate of the Guide

Certified that the work incorporated in the thesis entitled ***"Solid catalysts with modified redox properties for developing green processes for fragrance chemicals"*** *submitted by* ***Mr. Vivek R. Mate*** *was carried out by the candidate under my supervision/guidance. Such material as has been obtained from other sources has been duly acknowledged in the thesis.*

Date 21-05-2013

Dr. Chandrashekhar V. Rode

(Supervisor/Research Guide)

डॉ. चं. व. रोडे/Dr. C. V. RODE
वैज्ञानिक/Scientist
राष्ट्रीय रासायनिक प्रयोगशाला
National Chemical Laboratory
पुणे/ PUNE-411 008.

Communication Channels
NCL Level DID : 2590
NCL Board No. : +91-20-25902000
EPABX : +91-20-25893300
: +91-20-25893400
FAX
Director's Office : +91-20-25902601
COA's Office : +91-20-25902660
COS&P's Office : +91-20-25902664
WEBSITE
www.ncl-india.org

Declaration by the Candidate

I declare that the thesis entitled ***"Solid catalysts with modified redox properties for developing green processes for fragrance chemicals"*** *submitted by me for the degree of Doctor of Philosophy is the record of work carried out by me during the period from 24-10-2010 to 21-05-2013 under the guidance of* ***Dr. Chandrashekhar V. Rode*** *and has not formed the basis for the award of any degree, diploma, associateship, fellowship, titles in this or any other University or other institution of Higher learning.*

I further declare that the material obtained from other sources has been duly acknowledged in the thesis.

Date 21-05-2013

Mr. Vivek R. Mate

Dedicated

To

My Family and Friends

ACKNOWLEDGEMENT

It is a great pleasure to express my gratitude and sincere thanks to all those who helped me directly and indirectly to complete this research work. This thesis would not have been possible without all these people and their constant encouragement.

At the outset, I wish to place on record my immense and sincere gratitude to my guide ***Dr. Chandrashekhar V. Rode,*** *Chief Scientist, Chemical Engineering and Process Development Division, CSIR-National Chemical Laboratory (NCL), Pune, for his invaluable guidance, help, advice, encouragement and continuous support, throughout my PhD. I really admire the way he handled the scientific and nonscientific things with perfection and sincerity. There is no doubt that I learnt so many things from him especially, how to analyze and get valuable information even from small things, and how to solve a problem. My heartfelt thanks for his valuable time in bringing this output and shaping this thesis in the perfect manner.*

I am very much grateful to Dr. V. V. Ranade, the Chair, Chemical Engineering and Process Development Division, for providing me all the divisional facilities required for my research work.

I would like to thank Dr. S. Pal, Director, NCL, Pune, who gave me an opportunity to work in this esteemed research laboratory and providing all infrastructural facilities. I am also very much thankful to Council of Scientific and Industrial Research (CSIR) India, for awarding me the research fellowship.

I am very much grateful to Dr. H. S. Potdar, Dr. M. Shirai, (AIST, Sendai, Japan), Dr. K. R. Patil, Dr. P. N. Joshi, Dr. U. D. Joshi, (NSB College, Nanded) Dr. S. Kurungot, Dr. D. Srinivas, and Dr. R. Pant (NPL, NEW Delhi) for their valuable discussions and facilities that they offered to me to complete this work.

My deepest and heartiest thanks goes to all my seniors and friends, Dr. Vikas Kshirsagar, Dr. Jayprakash Nadgeri, Dr. Ajit Garade, Dr. Amit Choudhary, Dr. S. Vijayanand, Amol Hengne, Ajay Jha, Narayan Biradar, Anurag Sunda, Sumit Kamble, Sachin Sakate, Ajay Ghalwadkar, Mahadev Patil, Sachin Jadkar, Pravin Mohite, Nitin Kore, Rajendra Bhavsar, Rupak Patil, Atul Malawadkar, Rameshwer Swami, Virendra Patil, Nilesh Tangale, Ms. Rasika Mane, Mrs. Aparna Potdar, Ms. Sharada Kondawar, Ms. Mandakini Biswal, Ms.

Priyanka Patil, Ms. Shobha Birajdar, Mrs. Chetana Patil and Mrs. Pallavi Deshmukh, and all other research scholars and friends in research our group who are not named in person, for their valuable suggestions and helping hand.

It is a pleasure for me to thank my NCL friends Ms. Trupti Kotbagi, Hanumant Gurav, Mangesh, Dhanraj, Ankush, Nagesh, Ram, Anand, Vishal, Kuttan, Shantanu Kadam, Balaji, Ravi, Datta, Suleman, Jijil, Pradip Pachfule, Pradeep Biradar, Pradeep Lasonkar, Munshi, Aanuj, Pramod, Samadhan, Nilesh T., Nilkhant W., Rajamani, Dr. Savita, Ms. Thushara, Mrs. Swati, Mrs. Pradnya, Mrs. Manisha, Mrs. Shuklangi and Mrs. Hemangi.

Also I express my special thanks to all scientific and non-scientific staff of NCL, Dr. Mrs. Mayadevi, Dr. R. M. Deshpande, Dr. Saroj Jha, Mr. Raheja, Mr. David Soloman, Mr. V. Borkar, Mr. R. Jha, Dr. Niphadkar, Mr. Dure, Mr. Chinnadurai, Mr. Kamble, and Mr. Patne.

On this occasion, I would like to mention my friends Adv. Anil Mahale, Anand Rathor, Nitin Maliye, Pravin Maliye, Satish Mamidwad, Datta Patil, Vishal Patange, Abhijat Dubbewar, Sandeep Gawande, Amit Karchalwar, Mayur Maliye, Sachin Ingle, Nilesh Manwar, Nilesh Nerune, Adv. Mahesh Aher, Dr. Prashant Guthe, Ram Hodabe, Uchit Pole, Kailas Mate, Ganesh Mate, Dr. Chhaya and Dr. Madhuri, for their constant support and help especially during my toughest time.

This thesis would not have been possible without the strong faith, support and encouragement of my family. I wish to express my deep sense of gratitude to my parents for always providing unconditional support and helping me over the years. I would like to thank my wife and daughter for being patient and support me during the tough writing stage of the thesis.

Vivek Ramkrushna Mate

List of Contents

List of Tables

List of Schemes

List of Figures

Abbreviations

Co_3O_4	tricobalt tetraoxide
$ZnCo_2O_4$	Zinc cobaltate
$CoAl_2O_4$	Cobalt aluminate
Y	(%) Yield
M	(%) Mole
TON	Turnover number
TOF	Turnover frequency
M(TSPc)	Metal porphyrins
Fe(TF_5PP)Cl	Fe-tetrakis(pentafluorophenyl)porphyrins
TEMPO	2,2,6,6-tetramethylpiperidyl-1-oxy radical
EMIMDEP	1-ethyl-3-methylimidazolium diethyl phosphate
HRP	horseradish peroxidase
IBX	*o*-iodoxy benzoic acid
NA	not applicable
BET	Brunauer-Emmett-Teller
BJH	Barrett-Joyner-Halenda
XRD	X-ray diffraction
FWHM	Full width at half maximum
XPS	X-ray Photoelectron Spectroscopy
CSC	Cobalt surface composition
AO	Adsorptive oxygen
LO	Lattice oxygen
ASF	Atomic sensitivity factors
EXAFS	Extended X-ray absorption fine structure spectroscopy
FTIR	Fourier transform-infrared spectroscopy
HRTEM	High resolution-Transmission electron microscopy
SAED	Selected area electron diffraction
SEM-EDX	Scanning electron microscopy and Energy dispersive X-ray
TG- DTA	Thermogravimetric -Differential thermal analysis
DR-UV	Diffuse reflectance UV-visible spectroscopy
NMR	Nuclear magnetic resonance
EPR	Electron paramagnetic resonance spectroscopy
TPR/TPO	Temperature programmed reduction/ Temperature programmed oxidation

CV	Cyclic voltammogram
ICP-OES	Inductively coupled plasma - optical emission spectrometer
HPLC	High Performance Liquid chromatography
UV	Ultraviolet
CP	Co-precipitation
SG	Sol-gel
TD	Thermal decomposition
Co-a	Co_3O_4 preparation by co-precipitation at pH= 7-8
Co-b	Co_3O_4 preparation by co-precipitation at pH= 9-10
Co-c	Co_3O_4 preparation by co-precipitation at pH= 11-12
Co-d	Co_3O_4 preparation by co-precipitation at pH= 13-14
Co-3C-a	Co_3O_4 prepared at pH= 7-8 and calcined at 573 K
Co-3C-b	Co_3O_4 prepared at pH= 9-10 and calcined at 573 K
Co-3C-c	Co_3O_4 prepared at pH= 11-12 and calcined at 573 K
Co-3C-d	Co_3O_4 prepared at pH= 13-14 and calcined at 573 K
Co-4C-a	Co_3O_4 prepared at pH= 7-8 and calcined at 673 K
Co-5C-a	Co_3O_4 prepared at pH= 7-8 and calcined at 773 K
Co-6C-a	Co_3O_4 prepared at pH= 7-8 and calcined at 873 K
Co-3C-a-1	Co_3O_4 prepared at pH= 7-8, calcined at 573 K for 1 h
Co-3C-a-2	Co_3O_4 prepared at pH= 7-8, calcined at 573 K for 2 h
Co-3C-a-3	Co_3O_4 prepared at pH= 7-8, calcined at 573 K for 3 h
Co-3C-a-4	Co_3O_4 prepared at pH= 7-8, calcined at 573 K for 4 h
Co-3C-a-5	Co_3O_4 prepared at pH= 7-8, calcined at 573 K for 5 h
Co-3C-a-6	Co_3O_4 prepared at pH= 7-8, calcined at 573 K for 6 h
Co-3C-e	Co_3O_4 preparation via sol-gel and calcined at 573 K
Co-6C-e	Co_3O_4 preparation via sol-gel and calcined at 873 K
Co-f	Co_3O_4 preparation by Thermal Decomposition using cobalt nitrate
Co-g	Co_3O_4 preparation by Thermal Decomposition using cobalt acetate
Co-3C-f	Co_3O_4 preparation via TD (cobalt nitrate) and calcined at 573 K
Co-6C-f	Co_3O_4 preparation via TD (cobalt nitrate) and calcined at 873 K
Co-3C-g	Co_3O_4 preparation via TD (cobalt acetate) and calcined at 573 K
Co-6C-g	Co_3O_4 preparation via TD (cobalt acetate) and calcined at 873 K
Ea	Energy of activation
4H3MAMBA	4-hydroxy 3-methoxy alpha methyl benzylalcohol
ZC-a	Zn doped Co_3O_4 catalyst with Zn and Co ratio 1:1

ZC-b	Zn doped Co_3O_4 catalyst with Zn and Co ratio 1:2
ZC-c	Zn doped Co_3O_4 catalyst with Zn and Co ratio 1:3
ZC-3C-a	$ZnCo_2O_4$ catalyst with Zn and Co ratio 1:1 and calcined at 573 K
ZC-6C-a	$ZnCo_2O_4$ catalyst with Zn and Co ratio 1:1 and calcined at 873 K
ZC-3C-b	$ZnCo_2O_4$ catalyst with Zn and Co ratio 1:2 and calcined at 573 K
ZC-6C-b	$ZnCo_2O_4$ catalyst with Zn and Co ratio 1:2 and calcined at 873 K
ZC-3C-c	$ZnCo_2O_4$ catalyst with Zn and Co ratio 1:3 and calcined at 573 K
ZC-6C-c	$ZnCo_2O_4$ catalyst with Zn and Co ratio 1:3 and calcined at 873 K
CA-a	Al doped Co_3O_4 spinel catalyst with Co:Al ratio 1:2
CA-b	Al doped Co_3O_4 spinel catalyst with Co:Al ratio 1:1
CA-c	Al doped Co_3O_4 spinel catalyst with Co:Al ratio 3:1
CA-3C-a	$CoAl_2O_4$ catalyst with Co and Al ratio 1:2 and calcined at 573 K
CA-6C-a	$CoAl_2O_4$ catalyst with Co and Al ratio 1:2 and calcined at 873 K
CA-3C-b	$CoAl_2O_4$ catalyst with Co and Al ratio 1:1 and calcined at 573 K
CA-6C-b	$CoAl_2O_4$ catalyst with Co and Al ratio 1:1 and calcined at 873 K
CA-3C-c	$CoAl_2O_4$ catalyst with Co and Al ratio 3:1 and calcined at 573 K
CA-6C-c	$CoAl_2O_4$ catalyst with Co and Al ratio 3:1 and calcined at 873 K
CSA-1	15% cobalt aluminosilicate having silica alumina (Si:Al) ratio 10:1
CSA-2	15% cobalt aluminosilicate having silica alumina (Si:Al) ratio 1:1
CSA-3	15% cobalt aluminosilicate having silica alumina (Si:Al) ratio 1:5
CSA-4	15% cobalt aluminosilicate having silica alumina (Si:Al) ratio 1:10
CSA-4-3C	CSA-4 sample calcined at 573 K
CSA-4-4C	CSA-4 sample calcined at 673 K
CSA-4-5C	CSA-4 sample calcined at 773 K
CSA-4-3C-1h	CSA-4 sample calcined at 573 K for 1 h
CSA-4-3C-2h	CSA-4 sample calcined at 573 K for 2 h
CSA-4-3C-3h	CSA-4 sample calcined at 573 K for 3 h
CSA-4-3C-4h	CSA-4 sample calcined at 573 K for 4 h
CSA-4-3C-5h	CSA-4 sample calcined at 573 K for 5 h
CSA-4-3C-6h	CSA-4 sample calcined at 573 K for 6 h
5% CSA-4	CSA-4 sample having cobalt loading 5%
15% CSA-4	CSA-4 sample having cobalt loading 15%
30% CSA-4	CSA-4 sample having cobalt loading 30%
VASP	Vienna *ab-initio* Simulation Package
3D	Three dimensional

CuSA-4	15% copper aluminosilicate having silica alumina (Si/Al) ratio 1:10
FeSA-4	15% iron aluminosilicate having silica alumina (Si/Al) ratio 1:10
MnSA-4	15% manganese aluminosilicate having silica alumina (Si/Al) ratio 1:10

ABSTRACT OF THESIS

Solid catalysts with modified redox properties for developing green processes for fragrance chemicals

In the past few years, there has been a growing demand for solid catalysts which are efficient for the partial oxidation of alcohols for the production of fine and specialty chemicals. The use of stoichiometric inorganic reagents, though decreasing, is still practiced commercially [1]. The present stringent ecological standards is a major driving force to develop new, environmentally benign chemical manufacturing methods which also should meet the demand for high purity products particularly, in fragrance/flavour, food additives and pharmaceutical applications. The processes involving oxidation of variety of substrates leading to important oxygenated products can be developed by employing suitable solid catalysts. One such example is the oxidation of lignin substructure compound such as veratryl alcohol to veratryl aldehyde, which is an important starting material for the production of drugs intermediate and fragrance/flavor [2, 3]. Similarly, oxidation of other lignin substructure compounds such as vanillin alcohol, sinapyl alcohol, coniferyl alcohol, coumaryl alcohol, 4-hydroxy-3-methoxy alpha methyl benzyl alcohol to respective aldehyde products has been also studied in this work. Oxidation of these compounds is conventionally carried out using homogeneous catalysts such as Co, Fe, Mn complexes in presence of alkalies and organic oxidizing reagents. Although heterogeneous catalysts like methyl rhenium trioxide and vanadium phosphorus tetra oxide catalysts give excellent yield (<95%) but at the cost of mass balance (less than 80-50%) and demanding stoichiometric amount of H_2O_2 and TEMPO to keep the catalyst active in water medium. Hence, the search for green and inexpensive catalytic systems for oxidation remains a great challenge.

The specific objectives of this work are given below.

- Preparation of nano size metal oxide catalyst via various preparation methods such as co-precipitation/digestion, sol-gel and thermal decomposition.
- Preparation of aluminosilicate support with various compositions and properties.
- Detail characterization of prepared catalysts using various techniques such as Brunauer- Emmett-Teller (BET), FTIR, XRD, XPS, HRTEM, SEM, temperature programmed reduction (TPR), temperature programmed oxidation (TPO), cyclic voltammetry (CV), extended X-ray absorption fine structure (EXAFS), electron paramagnetic resonance (EPR), UV-Visible spectroscopy and ICP-OES.
- Activity testing of the above catalysts for liquid phase oxidation of veratryl alcohol.
- Optimization of reaction conditions for the best catalysts.
- Best catalyst tested for liquid phase oxidation reaction of lignin derived phenolic and non phenolic substructure compounds.
- Interpretation of activity results based on the characterization data.

The thesis is divided into six chapters with appropriate references given at the end of each chapter.

Chapter 1 gives the brief concept of catalysis, types of catalysis, green chemistry and general introduction to the oxidation reactions. A summary of literature on oxidation of various phenolic and non phenolic substrates substructure of lignin compounds using homogeneous, heterogeneous catalysts is also given in this chapter. At the end of this chapter scope and objectives of the thesis are elaborated.

Chapter 2 includes detailed experimental procedures used for preparation of various metal oxides, their characterization and activity testing for oxidation reactions.

Chapter 3 explains liquid phase oxidation of veratryl alcohol to veratryl aldehyde using nano Co_3O_4 spinel with its detailed characterization and co-relation between observed catalytic activity results and characterization data.

Spinel Co_3O_4 is widely used as a catalyst owing to its inherent redox ability. However, for liquid phase oxidation of veratryl alcohol to veratryl aldehyde reaction, catalyst with proper morphology with uniform distribution of nano particles are required in order to achieve high activity and selectivity. The distribution of uniform Co_3O_4 nano particle sizes could be obtained by adopting suitable preparation method and controlling the preparation parameters. The nano rod shape Co_3O_4 particles showed batter redox ability than the spherical morphology due to change in electronic configuration at edges and corners, which increased the probability of forming redox couple between tetrahedral Co^{2+} and octahedral Co^{3+} species [4, 5].

Co_3O_4 catalyst was prepared by the following different methods, co-precipitation/digestion, sol-gel, and thermal decomposition [5]. The prepared catalysts were screened for the oxidation of veratryl alcohol to veratryl aldehyde. Among the various catalysts Co_3O_4 prepared by co-precipitated showed excellent 75% and 38% conversion with > 97% selectivity to veratryl aldehyde in toluene and water respectively. Activation energy calculated from the Arrhenius plot was found to be 42.46 and 32.08 $kJmol^{-1}K^{-1}$ in toluene and water solvents respectively. FT-EXAFS of fresh and used samples showed the first peak at 1.52 Å corresponding to Co-O bond and second peak at 2.45 Å assigned to both Co-Co and Co-O bonds, while third peak at 4.60 Å assigned for Co-Co. The inter atomic distances between Co-O and Co-Co in were found to remain unaffected even after the catalyst was used in different solvents. The surface area (110 m^2/g) of the catalyst, rod shape morphology and formation of surface rich octahedral species (Co^{3+}) in nano size Co_3O_4 were found to be responsible for its higher activity as compared to bulk catalyst having tetrahedral Co^{2+}

species. The presence of these species was confirmed by FT-IR, EXAFS, EPR, TPR, TPO and CV. Effect of various reaction parameters such as temperature, oxygen pressure, catalyst loading, etc on activity and selectivity was also studied.

The liquid phase oxidation of various phenolic and non phenolic substructure of lignin compounds were tested over active nano Co_3O_4 catalyst. Among phenolic compounds, di-substituted vanillin alcohol showed a maximum conversion of 86% with 81% and 11% selectivities to vanillin and vanillic acid respectively. With increase in unsaturation, conversion dropped to 61% for the coniferyl alcohol with 82% selectivity to coniferyl aldehyde. The substituents on the phenolic compounds showed a significant influence on the oxidation activity depending on their ability of electron donation. The planer benzyl alcohol showed only 17.4% conversion while for the mono-substituted phenolic compounds, 51.8% conversion of the *p*-hydroxy benzylalcohol was obtained with 84% selectivity to *p*-hydroxy benzaldehyde. Similarly, 28% conversion of *p*-coumaryl alcohol was observed with 100% selectivity to *p*-coumaryl aldehyde. The tri-substituted phenolic compounds showed much higher activity, e.g. 77% conversion of the *p*-sinapyl alcohol was obtained with 78% selectivity to sinapyl aldehyde.

Among the non-phenolic substrates, the veratryl alcohol showed highest conversion of 85% with 96% selectivity to veratryl aldehyde. On the other hand, mono-substituted methoxy groups such as *p*-anisic alcohol showed 55% conversion with 100% selectivity to *p*-anisaldehyde while, 3,4,5-tri methoxy benzylalcohol showed higher conversion of 76.8% with 79% aldehyde selectivity. Highest conversion and selectivity of 90% was shown by the aromatic secondary alcohol, 4-hydroxy 3-methoxy alpha methyl benzylalcohol (4H3MAMBA).

The activity of various lignin substructure compounds studied in this work was found in the following order of secondary alcohol > di-substituted > tri-substituted > mono-substituted > without-substitution.

Chapter 4 explains oxidation of veratryl alcohol to veratryl aldehyde give using Zn and Al doped Co_3O_4 their detail characterization and co-relation between observed catalyst activity results and characterization data.

The zinc and aluminium doped $ZnCo_2O_4$ and $CoAl_2O_4$ spinel catalysts were prepared via co-precipitation/digestion method. The various compositions were prepared by varying amount of zinc in $ZnCo_2O_4$ such as 1:2, 1:1 and 1:3. While, 1:2, 1:1 and 3:1 compositions of aluminium were taken for $CoAl_2O_4$ preparation. Among these catalysts, $ZnCo_2O_4$ with 1:3 and $CoAl_2O_4$ with 3:1 proportion showed 24% and 26% activity with complete selectivity to veratryl aldehyde. The highest activity in case of lower doping was due to increase in cobalt octahedral and tetrahedral phase Co_3O_4 phase discussed in TPR and TPO.

Chapter 5, explains oxidation of veratryl alcohol to give veratryl aldehyde using cobalt oxide supported on aluminosilicates (SA) with different Si:Al ratios of 10:1, 1:1, 1:5 and 1:10. A detailed discussion on the co-relation between observed catalyst activity and their characterization data is presented.

Among the prepared catalysts Si/Al ratio of 1:10 showed the highest activity for oxidation of veratryl alcohol giving 24.4% conversion with complete selectivity to veratryl aldehyde. Based on the above results, catalysts with cobalt loadings in the range of 5-30% on SA-1:10 support were prepared. 15% Co-SA-1:10 showed the highest activity (100% selectivity to veratryl aldehyde with 24.4% conversion of veratryl alcohol). Further this catalyst was calcined at different temperatures from 573 K to 773 K. The catalyst calcined at 573 K with SA-1:10 showed the highest conversion of 86% and 98% selectivity to veratryl aldehyde.

Activation energy calculated from the Arrhenius plot was found to be 26.76 $kJmole^{-1}K^{-1}$. Effect of various reaction parameters such as temperature, oxygen pressure, catalyst loading, etc on activity and selectivity was also studied. UV-visible, XPS and CV spectroscopy proves divalent and trivallent cobalt species octahedrally and tetrahedrally coordinated with aluminosilicate support. The redox ability found to be depedent on distribution of cobalt octahedral and tetrahedral phase on the support.

Chapter 6 summarizes the work presented in all the chapters and general conclusions arrived from the discussed results.

References

1. T. Mallat, A. Baiker, *Chem. Rev*. 104 (2004) 3037.
2. A. L. Gutman, G. Nisnevich, E. Shkolnik, B. Tishin, I. Zaltzman, *U.S. Patent* 6,492,522 (2002).
3. K. G. Fahlbusch, F. J. Hammerschmidt, J. Panten, W. Pickenhagen, D. Schatkowski, K. Bauer, D. Garbe, H. Surburg, Ullmann's Encyclopedia of Industrial Chemistry, Wiley-VCH Verlag GmbH & Co. KGaA, 2000.
4. X. Xie, Y. Li, Z. Q. Liu, M. Haruta, W. Shen, *Nature* 458 (2009) 746.
5. V. R. Mate, M. Shirai, C. V. Rode, *Catal. Commun.* 33 (2013) 66.
6. V. S. Kshirsagar, S. Vijayanand, H. S. Potdar, P. A. Joy, K.R. Patil, C. V. Rode, *Chem. Lett.* 37 (2008) 310.

Chapter 1

Introduction

1. CATALYSIS

Over last couple of decades, much focus of chemistry is on developing new catalytic processes that are less hazardous to human health as well as environment. Catalysis has become attractive from its origin due to its inherent aspects of maximized output via energy and time-efficient alternative pathways and more so by using of non-conventional and eco-friendly resources in recent time. More than 80% of the present industrial processes using catalysts were established since 1980. The term "catalysis" was first defined by Berzelius in 1835 [1] as follows, *"Catalysis is a phenomenon in which chemical reactions are accelerated by small quantities of foreign substances, called catalysts"*. A suitable catalyst can enhance the rate of a thermodynamically feasible reaction but cannot change the position of the thermodynamic equilibrium. The catalytic reaction is a cyclic process and according to a simplified model, the reactant or reactants form a complex with the catalyst, thereby opening an alternate pathway with lower energy requirement for their transformation into the product or products [2]. Figure 1.1 shows the plot of reaction co-ordinate versus energy. The energy profiles of catalyzed and non-catalyzed reactions can be distinguished in terms of their energy of activation. The reactants require less energy of activation in the catalyzed reactions as compared to the non-catalyzed reaction as shown in Figure 1.1.

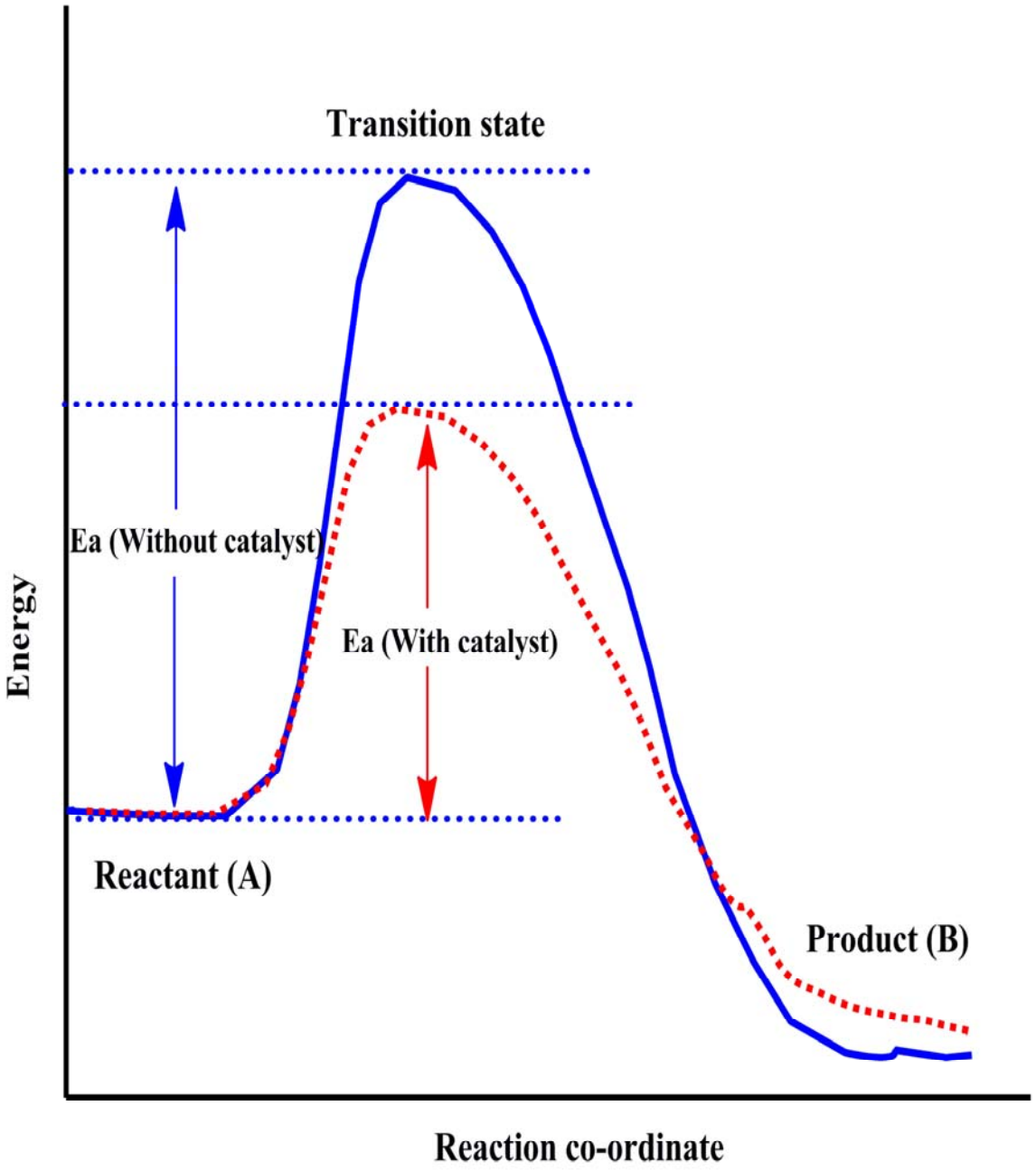

Figure 1.1. Energy profile of a catalytic reaction

Catalysts are classified as homogeneous and heterogeneous depending on their physical form in which they are present in the respective catalytic process. A broad classification of catalysis is shown below.

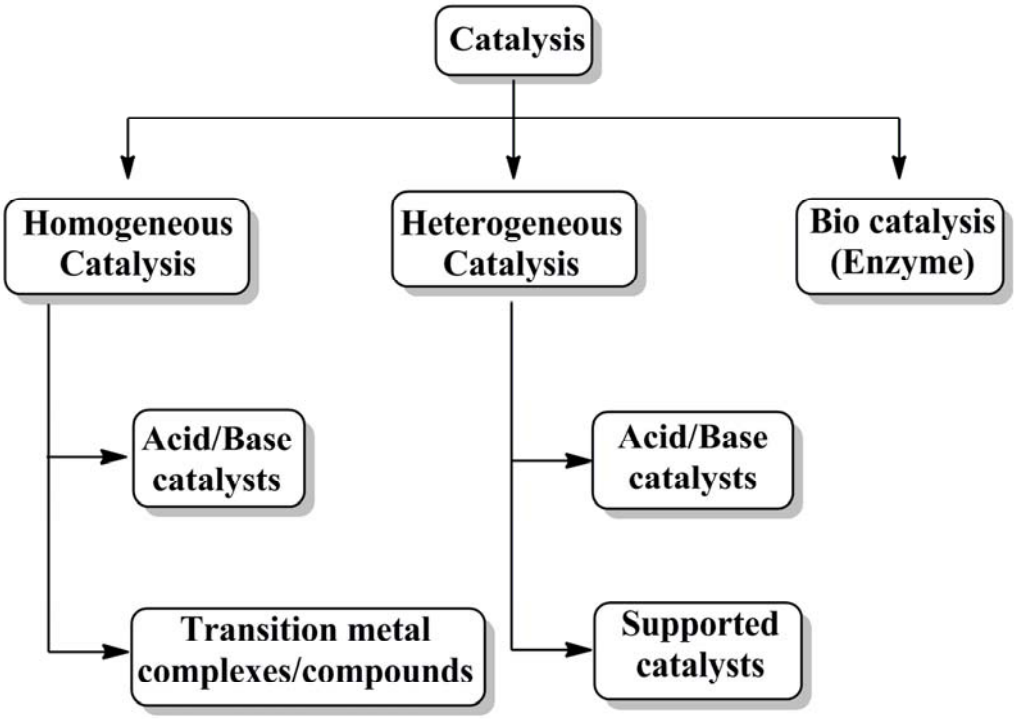

Figure 1.2. Classification of catalysis

1.1. HOMOGENEOUS CATALYSIS

Homogeneous catalysis represents a reaction system in which the substrates and the catalyst both are in one phase, more often in the liquid phase. More recently, a narrower definition is being used according to which homogeneous catalysis involves (organo) metallic complexes as the catalysts [3]. Homogeneous catalysts are more reactive in general, mainly due to the absence of phase boundaries, diffusion limitations and physisorption phenomenon. Soluble metal complexes as homogeneous catalysts provide selective synthetic routes under mild operating conditions for valuable chemicals from basic organic precursors such as ethylene to acetaldehyde by Wacker catalyst [4]. Some of the important reactions catalyzed by transition metal complexes are oxidation, hydrogenation, hydroformylation, carbonylation, and carbon-carbon bond formation reactions such as Heck reaction, co-polymerization and ring opening metathesis [5]. Important

examples of commercial applications of homogeneous catalysis are (a) hydroformylation of olefins to aldehydes/alcohols, (b) oxidation of *p*-xylene to terephthalic acid, (c) hydrocyanation of butadiene to adiponitrile, (d) ethylene oligomerization [6] and (e) oxidation of ethylene to acetaldehyde by $PdCl_2/CuCl_2$ [7].

Though, homogeneous catalysis has a major advantage of specificity, it suffers two serious drawbacks of catalyst-product separation from the reaction mixture and reusability of the catalyst. These shortcomings have led researchers to design and investigate new stable, reusable, efficient and easily separable catalyst systems.

1.2. HETEROGENEOUS CATALYSIS

Heterogeneous catalysts are those which act in a different phase than that of the reactants. Mostly, these are solid materials interacting with the substrate molecules either in a liquid or gaseous phase. The heterogeneous catalysts have numerous industrial applications in bulk as well as fine chemical, food, pharmaceutical, automobile and petrochemical industries [8]. It has been estimated that 90% of all chemical processes are heterogeneous [9]. The first industrially important heterogeneous catalytic process introduced in 1875, used platinum to oxidize SO_2 to SO_3, for the synthesis of sulphuric acid [10]. Another important discovery in that period was of alcohol dehydration over alumina and alcohol oxidation on platinum metal. In 1920s, heterogeneous catalysis by solid acids and supported metals was applied widely in oil refining and petrochemicals. In contrast, fine chemicals manufacture was dominated by synthetic organic chemists who adhered to stoichiometric methodologies. Primarily, heterogeneous catalyst has a major advantage of its easy recovery from the reaction mixture unlike the homogeneous catalyst, offering a simpler handling as well as preventing the loss of active catalyst function [11].

Another equally important advantage is heterogeneously catalyzed processes can be operated continuously on a commercial scale. A chemical reaction catalyzed by a solid catalyst, mainly occurs at the catalyst surface that involves the active sites (or active centres). The activity of a solid catalyst is directly proportional to the specific surface area of a solid per unit weight or volume. However, size of the catalyst particles used in industrial applications mainly depend on type of the reactor used. For example in fine chemical industry, batch slurry reactors are employed and in our work also we have studied the catalyst activity in the same. In such reactors, weight fractions of catalyst generally range between 0.05 to 2.5 % (w/w).

Some of the important characteristics of the best catalyst are:

- It should have highest selectivity to the desired product.
- It should give reasonable rates of reaction, in terms of conversion and/or productivity per unit time.
- It should be stable under the reaction conditions for a prolonged time and reusable.

These characteristics are fundamentally related to the adsorption-desorption phenomena and interaction of adsorbed molecules on the catalyst surface. In my work, I have focused on developing new solid catalysts involving metal oxides with a particular application to oxidation reactions of particle relevance. Hence further discussion is focused on various preparation methods of such catalysts.

1.3. CATALYST PREPARATION METHODS

Different protocols commonly employed for the preparation of metal oxides, involve a sequence of complex processes that impart advantages and disadvantages for catalytic applications. The properties of a good catalyst are determined based on its activity and selectivity to the desired product, as well as its thermal and mechanical stability under reaction conditions. Excellent

reviews on catalyst preparation methodologies are available in the literature and [12-14] some of the most commonly used methods are described below.

1.3.1. Simultaneous co-precipitation and digestion

Co-precipitation is a convenient and facile route employed for the synthesis of variety of materials by forming a sparingly soluble product from aqueous solutions. In a precipitation reaction, corresponding metal salt in the form of nitrate, chloride, sulphate, etc. is used. After precipitation with a precipitating agent, either the oxides are obtained directly or a precursor is formed in the form of hydroxide, oxalate, carbonate, hydroxy carbonate, etc. depending on the precipitating agent. These precursors, give rise to the required simple metal oxide or a mixed metal oxide after calcination at a suitable temperature. The major steps governing a precipitation reaction are nucleation, growth and agglomeration. The theory and mechanism behind each individual step is well described in the literature [15-21]. In a precipitation reaction, the primary process taking place is nucleation which can be considered as the key step. Nucleation process involves formation of numerous small particles. The formation of products results in a sparingly soluble species formed under the condition of higher supersaturation. Supersaturation can be induced by various parameters such as temperature, pressure and chemical reaction. The particles formed tend to grow/aggregate together either through the process of Ostwald ripening or through oriental attachment to minimize their energy to attain thermodynamic stability. If the crystallinity of the precursor is improved during precipitation, the high energy faces attach together to give precursors of controlled morphology. Those precursors upon calcination in air form their corresponding oxides retaining their morphology. This growth process is called topotactical growth [22].

1.3.2. Sol-gel

The sol-gel technique is one of the most widely used chemical methods and mainly applied for the synthesis of metal and doped metal oxides. In this process, oxides are synthesized by the formation of an oxide network directly in solution by hydrolysis of alkoxides, followed by gelation and finally by removal of the solvent [23]. There are two methods for the synthesis of metal oxides i) solid-state and ii) wet chemical synthesis. In contrast to the solid-state method, a wet chemical synthesis can provide homogeneous nanosize oxides of high purity at lower reaction temperatures. Sol-gel process is the most widely used route and involves a colloidal sol which is converted into a gel during aging [24, 25]. The main principle of the classical sol-gel process is the controlled hydrolysis of metalloorganic compound (alkoxides) in an organic solvent. The sol-gel process involves olation (formation of hydroxyl bridges) and oxolation (formation of oxygen bridges) reactions during hydrolysis (reactions, 1.1-1.3). The oxolation condensation reaction is responsible for the formation of colloidal agglomerates [26].

$$\equiv M\text{-}OR + H_2O \rightarrow \equiv M\text{-}OH + RHO \text{ (Hydrolysis)} \quad (1.1)$$

$$\equiv M\text{-}OH + RO\text{-}M\equiv \rightarrow \equiv M\text{-}O\text{-}M\equiv + RHO \text{ (Condensation)} \quad (1.2)$$

$$\equiv M\text{-}OH + HO\text{-}M\equiv \rightarrow \equiv M\text{-}O\text{-}M\equiv + H_2O \text{ (Condensation)} \quad (1.3)$$

Where, R is alkyl group

M is metal.

The gel formation depends on different parameters including the nature of starting material(s) (precursor(s)), types of solvent, precursor concentration in the solvent, alkoxy to water ratio, synthesis temperature, pH, stirring and aging time. Metal alkoxides serve as starting materials

and can be hydrolyzed by water. During hydrolysis, alkoxy groups are replaced by strong OH– nucleophiles, and the subsequent condensation and addition steps lead to the formation of oxide chains. The sol-gel synthesis goes through the formation of a sol of colloidal particles. Gelation is an intermediate step, formed due to agglomeration of sol particles as a result of both solvent removal and heat treatment. Depending on reaction conditions, the sol particles may grow further or form a gel. The sol-gel process can be used for the preparation of a variety of materials (Figure 1.3). The drying of the sol gives powder. The application of dip-coating or spin-coating leads to the preparation of thin films. The removal of the solvent by drying causes the shrinking of gel and significant reduction in the volume due to increasing capillary forces. The high capillary pressure in the pores causes the collapse of the gel network structure producing less porous powder (xerogel). In contrast in the supercritical extraction, the solvent is removed above its critical temperature. This preserves the structure of the gel network and yields a highly porous material (aerogel).

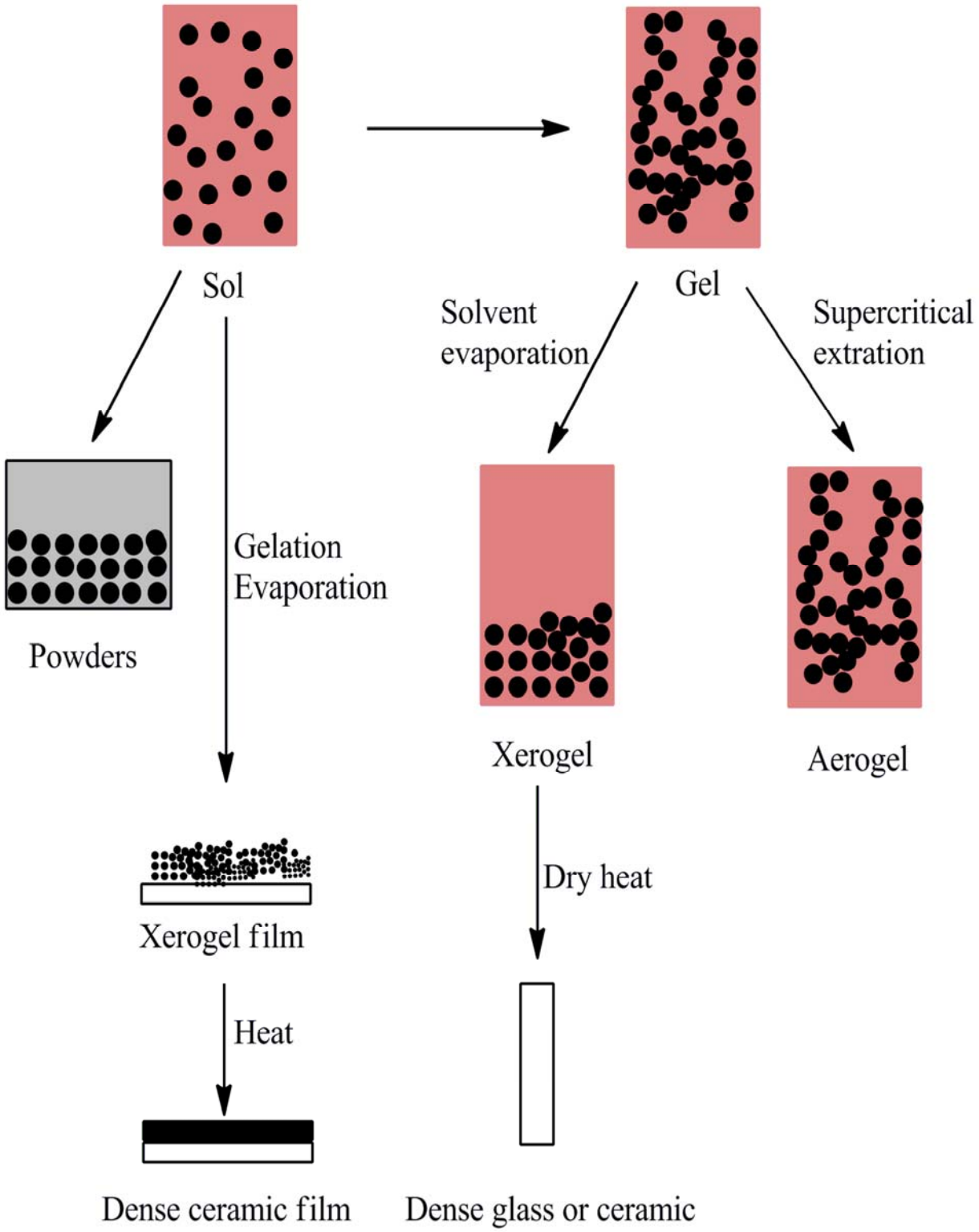

Figure 1.3. Production options for the Sol-gel process [27]

1.3.3. Thermal decomposition

Thermal decomposition is emerging as an important technique for the synthesis of composites, alloys, nanomaterials, etc. [28-30]. In this process, metal precursors are calcined at various temperatures in the furnace. The calcination temperatures were selected according to the TG–DTA data. The technique can give uniform material as long as phase separation does not occur during the heating or the subsequent cooling [31]. The product formed via this method has lower surface area.

1.4. GREEN CHEMISTRY

Catalysts play a vital role in replacing the reagents used in stoichiometric quantities by very minimal and recyclable/recoverable substances. The design of an appropriate catalyst for a specific reagent based reaction is therefore a significant step to develop green processes. From this view point, what is meant by "green chemistry" is discussed in this section.

In recent years, the term “green chemistry” and “environmental catalysis” are frequently used. Green chemistry is the science that deals with, *“carrying out chemical activities including chemical design, manufacture, use, and disposal-such that hazardous substance will not be used and generated”* [32]. Prof. Anastas, has first postulated the 12 principles of green chemistry as given below [33].

1. **Prevention**

   It is better to prevent waste than to treat or clean it after it has been created.

2. **Atom economy**

   Synthetic methods should be designed to maximize the incorporation of all materials used in the process into the final product.

3. **Less hazardous chemical syntheses**

   Wherever practicable, synthetic methods should be designed to use and generate substances that possess little or no toxicity to human health and environment.

4. **Designing safer chemicals**

   Chemical products should be designed to effect their desired function while minimizing their toxicity.

5. **Safer solvents and auxiliaries**

   The use of auxiliary substances (e.g., solvents, separation agents, etc.) should be made unnecessary wherever possible and innocuous when used.

6. **Design for energy efficiency**

   Energy requirements of chemical processes should be recognized for their environmental and economic impacts and should be minimized. If possible, synthetic methods should be conducted at ambient temperature and pressure.

7. **Use of renewable feedstock**

   A raw material or feedstock should be renewable rather than depleting whenever technically and economically practicable.

8. **Reduce derivatives**

   Unnecessary derivatization (use of blocking groups, protection/ deprotection, temporary modification of physical/chemical processes) should be minimized or avoided if possible, because such steps require additional reagents and can generate waste.

9. **Catalysis** Catalytic systems (as selective as possible) are superior to stoichiometric reagents.

10. **Design for degradation**

    Chemical products should be designed so that at the end of their function they break down into innocuous degradation products and do not persist in the environment.

11. **Real-time analysis for pollution prevention**

    Analytical methodologies need to be further developed to allow for real-time, in-process monitoring and control prior to the formation of hazardous substances.

12. **Inherently safer chemistry for accident prevention**

    Substances and the form of a substance used in a chemical process should be chosen to minimize the potential for chemical accidents, including releases, explosions and fires.

An attempt to develop a process by following at least one of the above 12 principles can lead to a green chemical process. Among these, principles 7 and 9 advocating the use of renewable feedstock and catalytic systems being most important were followed in my thesis work which involves oxidation of veratryl alcohol to veratryl aldehyde and oxidation of phenolic and non-phenolic lignin derived compounds to the respective aldehydes over solid catalysts. This has been elaborated in the Section 1.6.

1.5. OXIDATION

The chemical term oxidation is defined as, "The take-up of oxygen by organic and inorganic materials or removal of hydrogen from a substrate" [34]. The development of processes for oxidation of organic substances is a goal that has long been pursued, since it is one of the most important methods for producing oxygen containing diverse chemicals from oil derivatives of hydrocarbon origin [35, 36]. Various process options for oxidation processes are shown in Figure 1.4 [37].

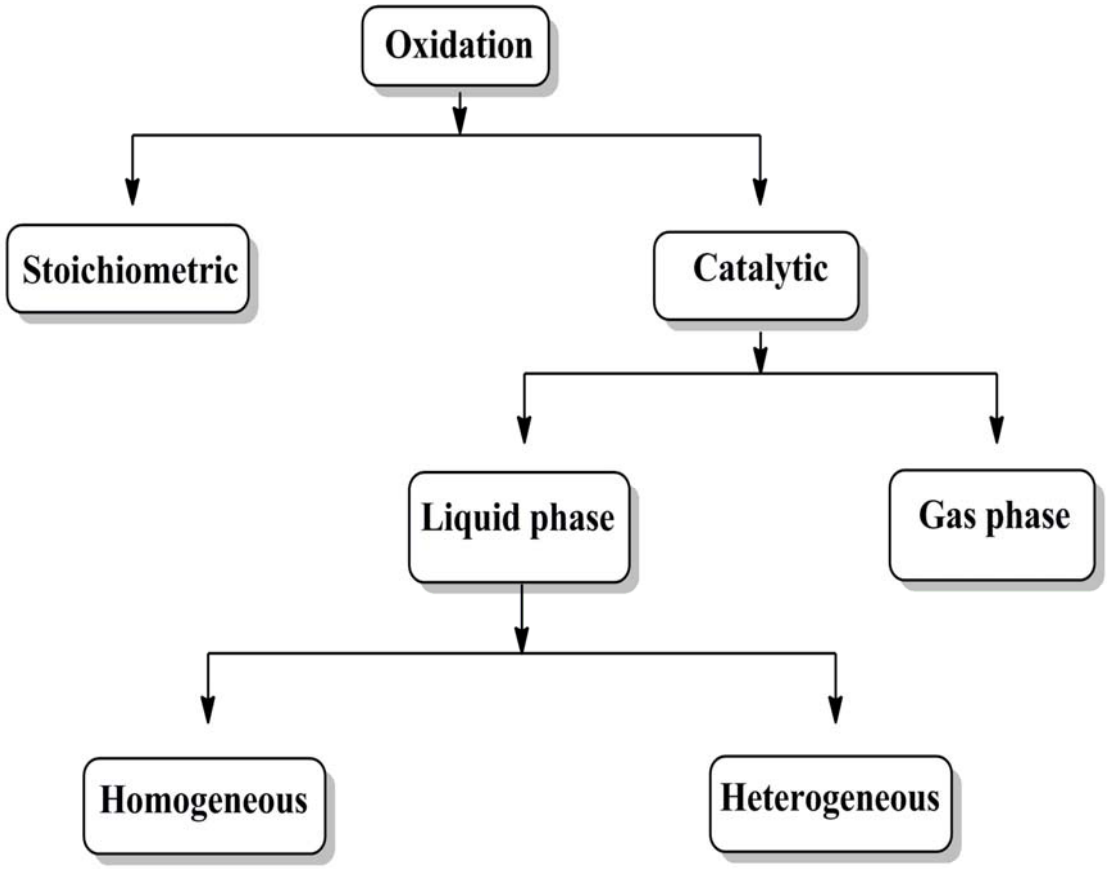

Figure 1.4. Classification of oxidation reactions

The examples of reagents used in stoichiometric (or even excess) quantities for oxidation reactions are given in Table 1.1. This is now becoming prohibitive by legislature all over the world due to the generation of huge quantities of inorganic waste posing a serious effluent disposal problem [38].

Table 1.1. Various oxidants used in liquid phase oxidations [39, 40]

Sr. No.	Name of oxidizing agent	Drawbacks
1	Pyridinium chlorochromate	Relatively acidic reagent (more acidic than PDC and Collins) - can cause problems with acid labile groups
2	Collins's reagent (CrO_3. 2 pyridine)	Requires a large excess of reagent for complete reaction.
3	Pyridinium dichromate	Work-up can be messy on large scale. Often require a large excess.
4	aq. sulfuric acid, acetone, chromic acid	toxic and mutagenic, requires in stoichiometric quantities
5	Potassium permanganate, potassium dichromate, lead tetra acetate	Not very chemo selective, which limits its use. Hazardous nature e.g. Pb, Cr.
6	Sodium chlorite	Requires in stoichiometric
7	Osmium tetra oxide	Osmium tetra oxide is very expensive and highly toxic

A comparison between catalytic and stoichiometric oxidation reactions is shown in Table 1.2. Catalytic oxidations provide an environmentally acceptable and cheap process as compared to stoichiometric oxidations.

Table 1.2. Comparison between catalytic and stoichiometric oxidation

Catalytic oxidation (O_2)	**Stoichiometric oxidation**
Advantages ▪ Cheap oxidant ▪ No effluent problem **Disadvantages** ▪ Limited scope	**Advantages** ▪ Broad scope **Disadvantages** ▪ Expensive and hazardous oxidants ($K_2Cr_2O_7$, $KMnO_4$, $Pb(OAc)_4$, etc. ▪ Generation of large amounts of inorganic wastes posing a serious effluent disposal problem. ▪ Tedious work up for recovery of pure product. ▪ Selectivity not up to the mark.

Depending on the reactant phase, the catalytic oxidation is classified in two types, liquid and gas phase. In gas phase oxidation, substrate concentrations are much lower and free radical (atoms, molecules or ions with unpaired electrons) oxidation pathway is less favored. Gas phase oxidation generally operates through Mars-van Krevelen mechanism (scheme 1.1a) while in liquid phase, the oxidation follows a free radical pathway as represented by scheme 1.1b.

Gas phase (Mars-van Krevelen mechanism)

$$S + M{=}O \longrightarrow SO + M \quad (1.4)$$

$$2\,M + O_2 \longrightarrow 2\,M{=}O \quad (1.5)$$

Scheme 1.1a. Gas phase oxidation.

Liquid phase

$$RH \longrightarrow R^{\bullet} \quad (1.6)$$

$$R^{\bullet} + O_2 \longrightarrow R\,O_2^{\bullet} \quad (1.7)$$

$$R\,O_2^{\bullet} + RH \longrightarrow R\,O_2H^{\bullet} + R^{\bullet} \quad (1.8)$$

Scheme 1.1b. Liquid phase oxidation involving free radical pathway

Among various substrates, selective oxidation of sp^3 hybridized carbon of inactive hydrocarbons to industrially important intermediates still remains a major challenge [41-45]. There are several large scale industrial vapor phase oxidation processes. Nevertheless, it has certain disadvantages such as very high operating temperature and the formation of a large amount of carbon dioxide, contributing to the global warming. Further, the conversion has to be kept low to attain a high selectivity of aldehydes, and the low concentration of substrates in the feed stock mixture poses the problem of recovery. In case of vapor phase oxidation of toluene with oxygen, carried out at temperature > 473 K and under 0.5– 2.5 MPa pressure [46-50], these conditions seems to be too harsh for improving the selectivity to benzaldehyde. Generally, the conversion has to be kept at less than 4% to attain 70% selectivity to benzaldehyde and to avoid the formation of carboxylic acids, phenols, and decomposition to carbon oxides (CO_2 and CO) and tar [51,52]. However, any diffusion limitations are expected to be much less severe in gas-solid systems as compared to

liquid-solid systems [53]. Liquid-phase oxidations processes are also commercially practiced such as *p*-xylene to terephthalic acid, cyclohexane to cyclohexanol/cyclohexanone and adipic acid, n-butane to acetic acid, etc. [54, 55]. Due to relatively milder reaction conditions, liquid phase oxidation is easy to operate and gives the quantitative conversion of the substrate. Liquid phase oxidation operates through the free radical pathway which is always associated with the formation of coupling as well as over oxidation products. Liquid phase oxidation is even more imperative than gas phase oxidation in the production of fine chemicals. Since the recovery of the desired oxidation product of highest purity is required due to their applications in health care, flavours and fragrance, pharmaceutical formulations [56, 57]. From this perspective, designing a solid catalyst system with a remarkable activity and highest stability for liquid phase oxidation reactions becomes a challenging task.

1.5.1. Molecular oxygen as an oxidizing agent

Lists of various oxygen donors used in catalytic oxidation reactions are shown in Table 1.3 [58]. Although H_2O_2 has the highest active oxygen content, it is usually used as 50% aqueous solution which occupies large reactor volume and its storage and handling conditions are rather difficult. Also, H_2O_2 is a secondary oxygen donor like others, since it is prepared from oxygen as a primary source of oxygen.

Table 1.3. Oxygen donors [59]

Donor	Active oxygen (%)	By-product
H_2O_2	47.0	H_2O
N_2O	36.4	N_2
O_3	33.3	O_2
t-BuO_2H	17.8	t-BuOH
CH_3CO_3H	21.0	CH_3CO_2H
$C_5H_{11}NO_2$	13.7	$C_5H_{11}NO$
$NaClO_2$	35.6	NaCl
NaClO	21.6	NaCl
NaBrO	13.4	NaBr
$KHSO_5$	10.5	$KHSO_4$
$NaIO_4$	10.0	$NaIO_3$
HNO_3	25.4	HNO_2
PhIO	7.3	PhI

The atmospheric air is the most abundant and cheapest primary oxygen donor without having any waste disposal problem. It is well known that biologically some of the enzymes perform selective oxidations of complex organic molecules under very mild conditions [60, 61]. Several synthetic transition metal complexes are able to mimic these enzymes and reversibly bind and activate molecular oxygen [62, 63]. During last few decades, there has been a growing interest in transition metal catalyzed activation of O_2 for organic oxidations [34, 52, 61, 65-71]. There are two forms of molecular oxygen in gas phase as dioxygen (O_2) and trioxygen (O_3). These forms

are formed by electric discharge passed through oxygen molecule. The ground state of molecular oxygen contains (triplet state) two unpaired electrons, which are localized on the degenerate antibonding π_{2p} orbitals (Figure 1.5). This requires high energy of activation to react with singlet organic molecules. The symmetry barrier can be overcome by activating oxygen to the singlet state which can be achieved by different ways, e.g. thermal excitation of the molecules from triplet state of oxygen to singlet state of oxygen. However, oxygen may also be activated chemically, by bonding it to an appropriate centre which may be the transition metal ions in the coordination complex or the surface of solid e.g. transition metal oxide.

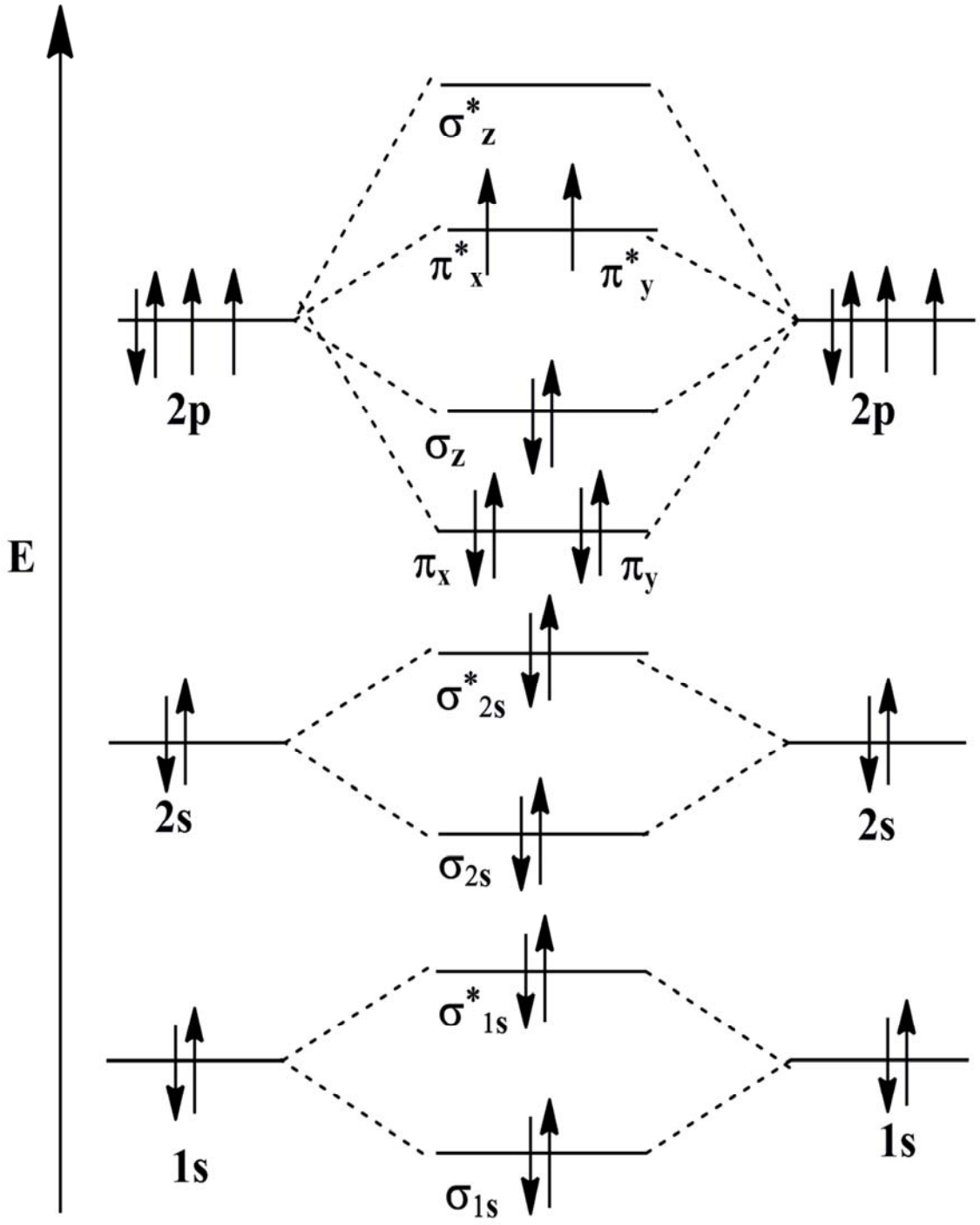

Figure 1.5. Molecular orbital diagram of oxygen

In the present work, chemical activation of molecular oxygen has been attempted by several solid catalysts hence, some theoretical background on this aspect is summarized in the following section.

1.5.2. Activation of oxygen by transition metal complexes

Metal complexes in low oxidation states can interact with dioxygen in successive steps in which electrons are transferred from the metal to dioxygen forming successively superoxo, μ-peroxo, oxo, and μ-oxo complexes

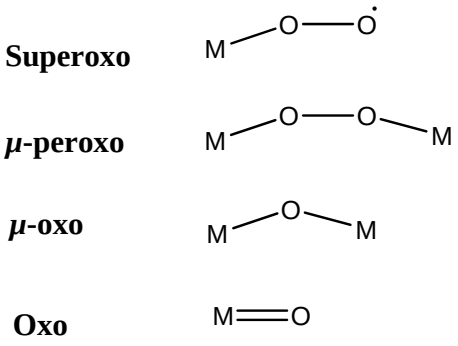

Figure 1.6. Binding of oxygen with the metals [71]

Many transition metal complexes are reported to catalyze the oxidation reactions, some of the examples are:

1. Ruthenium compounds are widely used as a catalysts in many reactions e.g. $RuCl_3.nH_2O$, $RuCl_2(Ph_3P)_3$ catalyze the aerobic oxidation of allylic and benzylic alcohols under mild reaction conditions [71].
2. $Pd(OAc)_2$-NaOAc is reported for aerobic oxidation of alcohol [72].
3. In 1984, Semmelhack reported the first practical Cu-catalyzed aerobic oxidation of alcohols by 10 mol% CuCl and 10 mol% TEMPO under oxygen atmosphere [73].
4. Various cobalt complexes usually referred to as synthetic dioxygen carriers are known to interact reversibly with dioxygen under ambient conditions [74-76]. The oxidation of

cyclohexane and *p*-xylene by dioxygen in air are chain reactions involving organic free-radicals; these are considered as homolytic fission processes. In these systems, cobalt (III and II) and/or manganese (III and II) ions catalyze the initiation steps. Reactions of this type, in which the organic substrates are directly oxidized by air or by pure dioxygen, are often classified as autoxidation processes [53]. Among all transition metals, cobalt is most commonly used for activating dioxygen. Transition metal ions have the ability to donate unpaired electrons and at the same time receive and donate electron density (π-back bonding), which enables the paramagnetic ($^3O_2$) oxygen molecule to bind reversibly with these metal ions.

1.6. OXIDATION OF LIGNIN DERIVED PHENOLIC AND NON-PHENOLIC MODELCOMPOUNDS

One of the major applications of oxidation reaction is for the production of specialty chemicals e.g. flavor and fragrance agents used in food and pharmaceutical industries. Among various flavoring and fragrance agents, those synthesized from lignin derived compounds involve vanillin, veratryl aldehyde, *p*-anisaldehyde, etc. are well known and commonly used in confectionaries. Due to the high production cost from natural resources, these compounds are generally prepared by chemical processes e.g. the cost of vanillin extracted from vanilla pods has increased from $ 20 per kilo in 1924 to $ 4000 per kilo in 2011, in contrast to the price of synthetic vanillin, stable at < $ 15 per kilo [78-80]. Table 1.4 shows the exponential increase in natural vanillin cost while that of synthetic vanillin cost remaining more or less stable over the past more than 80 years.

Table 1.4. Production cost of vanillin from natural resource (vanilla bean) and synthetic route [78-80]

Year	Vanillin from vanillin bean		Vanillin from synthetic route		Industries
	Metric Tone	U.S. $/kg	Metric Tone	U.S. $/kg	
1924	360	19.8	-	18	Salvo Chemical Corporation, USA; Marathon Paper Mill Company, USA
1934	360	7.7	-	6	
1971	-	11-18.5	-	11	
1980	-	88-101	-	11-12	Ontario Pulp and Paper Canada
1991	498	33.3	4500-5500	11-14	
1992	437	27.6	4500-5500	11-14	
2001	1800	1200	~10000	15	
2011	1600	4000	~20000	15	Rhodia Organics

Due to immense commercial importance of these compounds, developing cheaper and eco-friendly routes for the oxidation processes are of great importance. Several chemical processes were reported for the production of flavouring and fragrance agents, among which first one was reported by Rhodia for vanillin using solid catalysts [80]. This process is evidently superior to the processes based on the use of conventional reagents in stoichiometric amounts for the production of vanillin, from both economic and environmental point of view.

1.7. SOLID MATERIALS FOR CATALYTIC OXIDATION

1.7.1. Metal oxide

Metal oxides play a very important role in many areas of science and technology [81]. These are found as one of the most abundant materials in the earth's crust. Almost, all the metals can show activity towards air and give rise to oxides through oxidation by oxygen at certain temperature and pressure. The existence of different metal oxides such as alkali and alkaline earth metal oxides, rare-earth oxides, transition metal oxides, etc., are of special interest because of their certain interesting catalytic, electrical and magnetic properties.

The transition metal oxides are used extensively as heterogeneous catalysts in many organic transformations such as oxidation, oxidative/non-oxidative dehydrogenation, reduction, ammoxidation, metathesis (production of long chain alkenes), esterification and in water gas shift reaction [82-84]. The high catalytic activity of transition metal oxides is mainly attributed to their multiple valencies. Transition metal ions exhibit variable oxidation states due to their intrinsic oxidation-reduction or by catalytic reactions, which can occur at the same or different cationic sites [85-86]. Spinel and doped metal oxides are two important structural classes of oxides which exhibit excellent redox properties and wide range of applications.

1.7.1.1. Spinel oxide

Spinel oxide of AB_2O_4 type is a class of metal oxide material which shows catalytic activity in a face centered cubic (FCC) structure. In spinel structure (Figure 1.7) [87], A and B can be divalent, trivalent, or quadravalent cations of cobalt, iron, magnesium, zinc, manganese, aluminium, chromium, titanium, etc. Spinel structure that consists of iron as one of the metal component is called a ferrite. Ferrites can crystallize as hard ferrites in structures like garnet and magnetoplumbite structures which are derived from the spinel structure. The crystal structure of

spinel oxides was determined independently by Bragg [88] and Nishikawa [89]. The unit cell of a spinel consists of eight formula units and can be represented by $A_8B_{16}O_{32}$. The metallic cation occupies interstitial positions. There exist two types of interstitial positions formed by 32 oxygen ions of FCC lattice. There are 64 tetrahedral interstitial sites each surrounded by 4 oxygens (called as A site) and 32 octahedral sites each surrounded by 6 oxygens (called as B site). In the spinel structure, 8 out of 64 tetrahedral sites and 16 out of 32 octahedral sites are occupied by the metal cations. For better understanding and visualization, the unit cell can be subdivided into eight octants with an edge $a/2$, where a is edge length of the unit cell. The space group for the spinel ferrite is Fd3m with the space group number, 227 [90, 91]. On the basis of occupied positions and distribution of the cations in the tetrahedral and octahedral sites, spinels can be further classified as normal, inverse and mixed spinels. These spinels are represented in general as $(AxB_1\text{-}x)[A_1\text{-}xB_1\text{+}x]O_4$ where metal oxides in '( )' brackets occupy the tetrahedral sites and those in '[ ]' brackets represent the octahedral sites. If each sublattice is occupied by only one type of cation i.e. when $x = 0$, the spinel is said to be normal whereas if $x = 1$, it is called as inverse spinel. For $0 < x < 1$, the spinel is defined as the mixed one. The types of spinels with the general formula for their representation are shown in Table 1.5. By changing the distribution of cations one can tune some of their properties such as magnetic, electric, catalytic, etc. [92-94] which are of scientific interest.

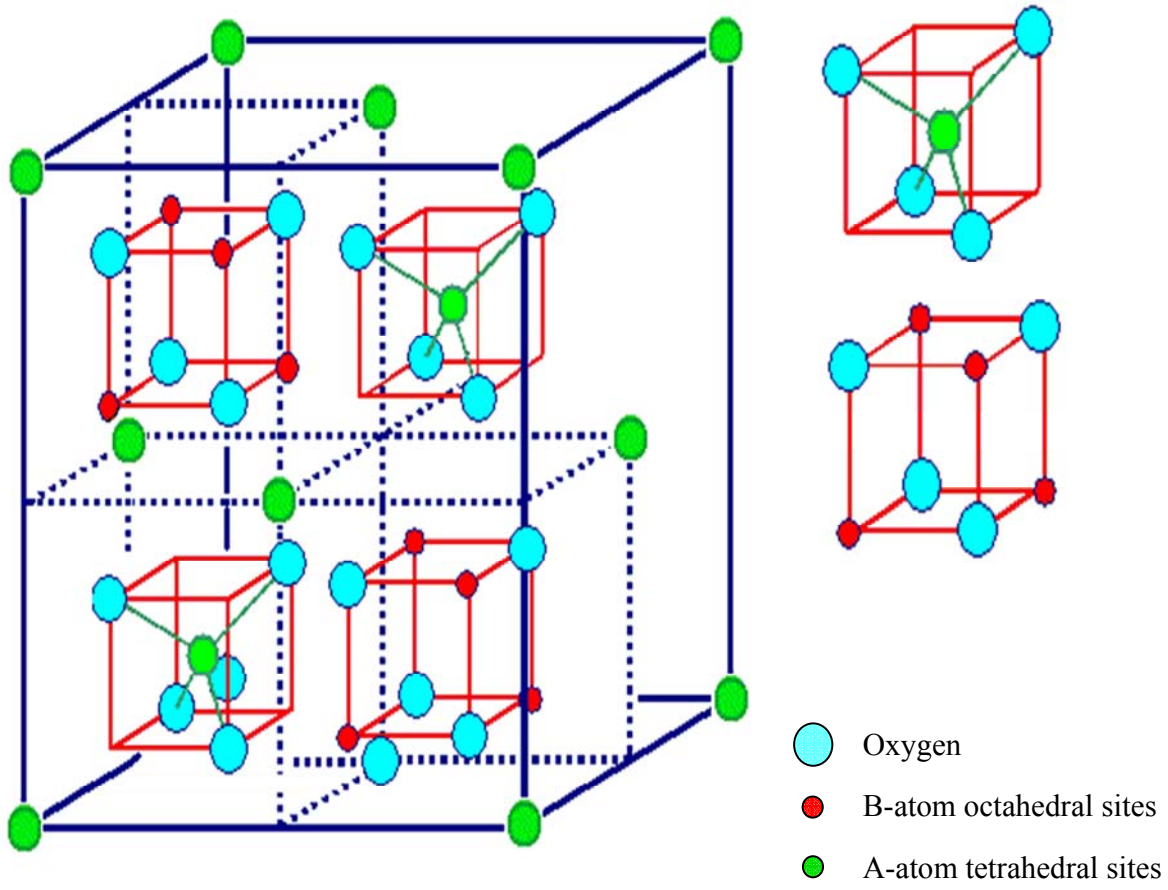

AB_2O_4 spinel The red cubes are also contained in the back half of the unit cell

Figure 1.7. Tetrahedral and octahedral sites in the spinel structure

Table 1.5. Different types of spinels

S. No.	Type	General formula
1	Normal	$(A^{2+})[B_2{}^{3+}]O_4$
2	Inverse	$(B^{3+})[A^{2+}B^{3+}]O_4$
3	Mixed	$(A^{2+}{}_{1-x}B_x{}^{3+})\ [Ax^{2+}B^{3+}B^{3+}{}_2\text{-}x]O_4$

() represents Tetrahedral sites, [] represents Octahedral sites.

1.7.1.2. Doped oxides

Sometimes metal oxides may not be active enough to achieve the highest performance in a given catalytic transformation. In order to overcome this limitation, metal oxide can be doped with a suitable transition element. Such interaction of metal oxide and dopant helps to change the physiochemical properties such as electronic configuration, orientation of particles, redox ability, and acid–base properties to accomplish the desirable performance. The material chosen as appropriate dopants depends on the atomic properties of both the dopant and on the host material. The importance of doping on the catalytic activity of a given material can be understood by considering the following examples.

Oxidation and reduction temperature of a metal can be varied as per the reaction conditions by choosing a suitable dopant material. For example, pure Co_3O_4 gives two reduction peaks at 600 K and 813 K. Reported TPR studies demonstrated that cobalt oxides in different environment undergo reduction of Co ion at different temperatures, e.g. cobalt supported on alumina [95]. The temperature at which reduction of cobalt ion occurs is strongly influenced not only by the oxidation state of the cobalt, but also by the nature of neighboring metal cations and/or metal oxide phases. In Co and Cu doped together on ceria, the presence of neighboring Cu and Ce ions strongly influences the reducibility of Co cations, which can be seen by decrease in reduction temperature of cobalt species [96-98]. Co or Cu supported on ceria does not offer good catalytic activity for preferential oxidation of CO under excess hydrogen atmosphere at low temperature. However, copper-cobalt doped on ceria gives enhancement in catalytic activity. This gives evidence to strong synergism between Co and Cu doped on ceria catalyst. Further, metal can be active in its zero oxidation state, but lack in stability could be resolved by choosing a proper dopant.

By suitable doping, thermal stability and surface area of the material can also be enhanced due to improvement of the mechanical strength of unstable phase of parent material. For example, significant improvement in surface area and thermal stability of small size alumina crystallites were obtained by incorporating cobalt species. In contrast, zinc as a dopant does not affect the cubic structure of the spinel and steadily improves the thermal stability with increased concentration of zinc.

1.8. QUANTITATIVE MEASUREMENT OF THE CATALYST PERFORMANCE

The overall performance of a catalytic reaction is determined in several ways such as TON (Turnover number), TOF (Turnover frequency), conversion, yield, selectivity and rate of the reaction. These terms are defined as follows.

1.8.1. Turnover number (TON): It is the ratio of moles of reactant reacted per mole of catalyst.

1.8.2. Turnover frequency (TOF): It is defined as number of moles of reactant reacted per mole of catalyst per unit time. Since it is normalized with respect to time, a true comparison of performance of various catalysts can be quantitatively obtained.

1.8.3. Conversion

Consider a chemical reaction,

$$A + B \longrightarrow C + D \tag{1.9}$$

% conversion of reactant A is defined as the percentage of reactant 'A' that is consumed in the reaction.

$$\text{Conversion (\%)} = \frac{\text{Inital conc. of A - Final conc. of A}}{\text{Inital conc. of A}} \text{ x100} \tag{1.10}$$

1.8.4. Yield

$$A + B \longrightarrow C + D \quad (1.11)$$

Where C is the desired product

$$\text{Yield (\%) of (C)} = \frac{\text{Conversion (\%) x Selectivity (C) (\%)}}{100} \quad (1.12)$$

1.8.5. Selectivity

Consider a chemical reaction,

$$A + B \longrightarrow C + D \quad (1.13)$$

Where C is the desired product

$$\text{Selectivity (\%) of (C)} = \frac{\text{Concentration of C formed}}{\text{Conc. of substrate consumed}} \text{ x100} \quad (1.14)$$

1.9. LITERATURE SUMMARY ON OXIDATION OF LIGNIN MODEL COMPOUNDS AND DERIVATIVES

Oxidation of lignin derived phenolic compounds such as vanillin alcohol, *p*-sinapyl alcohol, coniferyl alcohol, *p*-coumaryl alcohol, *p*-hydroxy benzyl alcohol, 4-hydroxy-3-methoxy alpha methyl phenol and non phenolic derivatives such as veratryl alcohol, 3-4-5 tri-methoxy benzyl alcohol, *p*-anisic alcohol, benzyl alcohol gives their respective aldehydes which are of an industrial importance. Conventionally, oxidation reactions are carried out using strong oxidants like pyridinium chlorochromate, pyridinium dichromate, aqueous sulfuric acid acetone-chromic acid, potassium permanganate, potassium dichromate, lead tetra acetate, sodium chlorite and

osmium tetra oxide [99-100] which create serious effluent problems. Due to the harmful effects of these conventional toxic and corrosive reagents on the environment and stringent result in set up of environmental laws and regulations all over the world. The use of eco-friendly catalysts for oxidation for the manufacture of fine and bulk chemicals has increased exponentially during the last couple of decades [101-104]. Since oxygen is the most abundant and cheapest primary oxygen donor without having any waste disposal problem, several publications have appeared in the literature on catalytic oxidation reactions of lignin model compounds (phenolic and non phenolic) using air/oxygen as an oxidant during last couple of decades and these are summarized in Table 1.6.

Table 1.6. Literature summary on oxidation of veratryl alcohol [105-136]

Sr. No.	Catalyst	Reactant	Product	Reaction conditions	Yield/ Conv. (%)	Product selectivity (%)	Refs.
1	Co(salen); Co(acacene); Co(salfosalen)	veratryl alcohol	veratryl aldehyde	373 K; O_2 pressure, 1 bar; pH=12; water + Pyridine; 23 h	TON= 25	80	105
2	[Cu(phen)(OH)$_2$]	veratryl alcohol	veratryl aldehyde	363 K; O_2 pressure, 1 bar; pH=12.6; water; 23 h	90	-	106
3	bis(o-phen) Cu	veratryl alcohol	veratryl aldehyde	373 K; O_2 pressure, 0.6 MPa; pH=12; (NaOH); water; 1 h	10	100	107

4	Co Acetate	veratryl alcohol	veratryl aldehyde	397 K; air flow, 30 mL/min; pH=12; Methanol; 3 h	100	-	108
5	Co-schiff base complexes/ 10%CuCl/ 10%LiCl	veratryl alcohol	veratryl aldehyde	RT; Methanol; 17 h	16	100	109
6	Cu(DACH), Cu(DAPHEN)	veratryl alcohol	veratryl aldehyde	303-403 K; O_2; pH = 12; NaOH; H_2SO_4; 3 hr	50	100	110
7	Co(salen)	veratryl alcohol	veratryl aldehyde	353 K; O_2 pressure, 0.1 MPa; pH=12; water; NaOH; 28 h	43	100	111
8	Co(Cl). $6H_2O$ 1-ethyl-3-methylimidazolium diethylphosphate (EMIMDEP)	veratryl alcohol	veratryl aldehyde	400 K; O_2 pressure, 0.5 MPa; NaOH, 1 mmol; EMIMDEP, 5 g; 3 h	100	100	112
9	Co(salen), Co(acacen)	veratryl alcohol	veratryl aldehyde	363 K; pH = 11; 1 h	100	-	113
10	Fe(III) porphyrins; $Cl_8TPPS_4Fe(III)$ $TPPS_4Fe(III)$	veratryl alcohol	veratryl aldehyde	pH 4.5; H_2O_2	83	12	114
11	Mn(TSPc)Cl;	veratryl	veratryl	297 K; aq. phosphate buffer;	16	100	115

	Fe(TSPc)Cl	alcohol	aldehyde	pH=10; *t*-BuOOH; 1 h			
12	Cucurbit[8]uril	veratryl alcohol	veratryl aldehyde	323 K; IBX:Cucurbit, [1:1]; 1 h	80	10	116
13	CH_3ReO_3	veratryl alcohol	veratryl aldehyde	298 K; O_2 pressure; H_2O_2; CH_3COOH	99	3 (Y)	117-118
14	CH_3ReO_3	vanillin alcohol	vanillin	298 K; O_2 pressure, 1 MPa; H_2O_2; CH_3COOH	98	4 (Y)	117-118
15	$VOPO_4$	veratryl alcohol	veratryl aldehyde	353 K; O_2 pressure, 0.4 MPa; Substrate, 0.125 mmol; TEMPO, 0.125 mmol; 4 h	100	99	119
16	Co-ZIF-9	veratryl alcohol	veratryl aldehyde	423 K; O_2 pressure, 0.5 MPa; NaOH, 1 mmol; toluene; 1 h	45(Y)	100	120
17	Ru/TiO_2	vanillin alcohol	vanillin	353 K; O_2 pressure, 80 bar; 2 h	46 (Y)	55	121
18	Au/CeO_2	vanillin alcohol	vanillin	323 K; O_2 pressure, 1 atm.; 2 h	96	98	122
19	9% Pt/SKT-4	vanillin alcohol	vanillin	353 K; air, 1 atm.; 1 h	94	95	123

	(Carbon)						
20	Co-saponite	vanillin alcohol	vanillin	338 K; O_2 flow 60 ml/min; iso-propanol; NaOH, 26 mmol; 3 h	55	100	124
21	Co(salen)	coniferyl alcohol	coniferyl aldehyde	298 K; O_2 pressure, 1 MPa; pH=12; $CHCl_3$; 1 h	60	100	125
22	Fe(HRP)–H_2O_2	*p*-coumaryl alcohol	*p*-coumaryl aldehyde	297 K; 0.1M, potassium phosphate buffer (pH 7.4)	42 (M)	-	126
		coniferyl alcohol	coniferyl aldehyde		26 (M)	-	
		sinapyl alcohol	sinapyl aldehyde		2 (M)	-	
23	Au/ZrO_2	benzyl alcohol	benzalde hyde	373 K; TBHP; 2 h	60	80	127
24	K-$CuTiO_2$	benzyl alcohol	benzalde hyde	483 K; O_2 pressure, 1 MPa	75	95	128
25	Au/Fe_2O_3	hydroxy benzyl alcohol	hydroxy benzalde hyde	323 K; O_2 pressure, 1 atm.; 2 h	90	92	129
26	2% Au-PVP	*p*-hydroxy benzyl alcohol	*p*-hydroxy benzalde hyde	300 K; air, 1 atm.; 8 h	91 (Y)	-	130

27	$Fe(TF_5PP)Cl$	anisole alcohol	anisaldehyde	298 K; pH=3 buffer; H_2O_2; 3 h	~35	-	131
28	$Fe(TF_5PP)Cl$	3,4,5-trimethoxybenzyl alcohol	3,4,5-trimethoxybenzylde hyde	298 K; pH=3; H_2O_2; 3 h	~50	-	131
29	Polyaniline supported vanadium catalyst	*p*-hydroxy benzyl alcohol	*p*-hydroxy benzalde hyde	373 K; O_2 pressure, 1 atm.; 9 h	96 (Y)	-	232
30	Cu-Mn oxide/C	*p*-hydroxy benzyl alcohol	*p*-hydroxy benzaldehyde	353 K; O_2 pressure, 0.4 MPa; 3.5 h	83	99	133
31	Mo-V-O	*p*-hydroxy benzyl alcohol	*p*-hydroxy benzaldehyde	353 K; O_2 pressure, 1 atm.; 24 h	83	99	134
32	Cu-Al hydrotalcite/ *rac*- BINOL	*p*-hydroxy benzyl alcohol	*p*-hydroxy benzalde hyde	278 K; air, 1 atm.; 12 h	75 (Y)	-	135
33	γ-Fe_2O_4	*p*-hydroxy benzyl alcohol	*p*-hydroxy benzalde hyde	370-373 K; Air flow , 40 mL/min; NaOH, 32 mmol; iso-propanaol; 8 h	50	60	136

Note: Y = (%) Yield, M= (%) Mole

M(TSPc) = Metal porphyrins

$Fe(TF_5PP)Cl$ = Fe-tetrakis(pentafluorophenyl)porphyrins

TEMPO = 2,2,6,6-tetramethylpiperidyl-1-oxy radical

EMIMDEP =1-ethyl-3-methylimidazolium diethyl phosphate

HRP = horseradish peroxidase

IBX = *o*-iodoxy benzoic acid

The literature survey showed that broadly, three types of catalysts systems were developed for liquid phase oxidation of lignin sub-structured molecules namely homogeneous, bio-catalyst and heterogeneous. In homogeneous type of catalytic systems, the complexes of metals used were Co, Cu, Mn and Fe [105-113]. Though these catalysts showed good catalytic activity in a basic medium (pH >12) they also suffered from serious drawbacks such as multistep synthesis of catalyst, requirement of stoichiometric amounts, tedious separation procedure of the catalyst-product from the reaction mixture, reusability of the catalyst, high production cost, trace amount of metal impurity in the final product which cannot be tolerated especially, when the product having applications in a pharmaceutical industry.

The bio-catalysts (enzyme) such as Fe(III)-porphyrins & horseradish peroxidase, Mn & Fe(TSPc)Cl, cucurbit(8)uril, etc., are reported for delignification of lignin via conversion of veratryl alcohol to veratryl aldehyde [114-116]. These enzyme catalyzed reactions showed superior activity, while some problems associated with this catalytic systems are lower selectivity, requires either strong basic (phosphate buffer) or acidic (ionic liquid) medium and in some cases, longer duration of reaction time compared to the homogeneous catalyst.

For the liquid phase oxidation of lignin sub-structured molecules, heterogeneous catalysts such as vanadium phosphate, ReO_3, γ-Fe_2O_4, Co-ZIF-9, Ru/TiO_2, Cu-Al-Hydrotalcite/rac-BINOL, Mo-V-O, Au/CeO_2, Pt & Pd & Cu-Mn oxide supported on carbon, Au/ZrO_2, cobalt saponite, Co-

salen/mont, Au/CeO_2, Pt & Pd based 9% Pt/SKT-4 are reported [117-136]. Among these Pt, Pd, Au, Ru and Re are noble metals and Co, Fe, Mn, Cu and Mo are non noble metal complexes. The noble metals are highly expensive and use of such catalysts will obviously enhance the production cost. However, among the non-noble catalysts vanadyl phosphate showed good activity. The problems associated with this catalytic system are oxidizing agent like TEMPO is required, possibility of leaching of vanadium in an aqueous medium cannot be ignored, recovery & reusability of catalyst and finally tedious separation of the final product due to use of TEMPO. Thus, considering all these facts there is a need to develop sustainable (green) catalyst system which can activate molecular oxygen without using any oxidizing agent in an aqueous medium for liquid phase oxidation of lignin sub-structured molecules. So far, there is no report on use of nano metal oxide (non-noble) prepared via inexpensive co-precipitation method for liquid phase oxidation of lignin sub-structured molecules, using molecular oxygen and without use of any alkali in aqueous medium. Also the correlation of morphology and redox ability of surface active species with observed catalytic activity is not reported.

Due to inherent property of cobalt to form a redox couple necessary for oxidation reaction, several heterogeneous cobalt catalysts have been studied reported for oxidation of various substrates. As a part of our research activities on designing and developing solid catalysts, various heterogeneous cobalt catalysts were reported recently for oxidation of side chain of phenol derivatives [137-142]. In the present thesis work, additional new cobalt catalysts such as Co_3O_4, $ZnCo_2O_4$, $CoAl_2O_4$ and Co/aluminosilicate catalysts are reported for liquid phase oxidation of lignin derived sub-structured compounds with molecular oxygen without using a base.

1.10. SCOPE AND OBJECTIVE OF THE PRESENT INVESTIGATION

Oxidation of lignin derived veratryl alcohol over solid catalysts selectively gives veratryl aldehyde of commercial importance. Mainly homogeneous metal complexes of cobalt, manganese, iron and copper were used for oxidation of the above substrates. However major problems associated with these catalysts are (a) deactivation of the catalysts due to thermal instability (b) pore blockage (c) use of alkali and peroxide required (d) multistep synthesis of catalyst and (e) formation of inactive, OH-bridged Co complexes under aqueous basic conditions causing catalyst deactivation. Hence, there is still a scope to develop active, selective and reusable solid catalysts for the oxidation reactions by modifying their redox properties. The major goal of this thesis is to design and develop highly active and selective solid catalysts for oxidation of lignin sub-structured phenolic and non phenolic compounds. Specific objectives of the present study are given below:

- Preparation of nano Co_3O_4 catalyst by various methods such as co-precipitation/digestion, sol-gel and thermal decomposition.
- Preparation of Zn and Al doped nano Co_3O_4 catalyst by co-precipitation/digestion method.
- Preparation of metal aluminosilicates with various compositions.
- Detail characterization of the prepared catalysts using various techniques such as N_2-adsorption-desorption isotherm, Brunauer-Emmett-Teller (BET), FTIR, XRD, XPS, HRTEM, SEM-EDX, TG-DTA, temperature programmed reduction (TPR), temperature programmed oxidation (TPO), cyclic voltammetry (CV), extended X-ray absorption fine structure (EXAFS), electron paramagnetic resonance (EPR), UV-Visible spectroscopy and ICP-OES.
- Activity testing of the above catalysts for liquid phase oxidation of veratryl alcohol.

- Optimization of reaction conditions for the best catalysts.
- Evaluation of the best catalyst chosen from the above studies for liquid phase oxidation of lignin sub-structured phenolic and non phenolic compounds.
- Interpretation of activity results based on the characterization data.

1.11. REFERENCES

1. J. J. Berzelius, *Ann. Chim. Phys.* 61 (1836) 146.
2. P. S. Weisz, *Ind. Eng. Chem. Fundamen.* 8 (1969) 325.
3. W. N. M. Piet van Leeuwen, in Homogeneous Catalysis Understanding the Art Kluwer academic Publishers 2004.
4. C. D. Frohling, C. W. Kohlpaintner, in Applied Homogeneous Catalysis with Organometallic Compounds, Volume 1, Eds.: Cornils, B; Herrmann, W. A., Wiley-VCH: Weinheim, 1996, p. 27.
5. C. Pariya, K. N. Jayaprakash, A. Sarkar, *Coord. Chem. Rev.* 168 (1998) 1.
6. G. W. Parshall, S. D. Ittel, Homogeneous Catalysis; John Wiley: New York, 1992.
7. R. Jira, Ethylene and its industrial derivatives, Miller S.A. (Ed.), Ernest Benn Ltd. 1969, p. 650.
8. J. N. Armor, *Appl. Catal. A: Gen.* 222 (2001) 407.
9. National Research Council Panel on New Directions in Catalytic Sciences and Technology, Catalysis Looks to the Future, National Academy Press, Washington D. C., (1992) p.1.
10. S. M. George, *Chem. Rev.* 95 (1995) 3.
11. Manassen, in Catalysis, Progress in Research, Eds.: Basolo, F; Burwell Jr., R. E., Plenum Press: New York, (1973) p. 177.
12. J. A. Schwarz, C. Contescu, A. Contescu, *Chem. Rev.* 95 (1995) 477.
13. G. Ertl, H. Knozinger, J. Weitkamp, Handbook of Heterogeneous Catalysis, Weinheim, VCH, vol. 1, 1997, p. 49.
14. T. Mallat, A. Baiker, *Chem. Rev*. 104 (2004) 3037.

15. A. E. Nielsen, Kinetics of Precipitation, Pergamon, 1964.

16. T. A. Ring, Fundamentals of Ceramic Powder Processing and Synthesis, Academic Press, 1996.

17. H. Furedi-Milhofer, *Pure Appl. Chem.* 53 (1981) 2041.

18. J. A. Dirksen, T. A. Ring, *Chem. Eng. Sci.* 46 (1991) 2389.

19. M. Lifshitz, V. V. Slyozov, *J. Phys. Chem. Solids.* 19 (1961) 35.

20. R. M. Tromp, J. B. Hannon, *Surf. Rev. Lett.* 9 (2002) 1565.

21. B. L. Cushing, V. L. Kolesnichenko, C. J. O'Connor*, Chem. Rev.* 104 (2004) 3893.

22. L. S. Dent Glasser , F. P. Glasser, H. F. W. Taylor, *Q. Rev. Chem. Soc.* 16 (1962) 343.

23. J. Gopalakrishnan, *Chem. of Mater.* 7 (1995) 1265.

24. L. G. Hubert-Pfalzgraf, S. Daniele, J. M. Decams, *J. Sol-Gel Sci. Technol.* 8 (1997) 49.

25. X. Wang, Z. Zhang, S. Zhou, Mater. *Sci. Eng. B: Solid-State Mater. Adv. Technol*. B86 (2001) 29.

26. H. D. Gesser, P .C. Goswami, *Chem. Rev.* 89 (1989) 765.

27. U. Schubert, N. Hüsing, Synthesis of Inorganic Materials, Wiley-VCH, 2000, pp. 396.

28. L. Zhou, J. Xu, X. Li, F. Wang, *Mater. Chem. and Phys.* 97 (2006) 137.

29. K. C. Patil, S. T. Aruna, S. Ekambaram, *Combustion synthesis. Curr. Opin. Solid State Mater. Sci.* 2 (1997) 158.

30. M. Hamdani, R. N. Singh, P. Chartier, *Int. J. Electrochem. Sci.* 5 (2010) 556.

31. S. Farhadi, K. Pourzare, *Mater. Research Bulletin* 47 (2012) 1550.

32. P. T. Anastas, T. C. Williamson, Green Chemistry, Oxford University Press, New York, 1998. 17

33. P. T. Anastas, J. C. Warner, Green Chemistry: Theory and Practice, Oxford University Press: New York, 1998, p.30.

34. R. A. Sheldon, in The Activation of Dioxygen and Homogeneous Catalytic Oxidation, D. H. R. Barton, A. E. Martell and D. T. Sawyer, Eds., Plenum Press, New York, 1993.

35. J. Ebner , D. Riley in Active Oxygen in Chemistry, J. S. Valentine, A. Greenberg and J. F. Liebman, Eds., Chapman and Hall, London, vol.1, 1995.

36. P. Skibida, A. M. Sakharov, *Catal. Today* 27 (1996) 187.

37. R. A. Sheldon, In Catalytic Oxidation: Principles and Applications: R. A. Sheldon, van Santen, Eds.; World Scientific: Singapore, 1995; p 177.

38. J. Ebner, D. Riley in Active Oxygen in Chemistry, J. S. Valentine, A. Greenberg and J. F. Liebman, Eds., Chapman and Hall, London, vol.1, 1995.

39. S. V. Ley, A. Madin in Comprehensive Organic Synthesis, Eds. B. M. Trost and I.Fleming, Pergamon, Oxford, 1990, vol. 7, pp 251.

40. F. A. Luzzio, *Org. React.* 53 (1998) 1.

41. R. A. Sheldon, H. van Bekkum, Fine Chemicals through Heterogeneous Catalysis, Wiley-VCH, Weinheim, 2001, p 1.

42. J. M. Thomas, R. Raja, G. Sankar, R. G. Bell, *Nature* 398 (1999) 227.

43. S. S. Stahl, *Angew. Chem. Int. Ed.* 43 (2004) 3400.

44. C. Limberg, *Angew. Chem. Int. Ed.* 42 (2003) 5932.

45. D. Sadow, T. D. Tilley, *Angew. Chem. Int. Ed.* 42 (2003) 803.

46. Subrahmanyam, B. Louis, F. Rainone, B. Viswanathan, A. Renken, T. K. Varadarajan, *Catal. Commun*. 3 (2002) 45.

47. Martin, U. Bentrup, A. B. Pckner, B. L. Pcke, *Catal. Lett.* 59 (1999) 61.

48. F. Konietzni, H. W. Zanthoff, W. F. Maier, *J. Catal.* 188 (1999) 154.

49. Martin, U. Bentrup, G. U. Wolf, *Appl. Catal. A: Gen.* 227 (2002) 131.

50. F. Bruhne, E. Wright, Ullmann's Encyclopedia of Technical Chemistry, 6th Edn., 1998, Electronic Release (benzaldehyde entry).

51. F. Konietzni, U. Kolb, U. Dingerdissen, W. F. Maier, *J. Catal.* 176 (1998) 527.

52. K. Suresh, M. M. Sharma, T. Sridhar, *Ind. Eng. Chem. Res.* 39 (2000) 3958.

53. G. W. Parshall, S. D. Ittel, Homogeneous Catalysis; John Wiley: New York, 1992.

54. R. Jira, Ethylene and its industrial derivatives, Miller S.A. (Ed.), Ernest Benn Ltd. 1969, p. 650.

55. R. A. Sheldon, I. W. C. E. Arends, A. Dijksman, *Catal. Today* 57 (2000) 157.

56. D. Riley, M. Stern, J. Ebner, in The Activation of Dioxygen and Homogeneous Catalytic Oxidation, D. H. R. Barton, A. E. Martell and D. T. Sawyer, Eds., Plenum Press, New York, 1993.

57. R. A. Sheldon, In Catalytic Oxidation: Principles and Applications: R. A. Sheldon, van Santen, Eds.; World Scientific: Singapore, 1995; p 177.

58. R. A. Sheldon, J. Dakka, *Catal. Today* 19 (1994) 15.

59. W. Kaim, B. Schwederski, Bioinorganic Chemistry: Inorganic Elements in the Chemistry of Life, John Wiley & Sons, 1994.

60. S. Lippard, J. Berg, Principles of Bioinorganic Chemistry, University Science Books, 1994.

61. R. A. Sheldon, Metalloporphyrins in Catalytic Oxidations, Marcel Dekker, Inc., New York, 1994.

62. R. D. Jones, D. A. Summerville, F. Basolo, *Chem. Rev.* 79 (1979) 139.

63. M. Costas, M. P. Mehn, M. P. Jensen, L. Que, Jr., *Chem. Rev.* 104 (2004) 939.

64. P. Skibida, A. M. Sakharov, *Catal. Today* 27 (1996) 187.

65. K. Karlin and Z. Tyeklár, in Bioinorganic Chemistry of Copper, Eds., Chapman & Hall, 1993.

66. Y. Cui, R. Patt, R. Chen, J. Gratzl, *J. Mol. Catal. A: Chem.* 144 (1999) 411.

67. R. Hage, J. E. Iburg, J. H. Koek, R. Martens, J. Kerschner, E. L. M. Lempers, R. J. Martens, U. S. Racheria, S. W. Russell, T. Swarthoff, M. R. P van Vliet, J. B. Warnaar, L. van der Wolf, B. Krijnen, *Nature* 369 (1994) 637.

68. W. Kaim, B. Schwederski, Bioinorganic Chemistry: Inorganic Elements in the Chemistry of Life, John Wiley & Sons, 1994.

69. J. E. Huuhey, E. A. Keiter, R. A. Keiter Eds., Inorganic Chemistry: Principles of structure and Reactivity Harper Collins College Publishers, New York, 1993.

70. M. Matsumoto, S. Ito, *J. Chem. Soc. Chem. Commun.* (1981) 907.

71. T. F. Blackburn, J. Schwartz, *J. Chem. Soc. Chem. Commun.* (1977) 157.

72. M. F. Semmelhack, C. R. Schmid, D. A. Cortes, C. S. Chou, *J. Am. Chem. Soc.* 106 (1984) 3374.

73. R. D. Jones, D. A. Summerville, F. Basolo, *Chem. Rev*. 79 (1979) 139.

74. E. C. Niederhoffer, J. H. Timmons, A. E. Martell, *Chem. Rev.* 84 (1984) 137.

75. D. H. Busch, N. W. Alcock, *Chem. Rev.* 34 (1994) 585.

76. N. J. Walton, M. J. Mayer, A. Narbad. *Vanillin. Phytochemistry* 63 (2003) 505.

77. D. G. Diddams, J. K. Krum in: Kirk–Othmer Encyclopedia of Chemical Technology, 2nd ed., Vol. 21, Interscience: New York, 1970, p. 183.

78. W. Haynes, This Chemical Age, 2nd ed., Knopf: New York, 1942, p. 37.

79. E. H. Hansen, B. L. Moller, G. R. Kock, C. M. Bunner, C. Kristensen, O. R. Jensen, F. T. Okkels, C. E. Olsen, M. S. Motawia, J. Hansen, *Appl. Environ. Microbiol.* 75 (2009) 2765.

80. R. A. Sheldon, H. van Bekkum, Fine Chemicals through Heterogeneous Catalysis, Wiley-VCH, Weinheim, 2001, p. 13.

81. J. L. G. Fierro, Metal Oxides: Chemistry and Applications, CRC Press, 2006.

82. K. Tanabe, M. Misono, Y. Ono and H. Hattori, Stud. Surf. Sci. Catal. Vol. 51 New Solid Acids and Bases and Their Catalytic Properties, 1989.

83. H. L. Emerson, *Catal. Rev*. 8 (1973) 285.

84. A. Clark, *Catal. Rev.* 3 (1969) 145.

85. G. M. Schwab, E. Roth, C. H. Grinzoz and N. Mavrakis, in "Structure and properties of solid surfaces" (R. Gomer and C. S. Smith, Eds.), Univ. Chicago Press, Chicago, 1953.

86. J. P. Suchet, "Chemical Physics of Semiconductors", Chap.5, p.82, Van Nostrand, London, 1965.

87. O. Muller, R. Roy, Major Ternary Structural Families, Springer-Verlag, 1974.

88. W. H. Bragg, *Philos. Mag.* 30 (1915) 305.

89. S. Nishikawa, *Proc. Tokyo Math. Phys.* 199 (1915) 4.

90. F. S. Galasso, Structure and Properties of Inorganic Solids, Pergamon, 1970.

91. R. W. G. Wycko, Crystal Structures. *Vol. 4,* Miscellaneous inorganic compounds, silicates, and basic structural information, Wiley and Sons, New York, 1969.

92. J. G. Na, T. D. Lee, S. J. Park, *IEEET. Magn.* 28 (1992) 2433.

93. Z. J. Zhang, Z. L. Wang, B. C. Chakoumakos, J. S. Yin, *J. Am. Chem. Soc.* 120 (1998) 1800.

94. R. Arulmurugan, B. Jeyadevan, G. Vaidyanathan, S. Sendhilnathan, *J. Magn. Magn. Mater.* 288 (2005) 470.

95. W. Chu, P. A. Chernavskii, L. Gengembre, G. A. Pankina, P. Fongarland, *J. Catal.* 252 (2007) 215.

96. P. Arnoldy, J. A. Moulijn, *J. Catal*. 93 (1985) 38.

97. L. Ji, J. Lin, H. C. Zeng, *J. Phys. Chem. B* 104 (2000) 1783.

98. T. Paryjczak, J. Rynkowski, S. Karski, *J. Chromatogr.* 188 (1980) 254.

99. F. A. Luzzio, *Org. React*. 53 (1998) 1.

100. R. A. Sheldon, H. van Bekkum, Fine Chemicals through Heterogeneous Catalysis, Wiley-VCH, Weinheim, 2001, p. 1-2.

101. W. C. E. Arends, R. A. Sheldon, *Appl. Catal. A: Gen.* 212 (2001) 175.

102. D. E. De Vos, M. Dams, B. F. Sels, P. A. Jacobs, *Chem. Rev*. 102 (2002) 3615.

103. D. C. Bailey, S. H Langer, *Chem. Rev*. 81 (1981) 109.

104. B. C. Gates, *Stud. Surf. Sci. Catal*. 29 (1986) 4153.

105. K. Kervinen, P. Lahtinen, T. Repo, M. Svahn, M. Leskelä, *Catal. Today* 75 (2002) 183.

106. H. Korpi, P. J. Figiel, E. Lankinen, P. Ryan, M. Leskelä, T. Repo, *Eur. J. Inorg. Chem.* 17 (2007) 2465.

107. V. O. Sippola, A. O. I. Krause, *Catal. Today* 100 (2005) 237.

108. S. Mukhopadhyay , S. Ananthakrishnan, Sampatraj B. Chandalia, *Org. Proc. Res. Dev.* 3 (1999) 365.

109. J. Bozell, B. R. Hames, *J. Org. Chem.* 60 (1995) 2398.

110. P. Lahtinen, H. Korpi, E. Haavisto, M. Leskela, T. Repo *J. Comb. Chem.* 6 (2004) 967.

111. K. Kervinen, H. Korpi, J. G. Mesu, F. Soulimani, T. Repo, B. Rieger, M. Leskela, B. M. Weckhuysen, *Eur. J. Inorg. Chem.* 24 (2005) 2591.

112. J. Zakzeski, A. L. Jongerius, B. M. Weckhuysen, *Green Chem.* 12 (2010) 1225.

113. V. O. Sippola, A. O. I. Krause, *J. of Mole. Catal. A: Chem.* 194 (2003) 89.

114. A. Kumar, N. Jain, S. M. S. Chauhan, *Synlett*. 3 (2007) 411.

115. F. Cui, D. Dolphin, *Biorg. Med. Chem.* 3 (1995) 471.

116. C. Hang, Z. F. Fang, Z. J. Xin, Z. Xi, T. Zhu, X. S. Feng, Z. Q. Jiang, *Catal. Commun.* 11 (2009) 167.

117. C. Crestini, P. Pro, V. Neri, R. Saladino, *Bioorg. Med. Chem. Lett.* 13 (2005) 2569.

118. C. Crestini, M. C. Caponi, D. S. Argyropoulos, R. Saladino, *Biorg. Med. Chem*. 14 (2006) 5292.

119. Z. Du, J. Ma, H. Ma, J. Gao, J. Xu, *Green Chem.* 12 (2010) 590.

120. J. Zakzeski, A. Debczak, P. C. A. Bruijnincx, B. M. Weckhuysen, *Appl. Catal. A: Gen.* 394 (2011) 79.

121. Kockritz, M. Sebek, A. Dittmar, J. Radnik, A. Bruckner, U. Bentrup, M. M. Pohl, H. Hugl, W. Magerlein, *J. Mol. Catal. A: Chem.* 246 (2006) 85.

122. A. Abad, P. Concepcion, A. Corma, H. Garcia, *Angew. Chem. Int. Ed.* 44 (2005) 4066.

123. L. Tarasov, L. M. Kustov, A. A. Bogolyubov, A. S. Kiselyov, V. V. Semenov, *Appl. Catal. A: Gen.* 366 (2009) 227.

124. A. C. Garade, N. S. Biradar, S. M. Joshi, V. S. Kshirsagar, R. K. Jha, C. V. Rode, *Appl. Clay Sci.* 53 (2011) 157.

125. Canevali, M. Orlandi, L. Pardi, B. Rindone, R. Scotti, J. Sipila, F. Morazzoni, *J. Chem. Soc., Dalton Trans.* 15 (2002) 3007.

126. T. Kobayashi, H. Taguchi, *Wood Sci*. 51 (2005) 607.

127. V. R. Choudhary, D. K. Dumbre, S. K. Bhargava, *Ind. Eng. Chem. Res.* 48 (2009) 9471.

128. Y. Dai, X. Yan, Y. Tang, X. Liu, L. Xiao, J. Fan, *ChemCatChem* DOI: 10.1002/cctc.201200196.

129. C. Milone, R. Ingoglia, G. Neri, A. Pistone, S. Galvagno, *Appl. Catal. A: Gen.* 211 (2001) 251.

130. H. Tsunoyama, H. Sakurai, Y. Negishi, T. Tsukuda, *J. Am. Chem. Soc.* 127 (2005) 9374.

131. P. Zucca, F. Sollai, A. Garau, A. Rescigno, E. Sanjust, *J. Mol. Catal. A: Chem.* 306 (2009) 89.

132. S. R. Reddy, S. Das, T. Punniyamurthy, *Tetrahedron Lett.* 45 (2004) 3561.

133. G.Yang, W. Zhu, P. Zhang, H. Xue, W. Wang, J. Tian, M. Song, *Adv. Synth. Catal.* 350 (2008) 542.

134. Wang. W. Ueda, *Catal. Today* 144 (2009) 358.

135. R. Lakshmi Kantam, P. R. Arundhathi, D. D. Likhar, *Adv. Synth. Catal.* 351 (2009) 2633.

136. V. R. Mate, M. Shirai, C. V. Rode, *Catal. Commun.*33 (2013) 66.

137. A. C. Garade, M. Bharadwaj, S. V. Bhagwat, A. A. Athawale, C. V. Rode, *Catal. Commun.*10 (2009) 485.

138. V. S. Kshirsagar, S. Vijayanand, H. S. Potdar, P. A. Joy, K. R. Patil, C. V. Rode, *Chem. Lett.* 37 (2008) 310.

139. V. S. Kshirsagar, K. R. Patil, M. Shirai, C. V. Rode, *Top. Catal.* 52 (2009) 784.

140. V. S. Kshirsagar, A. C. Garade, K. R. Patil, R. K. Jha, C. V. Rode, *Ind. Eng. Chem. Res.* 48 (2009) 9423.

141. V. S. Kshirsagar, A. C. Garade, K. R. Patil, A. Yamaguchi, M. Shirai, C. V. Rode, *Appl. Catal. A: Gen.* 370 (2009) 16.

142. A. C. Garade, M. Bhardwaj, S. V. Bhagwat, A. A. Athawale, C. V. Rode, *Catal. Commun.* 10 (2009) 485.

Chapter 2

Experimental

The catalytic activity of oxide materials with unique physical and chemical properties such as surface area, morphology, redox ability, etc., are entirely based on the synthetic strategies followed for their preparation [1-10]. Hence, selection of a proper method for the preparation of catalysts and their detailed characterization are very crucial in order to understand the structure-activity correlation. Present chapter describes the details of procedures followed for the preparation of various catalysts, their characterization and activity testing for oxidation reactions.

2.1. MATERIALS

$(Co(NO_3)_2.6H_2O)$, $(Zn(NO_3)_2.6H_2O)$, $(Al(NO_3)_3.9H_2O)$, (K_2CO_3), veratryl alcohol, veratryl aldehyde, 3,4-di-methoxy benzoic acid, vanillin alcohol, vanillin, vanillic acid, *p*-methoxy benzyl alcohol (*p*-anisic alcohol), *p*-anisaldehyde, *p*-anisic acid, *p*-hydroxy benzyl alcohol, *p*-hydroxy benzaldehyde, *p*-hydroxy benzoic acid, *p*-sinapyl alcohol, *p*-sinapyl aldehyde, *p*-sinapic acid, coniferyl alcohol, coniferyl aldehyde, coniferic acid, *p*-coumaryl alcohol, *p*-coumaryl aldehyde, *p*-coumaric acid, 4-hydroxy-3-methoxy-alpha methyl benzylalcohol, 4-hydroxy-3-methoxy phenyl ethanone, benzylalcohol, benzaldehyde, benzoic acid, 3,4,5 tri methoxy benzylalcohol and 3,4,5 tri methoxy benzaldehyde were purchased from Sigma-Aldrich, Bangalore, India. Acetate precursors of cobalt, magnesium, copper, iron, and other chemicals such as sodium silicate, urea, sodium hydroxide, were purchased from Merck limited, India. HPLC grade methanol was obtained from M/s Runa Chemicals, India. UHP grade oxygen cylinder purchased from Deluxe Pvt. Ltd. Pune, India.

2.2. CATALYST PREPARATION

2.2.1. Simultaneous co-precipitation and digestion method

The nano structured Co_3O_4 was prepared using $Co(NO_3)_2 \cdot 6H_2O$ and K_2CO_3 by a simple protocol without using any template, involving a simultaneous co-precipitation and digestion method

followed by calcination in the range of 573-873 K in air for 1-6 h [11]. For the preparation of nano structured Zn and Al doped Co_3O_4 catalysts, $Zn(NO_3)_2 \cdot 6H_2O$ and $Al(NO_3)_3 \cdot 9H_2O$ were used following the above preparation procedure. Experimental setup is shown in Figure 2.1.

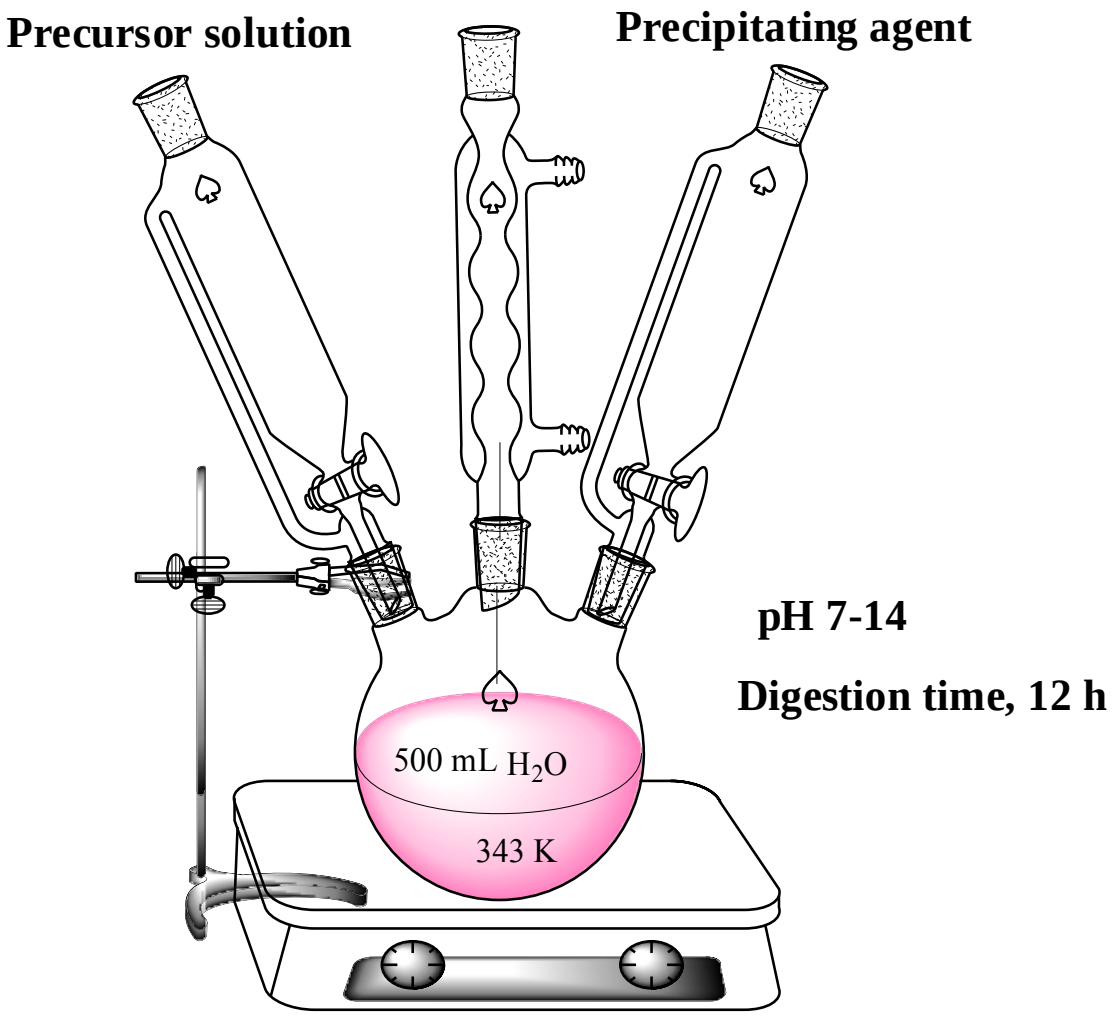

Figure 2.1. Catalyst preparation set up

2.2.1.1. Co_3O_4

Nano structured spinel Co_3O_4 catalyst was prepared by a co-precipitation method with simultaneous addition of (0.03 M) aqueous solution of $Co(NO_3)_2 \cdot 6H_2O$ and 0.6 M aqueous

K_2CO_3 in a round bottom flask having 100 mL of distilled water at 343 K temperature. The pH of the solution was maintained in the range of ~7.5-8 by adding K_2CO_3 (0.6 M) solution during precipitation. The obtained precipitate was digested for 12 h and then filtered and washed with deionized water to remove the traces of potassium. The precipitate was dried in an oven at 373 K for 6 h. EDX of the as-dried precursor confirmed the presence of cobalt, oxygen, carbon elements and absence of any potassium in all the samples (Chapter 3, Section 3.3.1.8). The as-dried precursor was calcined at 573 K temperature for 5 h in air.

The different catalysts were prepared by adjusting pH of the solution in the range of ~9-10 (Co-b), ~11-12 (Co-c) and ~13-14 (Co-d). These prepared catalysts were calcined at 573 K for 5 h in air. The effect of calcination time in the range of 1-6 h (at constant calcination 573 K) was also studied for the as-dried precursors of Co-a (pH=7-8) and Co-b (pH=13-14) samples.

2.2.1.2. Zn doped Co_3O_4

Zn doped Co_3O_4 catalyst was prepared by a co-precipitation method with simultaneous addition of (0.01 M) mixture of an aqueous solutions of $Zn(NO_3)_2.6H_2O$ and $Co(NO_3)_2 \cdot 6H_2O$ and 0.6 M aqueous K_2CO_3 in a round bottom flask having 100 mL of distilled water at 343 K temperature. The pH of the solution was maintained in the range of ~7.5-8 by adding K_2CO_3 (0.6 M) during precipitation. The obtained precipitate was digested for 12 h and then filtered and washed with deionized water to remove the traces of potassium. The precipitate was dried in an oven at 373 K for 6 h. EDX of the as-dried precursor confirmed the presence of zinc, cobalt, oxygen, carbon elements and absence of any potassium in all the samples (Chapter 4, Section 4.2.1.7). The as-dried precursor was calcined at 573 K and 873 K temperature for 5 h in air.

Likewise, different catalyst samples were prepared by changing Zn and Co compositions such as 1:2 and 1:3. These as-dried precursors were calcined at 573 K and 873 K for 5 h in air.

2.2.1.3. Al doped Co_3O_4

Al doped Co_3O_4 catalyst was prepared by a co-precipitation method with a simultaneous addition of (0.01 M) mixture of an aqueous solutions of $Co(NO_3)_2 \cdot 6H_2O$ and $Al(NO_3)_3.9H_2O$ and 0.6 M aqueous K_2CO_3 in a round bottom flask having 100 mL of distilled water at 343 K temperature. The pH of the solution was maintained in the range of ~7.5-8 by adding K_2CO_3 (0.6 M) solution during precipitation. The obtained precipitate was digested for 12 h and then filtered and washed with deionized water to remove the traces of potassium. The precipitate was dried in an oven at 373 K for 5 h. EDX of the dried precursor confirmed the presence of aluminium, cobalt, oxygen, carbon elements and absence of any potassium in all the samples (Chapter 4, Section 4.2.2.7). The as-dried precursor was calcined at 573 K and 873 K temperature for 5 h in the air.

Likewise, different samples were prepared by changing Co and Al compositions such as 1:2 and 3:1. These as-dried precursors were calcined at 573 K and 873 K for 5 h in the air.

2.2.2. Sol-Gel method

The solution of ethylene glycol (0.16 mole) and $CoC_2O_4 \cdot 4H_2O$ (0.07 mole) in methanol (0.28 mole) was stirred magnetically for half an hour to obtain a sol. This sol was dried at 413 K for half an hour for gelation [12-15]. The gel was than calcined at 573 and 873 K for 5 h in air. The chemical route of the synthesis can be represented as:

$$(CH_3COO_2)_2\,Co \xrightarrow[\text{Methanol}]{\text{Ethylene glycol}} \text{Sol} \xrightarrow{413\ K} \text{Gel} \xrightarrow{573\ K} Co_3O_4$$

2.2.3. Thermal decomposition

In thermal decomposition method, precursor, $Co(NO_3)_2 .6H_2O$ was calcined at 573 K in a static air for 5 h. Similarly, cobalt acetate precursor was calcined at 573 K in a static air for 5 h [16-19]. The chemical route of the synthesis can be represented as:

$$3[Co(NO_3)_3.6H_2O] \xrightarrow[\text{in air}]{573\ K} Co_3O_4$$

$$3[(CH_3COO_2)_2\,Co] \xrightarrow[\text{in air}]{573\ K} Co_3O_4$$

2.2.4. Metal aluminosilicate catalysts

The aluminosilicates with different Si/Al (SA-10:1, SA-1:1, SA-1:5 and SA-1:10) ratios were prepared by making a slurry (in proportion) of sodium silicate, aluminium nitrate and sodium hydroxide [20-21]. In a typical procedure, for *in-situ* preparation of cobalt aluminosilicate catalyst, the solutions of the cobalt acetate and urea were added over aluminosilicates of various Si/Al ratios.

A slurry of sodium silicate (10 M), aluminium nitrate (1 M) and sodium hydroxide (0.01 M) was made in deionized water (100 mL) and was stirred for half an hour at 368 K. After obtaining the homogeneous mixture, cobalt acetate (0.012 M) and urea (0.215 M) were added. This whole mixture was stirred for 12 h at 368 K. After cooling, resulting solution was filtered and dried in a static air at 413 K.

The catalysts with various loadings of cobalt (5–30%) in aluminosilicates were prepared by changing alumina silica ratios such as Si/Al-10:1 (CSA-1), Si/Al-1:1 (CSA-2), Si/Al-1:5 (CSA-3) and Si/Al-1:10 (CSA-4. Similarly, copper (CuSA-4), manganese (MSA-4) and iron (FSA-4)

catalysts were prepared by keeping silica alumina ratio constant (1:10). The solutions of the copper, manganese and iron acetate precursors were added to aluminosilicate by following the above preparation procedure. Preparation steps are shown schematically in Figure 2.2.

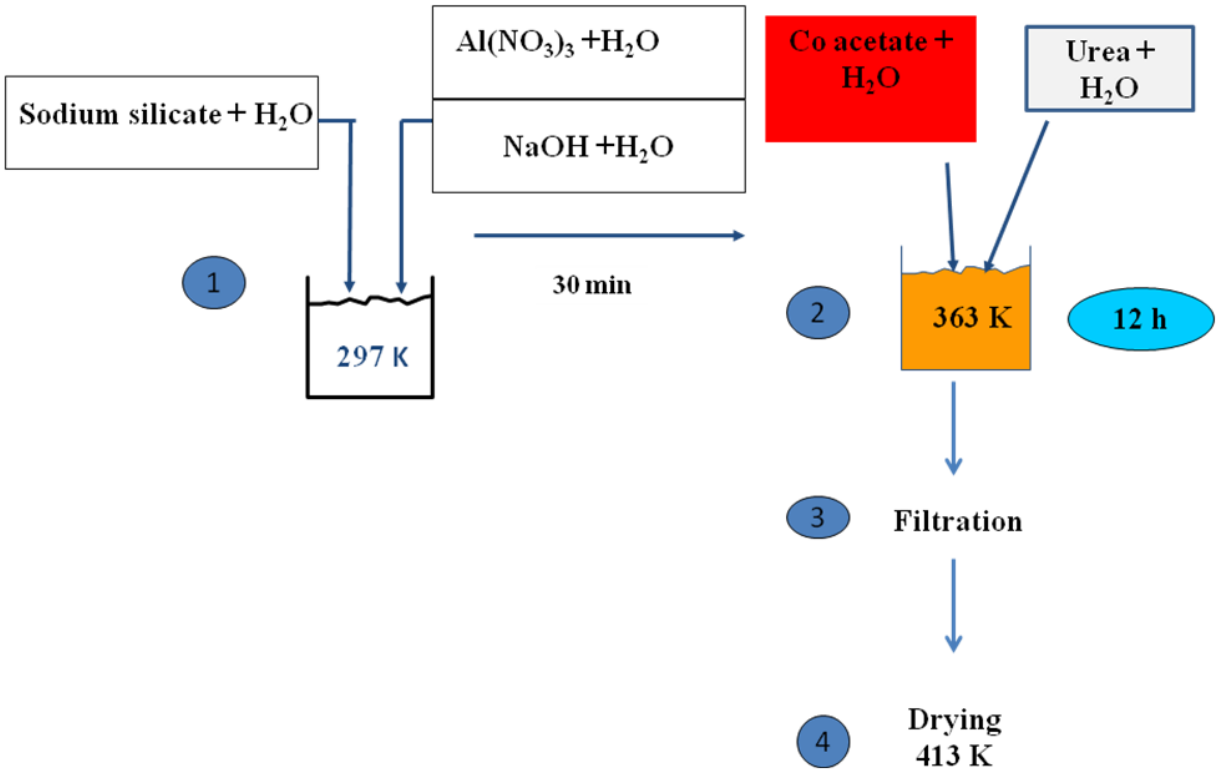

Figure 2.2. Preparation of metal aluminosilicate catalyst

2.3. PHYSICO CHEMICAL CHARACTERIZATION

The prepared catalyst samples were characterized by various physico chemical methods such as surface area, adsorption-desorption isotherm, pore size distribution, pore volume, XRD, XPS, FTIR, SEM, EXAFS, TGA, HRTEM, SEM, EDAX, TPR, TPO, CV, and EPR. This section gives a brief account of the theory and principle of various characterization techniques used for the present study for establishing the correlation between activity of catalyst and their physico

chemical properties. The procedure for each characterization technique is described here while, the detailed characterization results are discussed in the relevant chapters.

2.3.1. Surface area measurement

Brunauer, Emmett and Teller (BET) method: This is based on the multilayer adsorption. The BET equation can be represented as

$$\frac{P}{V(P_0-P)} = \frac{1}{c} Vm + [(c-1)/cVm](P/P_0) \quad (2.1)$$

Where,

P is adsorption equilibrium pressure (N/m^2)

P_0 is saturation vapor pressure of the adsorbate at the experimental temperature (K)

V is volume (m^3) of N_2 adsorbed at a pressure 'P'

Vm is the volume of adsorbate required for monolayer coverage, (m^3/mole)

c is a constant that is related to the heat of adsorption and liquefaction [22].

A linear relationship between $P/V(P_0-P)$ and P/P_0 is required to be obtained for the quantity of nitrogen adsorbed. The monolayer volume, 'Vm' is given by

$$Vm = \frac{1}{S+I} \quad (2.2)$$

Where,

S is the slope and is equal to $(c-1)/c\ V_m$

I is the intercept equal to $1/c\ V_m$

The surface area of the catalyst (S_{BET}) is related to V_m, by the equation

$$S_{BET} = \frac{Vm}{22414} Na \qquad (2.3)$$

Where,

Na : Avogadro number (6.023×10^{23} atoms/mol)

Unit of S_{BET} = m^2/g

Adsorption of nitrogen measured by Brunauer-Emmett-Teller (BET) equation at low pressure (10^{-4} Torr) and liquification temperature of N_2 (77 K) is the standard method for determination of surface area, pore volume and pore size distribution of molecular sieves.

N_2 adsorption-desorption isotherms of the catalysts were obtained at liquid N_2 temperature (77 K) using Quantachrome Nova-1200 adsorption unit and Micromeritics Chemisorb 2720. About 100 mg of sample was degassed at 473 K for about 4 hours till the residual pressure was < 10^{-3} Torr. The isotherms were analyzed in a conventional manner, and the pore size distribution was calculated using the BJH method.

2.3.2. X-ray diffraction technique (XRD)

Powder X-ray diffraction (XRD) is a basic tool for characterization of material for its phase identification [23-24]. Each crystalline solid has its unique characteristic X-ray powder pattern, which may be used as a "fingerprint" for its identification. X-ray diffraction is a versatile, non-destructive analytical technique for identification and quantitative determination of the various crystalline compounds, known as 'phases', present in solid materials and powders. Identification is achieved by comparing the X-ray diffraction pattern or 'diffractogram' obtained from an unknown sample with an internationally recognized database containing reference patterns of almost all known phases. Modern computer-controlled diffractometer systems use automatic

routines to measure, record and interpret the unique diffractograms produced by individual constituents in even highly complex mixtures.

The characteristics of X-ray diffraction were discovered by W. H. Bragg [25]. When a monochromatic X-ray beam with wavelength λ is projected onto a crystalline material at an angle θ, diffraction occurs only when the distance traveled by the rays reflected from successive planes differ by a complete number 'n' of wavelengths. The incident X-radiation strikes the planes (hkl) at an angle θ. The spacing between these planes is 'd'. Relationship between the wavelength of X-ray beam, the angle of diffraction θ, and the distance between each set of planes separated with spacing 'd' is given by the Bragg's equation.

$$n\lambda = 2d\sin\theta \qquad (2.4)$$

Where 'n' is the order of the diffraction. The diffraction of X-rays on a set of crystals can be represented schematically as shown in Figure 2.3. Bragg's law is the necessary condition for diffraction.

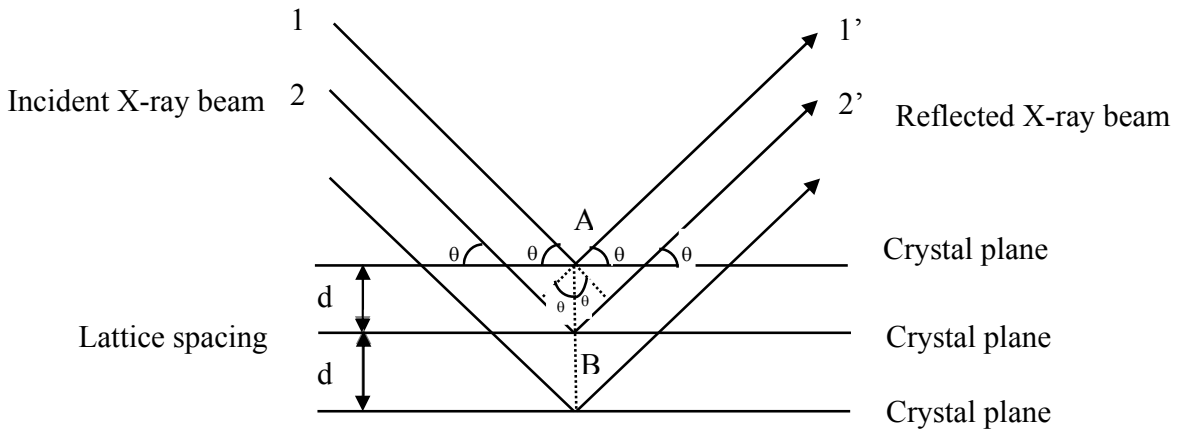

Figure 2.3. Diffraction of X-rays

The angular spread of the reflection from a crystal plane is affected not only by the perfection of the crystal but also by the size of the crystal. As the average size of the crystallites decreases, the angular spread of the reflection from a powder will increase. After suitable calibration, the full width at half maximum of a reflection in a powder diffractogram can be used as quantitative measure of the mean crystallite size of the sample.

The formula used for calculating crystallite size is the Scherrer formula as given in equation 2.5.

$$K = \frac{0.9\,\lambda}{B\,Cos\,\theta} \qquad (2.5)$$

Where,

λ is wavelength (nm) of X-ray

B is full width at half maximum of the pattern (radians)

θ is the Bragg angle (º)

B is corrected for contribution from instrument line broadening by recording the pattern of a standard sample having very large particle size in the micrometer range.

In the present work, all the X-ray diffraction patterns were recorded on a PANalytical X'PERT PRO model X-ray diffractometer, at the scan rate of 5^o/min in the 2θ range of 10º to 90º. Powder XRD patterns can be simulated from knowledge of the crystallographic parameters of the specific material. The minimum required parameters for simulating a pattern are the space group, unit cell lattice parameters, atomic positions and the occupancy parameters of different atoms in the unit cell. In the present work, the XRD patterns of various compounds were

simulated using a computer program 'Powder Cell for Windows', PCW version 2.4, developed by Krauz and Nolze [24-26]. Along with the simulated pattern, the corresponding XRD patterns were compared with the standard available data from the Joint Committee on Powder Diffraction Standards (JCPDS), International Center for Diffraction Data, with the card number.

2.3.3. X-ray Photoelectron Spectroscopy (XPS)

All solid materials interact with their surroundings through their surface. The physical and chemical composition of these surfaces determines the nature of the interactions. Their surface chemistry will influence factors such as catalytic activity, adhesive properties, contact potential and corrosion rates. Surface therefore, influence many crucially important properties of the solid. Despite the undoubted importance of surface, only a very small proportion of the atoms of most solids are found at the surface. Nonetheless, the proportion of surface contribution increases with a decrease in particle size, especially below 100 nm. XPS is based on the photoelectric effect discovered by Heinrich Hertz and explained later by Albert Einstein [27-29], which involves the bombardment of a solid surface with X-rays and the measurement of the concomitant photoemitted electrons. XPS is a widely used technique for obtaining chemical information of various material surfaces. The low kinetic energy ($0 \leq 1500$ eV) of emitted photoelectrons limit the depth from which it can emerge, so that XPS is a very surface-sensitive technique and the sample depth is in the range of 10 nanometers. Photoelectrons are collected and analyzed by the instrument to produce a spectrum of emission intensity versus electron binding (or kinetic) energy.

In general, the binding energies of the photoelectrons are characteristic of the element from which they are emitted, so that the spectra can be used for surface elemental analysis. Small

shifts in the elemental binding energies provide information about the chemical state of the elements on the surface. The peak area can be used to determine the surface compositions of the material. Therefore, the high-resolution XPS studies can provide the chemical state information of the surface.

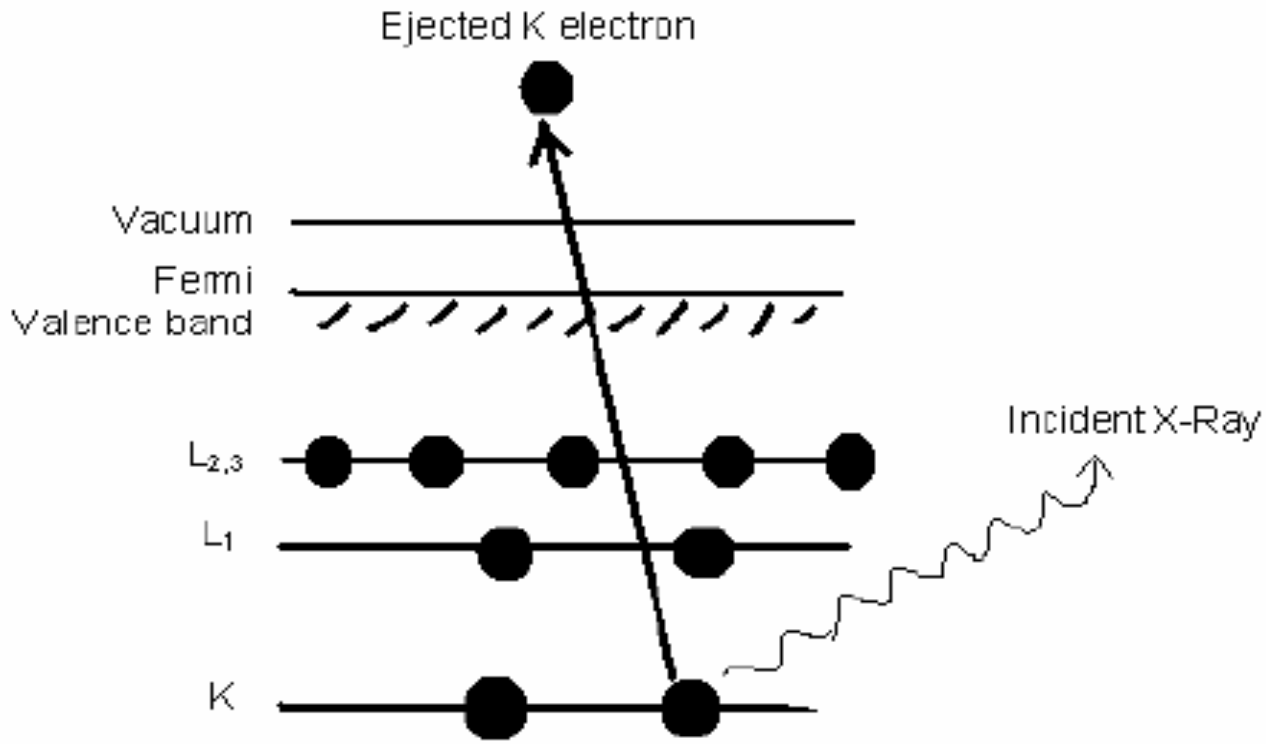

Figure 2.4. Schematic diagram of the XPS technique, showing photo ionization of an atom by the ejection of a 1s electron

The photoemitted electrons have discrete kinetic energy that is the characteristics of the emitting atoms and their bonding states. The kinetic energy, E_k of these photoelectrons is determined from the energy of the incident X-ray radiation ($h\nu$) and the electron binding energy (E_b) is given as

$$E_k = h\nu - E_b \quad (2.6)$$

The experimentally measured energies of the photoelectrons are given as

$$E_w = h\nu - E_b - E_w \quad (2.7)$$

Where E_w is the work function of the spectrometer.

The process of photoemission is shown schematically in Figure 2.4, where an electron ejected from the K shell of the atom (1s photoelectron). Once a photoelectron has been emitted, the ionized atom must relax in some way. This can be achieved by the emission of an X-ray photon, known as X-ray fluorescence. The other possibility is the ejection of an Auger electron through a secondary process. XPS can provide elemental analysis for essentially the entire periodic table.

X-ray Photoelectron spectra were acquired on a VG Microtech Multilab ESCA 3000 spectrometer using a non-monochromatized Mg Kα X-ray source (hν = 1253.6 eV). Base pressure in the analysis chamber was 4×10^{-10} Torr. Multichannel detection system with nine channels was employed to collect the data. The overall energy resolution of the instrument was better than 0.7 eV, determined from the full width at half maximum of the $4f_{7/2}$ core level of gold surface. The errors in all the B.E. values were within ±0.1 eV. The binding energy correction was performed using the C_{1S} peak of carbon at 284.6 eV as the reference.

2.3.4. Extended X-ray absorption fine structure spectroscopy (EXAFS)

Extended X-ray absorption fine structure spectroscopy uses the X-ray photoelectric effect and the wave nature of the electron to determine local structures around selected atomic species in materials. Unlike X-ray diffraction, it does not require long range translational order hence it works equally well in amorphous materials, liquids, (poly) crystalline solids, and molecular

gases. XANES (X-ray absorption near-edge structure) can be sensitive to charge transfer, orbital occupancy and symmetry. Precise local structural information can be obtained (inter atomic bond distances, coordination numbers, number of atoms, types of disorder) for the crystalline or noncrystalline systems e.g. metalloprotein, active sites, liquids, amorphous materials. Additional information on charge state, orbital occupancy may also be available by studying XANES depending on the system and the edge. X-ray absorption near edge structure (XANES) and extended X-ray absorption fine structure (EXAFS) measurements were performed using a synchrotron radiation ring at BL-9C, Photon Factory, KEK at Tsukuba (Japan) with a Si (111) double-crystal monochrometor in the transmission mode at room temperature. The spectra were analyzed by the UWXAFS package [30]. The XANES spectra were normalized by their edge jumps to be unity. After background subtraction, k-weighted EXAFS functions in the k range of 20–110 nm^{-1} were Fourier transformed into an R-space. The spectrum was fitted in the corresponding k-space of the R range 0.10–0.20 nm. The backscattering amplitudes and phase shifts were calculated by the FEFF8 code [31].

2.3.5. Thermal gravimetric analysis (TGA)

Thermal gravimetric analysis is an analytical technique used to determine the thermal stability of the material and its fraction of volatile components by monitoring the weight change that occurs as a specimen is heated. The measurement is normally carried out in air or in an inert atmosphere, such as helium, nitrogen or argon, and the weight is recorded as a function of increasing temperature. The variation in mass of a sample is measured when it undergoes a temperature scanning in a controlled atmosphere. Such analysis relies on a high degree of precision in three measurements: weight, temperature, and temperature change. As many weight loss curves look similar, the weight loss curve may require transformation before results may be

interpreted. A derivative weight loss curve can be used to tell the point at which weight loss is most apparent. Differential thermal analysis (DTA) is a technique measuring the difference in temperature between a sample and a reference (a thermally inert material) as a function of the time or the temperature, when they undergo temperature scanning in a controlled atmosphere. The DTA method enables any transformation to be detected for all the categories of materials, providing information on exothermic and endothermic reactions taking place in the sample, which include phase transitions, dehydration, decomposition, redox, or solid-state reactions. In catalysis, these techniques are used to study the genesis of catalytic materials via solid-state reactions where alumina is used as a reference material [32].

In TGA experiment, test material is placed into alumina cup that is supported on, or suspended from an analytical balance located outside the furnace chamber. The balance is tared, and the sample cup is heated according to a predetermined thermal cycle. The balance sends the weight signal to the computer for storage, along with the sample temperature and the elapsed time. The TGA curve plots the TGA signal, converted to percent weight change on the Y-axis against the reference material temperature on the X-axis. Thermogravimetric analyses (TGAs) were performed on Perkin-Elmer TGA-7 analyzer at 10 K/min scan rate in nitrogen atmosphere.

2.3.6. Fourier transform-infrared (FTIR) spectroscopy

IR spectroscopy analysis is based on the interaction of electromagnetic radiation with matter [33-34]. It has been widely used for structural analysis, chemical compound identification and monitoring of changes occurring during the course of a chemical reaction. Normally all atoms in the molecules are in motion to some extent. Molecules tend to rotate, translate and vibrate. The energy of IR radiation is sufficient to change the vibrational energy states of molecules. There will be an interaction of IR radiation with the molecule if the dipole moment changes due to

vibration. Hence, such mode of vibration is said to be IR active. We can observe increase in amplitude of vibration when energy is transferred to the molecule if the frequency of radiation matches with the frequency of a particular vibration. The frequency of vibration can be obtained from Hooke's law.

$$\nu = \frac{1}{2\pi c}\sqrt{\frac{K}{\mu}} \tag{2.8}$$

Where,

ν is the vibrational frequency (cm^{-1})

K is the force constant

μ is reduced mass (g/atom)

From the characteristic bands of certain vibrational frequencies in the IR spectra, one can get structural information about the molecules. In the present work, the IR studies were carried out on the oxide samples using a Perkin Elmer Spectrum-One FTIR Spectrometer in the frequency range 400 to 4000 cm^{-1} by properly mixing the sample with spectroscopic grade KBr.

2.3.7. Transmission electron microscopy

Transmission electron microscopy (TEM) is used for high resolution imaging of thin films of a solid sample for microstructural and compositional analysis. The technique involves: (i) irradiation of a very thin sample by a high-energy electron beam, which is diffracted by the lattices of crystalline or semicrystalline material and propagated along different directions, (ii) imaging and angular distribution analysis of the forward scattered electrons (unlike SEM where backscattered electrons are detected) and (iii) energy analysis of the emitted X-rays [35]. The topographic information obtained by TEM in the vicinity of atomic resolution can be utilized for

structural characterization and identification of various phases of mesoporous materials, viz., hexagonal, cubic or lamellar [36-37]. TEM also provides real space image on the atomic distribution in the bulk and surface of a nano crystal [38].

2.3.8. Scanning electron microscopy and Energy dispersive X-ray (SEM and EDX)

Scanning electron microscopy (SEM) is an important tool for determining the catalyst morphology and particle size in the range of 100 nm to 50 μm. A scanning electron microscope can generate an electron beam scanning back and forth over a solid sample. The interaction between the beam and the sample produces different types of signals providing detailed information about the surface structure and morphology of the sample. When an electron from the beam encounters a nucleus in the sample, the resultant Coulombic attraction leads to a deflection in the electron's path, known as Rutherford elastic scattering. A fraction of these electrons will be completely backscattered, reemerging from the incident surface of the sample. Since the scattering angle depends on the atomic number of the nucleus, the primary electrons arriving at a given detector position can be used to produce images containing topological and compositional information [39]. The high energy incident electrons can also interact with the loosely bound conduction band electrons in the sample. However, the amount of energy given to these secondary electrons as a result of the interactions is small, and so they have a very limited range in the sample. Hence, only those secondary electrons that are produced within a very short distance from the surface are able to escape from the sample. As a result, high resolution topographical images can be obtained in this detection mode [40]. The chemical composition of the sample was determined by energy dispersive X-ray (EDX) attached to SEM (JEOL JSM 500).

2.3.9. Diffuse reflectance UV-visible spectroscopy (DRUV)

Diffuse reflectance spectroscopy (DRS) is a spectroscopic technique based on the reflection of light in the ultraviolet (UV), visible (VIS) and near-infrared (NIR) regions by a powdered sample. In a DRS spectrum, the ratio of the light scattered from an "infinitely thick" closely packed catalyst layer and the scattered light from an infinitely thick layer of an ideal non-absorbing (white) reference sample is measured as a function of the wavelength λ. The scattered radiation, emitting from the sample, is collected in an integration sphere and detected. UV-Vis spectroscopy generally deals with the study of electronic transitions between orbital or bands of atoms, ions or molecules. One of the advantages of DR-UV is that the obtained information can be directly used for interpretation of chemical properties of the sample since outer shell electrons of the transition metal ions are probed. This further provides information about the oxidation state and coordination environment of transition metal ions in the solid matrices [41-42]. Also, the UV-Vis Spectroscopy is known to be very sensitive and useful technique for the identification of the electronic state of the metal atom as well as ligand geometry in heterogenized complexes. It gives information about the d-orbital splitting through the d-d transitions and the ligand-metal interaction through the ligand to metal charge-transfer transitions. The mechanism of reaction over "neat" complexes can be investigated by *in-situ* UV-Vis spectroscopy. The most popular continuum theory describing diffuse reflectance effect is Schuster-Kubelka-Munk (SKM) theory. If the sample is infinitely thick, the diffuse reflection of the sample ($R\infty$) is related to an apparent absorption (K) and apparent scattering coefficient (S) by the SKM equation [43].

2.3.10. Electron paramagnetic resonance (EPR) spectroscopy

EPR, often called electron spin resonance (EPR), is a branch of spectroscopy in which electromagnetic radiation (usually of microwave frequency) is absorbed by molecules, ions, or atoms possessing electrons with unpaired spins, i.e. electronic spin S > 0. In EPR, the sample material is immersed in a strong static magnetic field and exposed to an orthogonal low-amplitude high-frequency field. With EPR, energy is absorbed by the sample when the frequency of the radiation is appropriate to the energy difference between two states of the electrons in the sample, but only if the transition satisfies the appropriate selection rules. In EPR, because of the interaction of the unpaired electron spin moment (given by two projections, ms = ± 1/2, for a free electron) with the magnetic field, the so-called Zeeman effect, there are different projections of the spin gain different energies.

$$E_{ms} = gmBB_o ms \quad (2.9)$$

Here, Bo is the field strength of the external magnetic field. The SI units for magnetic field is tesla, but in EPR gauss (1 G = 0.0001 T) is still used. Other terms in equation (2.9): *ms* is a spin projection on the field (ms = ± 1/2 for a free electron), *m*B is the Bohr magneton [44-45]. EPR spectrums were obtained by Bruker A300 spectrometer using the oxford cryostat operating at X-band 9.5 GHz frequency and 100 kHz field modulation.

2.3.11. Redox ability measurement

2.3.11.1. Temperature programmed reduction/ Temperature programmed oxidation (TPR/TPO)

Temperature-programmed reduction (TPR) and oxidation (TPO) are thermo analytical techniques for characterizing chemical interactions between gaseous reactants and solid substances. [46-47]. TPR/TPO gives "fingerprint" information about the catalyst redox properties. This experiment was proposed in its current version by Robertson *et al.* in 1975 [48-49]. Reducibility is also of key importance for catalysts working via Mars van Krevelen redox mechanism, in which the oxidation of the hydrocarbons proceeds by reduction of an oxidized surface site, which is subsequently reoxidized by gas-phase molecular oxygen [50].

Catalyst characterization by TPR and TPO is based on measuring consumption of hydrogen and oxygen gases respectively. In case of TPR the catalyst placed in a tubular reactor is reduced in a H_2 flow (5 vol. % in Ar, 25 mL/min). The off-gases are continuously monitored by a mass spectrometer and the consumption of hydrogen is recorded as a function of the reaction temperature. The temperature of reactor is controlled by a processor, which heats the reactor at a linear rate of 1 to 20 K/min. The process is shown schematically in Figure 2.5. Integration of the H_2 consumed by consumption signal allows the determination of the total amount of hydrogen used to calculate the reactive oxygen in the catalyst and is expressed in moles of H_2 per mol of metal atoms. Similarly in TPO experiment, pre-reduced sample was subjected to oxygen flow (10 vol. % in He, 25 mL/min) with linear heating. The amount of oxygen consumption gives the reduced species in a catalyst material. The experimental setup of TPO equipment is identical to that of a TPR. Therefore, both techniques can be easily combined. In the present work, the

TPR/TPO studies were carried out on the oxide samples using Micromeritics Chemisorb 2720 instrument.

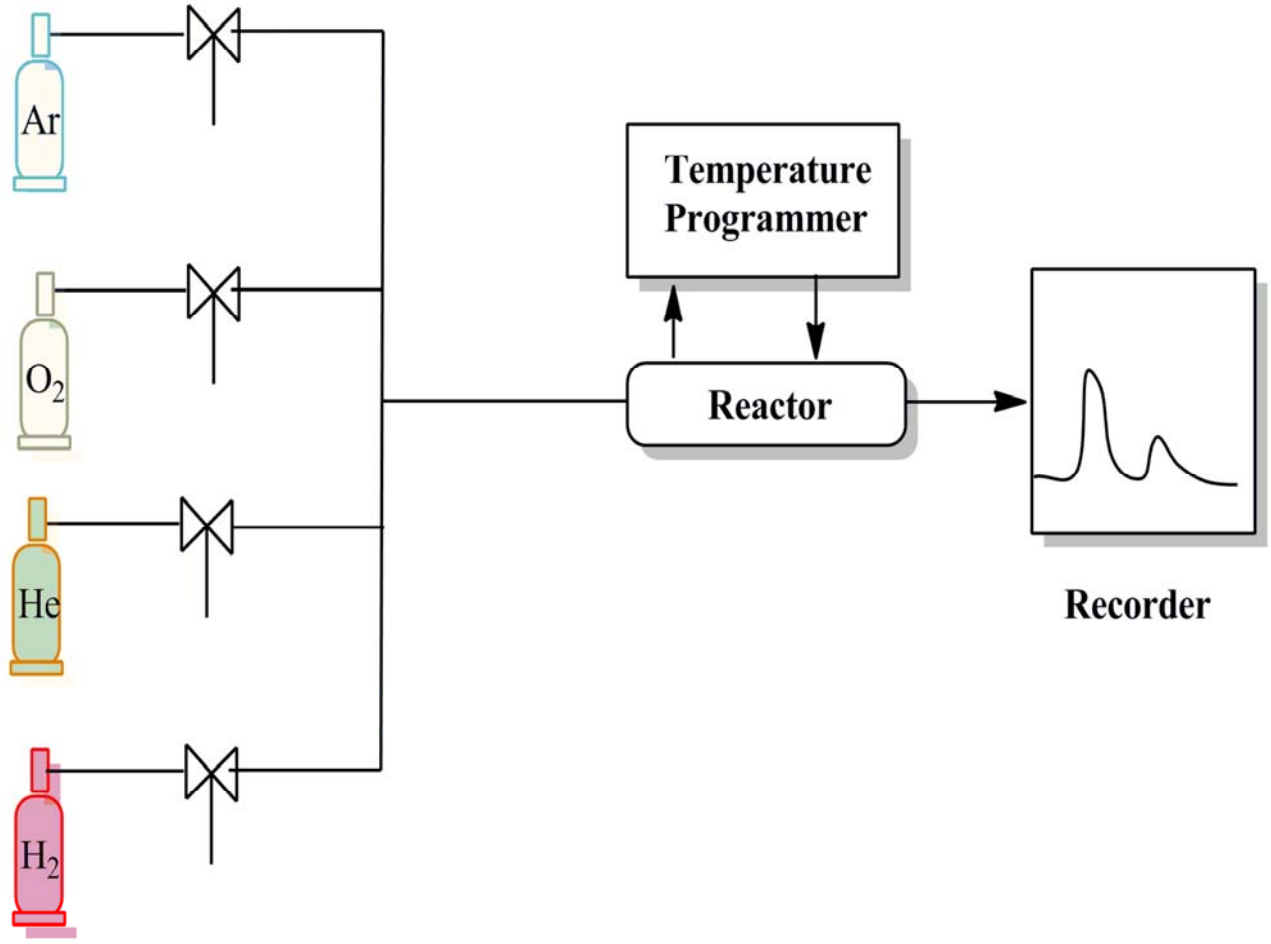

Figure 2.5. Schematic diagram for temperature programmed reduction and oxidation [49]

2.3.11.2. Cyclic voltammogram

Cyclic voltammogram (CV) is an effective tool to study the different electrochemical processes Faradaic and non-Faradaic associated with an electrode material [51-52]. It can be used to study the electrochemical behavior of species diffusing to an electrode surface, interfacial phenomena at an electrode surface, and bulk properties of materials in or on electrodes. In CV, normally three electrode systems are in common practice although two electrode systems can also be used.

In three electrode systems the potential is applied between working electrode and reference electrode while the current is measured in between the working electrode and the counter electrode. To tackle with large currents, normally counter electrode will be of very high surface area. CV measurement was carried out on Autolab 30 PGSTAT (Eco Chemie).

2.4. HIGH PRESSURE REACTOR SET UP FOR LIQUID PHASE OXIDATION REACTIONS

All the oxidation reactions at elevated pressure were carried out in a 300 mL capacity high pressure stirred autoclave supplied by Parr Instrument Company, USA.

Figure 2.6. Parr reactor setup

(1) Reactor (2) sampling valve (3) Pressure transducer (4) electric furnace (5) Thermocouple (6) magnetic stirrer (7) Control panel.

The autoclave was equipped with a heating arrangement, overhead stirrer, thermo well, internal cooling loop, pressure gauge as well as transducer, gas inlet, gas outlet, sampling valve and a rupture disc. There was a separate controller for agitation speed and temperature. Water circulation through the internal cooling loop equipped with automatic cut-off arrangement controlled the temperature inside the reactor with an accuracy of ±1 K. A schematic of the slurry reactor set-up is shown in Figure 2.6 [53].

In a typical oxidation experiment, 70 mL of solvent and 0.5 gm, (3 mmol) of veratryl alcohol were added. This reaction mixture was charged to a 300 mL Parr autoclave (Figure 2.6). A weighed amount of the catalyst was added, and the reaction mixture was heated to the desired temperature. When the desired temperature was attained, the reactor was pressurized with oxygen and then the reaction was started by agitating it at 900 rpm. Total oxygen pressure was kept constant by adding oxygen from time to time. The progress of the reaction was monitored by the observed pressure drop in the reservoir vessel as a function of time. Liquid samples were also withdrawn from time to time and analyzed by HPLC for the reactant and product concentrations. After the reaction was over, the contents were cooled to room temperature and discharged.

2.5. ANALYTICAL METHOD

A Hewlett-Packard model 1050 and Thermo Fisher 1000-4000 liquid chromatographs equipped with an ultraviolet detector were employed for the analysis of liquid samples. HPLC analysis was performed on a 25 cm RP-8e column supplied by Hewlett-Packard. The products and reactants were detected using a UV detector at λmax 223 nm using 35% methanol in water as mobile phase at a column temperature of 308 K and flow rate of 1 mL/min. Samples of 20 μL

were injected into the column using an auto sampler. The retention times of the reactants and products were compared with those of authentic samples. The quantitative analysis was carried out by calibration charts generated by injecting standard samples and their mixtures with different compositions.

2.6. REFERENCES

1. C. N. R. Rao, Chemical Approaches to the Synthesis of Inorganic Materials, Wiley Eastern Ltd., New Delhi, 1994.
2. A. S. Edelstein, R. C. Cammarata, Nanomaterials: Synthesis, Properties, and Applications, Taylor & Francis, 1998.
3. G. A. Ozin, A. C. Arsenault, Nanochemistry: A Chemical Approach to Nanomaterials, Royal Society of Chemistry, 2005.
4. G. Cao, Nanostructures & Nanomaterials: Synthesis, Properties & Applications, Imperial College Press, 2004.
5. D. Segal, Chemical Synthesis of Advanced Ceramic Materials, Cambridge Univ. Press, 1991.
6. J. P. Jolivet, Metal Oxide Chemistry and Synthesis: From Solution to Solid State, Wiley, New York, 2000.
7. K. C. Patil, Chemistry of Nanocrystalline Oxide Materials: Combustion Synthesis, Properties and Applications, World Scientific Pub. Co. Inc., 2008.
8. D. Segal, *J. Mater. Chem.* 7 (1997) 1297.
9. B. L. Cushing, V. L. Kolesnichenko, C. J. O'Connor, *Chem. Rev.* 104 (2004) 3893.
10. O. Masala, R. Seshadri, *Annu. Rev. Mater. Res.* 34 (2004) 41.
11. V. S. Kshirsagar, S. Vijayanand, H. S. Potdar, P. A. Joy, K. R. Patil, C. V. Rode, *Chem. Lett.* 37 (2008) 310.
12. M. A. Chougule, S. G. Pawar, P. R. Godse, R. D. Sakhare, S. Sen, V. B. Patil, *J. Mater. Sci. Mater. Electron.* 23 (2012) 772.
13. B. I. Ita, *IJNAS* 1 (2005) 81.

14. G. Suresh, P. Saravanan, D. R. Babu, *J. Magn. Magn. Mater.* 324 (2012) 2158.
15. N. N. Binitha, P. V. Suraja, Z. Yaakob, M. R. Resmi, P. P. Silija, *J. Sol Gel Sci. Technol.* 53 (2010) 466.
16. L. Zhou, J. Xu, X. Li, F. Wang, *Mater. Chem. Phys.* 97 (2006) 137.
17. M. Hamdani, R. N. Singh, P. Chartier, *Int. J. Electrochem. Sci.* 5 (2010) 556.
18. S. Farhadi, K. Pourzare, *Mater. Res. Bull.* 47 (2012) 1550.
19. K. C. Patil, S. T. Aruna, S. Ekambaram, *Curr. Opin. Solid State Mater. Sci.* 2 (1997) 158.
20. R. G. Leliveld, T. G. Ros, A. J. van Dillen, J. W. Geus, D. C. Koningsberger, *J. Catal.* 185 (1999) 513.
21. A. C. Garade, V. S. Kshirsagar, C. V. Rode, *Appl. Catal. A: Gen.* 354 (2009) 176.
22. S. Brunauer, P. H. Emmett, E. Teller, *J. Am. Chem. Soc.* 60 (1938) 309.
23. B. D. Cullity, S. R. Stock, Elements of X-Ray Diffraction, Addison-Wesley Reading, MA, 1978.
24. H. P. Klug, L. E. Alexander, X-Ray Diffraction Procedures, Wiley New York,1954.
25. W. H. Bragg, *Nature* 90 (1912) 410.
26. The software is freely available from http://www.ccp14.ac.uk.
27. T. A. Carlson, X-ray Photoelectron Spectroscopy, Dowden, Hutchinson & Ross: Stroudsburg, PA, 1978.
28. Practical Surface Analysis, Vol. 1: Auger and X-ray Photoelectron Spectroscopy, 2nd ed., D. Briggs and M. P. Seah, Eds., Wiley, New York, 1990.
29. S. Hüfner, Photoelectron Spectroscopy, Springer-Verlag: Berlin, 1995.
30. E. A. Stern, M. Newville, B. Ravel, Y. Yacoby, D. Haskel, *Physica B* 208 (1995) 117.
31. A. L. Ankudinov, B. Ravel, J. J. Rehr, S. D. Conradson, *Phys. Rev. B* 58 (1998) 7565.

32. P. Gabbott (Ed.) Principles and Applications of Thermal analysis, Wiley-Blackwell, 2007.

33. B. H. Stuart, Infrared spectroscopy: Fundamentals and Applications, Wiley, 2004.

34. D. L. Pavia, G. M. Lampman, G. S. Kriz, Introduction to Spectroscopy, Brooks Cole. Pub. Co., 2009.

35. J. R. Fryer, Chemical Applications of Transmission Electron Microscopy, Academic Press, San Diego, 1979.

36. J. M. Thomas, O. Terasaki, P. L. Gai, W. Zhou, J. G. Calbet, *Acc. Chem. Res.* 34 (2001) 583.

37. V. Alfredsson, M. Keung, A. Monnier, G. D. Stucky, K. K. Unger, F. Schuth, *J. Chem. Soc. Chem. Comm.* (1994) 921.

38. Z. L. Wang, Characterization of Nanomaterials, Ed: Z. L. Wang, Wiley-VCH, Weinheim. 2000, p. 37.

39. G. Lawes, Scanning Electron Microscopy and X-Ray Microanalysis, John Wiley and Sons Ltd., Chichester, 1987.

40. D. E. Newbury, D. C. Joy, P. Echlin, C. E. Fiori, J. I. Goldstein, Advanced Scanning Electron Microscopy and X-Ray Microanalysis, Plenum Press, New York, 1986.

41. B. M. Weckhuysen, I. P. Vannijvel, R. A. Schoonheydt, *Zeolites* 482 (1995) 15.

42. X. T. Gao, I. E. Wachs, *J. Phys. Chem. B* 104 (2000) 1261.

43. X. T. Gao, I. E. Wachs, *J. Catal.* 188 (1999) 325.

44. J. E. Wertz, J. R. Bolton, Electron Spin Resonance: Elementary Theory and Practical Applications. McGraw-Hill, New York, 1972.

45. S. A. Altshuler, B. M. Kozirev, Electron Paramagnetic Resonance. Academic, New York, 1964.

46. G. S. Sewell, E. van Steen, C.T. O'Connor, *Catal. Lett.* 37 (1996) 255.

47. H. Knözinger in G. Ertl, H. Knözinger, J. Weitkamp (eds.): Handbook of Heterogeneous Catalysis, Vol. 2, Wiley-VCH, Weinheim, 1997, p. 676.

48. J. M. Thomas, W. J. Thomas, Principles and Practice of Heterogeneous Catalysis, WCH Verlag GmbH, Weinheim, 1997.

49. I. Chorkendorff, J.W. Niemantsverdriet, Concepts of modern Catalysis and Kinetics, Wiley-VCH, Weinheim, 2003.

50. J. Haber, Oxidation of hydrocarbons, In Handbook of Heterogeneous Catalysis, Eds. G. Ertl, H. Knözinger, J. Weitkamp, Vol. 5, VCH, Weinheim 1997, p. 2253.

51. A. J. Bard, L. R. Faulkner, Electrochemical Methods, Wiley New York, 2001.

52. J. F. Rusling, S. L. Suib, *Adv. Mater.* 6 (2004) 922.

53. V. S. Kshirsagar, J. M. Nadgeri, P. R. Tayade, C. V. Rode, *Appl. Catal. A: Gen.* 339 (2008) 28.

Chapter 3

Effect of preparation methods on physico-chemical properties and activity of Co_3O_4 catalyst for oxidation of lignin sub-structured compounds

3.1. INTRODUCTION

Selective catalytic transformations for obtaining valuable products from biomass are becoming increasingly important for the evolution of green processes [1-3]. Liquid phase catalytic oxidation of various lignin derived sub-structured compounds such as veratryl alcohol, vanillin alcohol, sinapyl alcohol, coniferyl alcohol, *p*-coumaryl alcohol, etc, give respective aldehydes (Figure 3.1) and acids. These are used as flavoring agents and also as important pharmaceutical intermediates e.g. veratryl aldehyde for the manufacture of angiocardiopathy drugs such as donepezil [4].

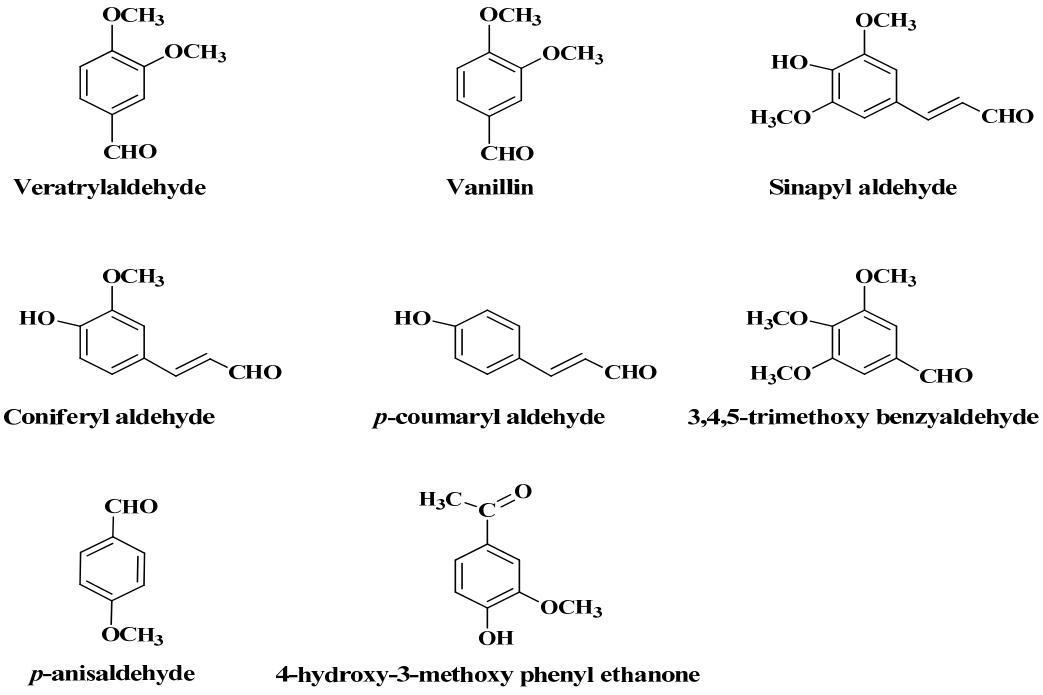

Figure 3.1. Oxidation products of lignin derived sub-structured compounds

These lignin derived sub-structured compounds come from the processes such as alkaline pulping of lignin [5, 6], pyrolysis of dimeric lignin [5], hydrolysis of the alcell lignin (Scheme

3.1), etc. Ultimatly, lignin depolymeriztion results into the breaking of the *β*-O-4 linkages to form monomeric and dimeric nonphenolic and phenolic sub-structured compounds as side products [2].

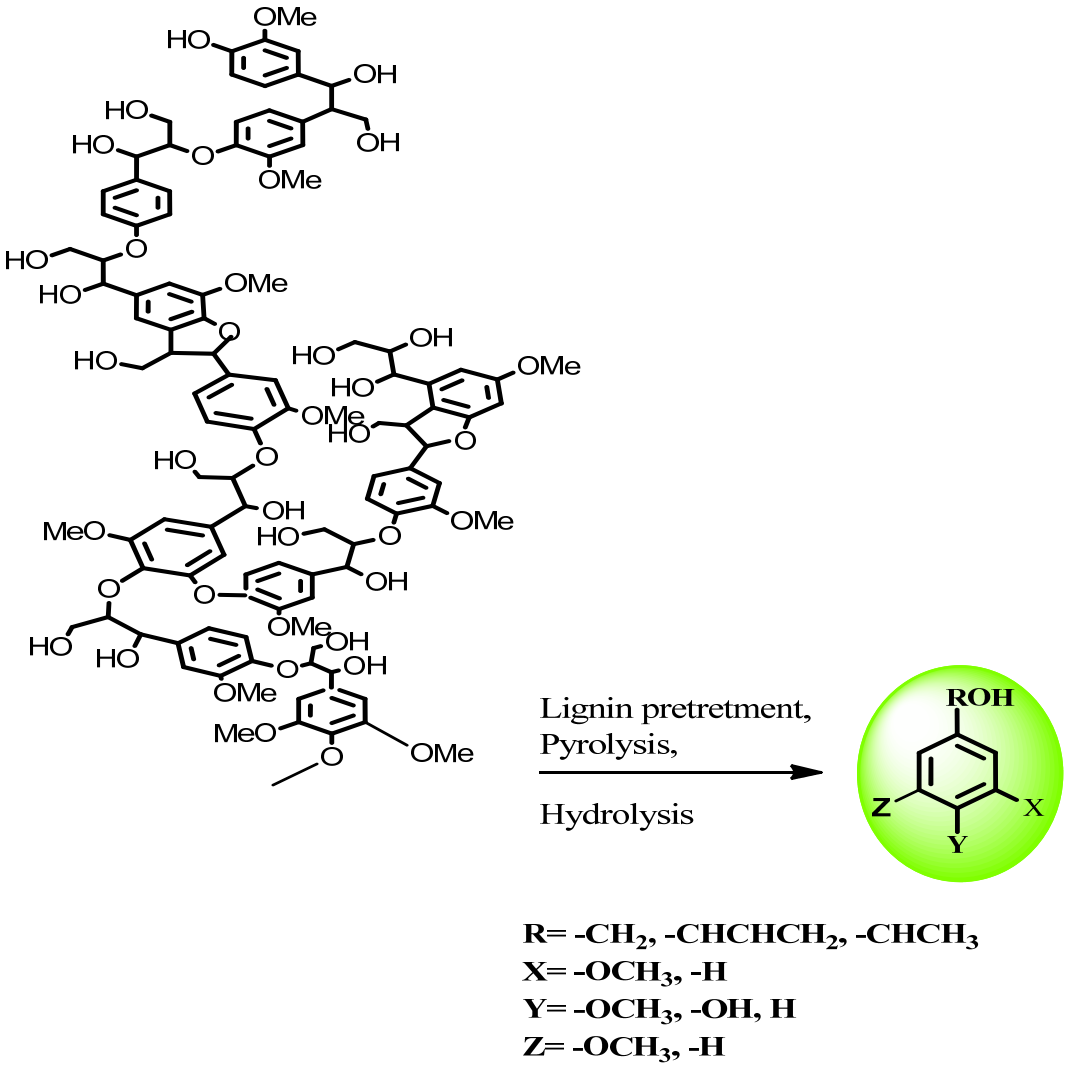

Scheme 3.1. Lignin bleaching/degradation

Oxidation of lignin derived sub-structured compounds was conventionally carried out using homogeneous complexes of non-noble and noble metals like Co, Fe, V, Mn, V, Au and Re in

alkaline medium (Scheme 3.2), which pose serious environmental and operational problems as discussed in chapter 1 (Section 1.9) [7-9].

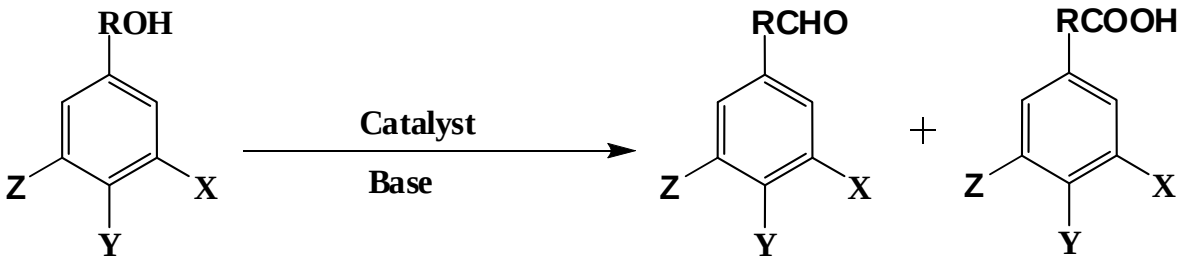

R= -CH_2, -$CHCHCH_2$, -$CH\text{-}CH_3$

X= -OCH_3, -H

Y= -OCH_3, -OH, H

Z= -OCH_3, -H

Scheme 3.2. Catalytic oxidation of lignin derived sub-structured compounds

In this work, I prepared heterogeneous oxidation catalysts involving metal oxides such as Co_3O_4, $ZnCo_2O_4$, $CoAl_2O_4$ and cobalt aluminosilicates with different silica/alumina ratios (Chapter 2). In recent years, interest in nano-scale metal oxides has been growing because of their relatively enhanced redox ability and electrochemical properties as compared to those of their bulk forms [10]. For this reason, various morphologies of Co_3O_4 such as nano rods and nano spheres with meso and/or microporous characteristics are reported by using different synthesis methods [10-15]. These are (i) hydrothermal [16, 17], (ii) combustion [18], (iii) micro emulsion [19], (iv) chemical spray pyrolysis [20], (v) chemical vapor deposition [21], (vi) ionic liquid assisted synthesis [22], (vii) an ultrasonic assisted route [23], (viii) ball milling [24], (ix) microwave-assisted route [25] and (x) mechanochemical [26]. However, most of these methods require

toxic, costly reagents, high temperatures, expensive sophisticated instruments and long reaction times. Thus, a simple, inexpensive and nontoxic route for the preparation Co_3O_4 nano particles at relatively low temperature is desirable. We have therefore preferred the preparation methods such as co-precipitation [10, 11], sol-gel [27, 28], and thermal decomposition [29, 30].

Among the preparation methods studied in this work, Co_3O_4 prepared via co-precipitation gave rod-like morphology in nano regime (10-20 nm) which was not observed either by sol-gel or by thermal decomposition. We report here for the first time, the use of molecular oxygen without using any alkali for oxidation of veratryl alcohol to veratryl aldehyde over non noble metal Co_3O_4 catalysts [10]. The nano-structured Co_3O_4 (Co-3C-a) catalyst showed 75% and 38% conversion of veratryl alcohol in toluene and water respectively, with complete selectivity to veratryl aldehyde. We also investigated the change in catalyst activity due to change in catalyst morphology which in turn was found to be a function of pH, calcination temperature and time. Co-3C-a catalyst was also tested for the liquid phase oxidation of other lignin sub structure compounds under optimized reaction conditions that showed the conversion >50%. The catalysts were characterized by various techniques like N_2-adsorption-desorption isotherm, XRD, XPS, TG-DTA, FT-IR, HRTEM, temperature programmed reduction and oxidation (H_2/O_2 TPR/TPO) measurement, cyclic voltammogram (CV), FT-EXAFS and EPR. The stability of the catalyst was studied by the catalyst recycle experiments.

3.2. EXPERIMENTAL

Details of preparation of nano Co_3O_4 via simultaneous co-precipitation and digestion, sol-gel and thermal decomposition methods are described in section 2.2. The prepared catalysts were evaluated for the liquid phase oxidation of veratryl alcohol and lignin derived phenolic and non

phenolic sub structured compounds. For this purpose, the experimental set up used and experimental procedure are described in section 2.4 while the catalyst characterization and analytical methods are given in sections 2.3 and 2.5 respectively.

3.3. RESULTS AND DISCUSSION

The results in this section discussed are on the characterization of Co_3O_4 catalysts prepared by various methods. At the same time, results on effect of preparation parameters on the physico-chemical characteristics are also presented. Finally, activity comparison of Co_3O_4 samples prepared by various methods is presented to understand the structure-activity relationship.

3.3.1. Co_3O_4 prepared by simultaneous co-precipitation and digestion method

3.3.1.1. Surface area

The influence of pH on the porous structure and particle size of spinel Co_3O_4 samples prepared by co-precipitation method was studied in a pH range of 7-8 (Co-3C-a), 9-10 (Co-3C-b), 11-12 (Co-3C-c) and 13-14 (Co-3C-d). The effect of calcination temperature on the physico-chemical properties of Co_3O_4 was also studied at 573 K and 873 K. The textural properties of these samples examined by the nitrogen adsorption-desorption measurements and the results are shown in Table 3.1 and Figures 3.2(a-d). All the samples showed type IV isotherm [31], showing the similar nature of mesoporous material being formed in the pH range of 8 to 10 (Co-3C-b) while at pH =12, the sample (Co-3C-c) showed the decrease in pore diameter from 16.7 to 2.5 nm indicating a change of nature of material from mesoporous to microporous (Figures 3.2(a-c)). The hysteresis feature of the Co_3O_4 sample at the relative pressure of 0.6-0.9 was classified as the H_3 loop, suggesting the presence of aggregates of nano tube particles with slit-shaped pores.

A sharp decrease in surface area (110 to 58.4 m^2/g) and pore diameter (16.7 to 2.5 nm) was observed for increase in pH from 8 to 12 while further increase in pH to 14 showed higher surface area 121.6 m^2/g and pore diameter of 2.5 nm (Table 3.1) (Figure 3.3). Initial decrease in surface area and pore diameter with increase in pH from 8 to 12 might be the result of aggregation of Co_3O_4 nano particles which induces disappearance of spaces between Co_3O_4 nano particles that was also observed in HRTEM and discussed later in Section 3.3.1.7 [32]. Interestingly, increase in pH to 14 resulted in increase in surface area also upto 121.6 m^2/g for the sample (Co-3C-d), due to increase in concentration of $(OH)_2$ which might restrict the aggregation of primary $Co(OH)_2$ particles.

Table 3.1. Textural properties of catalysts prepared at different pH and calcination temperatures

Catalysts	pH	Calcination temperature (K)	Surface area (m^2/g)	Pore size, BJH_{DES} (nm)	Pore volume, BJH_{DES} (cm^3/g)
Co-3C-a	8	573	110.0	16.7	1.30
Co-3C-b	10	573	74.5	15.1	0.71
Co-3C-c	12	573	58.4	2.5	0.33
Co-3C-d	14	573	121.6	2.5	0.34
Co-6C-a	8	873	24.5	1.8	0.11

From the pore size distribution curve (Figure 3.3), it was found that all the samples showed a bimodal pore distribution determined by using the Barrett-Joyner-Halenda (BJH) method, that is smaller pores in the region of 2-5 nm and larger pores ranging from 5 to 30 nm. Sample (Co-3C-a) calcined at 573 K (pH= 7-8, calcination time =5 h) showed type IV isotherm whereas sample

(Co-6C-a) calcined at 873 K (pH= 7-8, calcination time =5 h) showed a mixed behavior of type I and type IV isotherms (Figure 3.2(e)) [31], showing the shifting of mesoporous to microporous nature with rise in calcination temperature from 573 to 873 K. A sharp decrease in surface area (110 to 24.5 m^2/g) and pore diameter (16.7 to 1.8 nm) were also observed at higher calcination temperature of 873 K (Table 3.1, Entries 1 and 5, Figure 3.4). Decrease in surface area and pore diameter at higher calcination temperature might be the result of restructuring of Co_3O_4 nano particles which induces disappearance of spaces between Co_3O_4 nano particles [33]. The above observations establish that the textural properties of catalyst could be tuned by changing the pH during catalyst preparation and pretreatment conditions such as calcination temperature after the preparation. These variations in textural properties are expected to affect the catalytic performance of the same catalyst as discussed in Section 3.3.4.

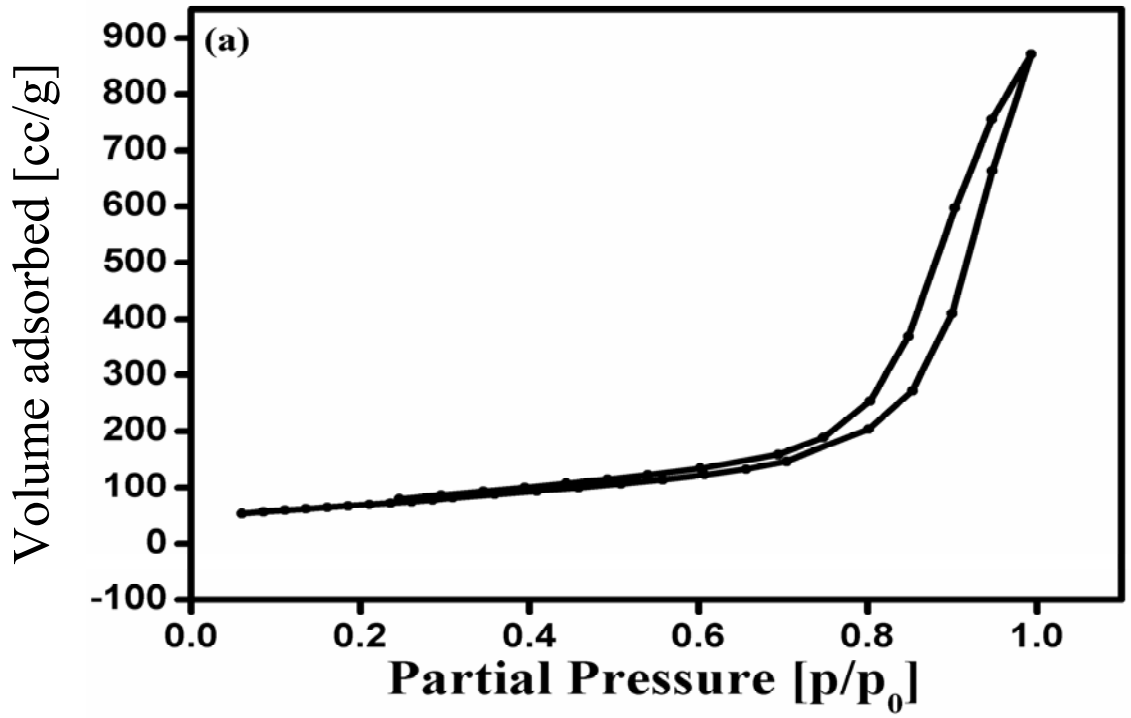

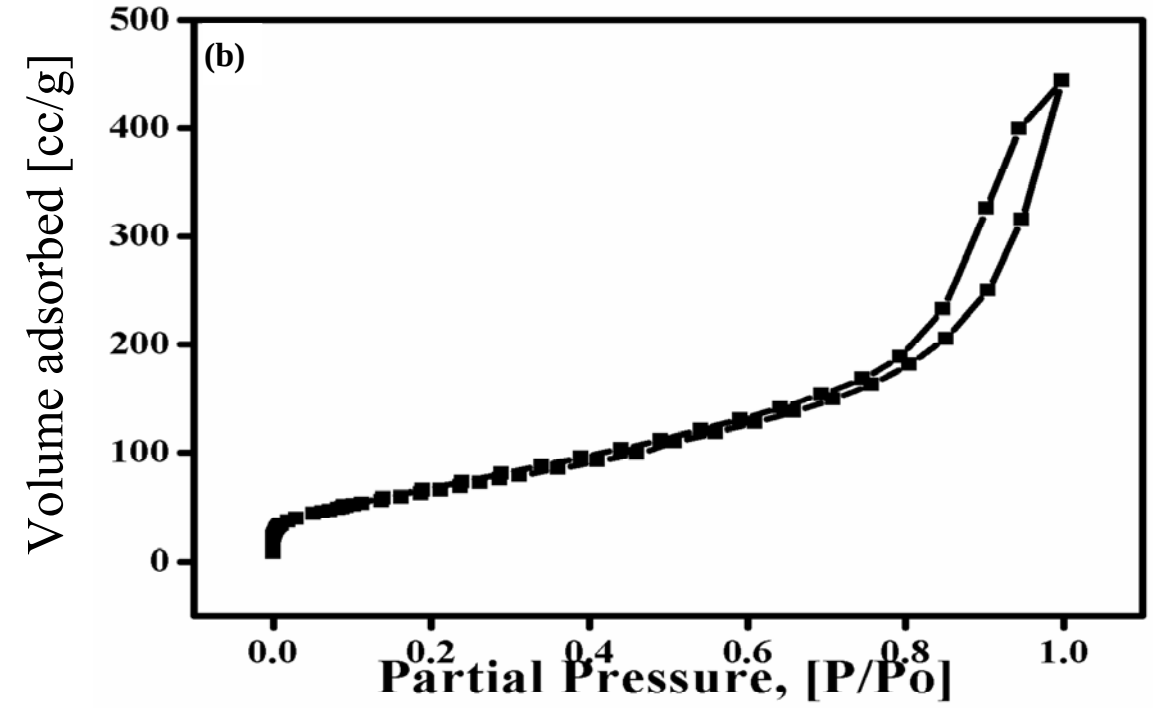
(b)
Volume adsorbed [cc/g]
500
400
300
200
100
0
0.0
0.2
0.4
0.6
0.8
1.0
Partial Pressure, [P/Po]

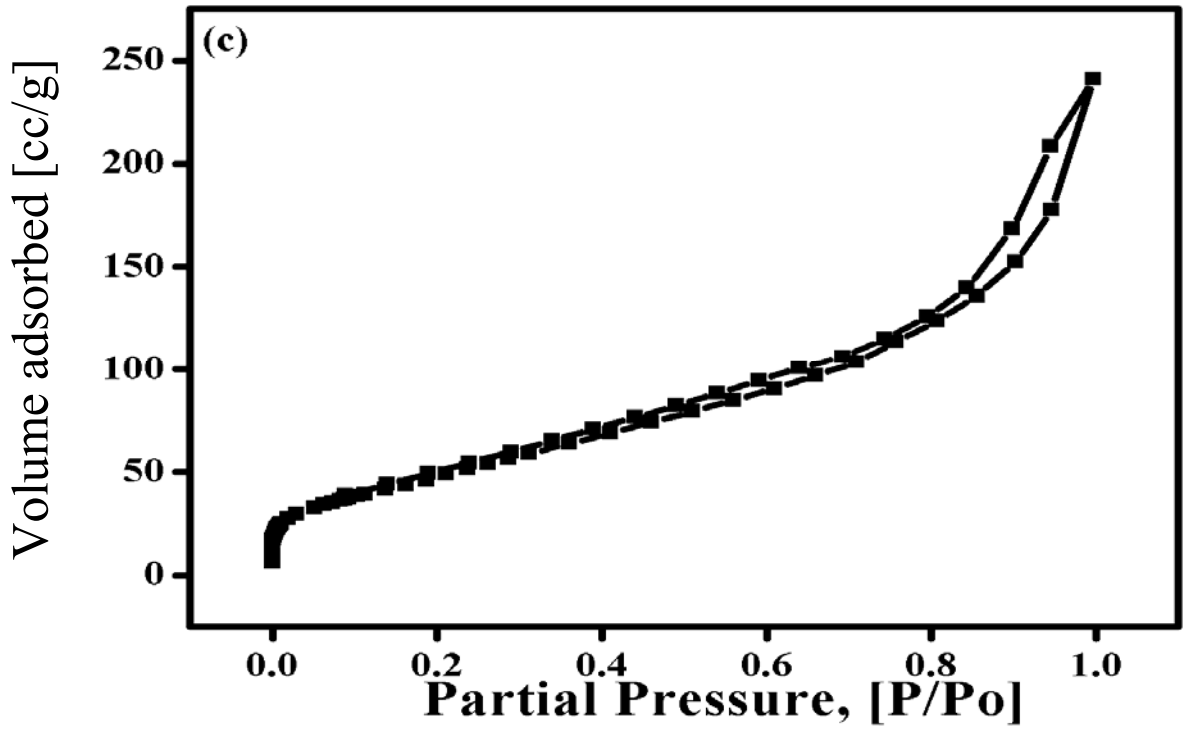
(c)
Volume adsorbed [cc/g]
250
200
150
100
50
0
0.0
0.2
0.4
0.6
0.8
1.0
Partial Pressure, [P/Po]

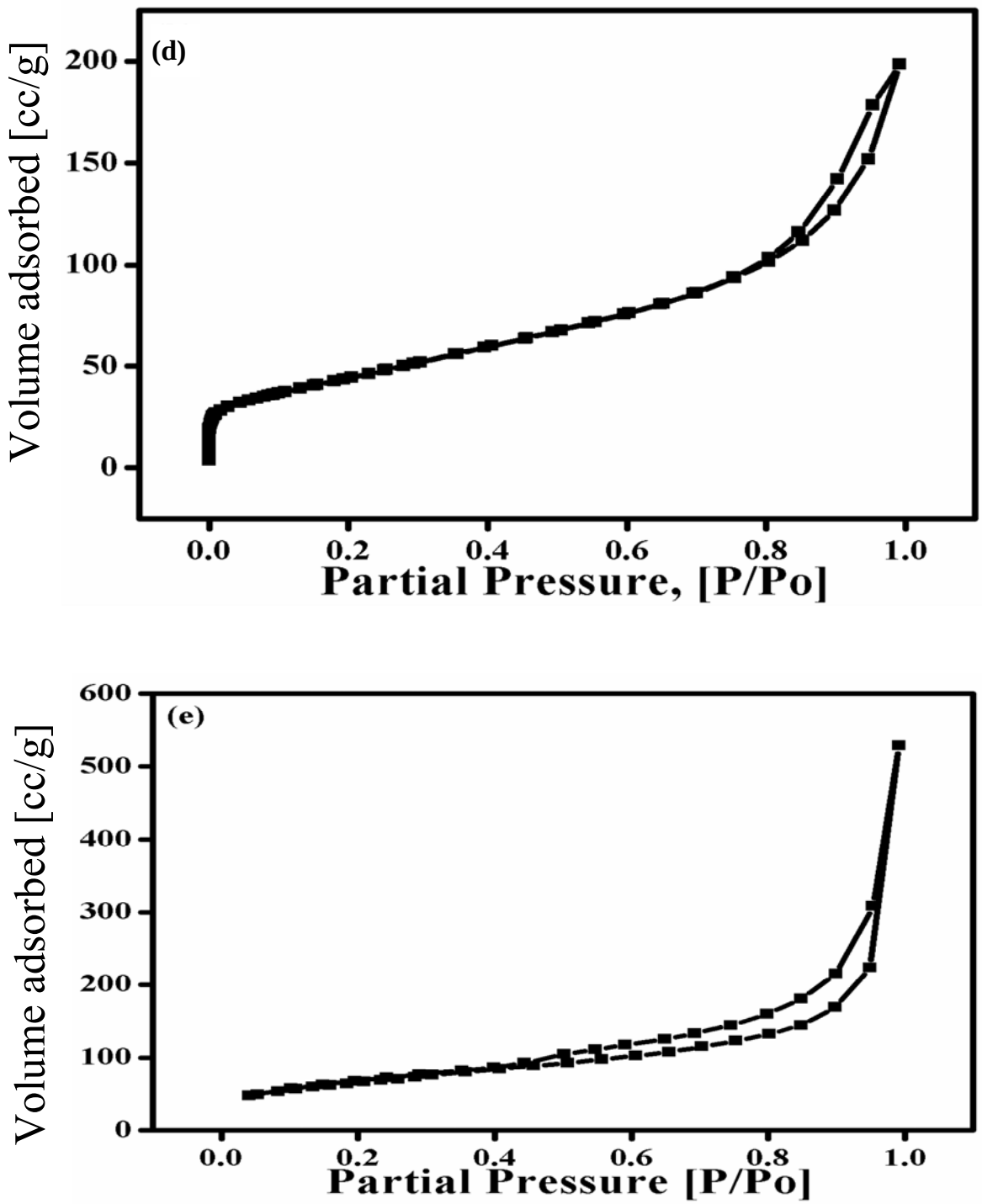

Figure 3.2. Adsorption isotherm of (a) Co-3C-a, (b) Co-3C-b, (c) Co-3C-c, (d) Co-3C-d and (e) Co-6C-a samples

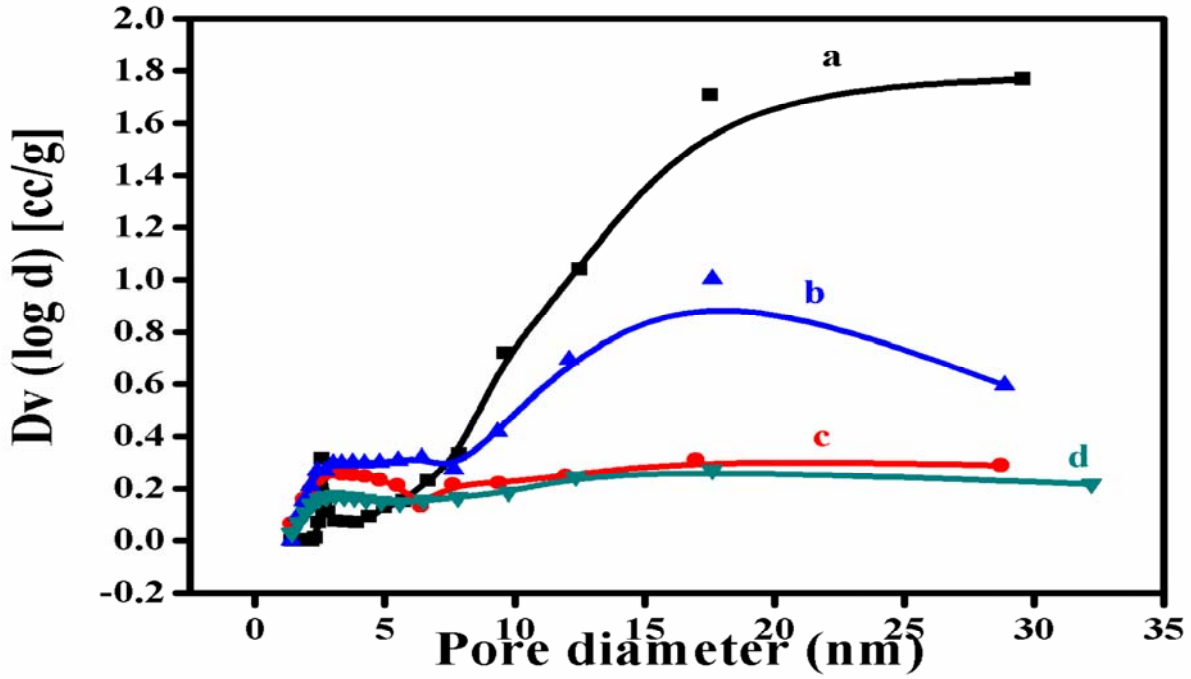

Figure 3.3. Pore size distribution of (a) Co-3C-a, (b) Co-3C-b, (c) Co-3C-c and (d) Co-3C-d samples

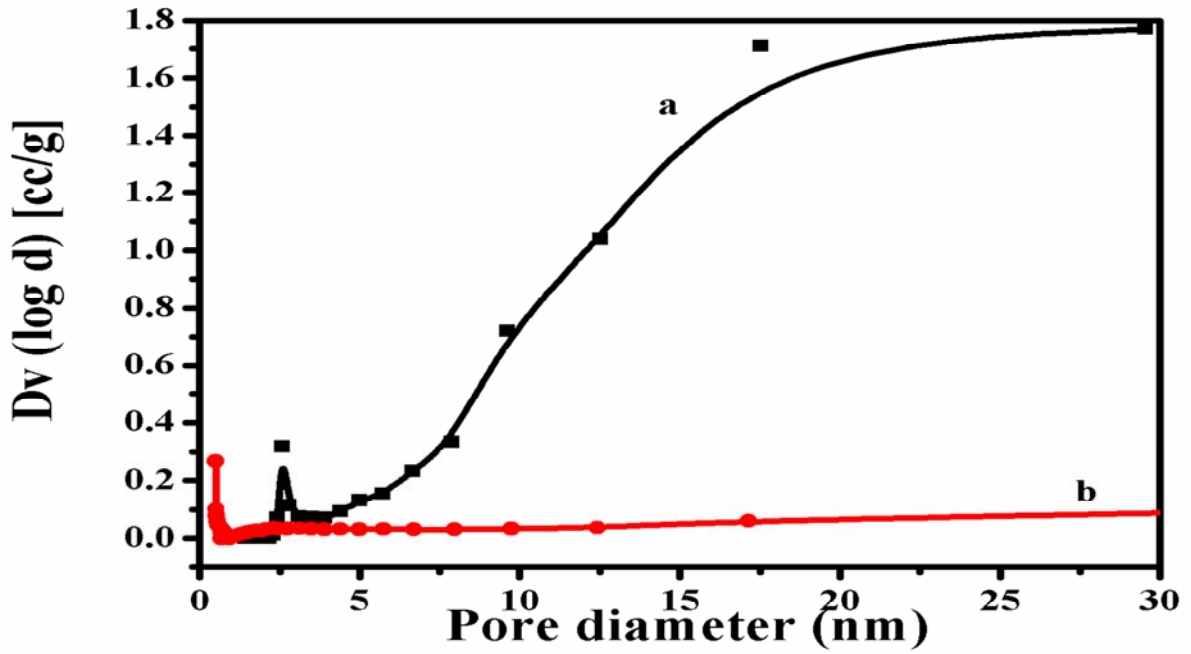

Figure 3.4. Pore size distribution of (a) Co-3C-a and (b) Co-6C-a samples

3.3.1.2. X-ray diffraction (XRD)

The powder X-ray diffraction patterns of spinel Co_3O_4 samples prepared at different pH values, calcination temperatures and time are shown in Figure 3.5(a-d). The calculated lattice parameter for all the samples, a = 8.087 Å corresponds to the cubic type which was in good agreement with the reported value for Co_3O_4 powder (a = 8.084 Å; JCPDS # 9-418), except as-dried Co-a and Co-d samples (Figure 3.5(c-d)) [11, 34]. For all the samples except as-dried samples (Co-a and Co-d), the peaks at 2θ = 19.2° (111), 31.2° (220), 36.84° (311), 44.84° (400), 55.65° (422), 59.42° (511) and 65.21° (422) reveal the reflections of a spinel Co_3O_4 (Figure 3.5b). For the change in pH from 8 to 12, intensity of the peaks at 2θ = 19.2° (111), 31.2° (220), 36.84° (311), 44.84° (400), 55.65° (422), 59.42° (511) and 65.21° (422) increased while at pH=14, broad and less intense peaks appeared at 2θ = 19.2° (111), 31.2° (220), 36.84° (311), 44.84° (400), 55.65° (422), 59.42° (511) and 65.21° (422). Initially at pH=8, concentration of (OH) is less however with increase in pH from 8 to 12, concentration of (OH) increased, as a result of which the primary particles of Co(OH) orientated in such way that crystallite size increased from 12 to 85 nm in case of Co-3C-a, Co-3C-b and Co-3C-c samples. However, further increase in concentration of (OH) might control the orientation of primary particles of cobalt hydroxyl carbonate (Co(OH) CO_3) (20-40 nm) that showed less intense peaks as in case of Co-3C-d (pH=14) sample (Table 3.2). The crystallite size determined by Scherrer equation (2.4) was found to be 12-38, 20-60, 30-85 and 20-40 nm, observed in case of the Co-3C-a, Co-3C-b, Co-3C-c and Co-3C-d samples and matched very well with the HRTEM results.

The XRD patterns of as-dried samples of Co-a (pH = 8) calcined at different temperatures from 573 K to 873 K at constant calcination time of 5 h is shown in Figure 3.5b. The increase in

calcination temperature (573-873 K) caused gradual increase in intensity and the slight decrease in the width of peaks at 2θ = 19.2° (111), 31.2° (220), 36.84° (311), 44.84° (400), 55.65° (422), 59.42° (511) and 65.21° (422). Crystallite sizes of Co-3C-a, Co-4C-a, Co-5C-a and Co-6C-a calculated using the Scherrer equation were found to be in the range of 12-38, 15-40, 15-52 and 20-70 nm respectively (Table 3.2). Thus, increase in crystallite size for Co-6C-a was mainly due to restructuring of the material at 873 K [35].

The XRD pattern of as-dried samples of Co-a (pH=8) and Co-d (pH=14) calcined at constant 573 K temperature with varying calcination times from 1 to 6 h are shown in Figures 3.5c-d. The intensity of the peaks at 2θ = 19.2° (111), 31.2° (220), 36.84° (311), 44.84° (400), 55.65° (422), 59.42° (511) and 65.21° (422) increased with increase in calcination time from 1 to 6 h in both Co-a and Co-d samples. With increase in calcination time from 2 to 6 h (Co-a), crystallite size of Co_3O_4 increased from 5-25 nm to 15-52 nm. Similarly, in case of Co-d (2 to 6 h) samples also crystallite size increased from 5-20 nm to 18-34 nm (Table 3.2). This increase of crystallite size is related with the increase in peak intensity and corresponds to the transformation of as-dried cobalt hydroxy carbonate to spinel Co_3O_4 [36].

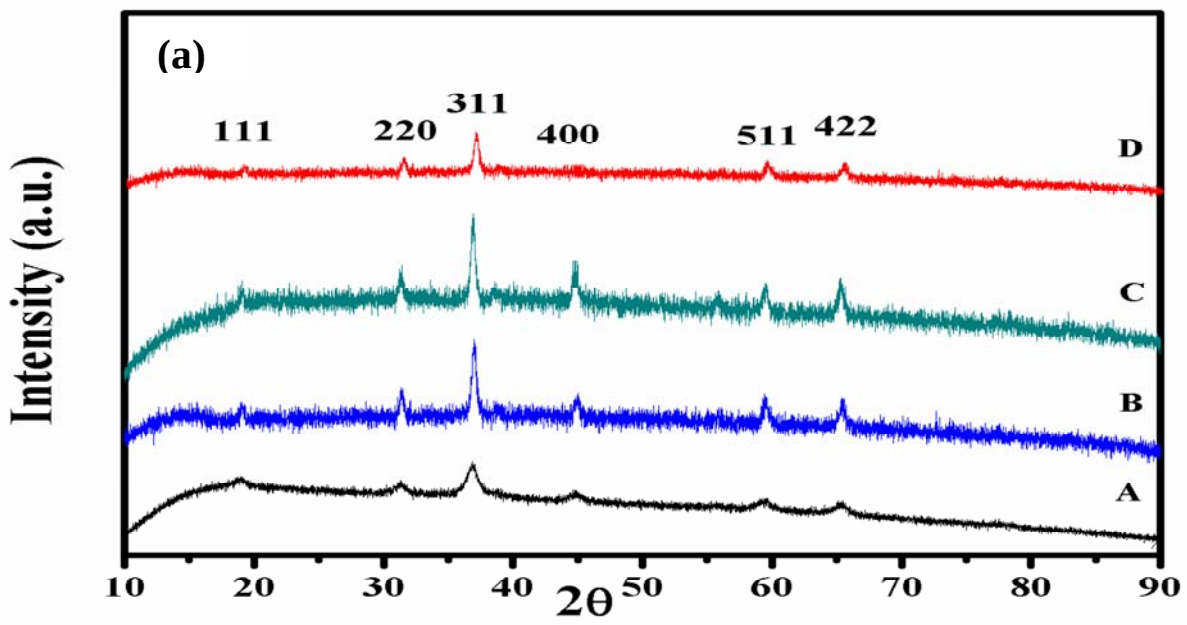

Figure 3.5a. XRD of spinels (A) Co-3C-a, (B) Co-3C-b, (C) Co-3C-c and (D) Co-3C-d catalysts

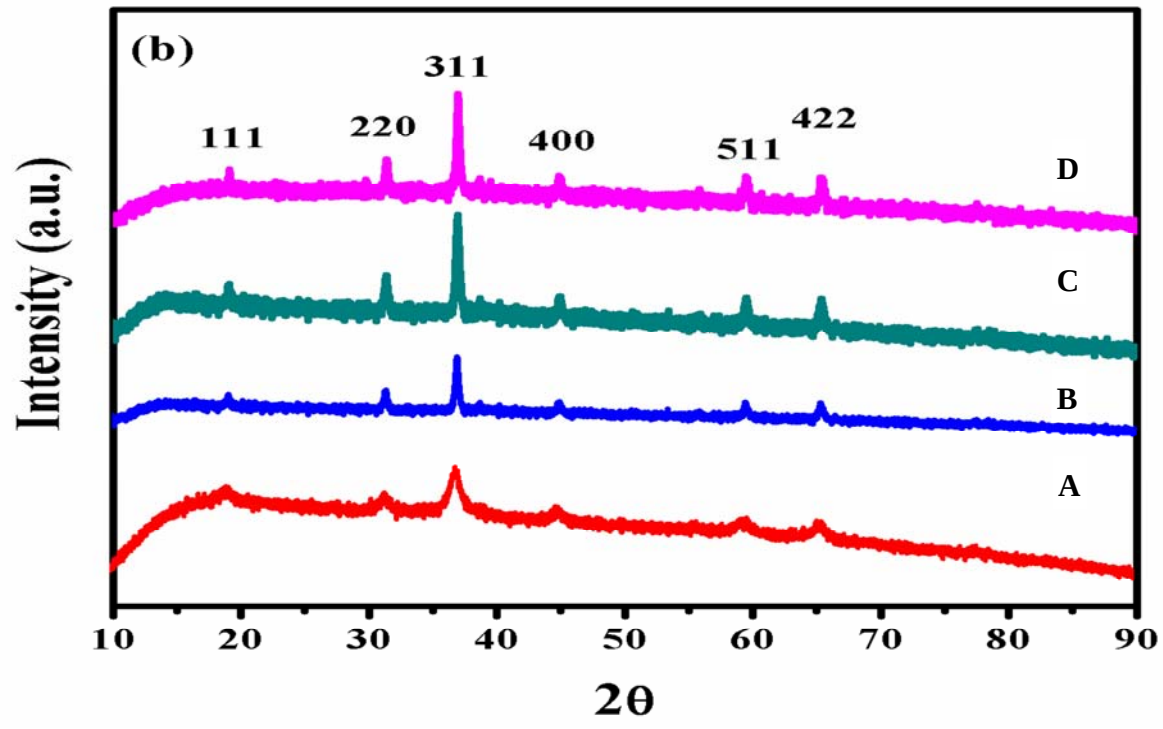

Figure 3.5b. XRD of spinels (A) Co-3C-a, (B) Co-4C-a, (C) Co-5C-a and (D) Co-6C-a catalysts

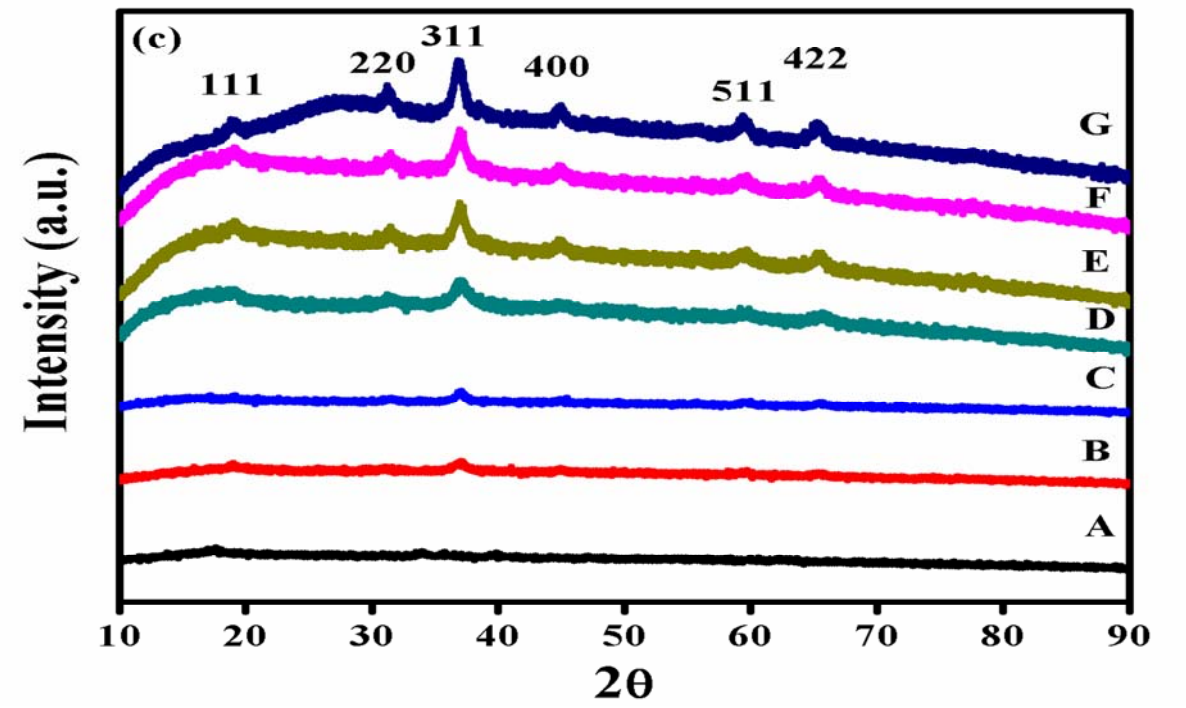

Figure 3.5c. XRD of spinels (A) Co-a as-dried, (B) Co-3C-a-1, (C) Co-3C-a-2, (D) Co-3C-a-3, (E) Co-3C-a-4, (F) Co-3C-a-5 and (G) Co-3C-a-6 catalysts

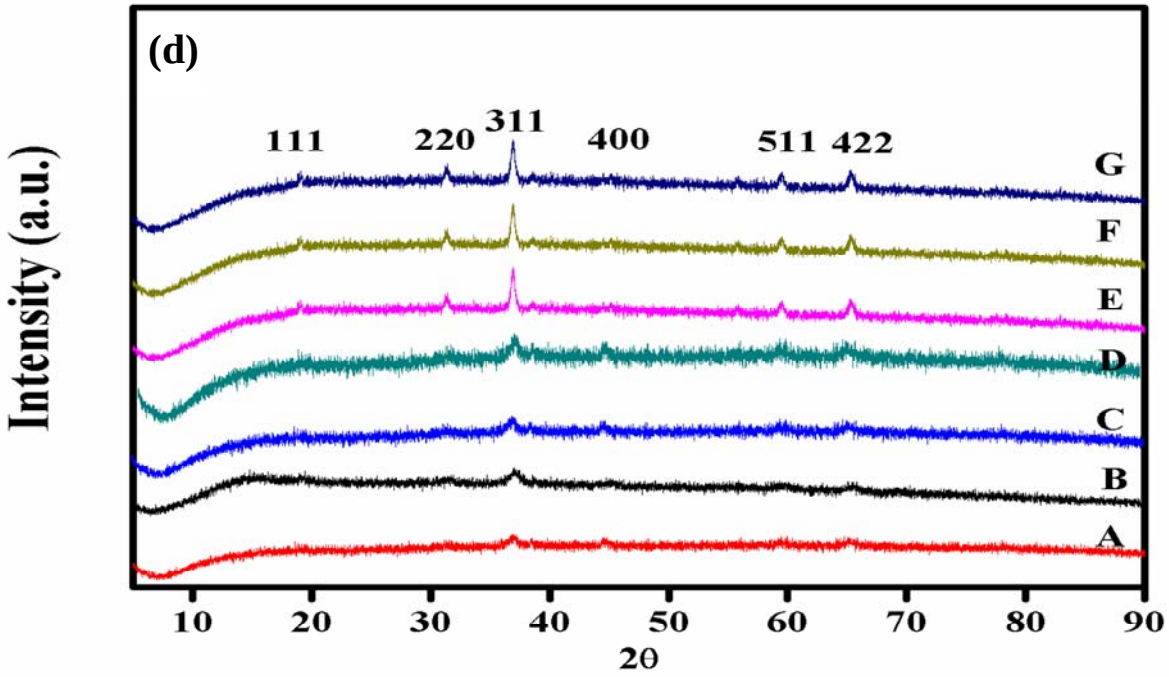

Figure 3.5d. XRD of spinels (A) Co-d as-dried, (B) Co-3C-d-1, (C) Co-3C-d-2, (D) Co-3C-d-3, (E) Co-3C-d-4, (F) Co-3C-d-5 and (G) Co-3C-d-6 catalysts

Table 3.2. Crystallite sizes of the prepared samples as determined by the Scherrer equation

Catalysts	Crystallite Size (nm)	Catalysts	Crystallite Size (nm)	Catalysts	Crystallite Size (nm)	Catalysts	Crystallite Size (nm)
Co-3C-a	12-38	Co-3C-a	12-38	as-dried	ND	as-dried	ND
Co-3C-b	20-60	Co-4C-a	15-40	Co-3C-a-1	ND	Co-3C-d-1	ND
Co-3C-c	30-85	Co-5C-a	15-52	Co-3C-a-2	5-25	Co-3C-d-2	5-20
Co-3C-d	20-40	Co-6C-a	20-70	Co-3C-a-3	6-30	Co-3C-d-3	8-22
-	-	-	-	Co-3C-a-4	9-32	Co-3C-d-4	12-25
-	-	-	-	Co-3C-a-5	12-38	Co-3C-d-5	15-28
-	-	-	-	Co-3C-a-6	15-52	Co-3C-d-6	18-34

3.3.1.3. X-ray photoelectron spectroscopy (XPS)

In order to study the oxidation states of various Co species formed under various preparation conditions of co-precipitation method, the Co 2p XPS spectra of Co-3C-a, Co-3C-b, Co-3C-c and Co-3C-d samples were observed. As can be seen from Figure 3.6a, the Co 2p XPS contains the Co $2p_{3/2}$ and Co $2p_{1/2}$ core level peaks at binding energies of 779.3 and 794.4 eV having a difference of 15.1 eV respectively, in all the samples [11]. The Co $2p_{3/2}$ peak on deconvolution gives two peaks at binding energies of 779.4 and 781.9 eV which correspond to Co^{3+} and Co^{2+} species (Figure 3.6b). This evidences the formation of spinel Co_3O_4 in all the samples [37, 38].

The surface compositions of fresh and used samples of active Co-3C-a catalyst in different solvents were investigated by deconvolution of $Co2p_{3/2}$ and O1s peaks (Figure 3.7(a-b)). The oxygen peak at 529.3 eV was attributed to the lattice oxygen (LO) of oxides of both tetrahedral

Co^{2+} and octahedral Co^{3+}, while peak at 531.3 eV was assigned to the adsorptive oxygen (AO) due to formation of $Co(OH)_2$ (Figure 3.7(b)) [39-41]. The surface composition calculated in terms of atomic percentage was quantified by atomic sensitivity factor and area under the curve after deconvolution of $Co2p_{3/2}$ and O1s spectra (Figure 3.8) [42-45]. The atomic sensitivity factors (ASF) for cobalt and oxygen were 3.88 and 0.66 ASF respectively [46-48]. The fresh Co-3C-a catalyst showed 40% cobalt surface composition (CSC) consisting of the Co^{2+} (13%) and Co^{3+} (27%) together while, remaining 60% included AO and LO with 44% and 16% (Figure 3.8). This evidenced the formation of stoichiometric AB_2O_4 type spinel ($CoOCo_2O_3$). The polar and non polar solvents were used to identify the species participating during the reaction. The used catalyst in toluene solvent showed decreased CSC from 40% to 25% (Co^{2+} (5%), Co^{3+} (20%)) consequently AO/LO composition increased to 75%, when catalytic activity was 75% as shown in section 3.3.4.3.5, indicating utilization of both CSC and AO/LO species during the reaction. However, in water as a solvent, CSC and AO/LO remained almost the same as that for the fresh catalyst 43% (Co^{2+} (15%), Co^{3+} (28%)) and 57% of AO/LO when catalytic activity was only 38%. In order to know CSC and AO/LO composition at intermediate stage in toluene solvent, timely withdrawn samples (from the reaction) containing reactant and the catalyst were taken and the catalyst was filtered, washed by toluene and the surface composition was determined by XPS (when catalytic activity was 40% equivalent to that in water) (Figure 3.8). CSC was found to be 50% (Co^{2+}) 17%, (Co^{3+}) 33% and AO/LO oxides composition was 50% (24 and 26%). These compositions were almost equivalent to the compositions found in fresh sample separated from the reaction crude in water medium. The CSC ratios in methanol and ethanol solvents were found to be 57% [(Co^{2+}) 17%, (Co^{3+}) 40%] and 31% [(Co^{2+}) 11%, (Co^{3+}) 20%] respectively (Figure 3.8). Thus, contribution of CSC and AO/LO species towards oxidative

dehydrogenation reaction was found to depend on the reaction medium [49]. The above observations established that similar types of surface species of the catalyst may be active during the reaction in polar as well as in non polar solvent however, the change in the concentration of these active species varied as per the reaction medium.

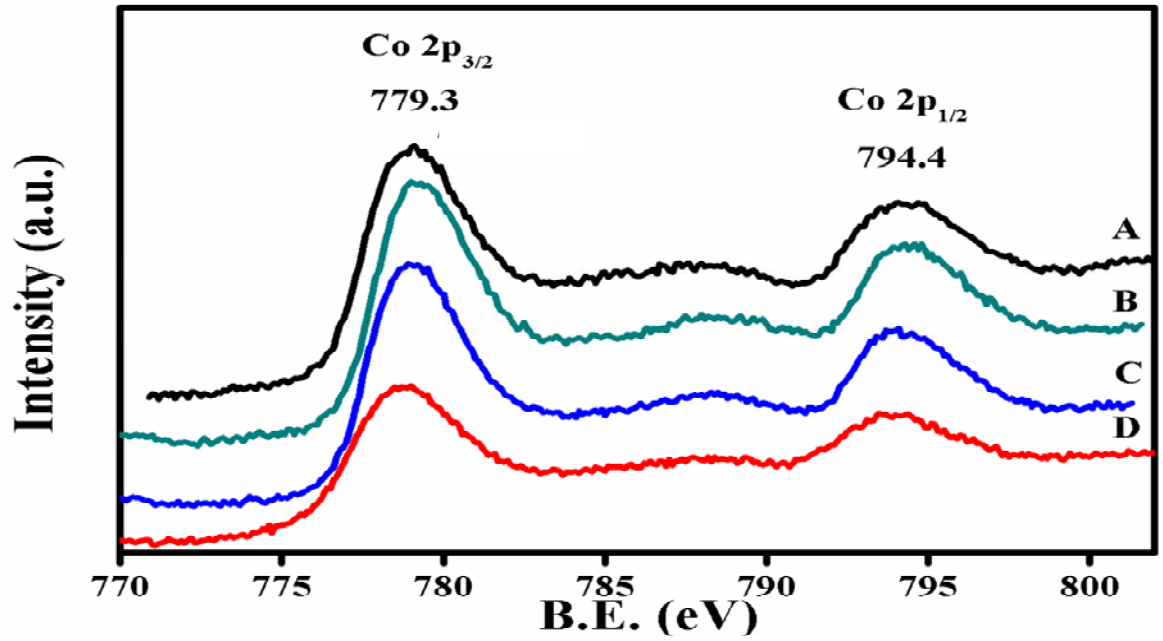

Figure 3.6a. XPS of (A) Co-3C-a, (B) Co-3C-b, (C) Co-3C-c and (D) Co-3C-d samples

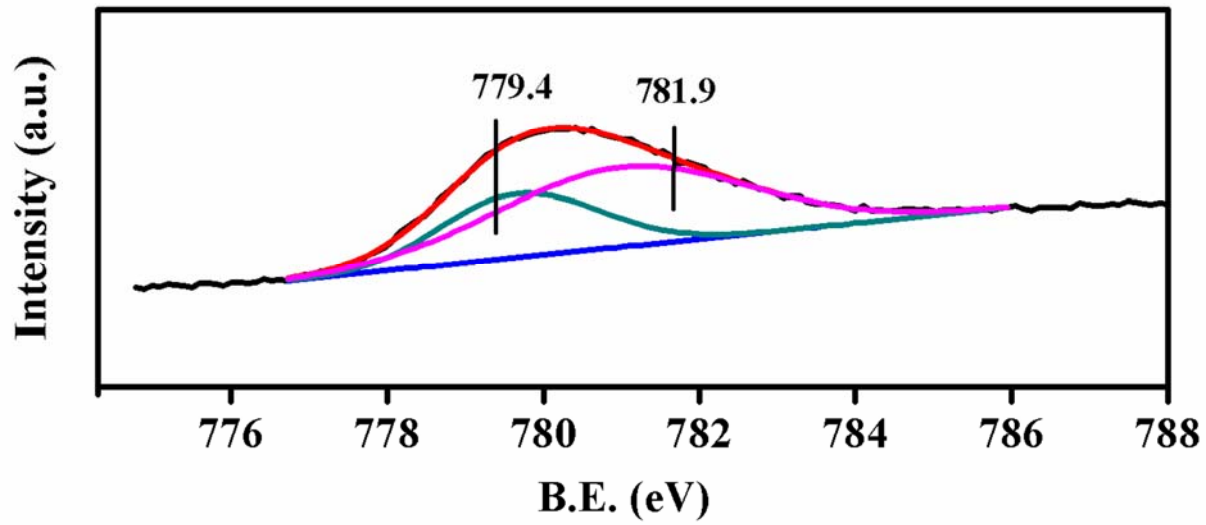

Figure 3.6b. Deconvolution spectra of $Co2p_{3/2}$

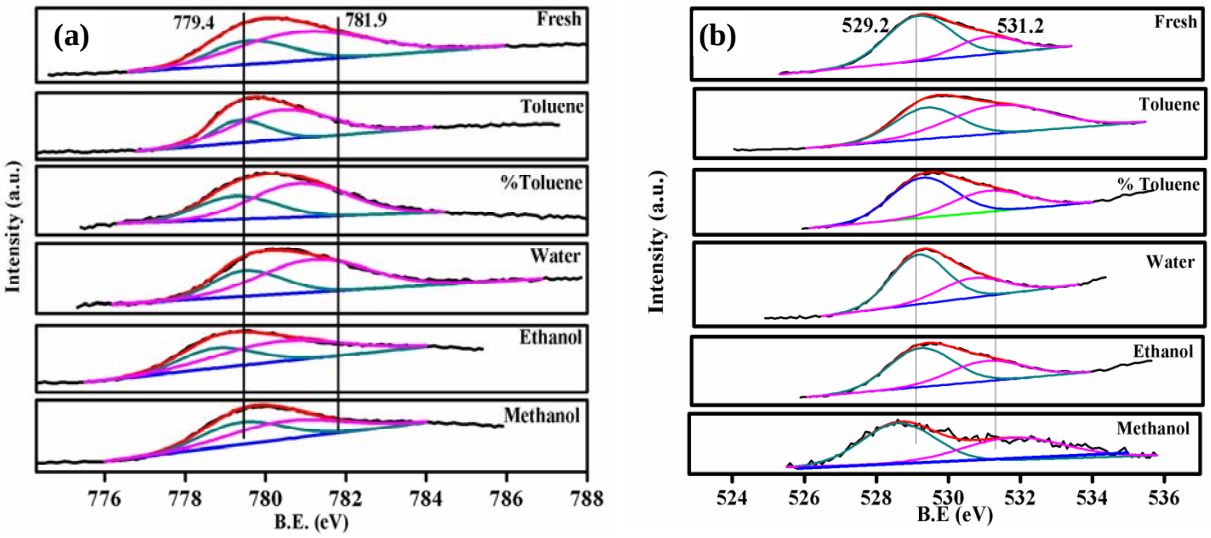

Figure 3.7. XPS deconvoluted **(a)** $Co2p_{3/2}$ and **(b)** O1s peaks of Co-3C-a-Fresh, Co-3C-a-Toluene, Co-3C-a-%Toluene, Co-3C-a-Water, Co-3C-a-Ethanol and Co-3C-a-Methanol samples

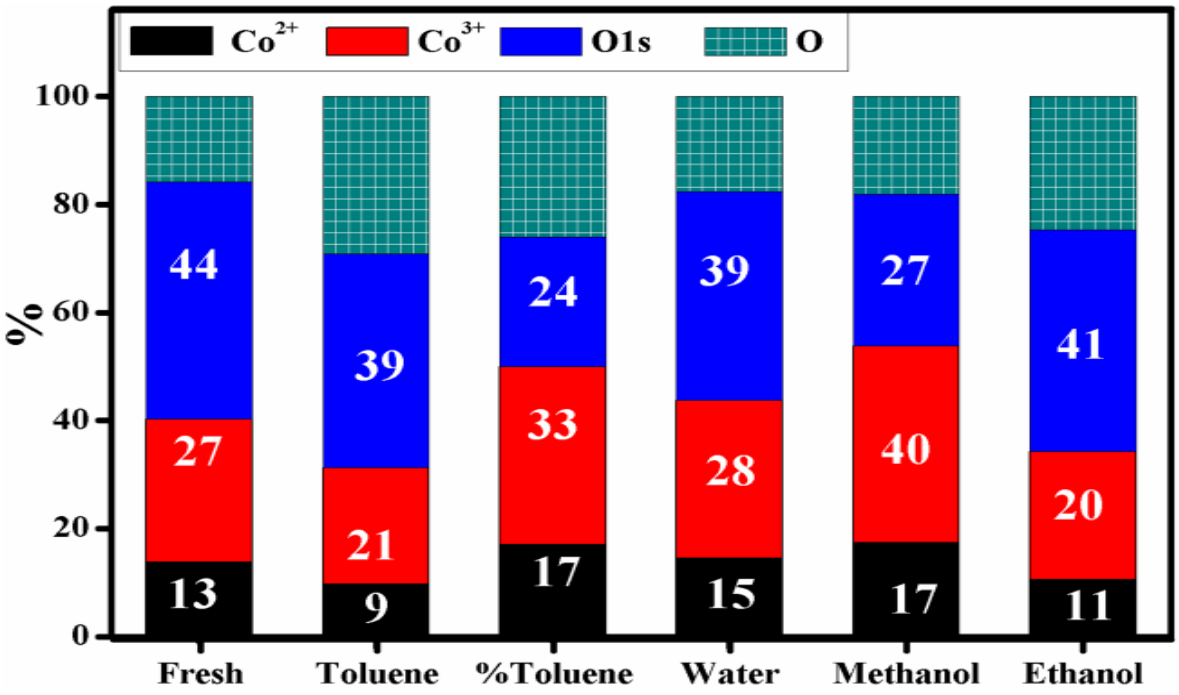

Figure 3.8. Quantification of surface active species in Fresh (Co-3C-a) and used Toluene (Co-3C-a), %Toluene (Co-3C-a), Water (Co-3C-a), Ethanol (Co-3C-a), Methanol (Co-3C-a) samples

3.3.1.4. Fourier transform Extended X-ray absorption fine structure (FT-EXAFS)

FT-EXAFS was studied to understand the extent of the structural disorder in fresh Co-3C-a, Co-6C-a and used samples of Co-3C-a in toluene, water, methanol and ethanol solvents and the results are shown in Figure 3.9. All the samples showed first FT peak at 1.52 Å corresponding to Co-O bond and second peak at ~2.4 Å (split in to 2.45 Å and 3.04 Å) assigned to Co-Co and Co-O bonds. While, third peak at 4.6 Å was assigned to the metallic Co-Co bond [34, 50]. The main inter atomic distances between Co and oxygen in case of used Co-3C-a and that for Co-6C-a sample calcined at high temperature (873 K) were almost identical to the fresh Co-3C-a sample (Figure 3.9).

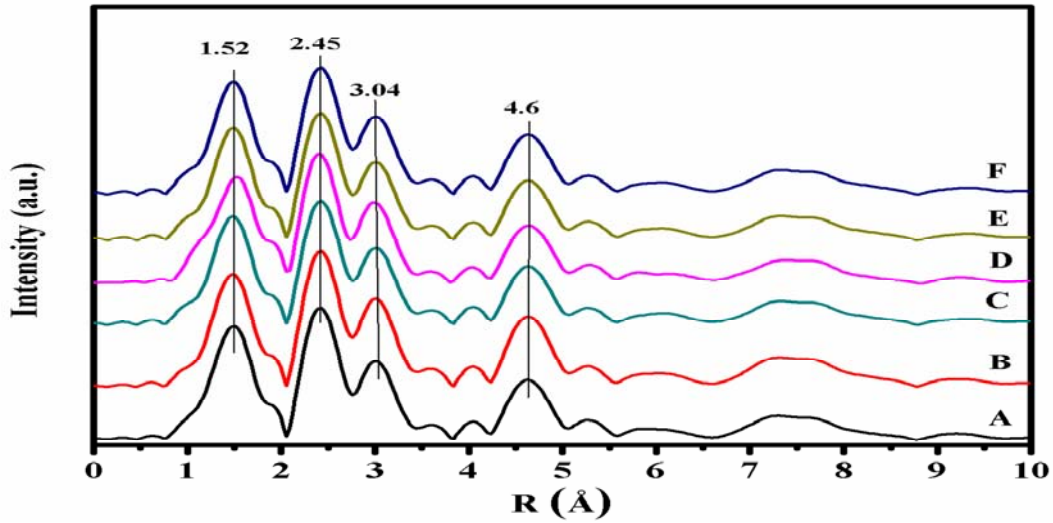

Figure 3.9. EXAFS of (A) Fresh Co-3C-a, (B) Fresh Co-6C-a, (C) Used Co-3C-a toluene, (D) Used Co-3C-a water, (E) Used Co-3C-a methanol and (F) Used Co-3C-a ethanol samples

3.3.1.5. Thermo gravimetric analysis (TGA)

TG-DTA curves of the as-dried Co-a (pH =8), Co-b (pH =10), Co-c (pH =12) and Co-d (pH =14) samples are shown in Figure 3.10. These catalysts showed weight losses in two-steps. The first continuous weight loss of 37%, 30%, 8% and 5% was observed from room temperature to 373 K

due to the loss of physically adsorbed/trapped water molecules in meso and micro pores of all the samples [34, 36]. The gradual decrease in weight loss might be due to the gradual decrease in pore diameter (16.7-2.5 nm) and pore volume (1.3-0.33 cm^3/g) with change in pH from 7 to 14. This resulted in decrease in the extent of physically adsorbed water. While, in the second step, weight losses of 11.4%, 17%, 18.5% and 17.6% for the respective catalysts below 540 K temperature were due to the decomposition of carbonate anions and dehydroxylation [34, 36]. Based on these observations, calcination temperature for the formation of spinel was chosen as 573 K in all the samples.

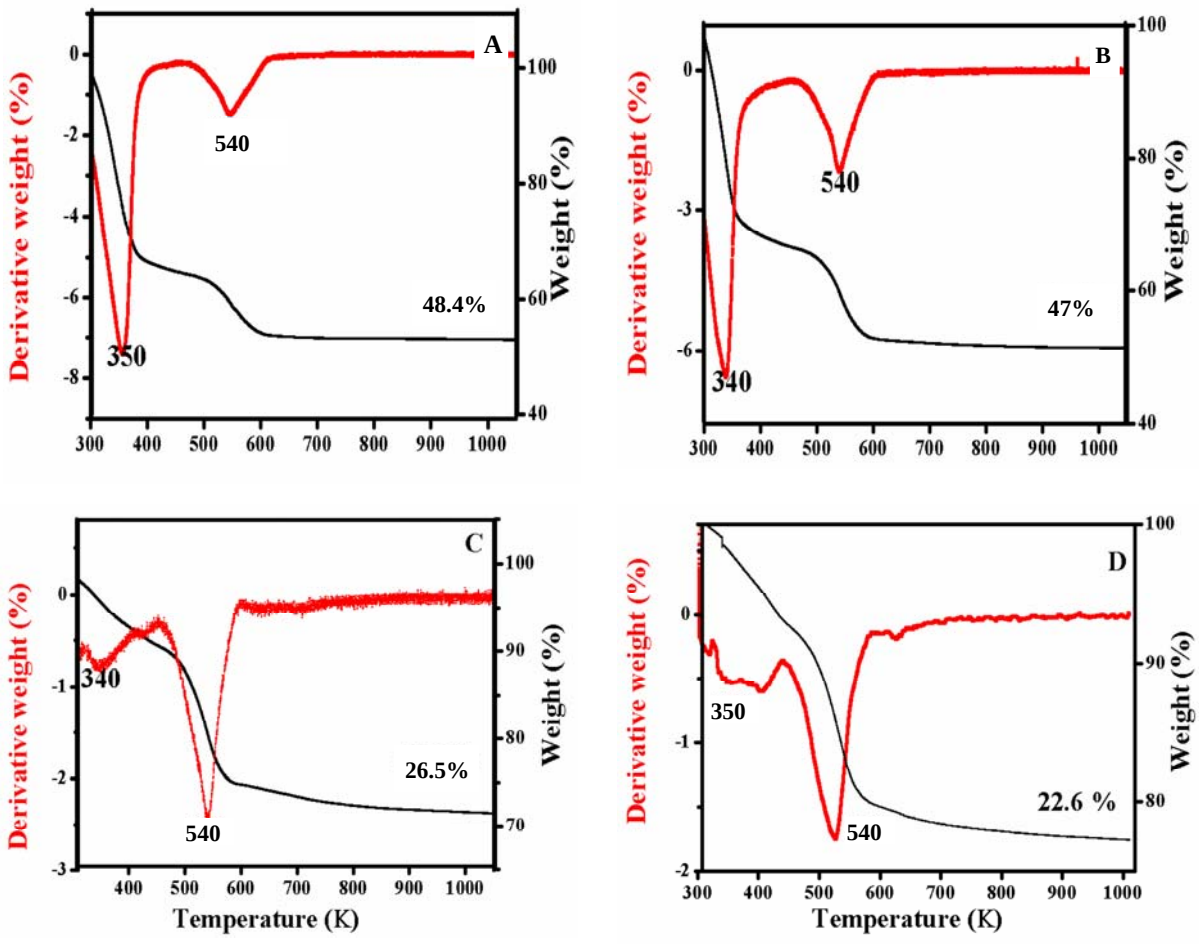

Figure 3.10. TG-DTA profile of (A) Co-a, (B) Co-b, (C) Co-c and (D) Co-d as-dried samples

3.3.1.6. Fourier transform infrared spectroscopy (FT-IR)

FT-IR spectra of Co-3C-a, Co-3C-b, Co-3C-c and Co-3C-d samples showed two distinct bands at 568 and 660 cm^{-1} assigned to stretching vibrations of the metal-oxygen bonds (Figure 3.11). The peak at 568 cm^{-1} corresponds to Co^{3+} in an octahedral position while the other peak at 660 cm^{-1} corresponds to the Co^{2+} in an tetrahedral position confirming the formation of Co_3O_4 spinel in all the samples [51, 52]. The broad peaks at 3460 and 1619 cm^{-1} were attributed to metal hydroxyl stretching vibrations in all the samples, however in case of Co-3C-a and Co-3C-d samples, additional low intensity weak peak at 3734 cm^{-1} was observed which is assigned to metal hydroxyl stretching vibrations [53, 54], whereas this peak (3734 cm^{-1}) was not observed in case of Co-3C-b and Co-3C-c samples. The presence of additional surface hydroxyl (3734 cm^{-1}) species at pH 8 and 14 may be probably due to better control of pH and *in-situ* generated hydroxyl species which might help to control the orientation of particles in the nano regime as observed in HRTEM. While hydroxyl bending vibration at 1061 cm^{-1} was observed only in Co-3C-a sample [53, 54]. The corresponding peaks in all used catalysts after the first recycle also remained intact indicating that the catalyst was stable under the reaction conditions (Figure 3.12).

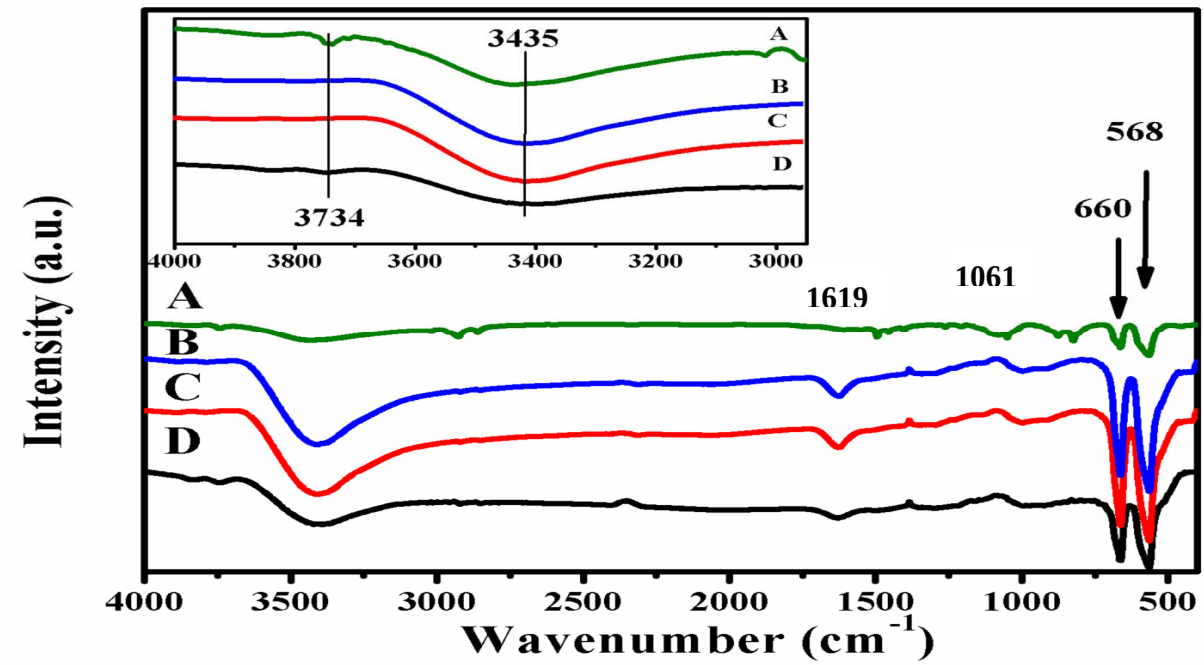

Figure 3.11. FTIR profile of (A) Co-3C-a, (B) Co-3C-b, (C) Co-3C-c and (D) Co-3C-d samples

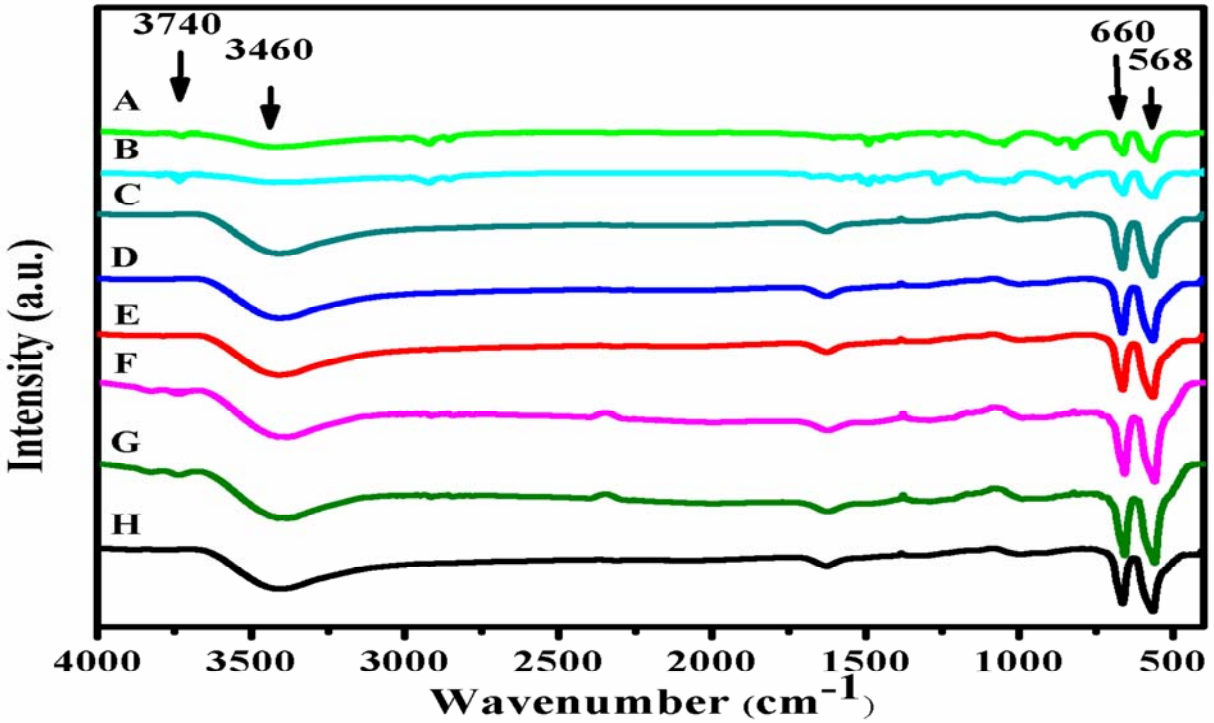

Figure 3.12. FTIR profile of (A) Co-3C-a fresh, (B) Co-3C-a used, (C) Co-3C-b fresh, (D) Co3C-b used, (E) Co-3C-c fresh, (F) Co-3C-c used, (G) Co-3C-d fresh and (H) Co-3C-d used samples

3.3.1.7. High resolution transmission electron microscopy (HR-TEM)

The morphologies along with the particle sizes of the catalysts prepared at various pH values ranging from 8 to 14 were examined by HR-TEM (Figure 3.13 (A-D)). Co-3C-a (pH=8) sample showed nano rod morphology having length in the range of 10-20 nm (Figure 3.13, A). Increase in pH from 8 to 10 (Co-3C-b) resulted in increase in the particle length upto 20-60 nm (Figure 3.13, B). Whereas Co-3C-c sample (pH=12) showed rod shape as well as agglomerated elongated spherical particles in the range of 20-80 nm (Figure 3.13, C). The sample prepared at pH=14 (Co-3C-d) showed distinctly separated rod shape as well as elongated spherical particles having diameters in the range of 25-30 nm (Figure 3.13, D). However with increase in calcination temperature from 573 to 873 K, increase in length in the range of 55-65 nm was observed for Co-6C-a sample, which is in good agreement with the XRD results (Figure 3.13, E) [36]. The sample calcined at 573 K for 1 h (Co-3C-a-1) showed rod length in the range of 5-10 nm (Figure 3.13, F). The increase in calcination time from 1 to 5 h caused increase in rod length in the range of 10-20 nm. The characteristic planes obtained from the SAED image and 'd' spacings of the pattern of fringes (Figure. 3.13 (A-F)) were found to be due to the planes (111), (220), (311), (400), (422), (511) and (422), which matched with the XRD data confirming the perfect orientation of the particles in spinel Co_3O_4 for all the samples.

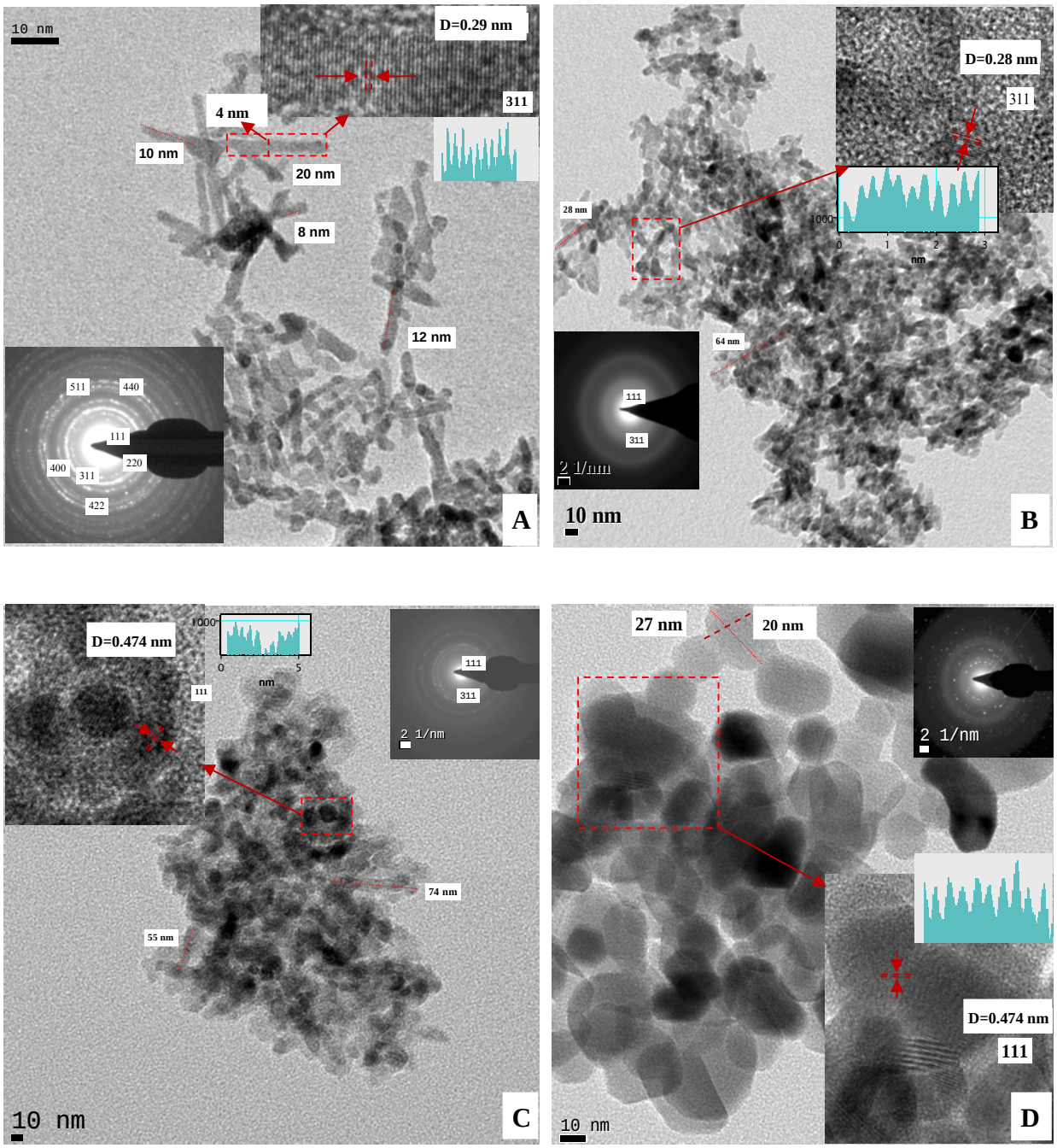
10 nm
D=0.29 nm
311
4 nm
10 nm
20 nm
8 nm
12 nm
511
440
111
400
311
220
422
A
D=0.28 nm
311
28 nm
64 nm
111
311
2 1/nm
10 nm
B
D=0.474 nm
111
74 nm
55 nm
10 nm
C
27 nm
20 nm
2 1/nm
D=0.474 nm
111
10 nm
D

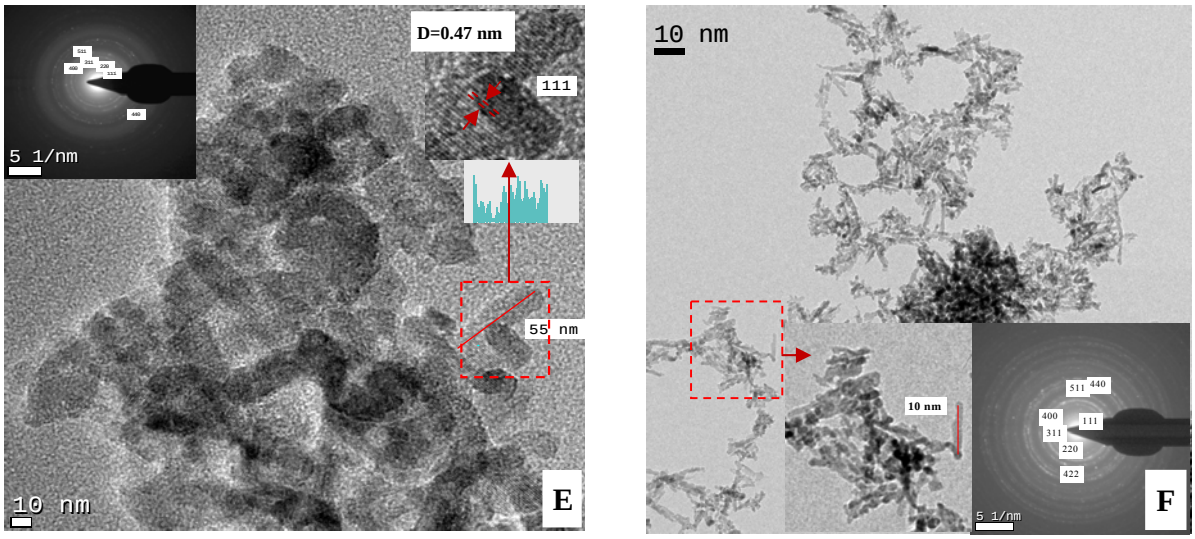

Figure 3.13. HRTEM of (A) Co-3C-a, (B) Co-3C-b, (C) Co-3C-c, (D) Co-3C-d, (E) Co-6C-a and (F) Co-3C-a-1samples

3.3.1.8. Energy dispersive X-ray (EDX)

Figure 3.14 shows EDX of Co-a, Co-b, Co-c and Co-d samples confirming the presence of cobalt, oxygen, carbon elements and absence of any residual potassium.

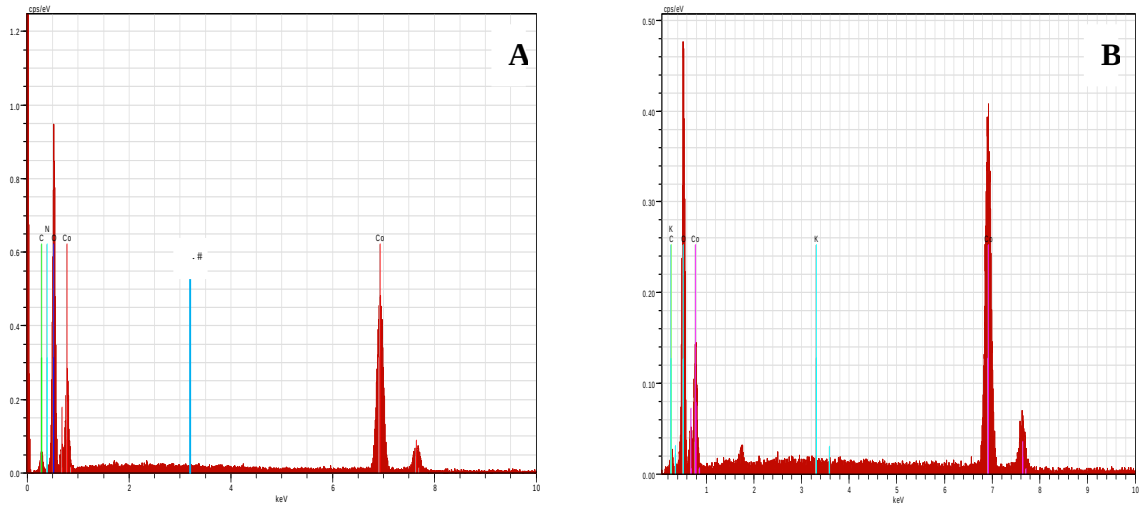

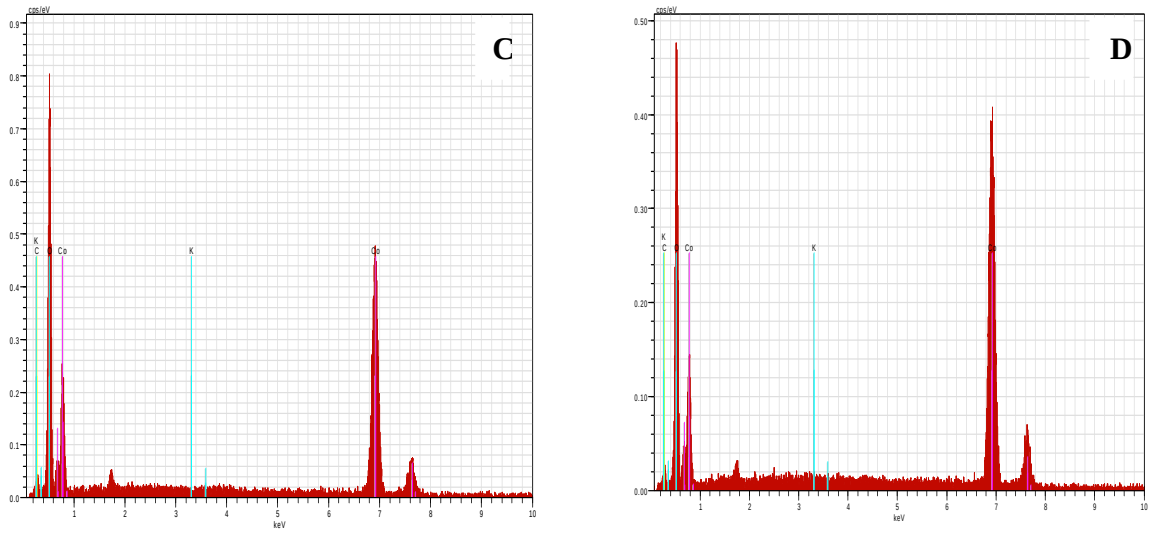

Figure 3.14. EDX of (A) Co-a, (B) Co-b, (C) Co-c and (D) Co-d samples

3.3.1.9. Temperature programmed reduction / Temperature programmed oxidation (TPR/TPO)

The reducibility of the catalysts prepared at various pH (7-14) and calcined at 573 K and 873 K was studied by H_2-TPR (Figures 3.15 and 3.16). The peaks observed in the range of 450-600 K were attributed to the reduction of trivalent cobalt oxide (Co_3O_4) to divalent cobalt oxide (CoO). Another broad peak in a higher temperature range of 600-850 K in all the samples was attributed to the reduction of divalent cobalt oxide (CoO) to metallic cobalt (Co^o) [51, 55]. The slight shift in the first peak from temperature 533 to 538 and 546 K for the samples Co-3C-a, Co-3C-b and Co-3C-c, were observed with a change in pH from 8 to 12, while for the sample prepared at pH=14, the peak appeared at the same temperature of 533 K as that for the sample prepared at pH= 8. This slight increase in temperature for reduction for the samples Co-3C-b and Co-3C-c might be due to the increase in crystallite sizes from ~12-40 to ~30-85 nm as observed in XRD and HRTEM, which might require higher temperature for reduction of the bigger particles [56].

Co-3C-a sample showed 435 mmol of H_2 up take (Table 3.3) while, with change in pH from 8 to 12 for the preparation of Co-3C-b and Co-3C-c samples, lower H_2 up take of 251 mmol and 176 mmol was observed as compared to Co-3C-a sample (Table 3.3). This was due to the aggregation of primary particles (cobalt hydroxyl carbonate) which also exhibited decrease in surface area (74.5 and 58.4 m^2/g for Co-3C-b and Co-3C-c samples respectively). Co-3C-d (prepared at pH=14) sample showed 347 mmol of H_2 up take which was also lower than that for Co-3C-a sample (Table 3.3). The Co-6C-a and Co-6C-d (calcined at 873 K) samples showed shift in reduction peaks to the higher temperatures of 567 and 570 K respectively than that for Co-3C-a and Co-3C-d samples (calcined at 573 K) (Figure 3.16, B). The slight shift in reduction peak to the higher temperature might be due to the increase in crystallite size from 12-32 to 20-70 nm and from 20-40 to 30-70 nm as confirmed by XRD and HRTEM. Calcination at high temperature (873 K) caused decrease in H_2 up take from 435 to 304 mmol and from 347 to 243 mmol for the samples Co-6C-a and Co-6C-d respectively (Table 3.3). ~30% lower reducibility of 873 K calcined samples (Co-6C-a and Co-6C-d) than those calcined at 573 K (Co-3C-a and Co-3C-d) was due to the re-structuring of primary particles at higher temperature (873 K) and decrease in surface area (from 110 to 24.5 m^2/g and 121 to 23.5 m^2/g for Co-6C-a and Co-6C-d samples respectively) resulting into incomplete reduction of bulk particles. The above observation shows that the extent of reducibility depends mainly on the calcination temperature and pH.

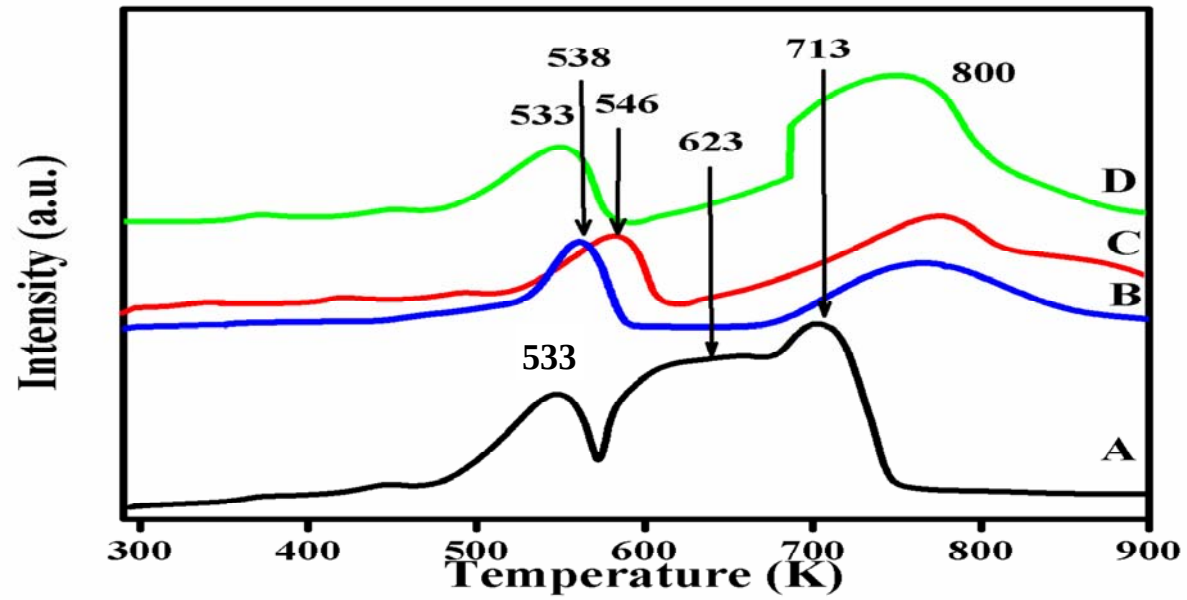

Figure 3.15. TPR profiles of (A) Co-3C-a, (B) Co-3C-b, (C) Co-3C-c and (D) Co-3C-d samples

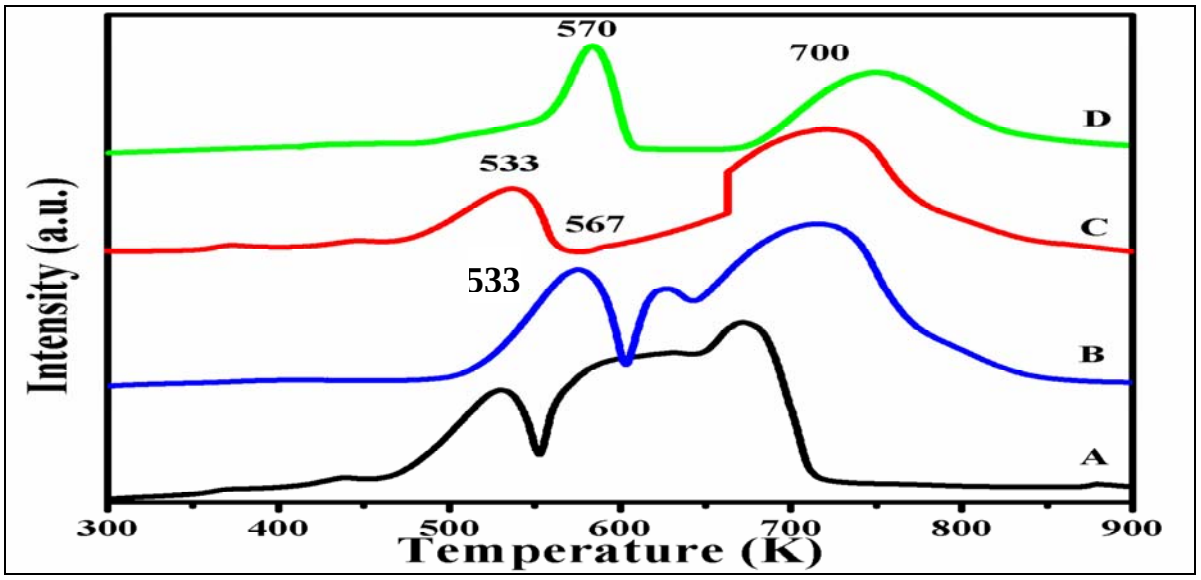

Figure 3.16. TPR profiles of (A) Co-3C-a, (B) Co-6C-a, (C) Co-3C-d and (D) Co-6C-d samples

The ability of oxidation of pre-reduced catalysts prepared at various pH (7-14) and calcined at 573 K and 873 K, was also studied using TPO technique and the results are shown in Figures 3.17 and 3.18. The peak in a range of 373-430 K in all the samples was attributed to the oxidation of metallic cobalt (Co^o) to divalent cobalt oxide (CoO). Another broad peak appearing

in the range 470-690 K in all the samples indicates the oxidation of divalent cobalt oxide (CoO) to trivalent cobalt oxide (Co_3O_4) [52, 53]. The slight shift in the first oxidation peak (curve A) from temperature 410 to 423, 439 and 420 K (curves B, C and D respectively) were observed with change in pH from 8 to 14 used in the preparation protocol. This slight increase in oxidation temperature might be due to the increase in crystallite size and change in morphology of the particles, which requires higher temperature for oxidation [56]. Co-3C-a sample showed 20.6 mmol of O_2 up take (Table 3.3), while Co-3C-b and Co-3C-c samples showed 16.1 and 9.9 mmol O_2 up take respectively. This could be due to decrease in surface area of the samples by changing the pH from 8 to 12. While, Co-3C-d sample showed 17.8 mmol of O_2 up take which was less than that required for Co-3C-a and higher than Co-3C-b and Co-3C-c samples (Table 3.3). The O_2 consumption of these samples was much less than H_2 consumption observed in TPR. This might be due to the fact that oxygen having the co-ordinative nature hence forming a multi-metal nucleated species and also due to distortion of the surface during chemical absorption [41]. Calcination at higher temperature of 873 K caused decrease in O_2 up take from 20.6 to 18.6 and from 17.8 to 14.5 mmol in case of Co-6C-a and Co-6C-d samples respectively (Table 3.3). The lower O_2 up take by sample calcined at higher temperatures was also due to the decrease in surface area values indicating that higher oxidizing ability of Co-3C-a catalyst was due to its rod-like morphology, appropriate surface area and higher redox ability.

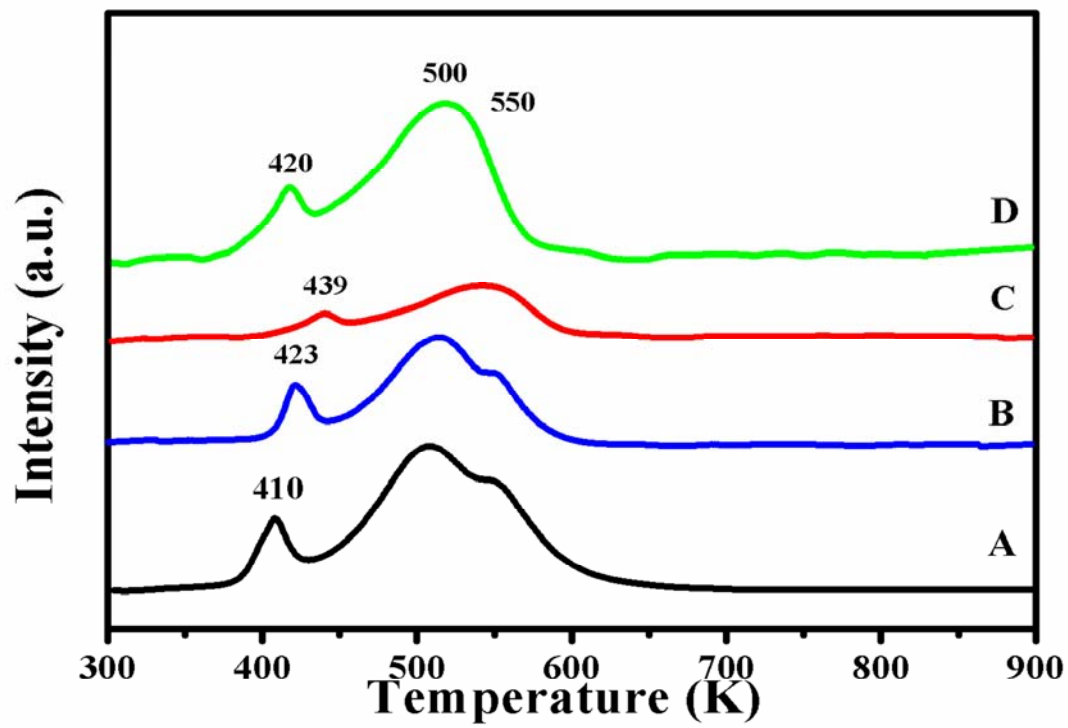

Figure 3.17. TPO profiles of (A) Co-3C-a, (B) Co-3C-b, (C) Co-3C-c and (D) Co-3C-d samples

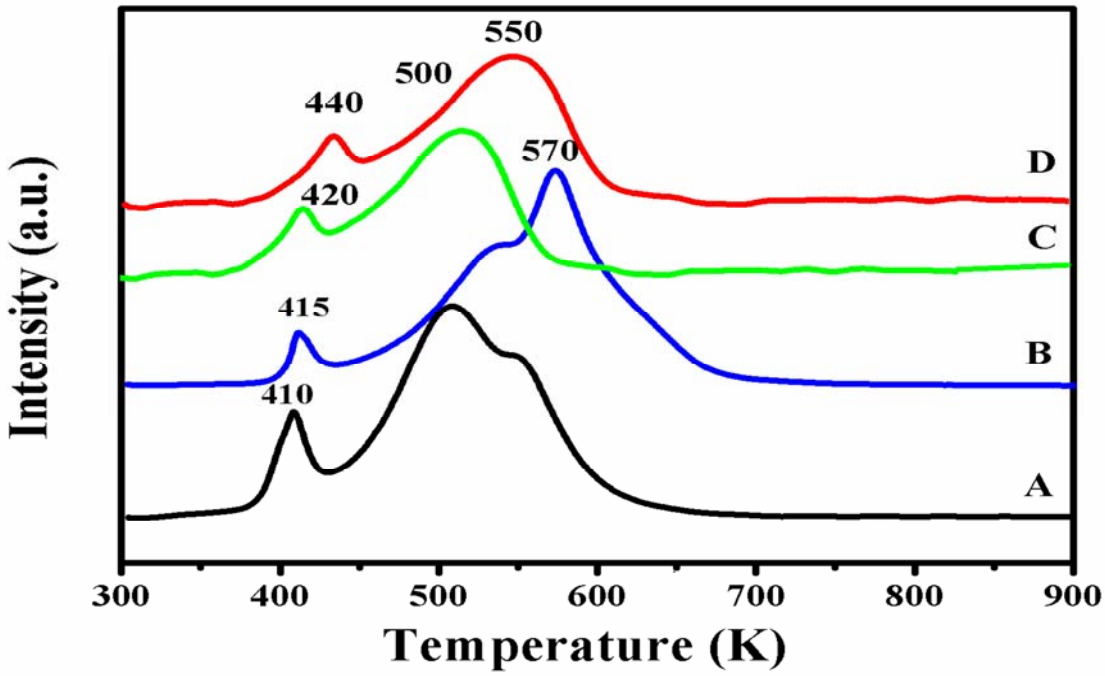

Figure 3.18. TPO profiles of (A) Co-3C-a, (B) Co-6C-a, (C) Co-3C-d and (D) Co-6C-d samples

Table 3.3. H_2/O_2 uptake profile of catalysts prepared at various pH

Entry	Catalysts	pH	Surface area (m^2/g)	TPR		TPO	
				Temperature (K)	H_2 (mmol)	Temperature (K)	O_2 (mmol)
1	Co-3C-a	8	110.0	440-750	435	370-620	20.6
2	Co-3C-b	10	74.5	440-820	251	370-650	16.1
3	Co-3C-c	12	58.4	450-820	176	370-600	9.9
4	Co-3C-d	14	121.6	450-850	348	370-600	17.8
5	Co-6C-a	8	24.5	490-820	304	380-650	18.6
6	Co-6C-d	14	23.5	530-850	243	370-650	14.5

3.3.1.10. Cyclic voltammogram (CV)

The redox potential profiles of the catalysts prepared at pH value ranging from 8 to 14 were examined by cyclic voltammogram (Figure 3.19). All the samples showed broad oxidation and reduction peaks. The cathodic peak in the lower potential region (1.21 V) could be assigned to the oxidation of Co^{2+} to Co^{3+}. Similarly, the anodic peak present at higher potential (1.28 V) could be assigned to the reduction of Co^{3+} to Co^{2+}. The peak intensity gradually decreased from samples Co-3C-a to Co-3C-c. Interestingly, Co-3C-d sample showed higher peak intensity than that for Co-3C-b and Co-3C-c samples. The decrease of peak intensity in case of Co-3C-b and Co-3C-c samples might be due to the decrease in surface area from 110 to 74.5 and 58.4 m^2/g respectively, which might in turn reduce the number of surface active species. In spite of having higher surface area (121 m^2/g) Co-3C-d sample showed lower peak intensity than the Co-3C-a

sample. This might be due to the lower redox ability of Co-3C-d, confirmed by TPR/TPO or mixed morphology of rod and elongated spherical particles. The Co-6C-a and Co-6C-d samples calcined at higher temperature of 873 K (Figures 3.20 and 3.21), showed the peaks of lower intensity and shift in anodic peaks from 1.28 to 1.20 and 1.25 V and cathodic peaks from 1.21 to 1.15 to 1.18 V respectively. The shift in electrochemical potential and lowering of peak intensity in case of high temperature calcined catalyst (873 K) might be due to lowering of surface area (from 110 to 24.5 m^2/g and 121 to 23.5 m^2/g). As a result of lowered electrochemical/redox potential, shifts in reduction peak to higher temperatures from 533 to 567 K and from 533 to 570 K in TPR profiles and oxidation peak from 410 to 415 K and from 420 to 440 K in TPO profile were observed (Figures 3.16 and 3.18). The lower electrochemical potential which could be due to decrease in surface active species at higher temperature as indicated by TPR and TPO profiles indicates lower oxidation ability which affects the CV behavior of samples calcined at higher temperature. Amongst the prepared catalysts, higher redox potential was observed for Co-3C-a catalyst leading to its higher oxidation activity as discussed later.

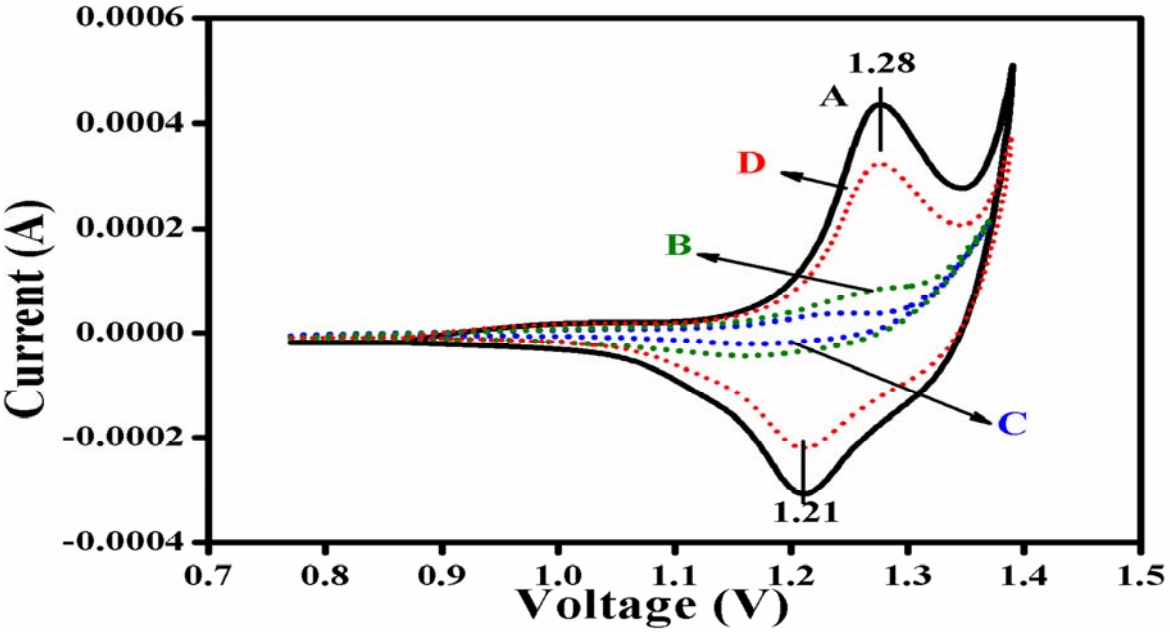

Figure 3.19. CV profiles of (A) Co-3C-a, (B) Co-3C-b, (C) Co-3C-c and (D) Co-3C-d samples

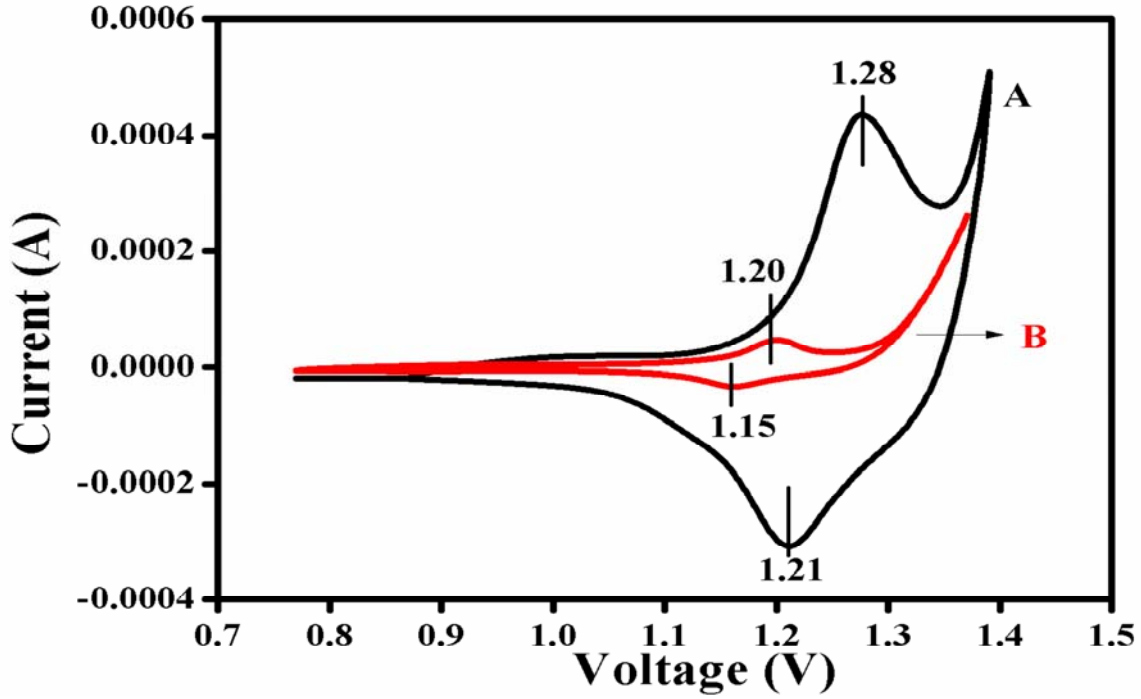

Figure 3.20. CV profiles of (A) Co-3C-a and (B) Co-6C-a samples

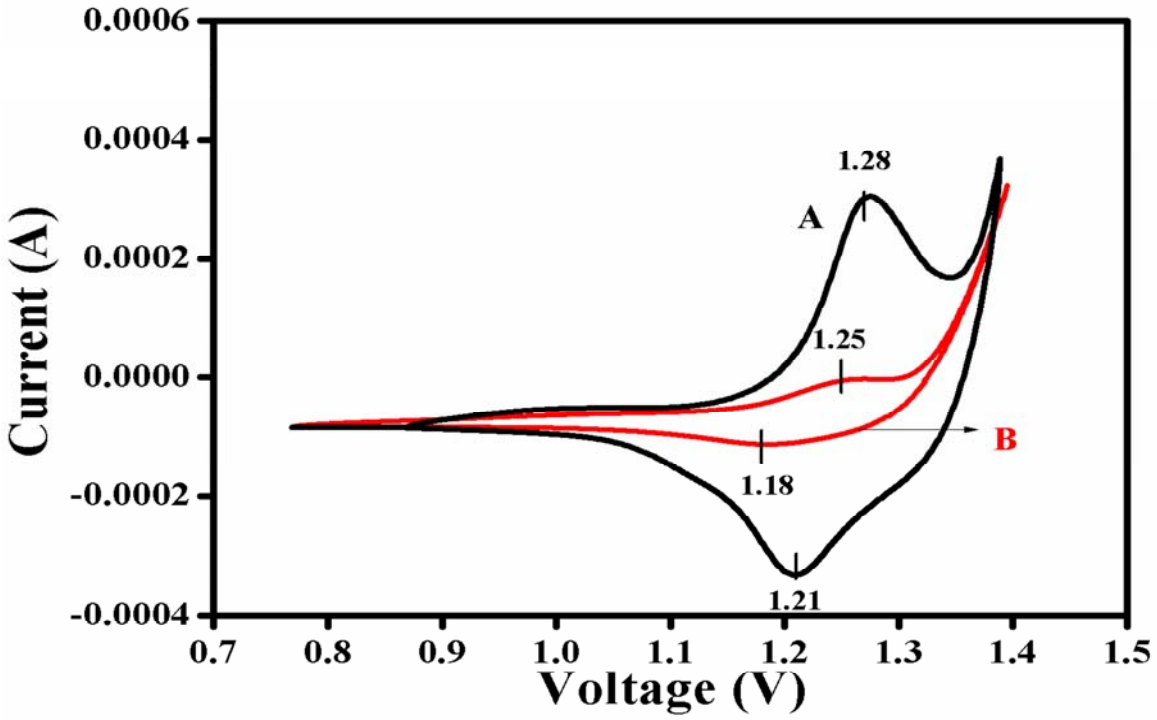

Figure 3.21. CV profiles of (A) Co-3C-d and (B) Co-6C-d samples

3.3.1.11. Electron paramagnetic resonance (EPR)

The EPR spectra of Co-3C-a catalyst recorded at temperature 50 K is shown in Figure 3.22. In case of spinel Co_3O_4 (Co-3C-a), magnetic moment arises due to Co^{2+} ions largely because of spins, with a small contribution from spin–orbit coupling [57, 58]. The stronger peak intensity and larger peak area of Co^{2+} prove the higher concentration of Co^{2+} ions, required for the higher availability for oxygen vacancies [59]. However, among all the catalysts prepared, the XPS, TPR/TPO and CV results showed that Co-3C-a had higher concentration of Co^{3+} species existing on the surface, which seemed to be contradictory to the EPR results. This was probably due to increased Co^{3+} concentration on the surface had promoting effect on the formation of Co^{2+} in the bulk phase [58, 59]. The higher concentration of surface Co^{3+} could promote the adsorption and

activation of substrate (such as veratryl alcohol), while increased Co^{2+} in the bulk benefited the formation of oxygen vacancy required for catalyzing the oxidation reaction.

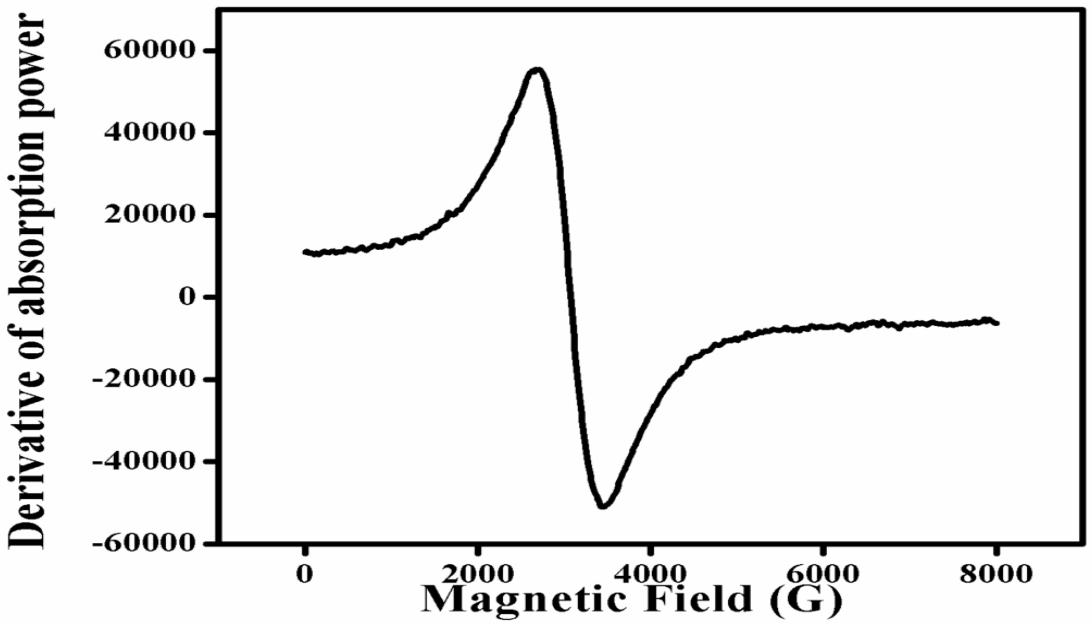

Figure 3.22. EPR of Co-3C-a sample

3.3.2. Co_3O_4 preparation by sol-gel method

Sol-gel is another efficient method for preparation of nano materials at moderate conditions. It is believed that sol-gel derived nano particles generally possess good chemical homogeneity (unlike in co-precipitation method which generally gives inhomogeneity) and high purity. Co_3O_4 prepared by sol-gel method was also evaluated for the liquid phase oxidation of veratryl alcohol.

3.3.2.1. Surface area measurement by BET method

Table 3.4 presents BET surface areas of catalysts prepared via sol-gel (Co-e) method and calcined at two different temperatures, 573 and 873 K. The Co-3C-e catalyst showed 21.2 m^2/g surface area which decreased to13.2 m^2/g for Co-6C-e sample with increase in calcination temperature from 573 to 873 K. The decrease in surface area was due to the increased crystallite

size as observed in the XRD and HRTEM discussed later. However, the surface area of these catalysts was found to be much lower (5-8 times) than the catalyst prepared by co-precipitation method and calcined at 573 K (Co-3C-a, 110 m^2/g). From the above observations, it is confirmed that one can prepare a catalyst with higher surface area via controlled co-precipitated method rather than by the sol-gel method.

Table 3.4. BET surface area of Co_3O_4 samples prepared via sol-gel method

Entry	Catalysts	Calcination temperature, (K)	Specific Surface area (m^2/g)
1	Co-3C-e	573	21.2
2	Co-6C-e	873	13.2
3	Co-3C-a	573	110

3.3.2.2. X-ray diffraction (XRD)

XRD patterns of Co-3C-e and Co-6C-e samples are presented in Figure 3.23. All the samples exhibited the diffraction peaks at 2θ =19.2° (111), 31.2° (220), 36.84° (311), 44.84° (400), 55.65° (422), 59.42° (511) and 65.21° (422), which were attributed to the spinel phase of Co_3O_4. The calculated lattice parameter for all the samples was found to be ~8.085 Å matching with the reported value of 8.084 Å (JCPDS # 9-418) of the cubic Co_3O_4. Crystallite sizes of Co-3C-e and Co-6C-e samples calculated using the Scherrer equation were found to be in the range of 75-100 and 90-160 nm respectively. Thus, increase in crystallite size for Co-6C-e was mainly due to restructuring of the sample at 873 K. However, sample prepared by co-precipitation method under the same calcination temperature showed crystallite size of 12-38 nm which is very much

lower than that prepared by sol-gel method (Section 3.3.1.2). The crystallite sizes of these samples matched very well with the HRTEM results.

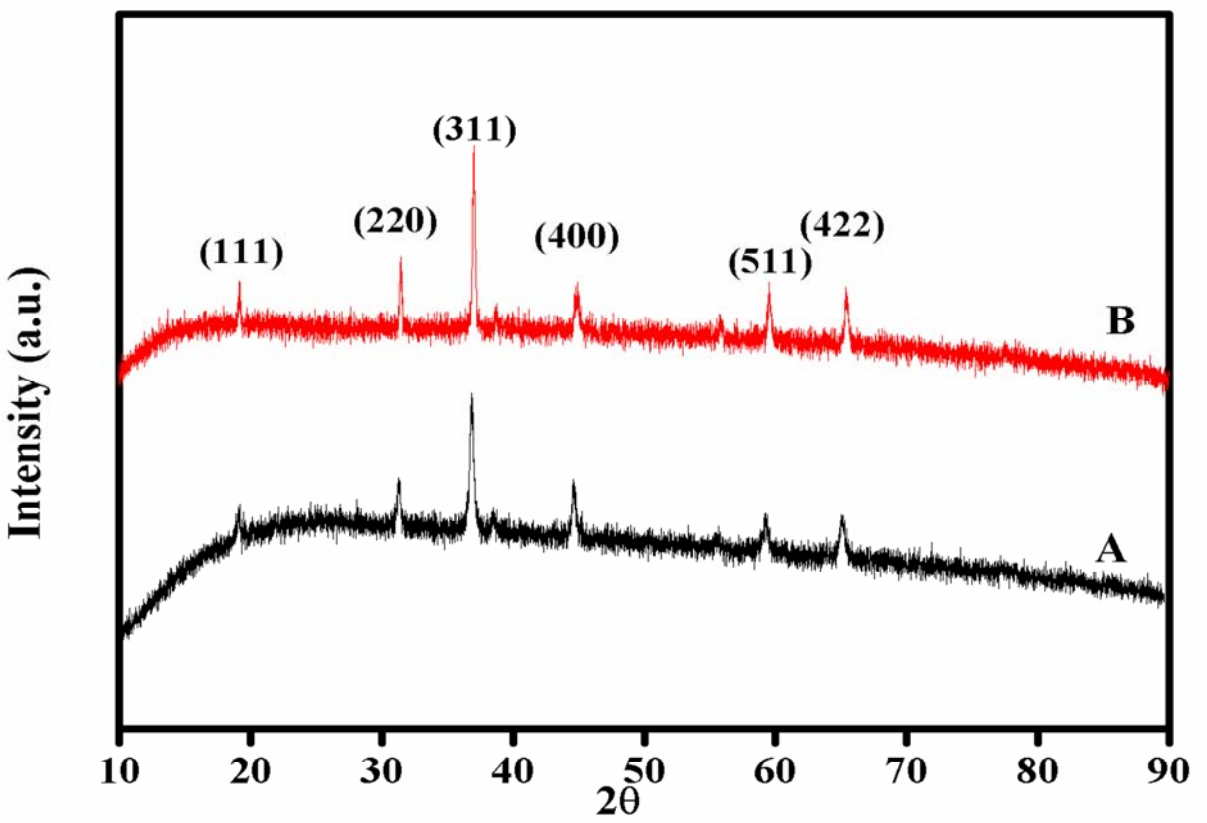

Figure 3.23. XRD of (A) Co-3C-e and (B) Co-6C-e samples

3.3.2.3. X-ray photoelectron spectroscopy (XPS)

Figure 3.24a shows the Co 2p XPS spectrum for the Co-3C-e sample. The Co 2p spectrum contains Co $2p_{3/2}$ and Co $2p_{1/2}$ core level peaks at binding energies of 779.1 and 794.4 eV having difference of 15.3 eV [11]. The Co $2p_{3/2}$ peak on decovolution gives two peaks at binding energies of 779.1 and 781.9 eV which correspond to Co^{3+} and Co^{2+} species respectively (Figure 3.24b). This evidenced the formation of spinel Co_3O_4 [37, 38].

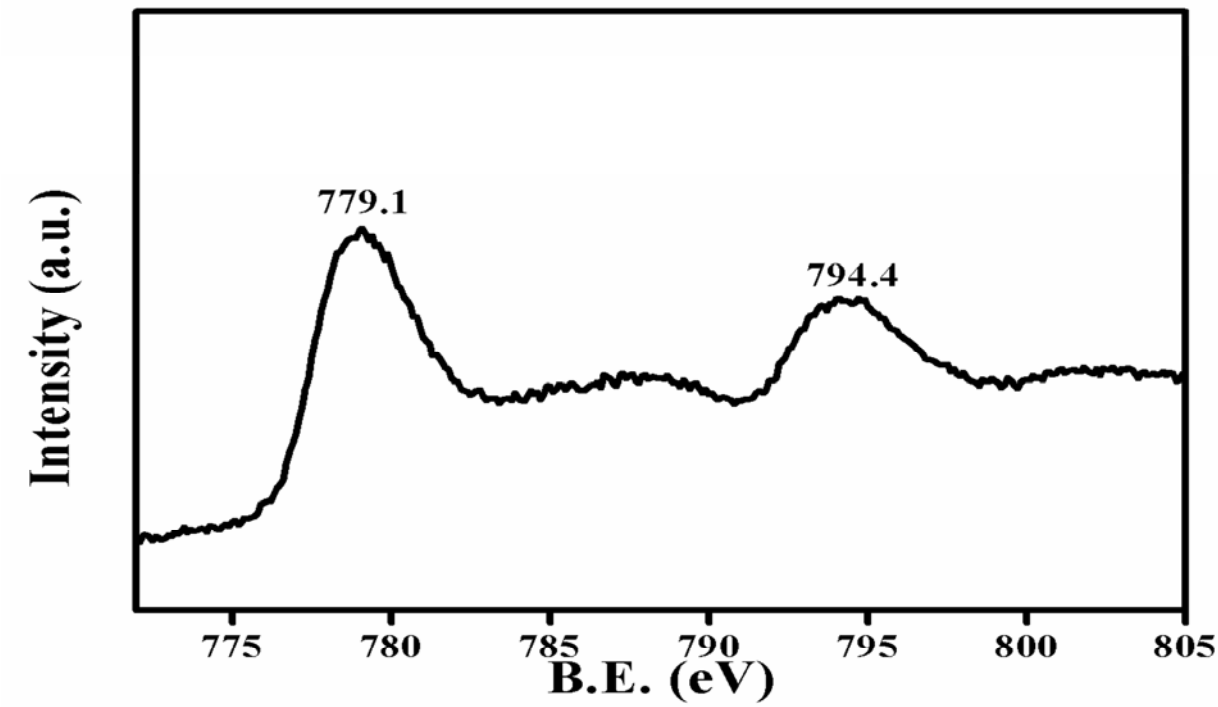

Figure 3.24a. XPS of Co-3C-e sample

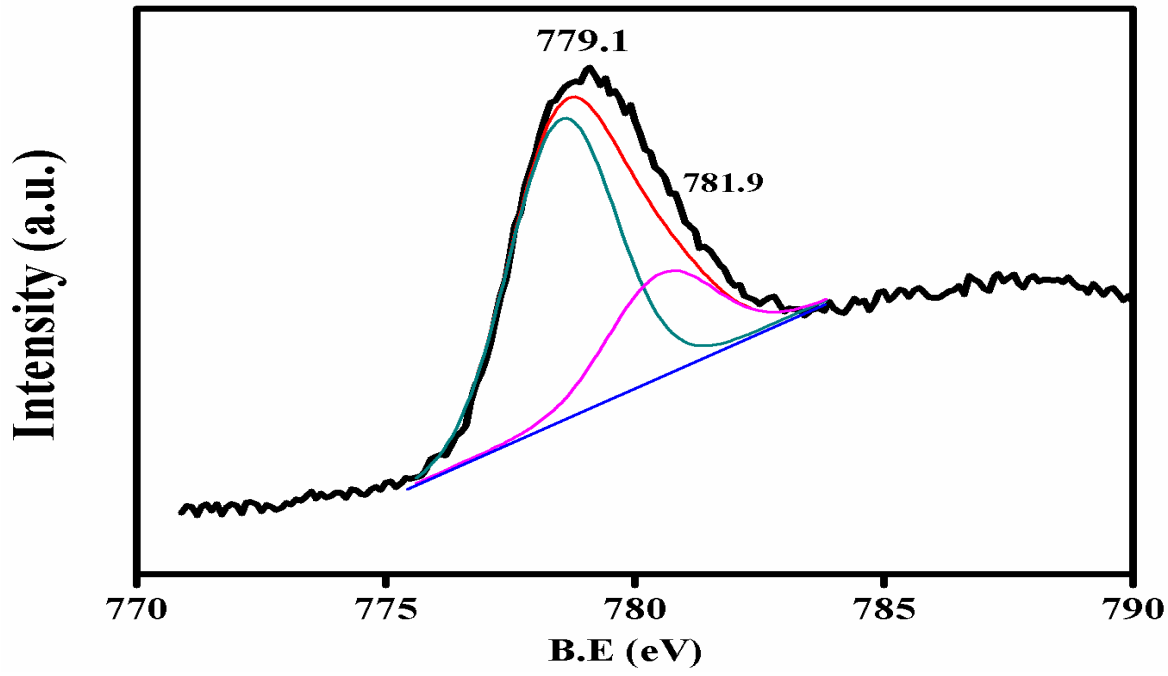

Figure 3.24b. Deconvolution spectra of Co $2p_{3/2}$

3.3.2.4. Thermo gravimetric analysis (TG-DTA)

Figure 3.25 exhibits the TG-DTA for the as-prepared Co-e (sol-gel) sample. The catalyst showed weight losses in four steps. The first weight loss of 9% was observed from room temperature to 413 K due to the loss of physically adsorbed water molecules. The second weight loss (28%) near to 443 K could be assigned for dehydration of chemically bonded water in the $CoC_2O_4.4H_2O$ [39] that was trapped in the gel after the gelation point. Third weight loss (25%) observed near to 650 K, which might be due to decomposition of ethylene glycol and acetate in to CO and CO_2. The fourth weight loss (10%) appeared near to 700 K, which could be assigned for dehydroxylation of surface hydroxy groups. Based on the above observations, temperature in the range of 773-823 K was required to calcine the Co-e catalyst (acetate/ethylene glycol) completely (Figure 3.43). This was much higher than the calcination temperature (573 K) required in case of co-precipitation catalyst (Figure 3.10).

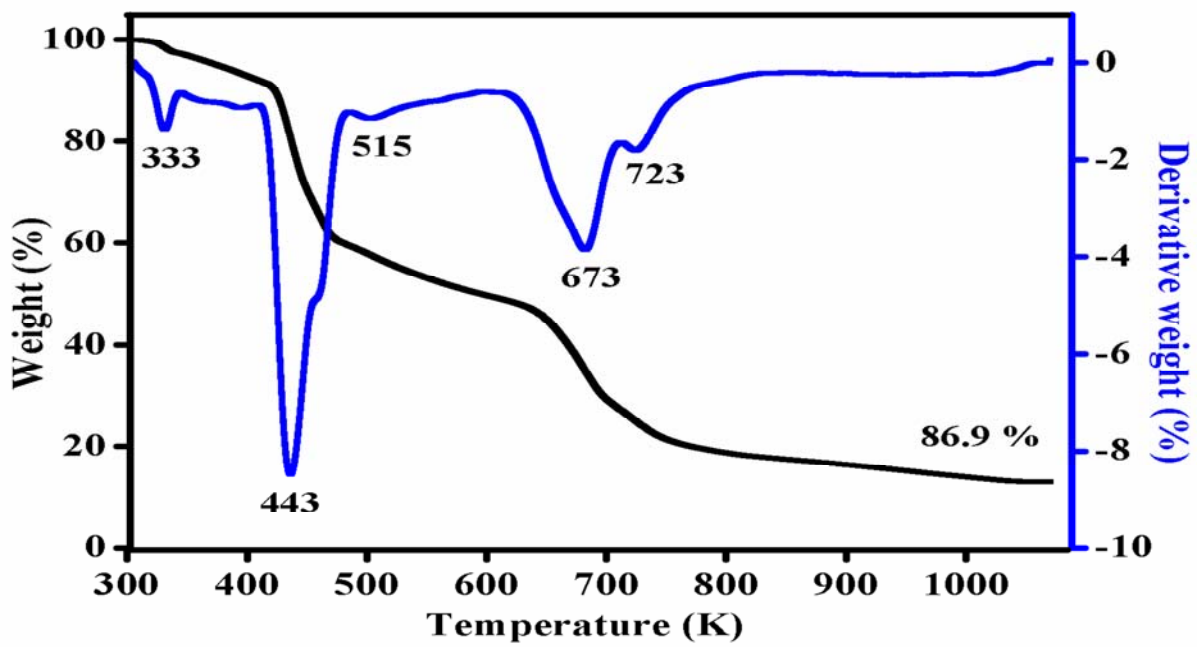

Figure 3.25. TG-DTA of Co-e sample

Table 3.5. Summary of thermogravimetric analysis

Sample	TG		DTA	Remarks
	Temperature (K)	Weight loss (w/w. %)	Peak maximum (K)	
Co-e (sol-gel)	413	9	333	Loss of physically adsorbed water
	443	28	443	Dehydration of chemically bonded water in the $CoC_2O_4 \cdot 4H_2O$
	650	25	673	Decomposition of physically adsorbed/excess ethylene glycol.
	700	10	723	dehydroxylation of surface hydroxy groups

3.3.2.5. Fourier-Transform infrared spectroscopy (FT-IR)

FT-IR spectra of Co-3C-e and Co-6C-e samples showed two distinct bands at 567 and 666 cm^{-1} assigned to stretching vibrations of metal-oxygen bonds (Figure 3.26). The peak at 567 cm^{-1} corresponds to Co^{3+} in an octahedral position while the other peak at 666 cm^{-1} corresponds to the Co^{2+} in a tetrahedral position confirming the formation of Co_3O_4 spinel in the Co-3C-e and Co-6C-e samples [51, 52]. The broad peaks observed at 1407 and 1428 cm^{-1} in case of as prepared (Co-e) and 573 K calcined samples, were assigned to asymmetric bending and stretching vibrations of ($-CH_3$) and (COO^-) in ethylene glycol and acetate respectively [57-58, 60]. These results were in accordance with the TG-DTA results. The broad peaks at 3420 and 1627 cm^{-1} were attributed to metal hydroxyl stretching vibrations observed in both as prepared (Co-e) and Co-3C-e samples [54, 55], indicating that the catalyst calcined at 573 K had Co_3O_4 phase and

also contained some sort of organic impurities, while these impurities were not present in case of 873 K calcined sample.

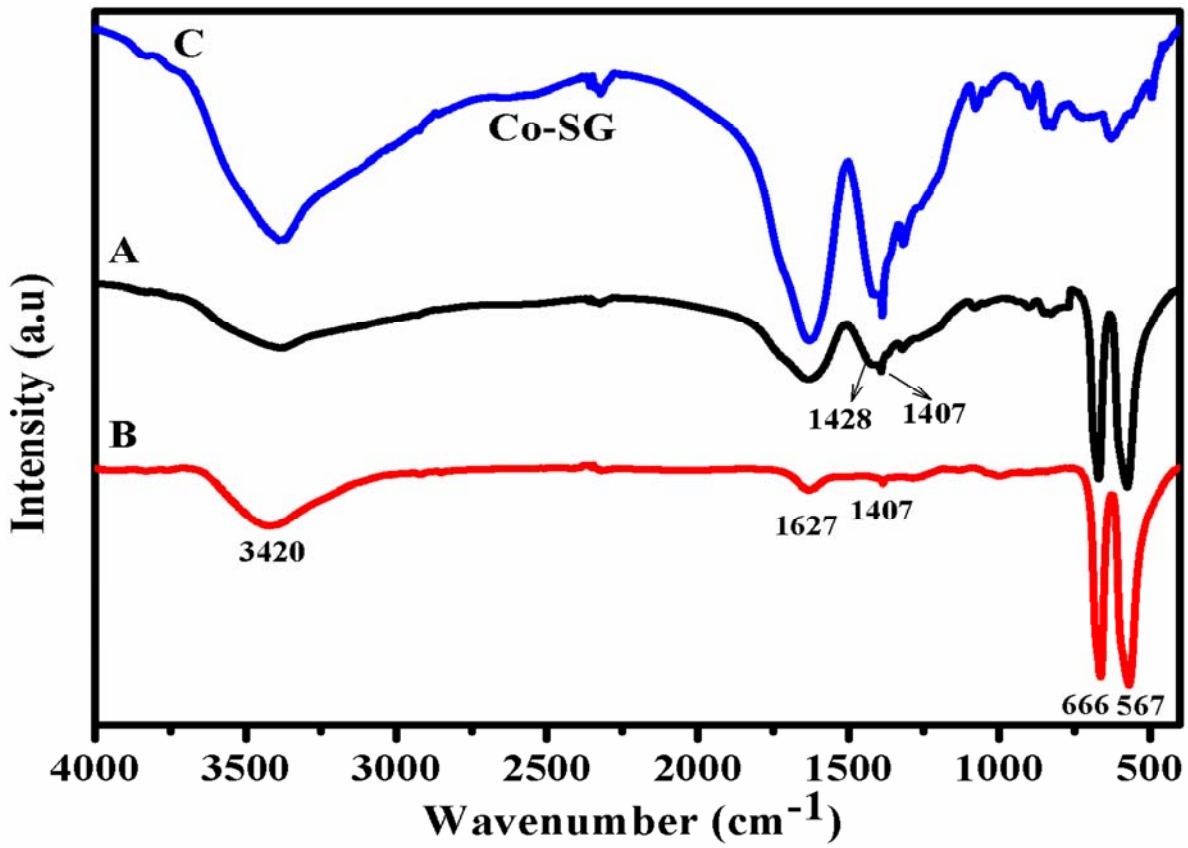

Figure 3.26. FTIR of (A) Co-3C-e, (B) Co-6C-e and (C) Co-e samples

3.3.2.6. High resolution transmission electron microscopy

The morphologies of the samples calcined at 573 K (Co-3C-e) and at 873K (Co-6C-e) were examined by HR-TEM (Figure 3.27). The Co-3C-e sample showed the aggregation of non uniform elongated spherical particles having diameter in the range of 80-100 nm. However with increase in calcination temperature from 573 to 873 K, increase in particle diameter in the range from 80-110 to 110-160 nm was observed for Co-6C-e sample, which was in good agreement with the XRD results.

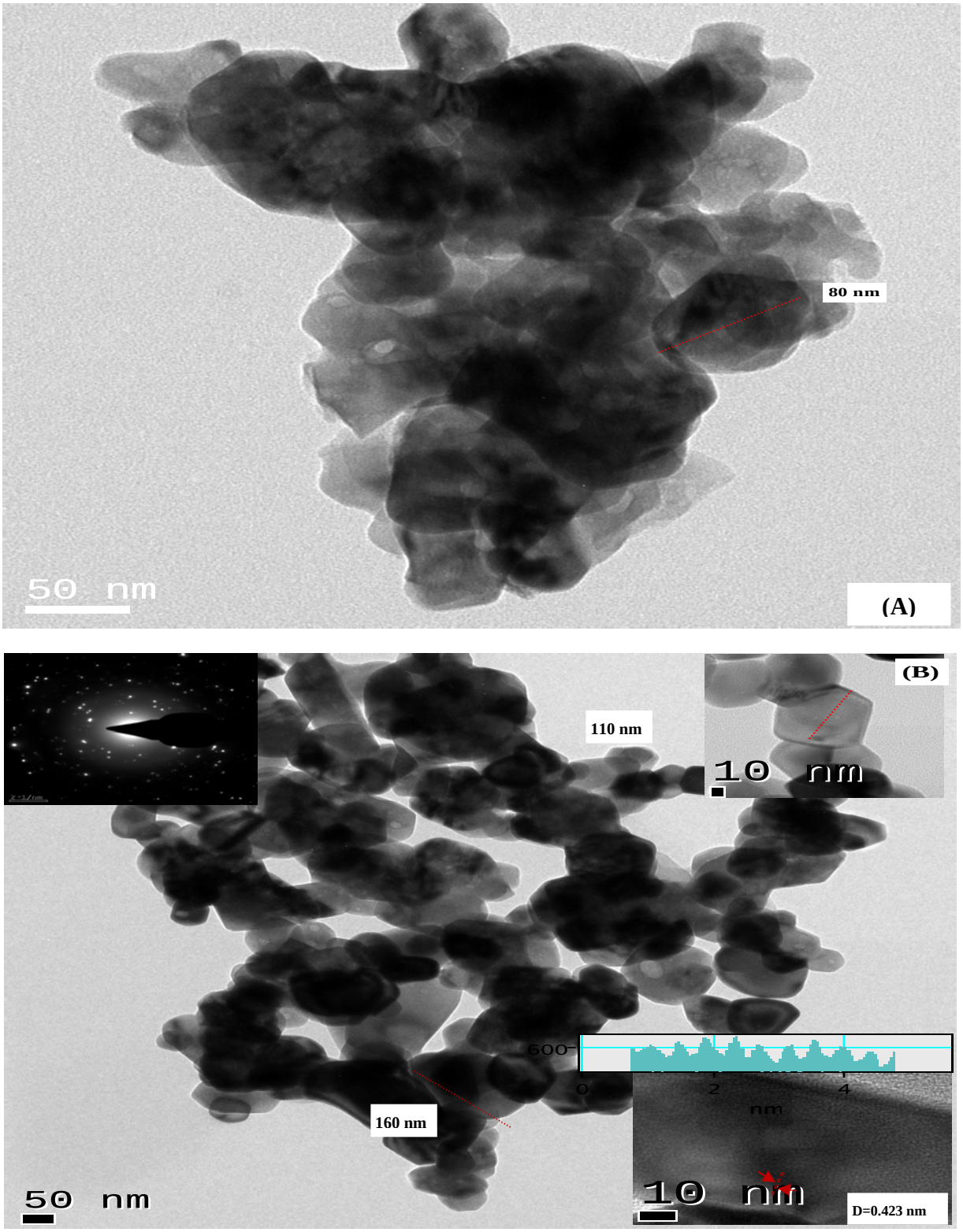

Figure 3.27. HRTEM of (A) Co-3C-e and (B) Co-6C-e samples

3.3.2.7. Temperature programmed reduction / Temperature programmed oxidation (TPR/TPO)

The reducibility of the Co-3C-e and Co-6C-e catalysts, was studied by H_2-TPR (Figure 3.28). The peak observed in the range of 500-680 K was attributed to the reduction of trivalent cobalt oxide (Co_3O_4) to divalent cobalt oxide (CoO). Another broad peak at higher temperature in the range of 700-950 K in both the samples was attributed to the reduction of divalent cobalt oxide (CoO) to metallic cobalt (Co^o) [54, 59]. The significant enhancement in the reduction temperature from 450-600 K to 500-680 K and 600-850 K to 700-950 K was observed for Co-3C-e of the catalyst prepared via sol-gel method as compared to co-precipitated catalysts (Section 3.3.1.9). This might be due to substantial increase in crystallite size from 12-32 nm to 75-100 nm as well as organic (trace of acetate) impurities present in the Co-3C-e catalyst as observed in TG-DTA and FTIR analysis. The Co-6C-e (calcined at 873 K) sample showed shift in reduction peaks to higher temperature from 590 to 610 K and from 640 to 650 K respectively. The slight shift towards higher reduction temperature might be due to increase in crystallite size from 75-100 to 90-160 nm which was confirmed by XRD and HRTEM. Co-3C-e sample showed 27 mmol of H_2 up take (Table 3.6). However, sample calcined at high temperature (873 K) showed three times increase in H_2 up take from 27 to 89 mmol in spite of having higher crystallite size (90-160 nm). The calcination at higher temperature of 873 K might have caused decomposition of organic impurities, which significantly cleaned the surface of active sites resulted in higher reducibility compared to 573 K calcined sample, as confirmed from the FTIR and TG-DTA analysis, indicating that catalysts prepared via sol-gel method required higher temperature for reduction and showed lower reducibility compared to co-precipitated catalysts due to bigger crystallite size.

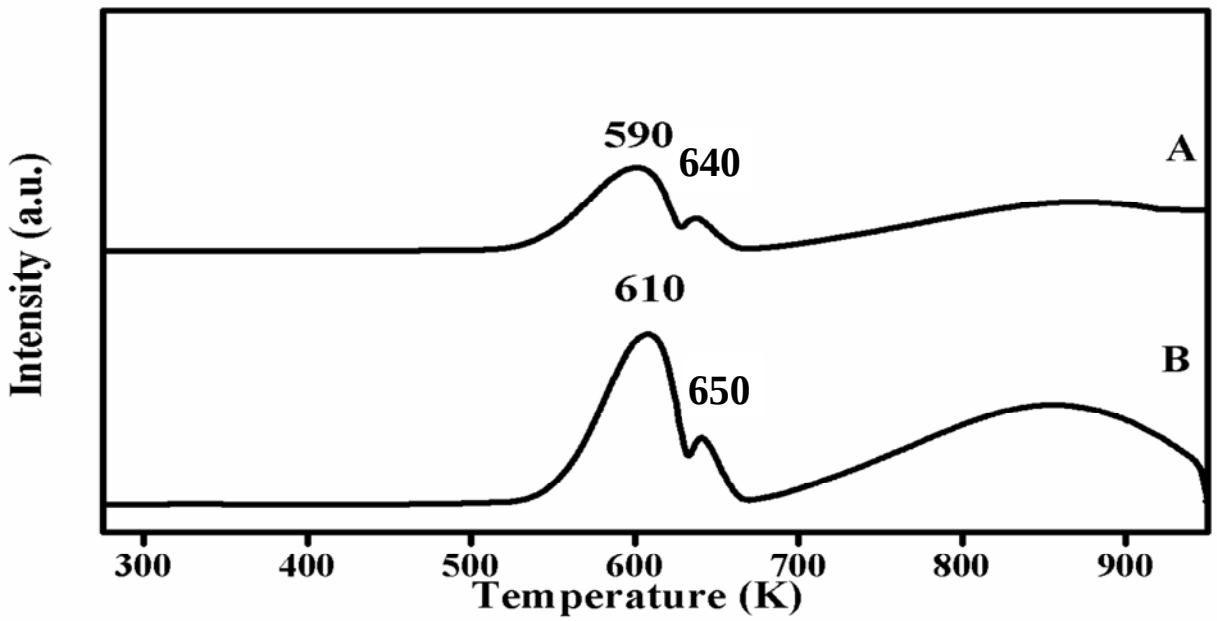

Figure 3.28. TPR of (A) Co-3C-e and (B) Co-6C-e samples

The oxidizability of pre-reduced Co-3C-e and Co-6C-e catalysts was studied by TPO and the results are presented in Figure 3.29. The first peak in a range of 400-450 K in both the samples was attributed to the oxidation of metallic cobalt oxide (Co^o) to divalent cobalt oxide (CoO). Second broad peak appearing in the range 450-650 K in both the samples indicated the oxidation of divalent cobalt oxide (CoO) to the trivalent cobalt oxide (Co_3O_4) [55, 56]. The slight shift in both oxidation peaks from temperature 373-430 K to 400-450 K and second peak from 470-690 K to 450-650 K compared to co-precipitated catalysts (Section 3.3.1.9), was due to increase in reduction temperature of these catalysts as established by TPR. Co-6C-e sample showed three times (3.8 mmol) higher O_2 up take than the Co-3C-e (1.2 mmol) sample (Table 3.6). From these results it can be inferred that the catalysts prepared by sol-gel method showed higher oxidizing ability than Co-6C-e catalyst hence, the former would have the maximum number of active sites available on the surface.

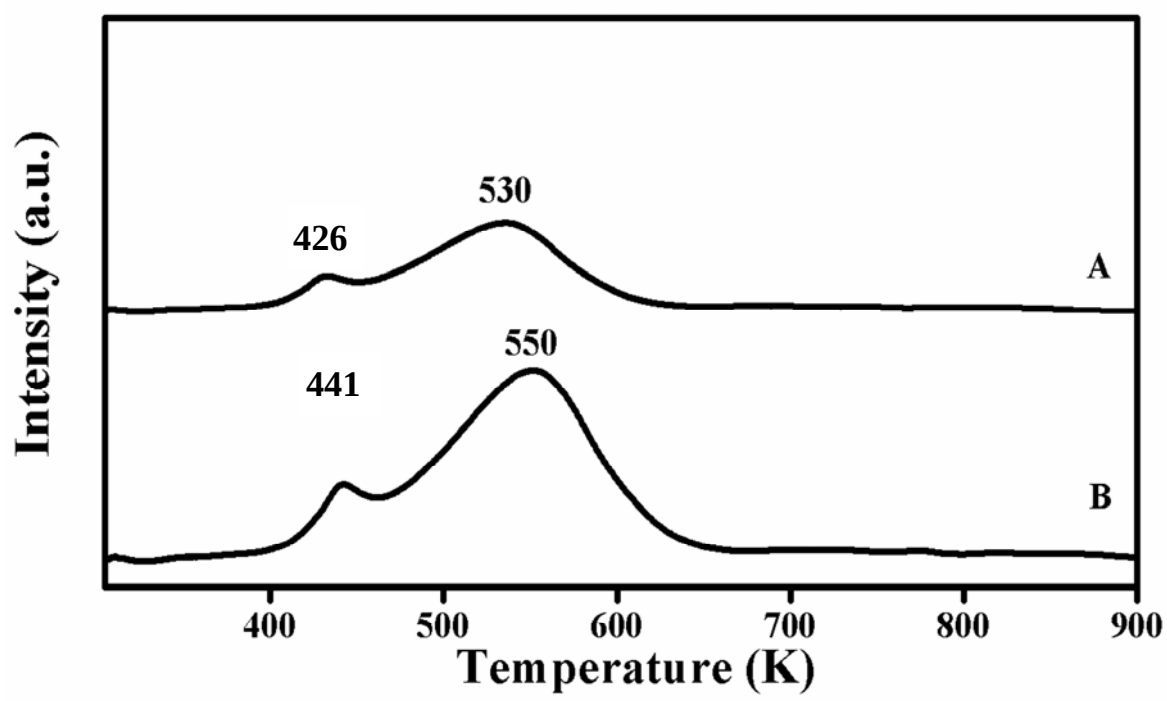

Figure 3.29. TPO of (A) Co-3C-e and (B) Co-6C-e samples

Table 3.6. H_2/O_2 uptake by TPR/TPO peak for Co_3O_4 catalysts prepared via sol-gel method

Entry	Catalysts	TPR		TPO	
		Temperature (K)	H_2 (mmol)	Temperature (K)	O_2 (mmol)
1	Co-3C-e	500-700	27	400-600	1.2
2	Co-6C-e	500-700	89	400-650	3.8
3	Co-3C-a	440--750	435	370-620	20.6

3.3.3. Co_3O_4 preparation by thermal decomposition

Thermal decomposition technique is a versatile process leading to synthesis of single phase, solid solutions, composites as well as complex oxide phases with uniform composition. For the production of a variety of advanced materials, the thermal decomposition method proves to be an efficient and simple process. This process is preferred for its additional characteristic features such as (i) rapid heating rates, (ii) use of relatively simple equipment (iii) formation of products of virtually any size and shape. Thus, this process leads to the formation of final products with higher order of purity and better mechanical properties. However, controlling the heating and cooling rates enables to obtain metastable materials with new and unique properties [61]. Deshpande *et al*. [62] reported that proper choice of starting precursor and its concentration could invariably produce materials with improvement in composition and properties. Therefore, I have selected cobalt nitrate (Co-f) and cobalt acetate (Co-g) samples for the preparation of Co_3O_4. Finally, the structure-activity correlation of the prepared samples was also studied and compared with the samples prepared by co-precipitation, sol-gel and commercial Co_3O_4.

3.3.3.1. Surface area measurement by BET method

BET surface areas of Co_3O_4 samples prepared via thermal decomposition (TD) of cobalt nitrate (Co-f) and cobalt acetate (Co-g) followed by calcination at 573 and 873 K and of commercial Co_3O_4 are presented in Table 3.7. The BET surface area decreased from 51.7 to 31 m^2/g with change in the cobalt precursor from nitrate (Co-3C-f) to acetate (Co-3C-g) due to the decomposition of nitrate at lower temperature (<523 K) compared to acetate (>543 K) precursor. The effect of decomposition temperature on the crystallite/particle size is discussed in more detail in XRD, HR-TEM and TG-DTA studies in the later sections. The commercial Co_3O_4

sample showed the lowest surface area of 21 m^2/g. Increase in calcination temperature from 573 to 873 K, resulted in three times decrease in surface area from 51.7 to 16.5 m^2/g and 31 to 11.8 m^2/g observed in case of Co-6C-f and Co-6C-g samples prepared by using nitrate and acetate precursors respectively. Nevertheless, the surface area of these (573 K) catalysts was found to be lower than that for Co-3C-a (110 m^2/g) catalyst. Thus, Co_3O_4 with higher surface area could be obtained by co-precipitation method rather than sol-gel and thermal decomposition methods.

Table 3.7. BET surface area of Co_3O_4 samples prepared via thermal decomposition method

Entry	Catalysts	Calcination temperature (K)	Specific Surface area (m^2/g)
1	Co-3C-f	573	51.7
2	Co-6C-f	873	16.5
3	Co-3C-g	573	31.0
4	Co-6C-g	873	11.8
5	commercial Co_3O_4	_	21.0

3.3.3.2. X-ray diffraction (XRD)

XRD patterns of samples prepared by thermal decomposition of cobalt nitrate (Co-f) and cobalt acetate (Co-g) samples and calcined at 573 and 873 K and of commercial Co_3O_4 are presented in Figure 3.30. All the samples exhibit the diffraction peaks at 2θ =19.2° (111), 31.2° (220), 36.84° (311), 44.84° (400), 55.65° (422), 59.42° (511) and 65.21° (422), which could be attributed to the spinel phase of Co_3O_4. The calculated lattice parameter for all the samples was found to be

~8.086 Å, which matched very well with the reported value of 8.084 Å (JCPDS # 9-418) of the cubic Co_3O_4. The crystallite sizes of Co-3C-f, Co-3C-g and commercial Co_3O_4 samples calculated using the Scherrer equation were found to be in the range of 25-40, 25-48 and 80-110 nm respectively. The increase in calcination temperature from 573 to 873 K caused gradual increase of peak intensity and the slight decrease in the peak width for the peaks at 2θ = 19.2° (111), 31.2° (220), 36.84° (311), 44.84° (400), 55.65° (422), 59.42° (511) and 65.21° (422). Thus, increase in crystallite size of Co-6C-f (50-70 nm) and Co-6C-g (65-90 nm) was mainly due to their restructuring at 873 K. The crystallite sizes of these samples matched very well with the HRTEM results.

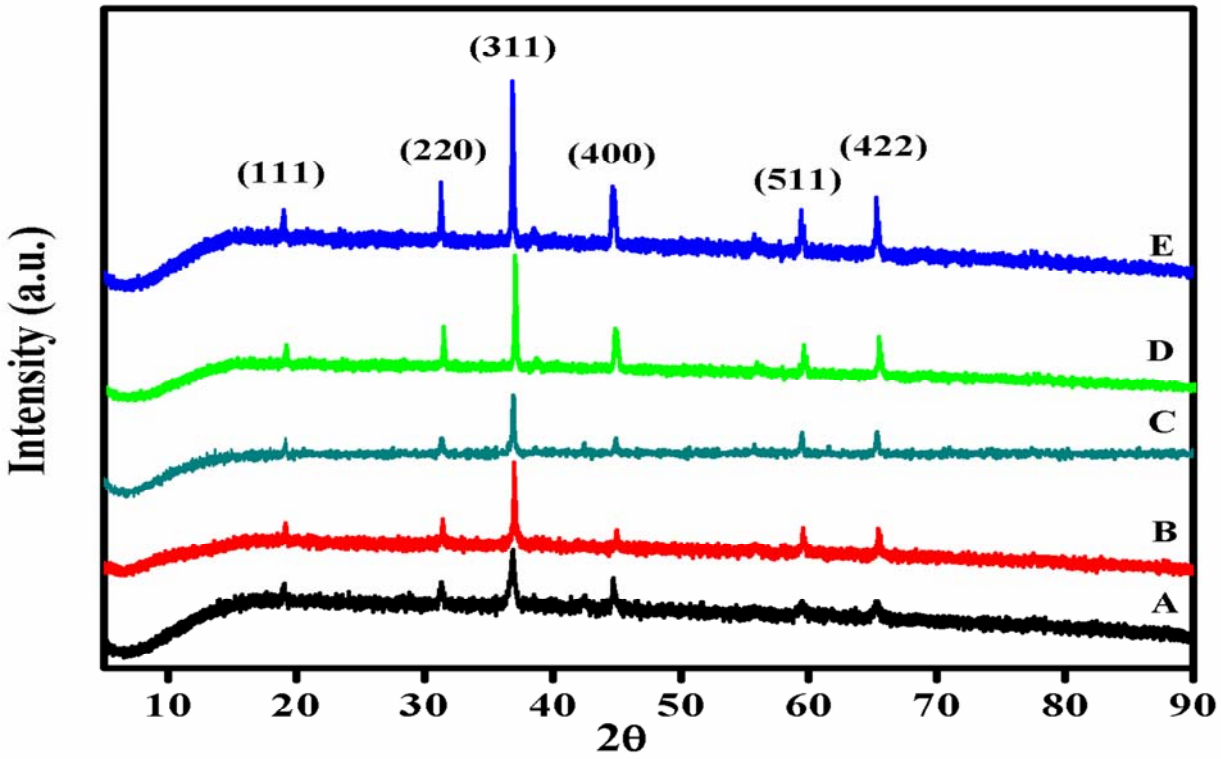

Figure 3.30. XRD of (A) Co-3C-f, (B) Co-6C-f, (C) Co-3C-g, (D) Co-6C-g and (E) commercial Co_3O_4 samples

3.3.3.3. X-ray photoelectron spectroscopy (XPS)

The XPS spectra of Co-3C-f, Co-3C-g and commercial Co_3O_4 samples are shown in Figure 3.31a. The Co 2p spectrum contains the Co $2p_{3/2}$ and Co $2p_{1/2}$ core level peaks at binding energies of (±0.4) 779.5 and 794.4 eV having a difference of 15.1 eV respectively, in all the samples [11]. The Co $2p_{3/2}$ peak deconvoluted into two peaks, at binding energies of (±0.4) 779.4 and 781.9 eV which correspond to Co^{3+} and Co^{2+} species (Figure 3.31b). This evidenced the formation of spinel Co_3O_4 in all the samples [37, 38].

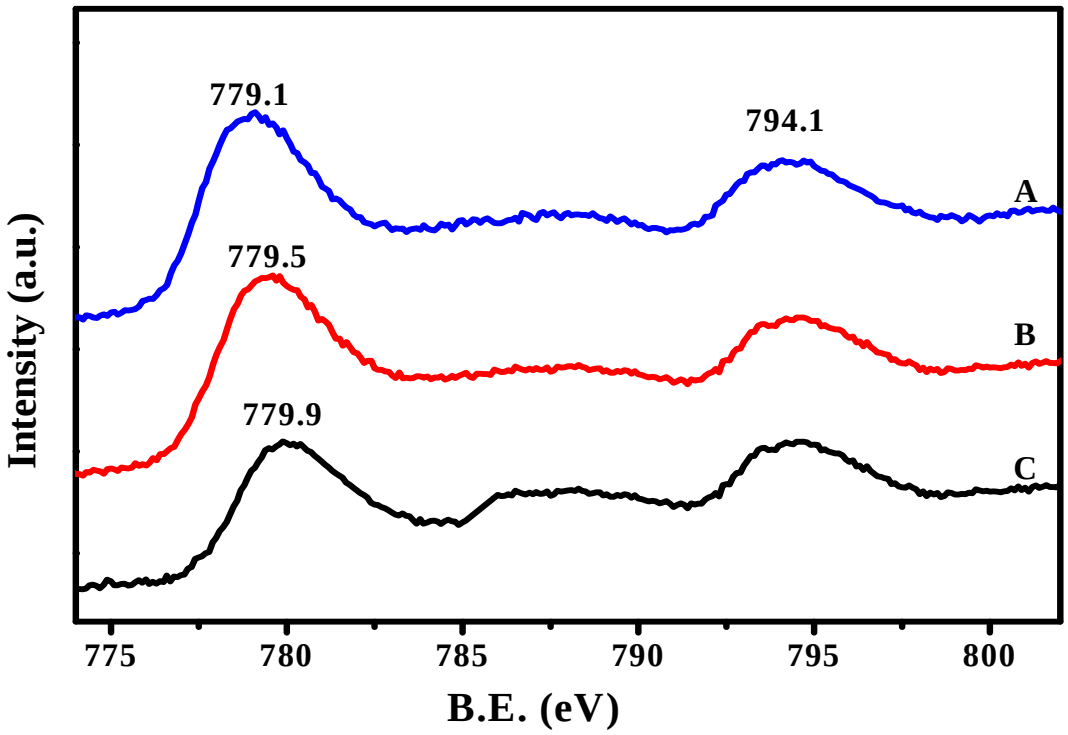

Figure 3.31a. XPS of (A) Co-3C-f, (B) Co-3C-g and (C) commercial Co_3O_4 samples

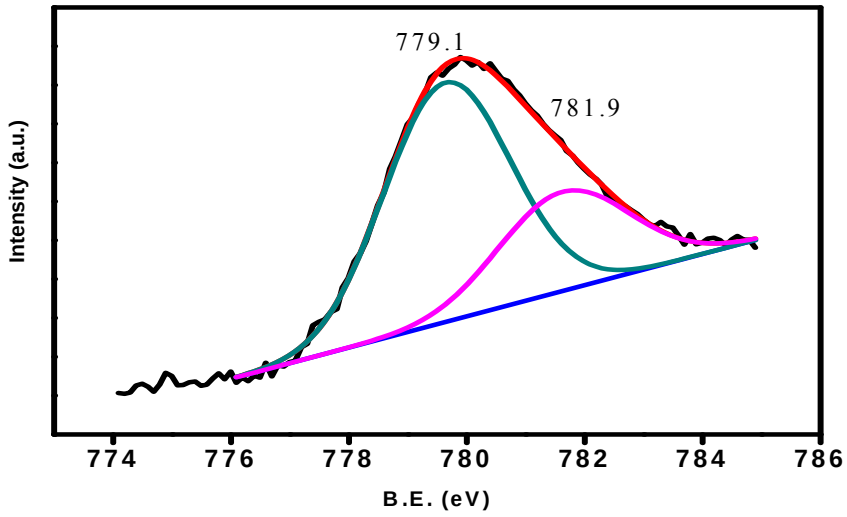

Figure 3.31b. Deconvolution spectra of Co $2p_{3/2}$

3.3.3.4. Thermo gravimetric analysis (TG-DTA)

The decomposition of cobalt nitrate hexahydrate (Co-f) and cobalt acetate tetrahydrate (Co-g) samples was examined by TG-DTA (Figure 3.32, A and B). The Co-f sample showed 77.5% weight loss in four steps (Table 3.8). First two small endothermic peaks showed a total 32% weight loss (12% and 20% weight loss) below 423 K, third endothermic peak at temperature 453 K showed 15% weight loss, that was due to the loss of physically adsorbed water and dehydration of chemically bonded water in the $Co(NO_3)_3 \cdot 6H_2O$ (Figure 3.32, A). While, in the forth step, 28% weight loss was observed below 518 K due to the decomposition of $Co(NO_3)_3$ into NO, N_2 and O_2 molecules [63]. However, Co-g sample showed 71.9% weight loss in three steps (Figure 32, B). In the first step, 20% weight loss was observed due to dehydration of chemically bonded water in the $CoC_2O_4 \cdot (4H_2O)$ below temperature at 403 K (Table 3.8). At 543 K, another small endothermic peak was observed, due to partial weight loss of chemically bonded acetate with cobalt. In the second step, 13% weight loss was observed below 553 K

temperature. In the third step, 36% weight loss observed below 673 K might be due to decomposition of acetate in to CO and CO_2 [64]. Based on the above results, an optimum calcination temperature required for Co-f and Co-g samples were 523 K and 633 K respectively. Among the preparation methods (co-precipitation method, thermal decomposition and sol-gel) studied in this work, co-precipitation required lowest calcination temperature to obtain spinel Co_3O_4.

Table 3.8. Summary of thermogravimetric analysis

Samples	**TG**		**DTA**	**Remarks**
	Temperature range (K)	**Weight loss (w/w. %)**	**Peak maximum (K)**	
Co-f (cobalt nitrate)	378-403	12	363	Escape of physically adsorbed water and dehydration of chemically bonded water in the $Co(NO_3)_3 \cdot 6H_2O$
	403-438	20	423	
	438-473	15	453	Decomposition of $Co(NO_3)_3$ in to NO, N_2 and $4O_2$.
	473-563	28	518	
Co-g (cobalt acetate)	333-413	20	393	Dehydration of chemically bonded water in the $CoC_2O_4 \cdot 4H_2O$
	413-563	13	543	Partial weight loss of chemically bonded acetate with cobalt.
	563-673	36	628	Decomposition of acetate in to CO and CO_2.

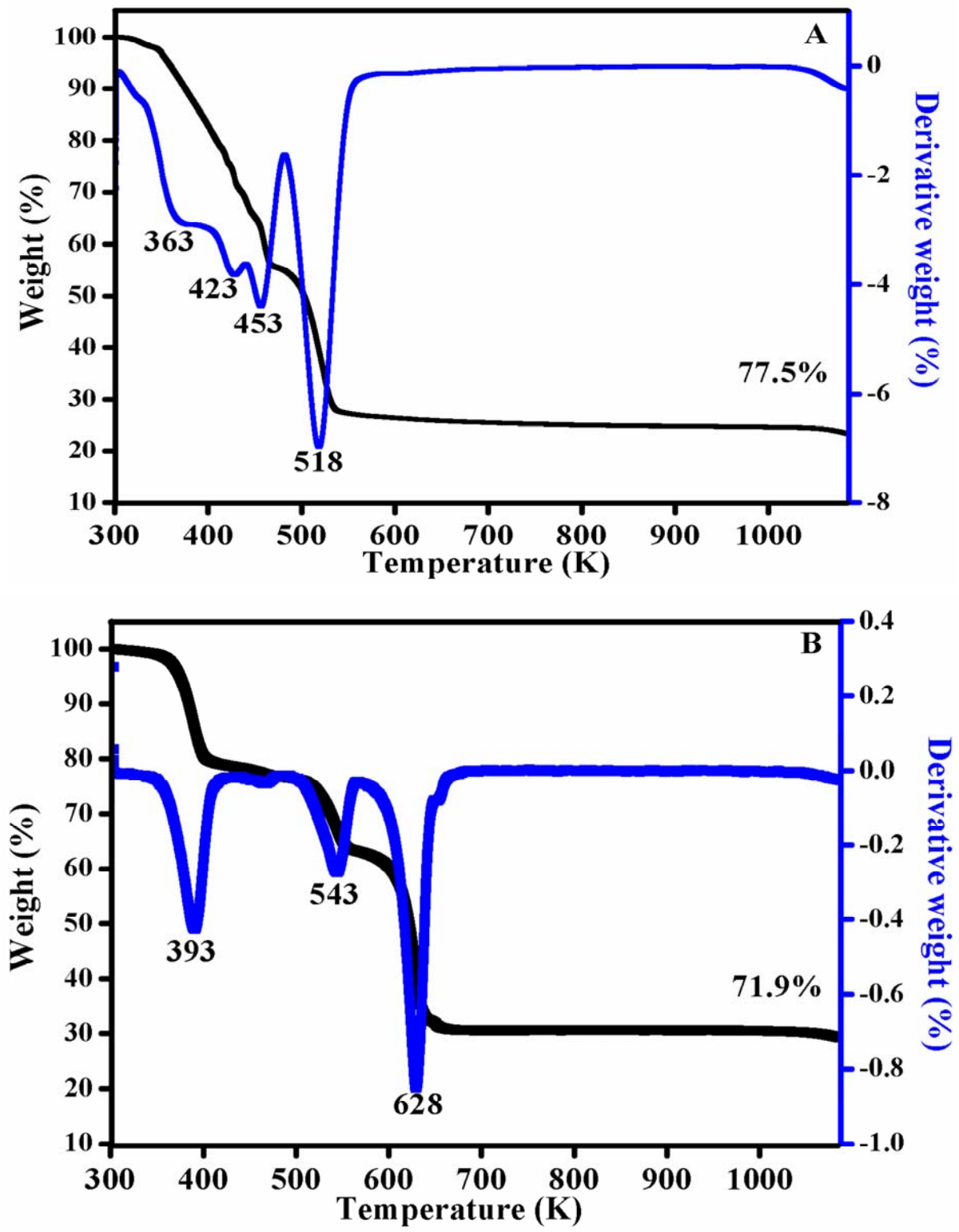

Figure 3.32. TG-DTA profile of (A) Co-f and (B) Co-g samples

3.3.3.5. Fourier-Transform infrared spectroscopy (FT-IR)

FT-IR spectra of Co_3O_4 (using nitrate and acetate precursors) samples and calcined at 573 K and commercial Co_3O_4 samples are shown in Figure 3.33. The peak at 567 cm^{-1} corresponds to Co^{3+} in an octahedral position while the other peak at 666 cm^{-1} corresponds to the Co^{2+} in a tetrahedral position confirming the formation of spinel Co_3O_4 in Co-3C-f, Co-3C-g and commercial Co_3O_4 samples [48, 55]. The broad peaks at 3420 cm^{-1} and 1630 cm^{-1} were attributed to metal hydroxyl stretching vibrations observed in all the samples [53, 54]. However, the Co-f sample showed a peak corresponding to the stretching vibration at 1331 cm^{-1} which was not observed in case of a sample calcined at 573 K temperature (Co-3C-f) (Figure 3.33, A and B) [65], indicating complete decomposition of cobalt nitrate to form pure Co_3O_4 spinel. While, the Co-g sample (cobalt acetate) showed the peaks at 1319, 1388 and 1548 cm^{-1} assigned to stretching vibrations of COO^- (acetate) group which were also present in Co-3C-g sample even though calcined at 573 K (Figure 3.33, C and D) [60, 61]. This indicated that Co-3C-g is a spinel Co_3O_4 however, contained an impurity of acetate which is due to the incomplete combustion of acetate. Similar observation was seen in case of TG-DTA examination (elaborated in Section 3.3.3.4).

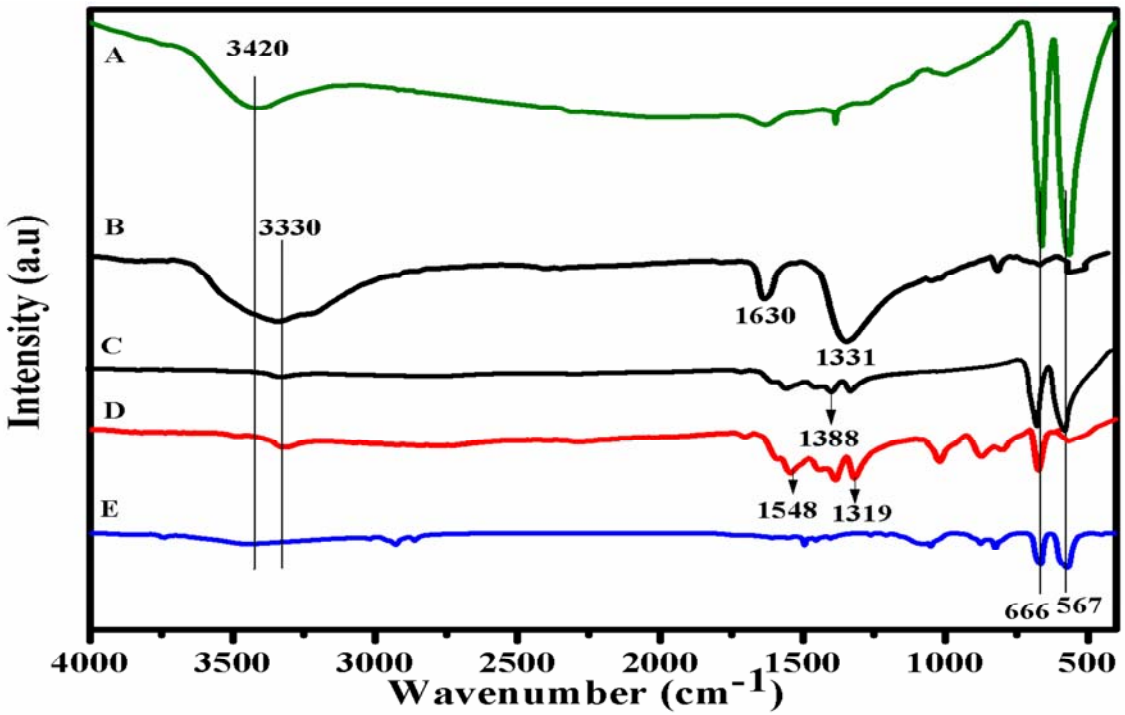

Figure 3.33. FTIR of (A) Co-3C-f, (B) Co-f, (C) Co-3C-g, (D) Co-g and (E) commercial Co_3O_4 samples

3.3.3.6. High resolution transmission electron microscopy

The morphologies of Co-3C-f, Co-6C-g and commercial Co_3O_4 samples were examined by HR-TEM (Figure 3.34). The Co-3C-f sample showed aggregate of rod-like morphology having a length in the range of 30-40 nm (Figure 3.34, A). The change of cobalt precursor from nitrate to acetate was associated with the aggregation of elongated rods in the range of 40-55 nm (Figure 3.34, B). The increase in rod length from 30-40 to 40-55 nm might be due to the presence of some acetate groups which might hold neighbouring particles [66]. This was also supported by TG-DTA and FTIR results as discussed above. The commercial sample of Co_3O_4 showed the aggregation of non-uniform rod shape particles having the length in the range of 80-110 nm (Figure 3.34, C). The particle size of these samples were in good agreement with the results of

XRD studies. From the above observations, it was estabilshed that in spinel type Co_3O_4 having a nano range particle size with controlled morphology can be best prepared by co-precipitation method.

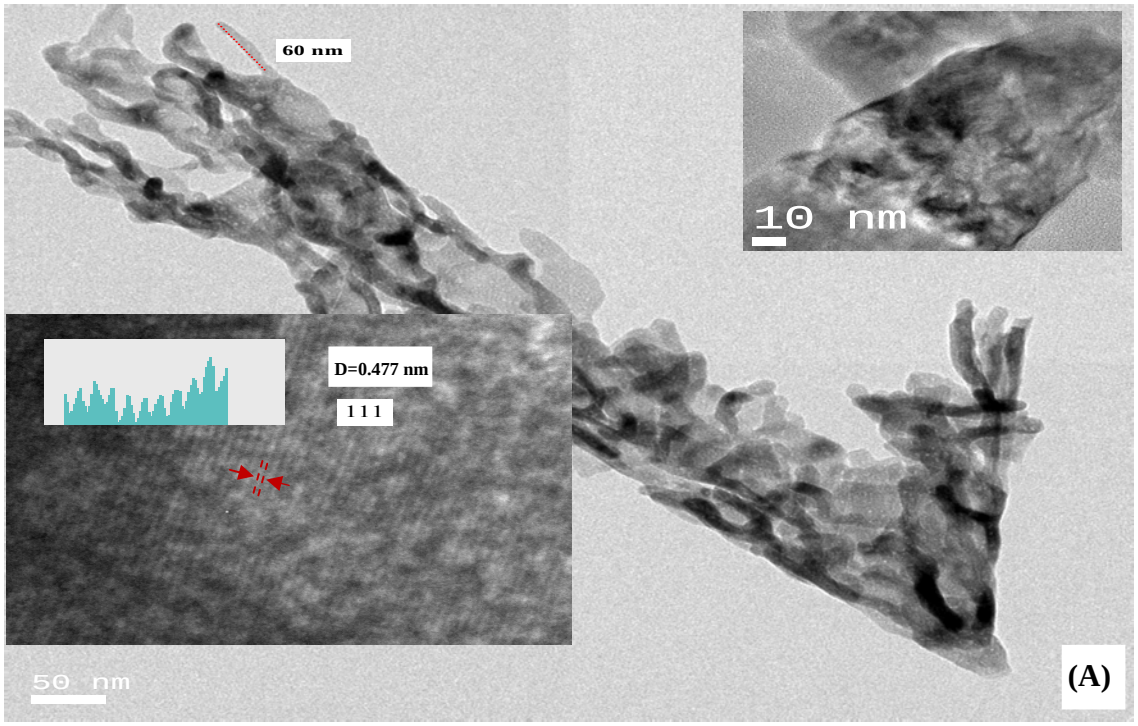

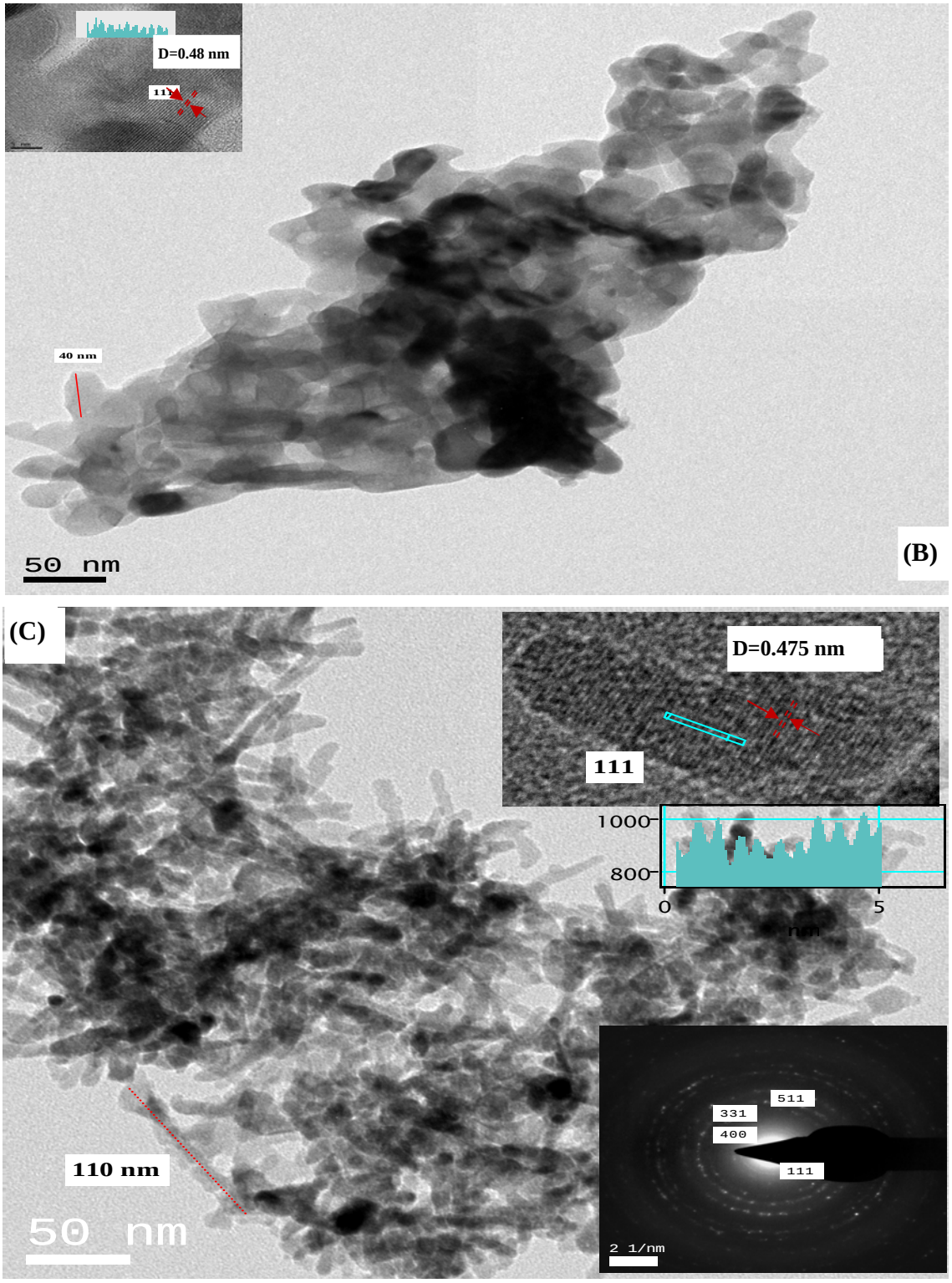

Figure 3.34. HRTEM of (A) Co-3C-f, (B) Co-3C-g and (C) commercial Co_3O_4 samples

3.3.3.7. Temperature programmed reduction / Temperature programmed oxidation (TPR/TPO)

H_2-TPR results of the Co-3C-f, Co-3C-g and commercial Co_3O_4 samples are presented in Figure 3.35. The peak observed in the range of 500-630 K was attributed to the reduction of trivalent cobalt oxide (Co_3O_4) to the divalent cobalt oxide (CoO) in case of Co-3C-f and Co-3C-g samples. Whereas, this peak was observed at higher temperature (550-820 K) in case of commercial Co_3O_4 sample. In case of Co-3C-f and Co-3C-g samples, second broad peak appeared in the range of 630-930 K, while in commercial Co_3O_4 sample the same peak appeared at higher range of 800-900 K that was assigned to the reduction of divalent cobalt oxide (CoO) to metallic cobalt (Co^o) [51, 55]. The change in cobalt precursor from nitrate to acetate showed a slight shift in the first reduction peak from 590 to 600 K and in case of commercial Co_3O_4 it was observed at still higher temperature of 720 K. This increase in reduction temperature might be due to the increase in crystallite size from ~30-40 to ~40-55 and 80-110 nm as observed in XRD and HRTEM, which requires higher temperature for reduction of bulk particles compared to the small particles [56]. Co-3C-f and Co-3C-g samples showed 145 and 68 mmol of H_2 up take respectively (Table 3.9). ~50% lower reducibility of Co-3C-g as compared to Co-3C-f sample was due to its higher crystallite size (40-55 nm) and the of trace of acetate groups might block the active sites resulted in lower reducibility, which were also in accordance with FTIR and TG-DTA results. Despite of having the higher crystallite size of 40-55 nm of commercial Co_3O_4 sample it showed ~35% higher reducibility than that for the Co-3C-f sample due to its crystallinity and exposure of specific planes as observed in HRTEM.

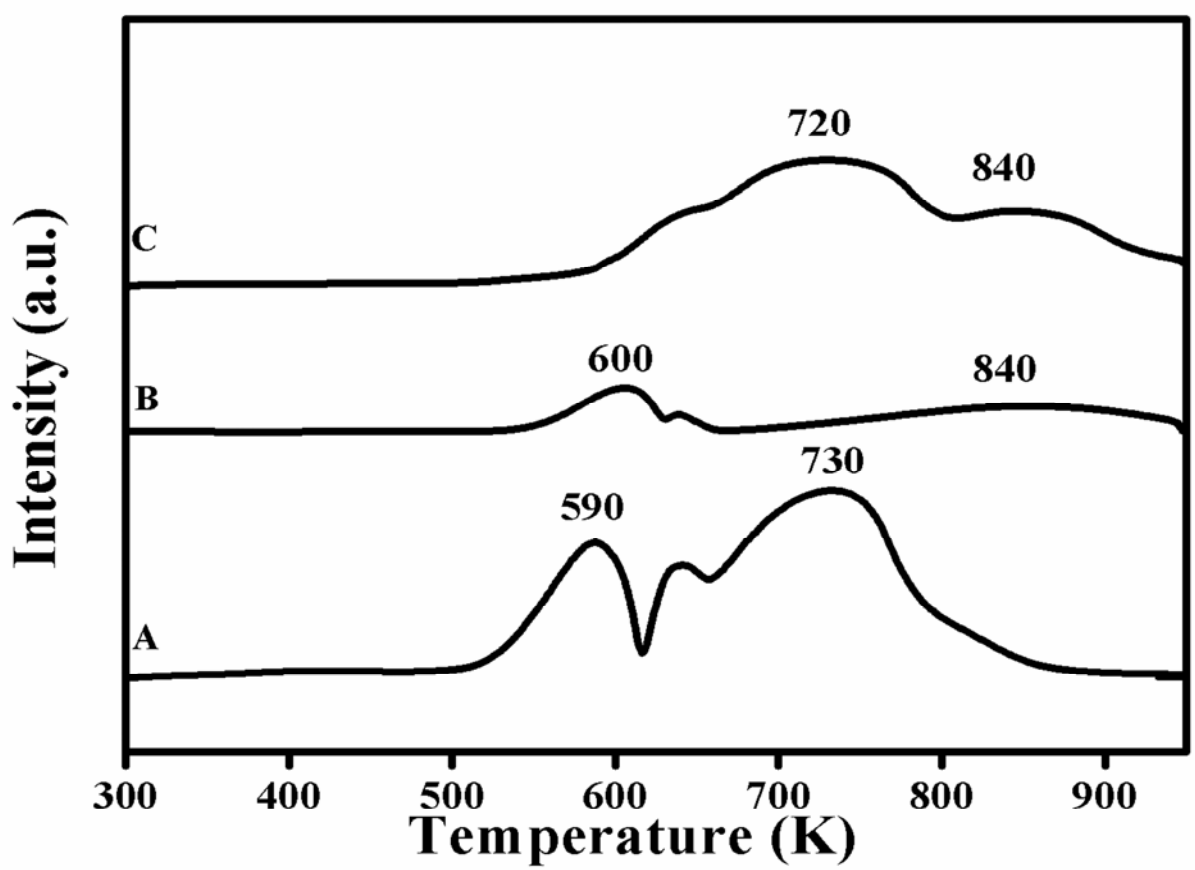

Figure 3.35. TPR of (A) Co-3C-f, (B) Co-3C-g and (C) commercial Co_3O_4 samples

The oxidizability of pre-reduced Co-3C-f, Co-6C-g and commercial Co_3O_4 catalysts was calculated by using TPO technique as shown in Figure 3.36. The first peak in a range of 380-480 K in both the samples was attributed to the oxidation of metallic cobalt oxide (Co^o) to divalent cobalt oxide (CoO) in case of Co-3C-f and Co-3C-g samples. Whereas, this peak in case of a commercial Co_3O_4 was observed at significantly higher temperature (500-650 K). In case of the Co-3C-f and Co-3C-g samples, second broad peak appeared in the range of 480-620 K, while in commercial Co_3O_4 sample, it was observed in the range of 650-850 K which was assigned to the oxidation of divalent cobalt oxide (CoO) to trivalent cobalt oxide (Co_3O_4) [52, 53]. Co-3C-f sample showed ~45% (6.2 mmol) higher O_2 up take than that of the Co-6C-g (3.5 mmol) sample

(Table 3.9). The reason for lower O_2 consumption in case of Co3C-g sample could be its higher crystallite size (40-55 nm) and the trace of acetate groups, which might block the active sites. However, commercial Co_3O_4 sample showed higher O_2 consumption (7.2 mmol) than the Co-6C-f and Co3C-g sample, in spite of its higher crystallite size. This might be because of higher extent of exposure of active sites arising from the difference of precursor used and method of its preparation.

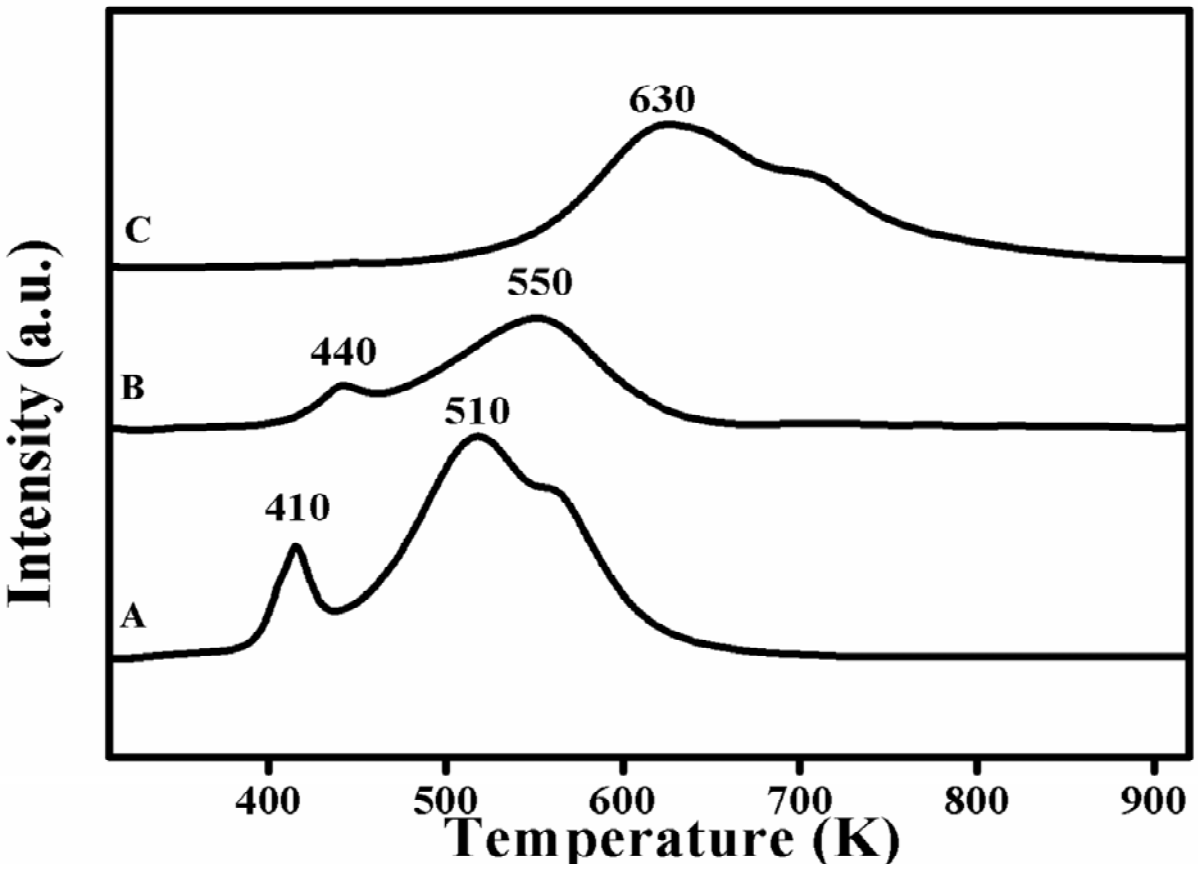

Figure 3.36. TPO of (A) Co-3C-f, (B) Co-3C-g and (C) commercial Co_3O_4 samples

Table 3.9. H_2/O_2 uptake of Co_3O_4 catalysts prepared via thermal decomposition method and commercial Co_3O_4 samples

Catalysts	Calcination temperature (K)	H_2 (mmol)	O_2 (mmol)
Co-3C-f	573	145	6.2
Co-3C-g	573	68	3.5
commercial Co_3O_4	Not Known	221	7.2
Co-3C-a	573	435	20.6

3.3.4. ACTIVITY MEASUREMENT

3.3.4.1. Screening of catalysts

The comparative catalytic activity results of spinel Co_3O_4 prepared by different preparation methods (co-precipitation, sol-gel and thermal decomposition) and calcined at 573 and 873 K temperatures and of commercial Co_3O_4 sample for the oxidation of veratryl alcohol are presented in Table 3.10. Among these, Co-3C-a sample prepared via co-precipitation method showed the highest conversion of 38% with complete selectivity to veratryl aldehyde (Table 3.10, Entry 1). The decrease in catalytic activity with change in pH (from 8 to 12) and preparation parameters/methods was due to decrease in active sites as a result of decrease in surface area, increase in crystallite/particle size and decrease in redox ability as evidenced by BET surface area, XRD, TPR, TPO and CV characterization [10, 67]. Inspite of having higher surface area (121.6 m^2/g) Co-3C-d catalyst showed decrease in conversion by 15% as compared to the Co-

3C-a catalyst (Table 3.10, Entry 7), due to change from mesoporous to microporous nature and lower oxidizability (~17%) of elongated rod-like particles which was also in accordance with the TPR/TPO results. However, Co-3C-e (prepared by sol-gel method) and Co-3C-g (prepared by thermal decomposition method using cobalt acetate) catalysts showed the lowest catalytic activity with only 2.5 and 6.5% conversion respectively. This was due to the blockage of active sites by organic impurities as was observed in FTIR, TG-DTA, TPR and TPO studeis (Table 3.10, Entry 7). The calcination at higher temperature of 873 K caused decrease in conversion to the extent of 25 to 40%, due to the sintering of nanoparticles as evidenced by lower surface area and larger crystallite size (Table 3.10) [10, 67]. Inspite of having lower surface area of Co-6C-e and Co-6C-g samples, both showed almost two times higher activity than those samples calcined at 573 K. This might be due blockage of active sites by organic impurites present in the sample calcined at 573 K as evidanced from TG-DTA and FTIR studeis. Under similar reaction conditions, commercial Co_3O_4 catalyst showed lower activity, that could be attributed to its lower surface area (21 m^2/g) and lower oxidizing ability than that of Co-3C-a catalyst.

Above observations establised that catalyst prepared by a co-precipation method and controlled pH (7-8) and calcined at 573 K showed the highest activity among all the samples prepared by other methods (sol-gel, thermal decomposition) and the commercial Co_3O_4 .

Table 3.10. Catalytic activity of prepared (Co_3O_4) catalysts via various methods and commercial Co_3O_4 samples for liquid phase oxidation of veratryl alcohol to veratryl aldehyde

Entry	Catalysts	Preparation method	Calcination temperature (K)	Surface area (m^2/g)	Conversion (%)	Selectivity (%) Veratryl aldehyde
1	Co-3C-a	CP	573	110.0	38.0	>99.9
2	Co-6C-a	CP	873	24.5	14.1	>99.9
3	Co-3C-b	CP	573	74.5	28.3	>99.9
4	Co-6C-b	CP	873	19.2	11.2	>99.9
5	Co-3C-c	CP	573	58.4	19.2	>99.9
6	Co-6C-c	CP	873	13.7	5.0	>99.9
7	Co-3C-d	CP	573	121.6	32.5	>99.9
8	Co-6C-d	CP	873	23.5	13.5	>99.9
9	Co-3C-e	SG	573	21.2	2.5	>99.9
10	Co-6C-e	SG	873	13.2	6.0	>99.9
11	Co-3C-f	TD	573	51.7	14.5	>99.9
12	Co-6C-f	TD	873	16.5	5.3	>99.9
13	Co-3C-g	TD	573	31.0	4.5	>99.9
14	Co-6C-g	TD	873	11.8	10.0	>99.9
15	Commercial Co_3O_4	NK	NK	21.0	22.0	>99.9

Reaction conditions: temperature, 413 K; oxygen pressure, 0.689 MPa; veratryl alcohol, 0.5 g (3 mmol); catalyst, 0.1 g (0.42 mmol); solvent water, 70 mL; reaction total volume, 70.6 mL; agitation speed, 900 rpm; reaction time, 7 h.

Where, CP: co-precipitation; SG: sol-gel; TD: thermal decomposition and NK: not known

3.3.4.2. Effect of catalyst preparation parameters

Since Co_3O_4 prepared by co-precipitation method showed the highest activity for liquid phase oxidation of veratryl alcohol to veratryl aldehyde, the effect of various parameters varied during its preparation on the activity performance was also studied.

3.3.4.2.1. Effect of calcination temperature

The calcination of co-precipitated Co_3O_4 sample was carried out at two different temperatures of 573 to 873 K and the results are shown in Table 3.11. The significant decrease in catalytic conversion from 38 to 14.1% was observed with increase in calcination temperature from 573 to 873 K (Table 3.11). Such a dramatic decrease in catalytic activity was due to the following reasons: i) change in mesoporous (pore size 16.7 nm and pore volume 1.3 cm^3/g) to microporous nature (pore size 1.8 nm and pore volume 0.11 cm^3/g), ii) substantial decrease in surface area from 110 to 24.5 m^2/g and iii) increase in crystallite/particle size from 12-38 to 20-70 nm as observed in XRD and HRTEM studies. The microporous nature would cause difficulties for the substrate to diffuse onto the active sites inside the pores. The number of active sites formed might be also less at high calcination temperature as has been evidenced from TPR, TPO and CV characterization. Thus the above observations established that optimum calcination temperature was 573 K for co-precipitated catalyst in order to achieve the highest catalytic activity.

Table 3.11. Effect of calcination temperature on catalytic activity

Catalysts	Calcination temperature (K)	Specific Surface area (m^2/g)	Conversion (%)	Selectivity (%)
				Veratryl aldehyde
Co-3C-a	573	110.0	38.0	>99.9
Co-4C-a	673	67.3	31.9	>99.9
Co-5C-a	773	28.5	16.5	>99.9
Co-6C-a	873	24.5	14.1	>99.9

Reaction conditions: temperature, 413 K; oxygen pressure, 0.689 MPa; veratryl alcohol, 0.5 g (3 mol); catalyst, 0.1 g (0.42 mmol); solvent water, 70 mL; agitation speed, 900 rpm; reaction time, 7 h.

3.3.4.2.2. Effect of calcination time

In order to study the influence of calcination time on catalytic activity, the Co-a and Co-d samples were calcined at constant temperature of 573 K for different time periods of 1 to 6 h (Tables 3.12, 3.13, 3.14 and 3.15). From the studies of effects of solvents as discussed in 3.2.4.1.2, toluene and water were selected for further studies on optimization of reaction parameters for the oxidation of veratryl alcohol. The catalytic activities of Co-a (1 to 6 h) catalysts in water and toluene as solvents were found to decrease by $1/4^{th}$ and $1/5^{th}$ respectively, with increase in calcination time from 1 to 6 h (Tables 3.12 and 3.13). The decrease in catalytic activity was due to the decrease in surface area by half (from 194.4 to 95.9 m^2/g) and increase in crystallite size from 5-25 nm to 15-52 nm (XRD and HRTEM) with increase in calcination time from 1 to 6 h. While in both the solvents, leaching of catalysts was observed for calcination period upto 3 h which then decreased with increase in calcination time from 4 to 6 h (Tables 3.12 and 3.13). The metal leaching for the sample calcined for 3 h, could be due to the fact that the

catalysts had lower crystallite size and unconverted cobalt hydroxy carbonate was present on the catalyst surface (XRD). Similarly, the activity of Co-d (1 to 6 h) catalyst in water and toluene was found to decrease by ~40% with increase in calcination time from 1 to 6 h (Tables 3.14 and 3.15). The decrease in catalytic activity might be due to the decrease in surface area by half (from 206.1 to107.2 m^2/g) and increase in crystallite size from 5-20 nm to 18-34 nm (XRD). The metal leaching pattern observed was similar to that for Co-d, as discussed above. However, Co-3C-a (1 h calcined) showed lower leaching as compared to that for Co-3C-d (1 h calcined) in both the solvents due to better crystallinity and high crystallite size. The highest activity of the catalyst could be achieved for catalyst that was calcined at 573 K for 5 h.

Table 3.12. Effect of calcination time on the activity of Co-a in water

Calcination time (h)	**Specific Surface area (m^2/g)**	**Conversion (%)**	**Selectivity (%)** **Veratryl aldehyde**	**Leaching of cobalt (ppm)**
1	194.4	53.5	>99.9	18.52
2	148.0	31.2	>99.9	6.81
3	131.5	33.2	>99.9	3.15
4	119.4	35.6	>99.9	0.98
5	110.0	38.0	>99.9	0.11
6	95.9	34.9	>99.9	0.10

Reaction conditions: temperature, 413 K; oxygen pressure, 0.689 MPa; veratryl alcohol, 0.5 g (3 mmol); catalyst, 0.1 g (0.42 mmol); water, 70 mL; agitation speed, 900 rpm; reaction time, 7 h.

Table 3.13. Effect of calcination time on the activity of Co-a in toluene

Calcination time (h)	Specific Surface area (m^2/g)	Conversion (%)	Selectivity (%)		Leaching of cobalt (ppm)
			Veratryl aldehyde	Veratric acid	
1	194.4	98.0	80.0	20.0	12.17
2	148.0	85.5	90.0	10.0	4.27
3	131.5	79.4	95.5	4.5	2.04
4	119.4	78.3	97.5	2.5	0.20
5	110.0	75.0	99.0	1.0	ND
6	95.9	53.0	>99.9	<0.1	ND

Reaction conditions: temperature, 413 K; oxygen pressure, 0.689 MPa; veratryl alcohol, 0.5 g (3 mmol); catalyst, 0.1 g (0.42 mmol); toluene, 70 mL; agitation speed, 900 rpm; reaction time, 7 h.

Table 3.14. Effect of calcination time on the activity of Co-d in water

Calcination time (h)	Specific Surface area (m^2/g)	Conversion (%)	Selectivity (%)	Leaching of cobalt (ppm)
			Veratryl aldehyde	
1	206.1	48.0	>99.9	20.50
2	162.7	41.8	>99.9	11.30
3	144.0	37.1	>99.9	6.17
4	132.6	34.6	>99.9	2.51
5	121.6	32.5	>99.9	0.17
6	107.2	29.0	>99.9	0.11

Reaction conditions: temperature, 413 K; oxygen pressure, 0.689 MPa; veratryl alcohol, 0.5 g (3 mmol); catalyst, 0.1 g (0.42 mmol); water, 70 mL; agitation speed, 900 rpm; reaction time, 7 h.

Table 3.15. Effect of calcination time on the activity of Co-d in toluene

Calcination time (h)	Specific Surface area (m^2/g)	Conversion (%)	Selectivity (%)		Leaching of cobalt (ppm)
			Veratryl aldehyde	Veratric acid	
1	206.1	89.0	91.0	9.0	15.24
2	162.7	85.5	95.0	5.0	8.71
3	144.0	79.4	95.5	4.5	2.80
4	132.6	78.3	97.3	2.7	0.68
5	121.6	75.0	99.0	1.0	ND
6	107.2	53.0	99.0	1.0	ND

Reaction conditions: temperature, 413 K; oxygen pressure, 0.689 MPa; veratryl alcohol, 0.5 g (3 mmol); catalyst, 0.1 g (0.42 mmol); toluene, 70 mL; agitation speed, 900 rpm; reaction time, 7 h.

3.3.4.3. Effect of reaction variables

The nano Co-3C-a catalyst was found to be stable and reusable in water as a solvent, while large activity drop ($1/3^{rd}$) was obseved in toluene after the first recycle (Section 3.3.4.3.6). Hence work on optimization of further reaction conditions was carried out in water as a solvent.

3.3.4.3.1. Effect of temperature

The effect of temperature on conversion of veratryl alcohol and selectivity to veratryl aldehyde was studied using the most active nano Co-3C-a catalyst in the range of 393-433 K (Figure 3.37). The conversion of veratryl alcohol increased from 67 to 90% while the selectivity to veratryl aldehyde decreased from 99.9% to 90% with an increase in temperature from 393 to 433 K (pressure 4 MPa) [10]. The decrease in selectivity to veratryl aldehyde was due to its further

oxidation to veratric acid at higher temperature. Hence the optimum temperature was found to be 413 K. Activation energy as calculated from the Arrhenius plot in water was found to be 42.46 $kJmole^{-1}K^{-1}$ (Figure 3.38).

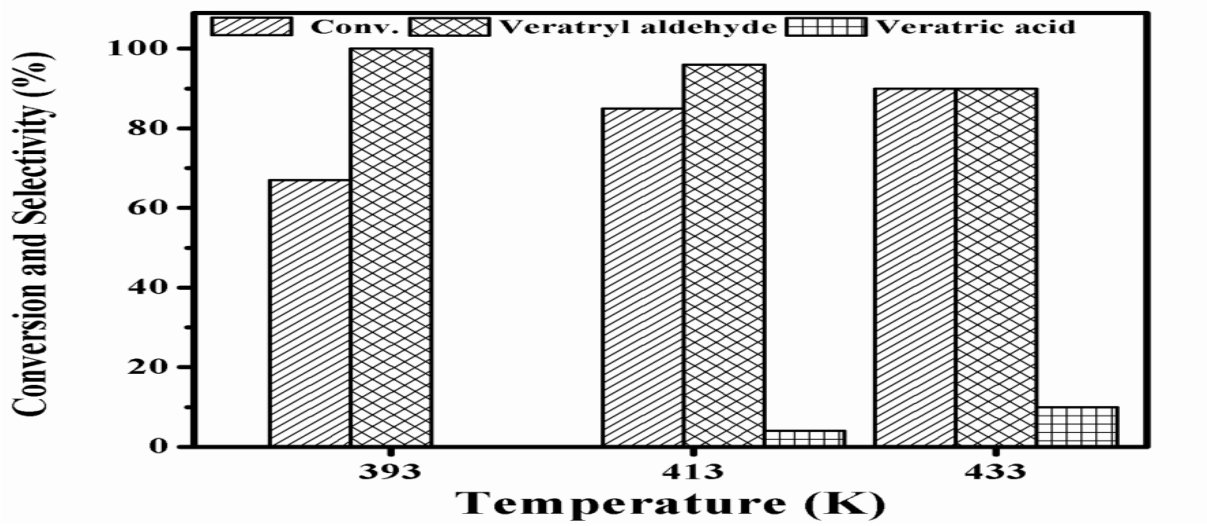

Figure. 3.37. Influence of temperature on oxidation of veratryl alcohol using Co-3C-a catalyst

Reaction conditions: oxygen pressure, 4 MPa; veratryl alcohol, 3 mmol; solvent water, 70 mL; catalyst loading, 0.84 mmol; reaction time, 7 h.

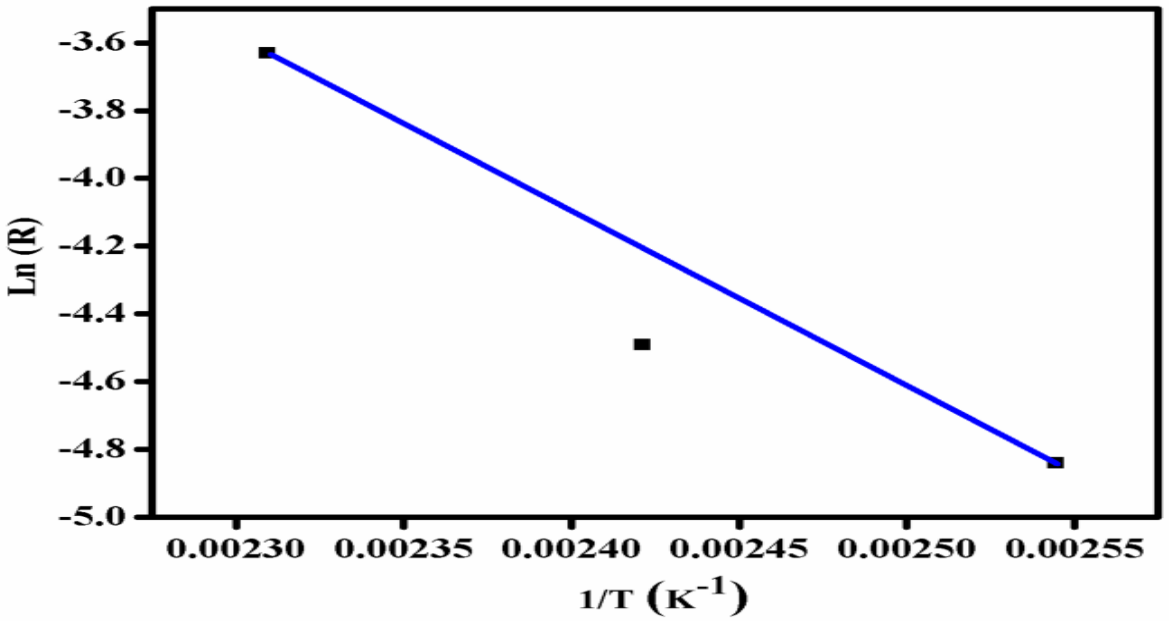

Figure 3.38. Arrhenius plot

3.3.4.3.2. Conversion and product distribution with time

Figure 3. 39 shows the conversion and product selectivities vs. time profile for veratryl alcohol oxidation using nano Co-3C-a catalyst at an optimum temperature of 413 K. The initial oxidation product formed was veratryl aldehyde that underwent further oxidation to give veratric acid with the highest conversion of 85% of veratryl alcohol.

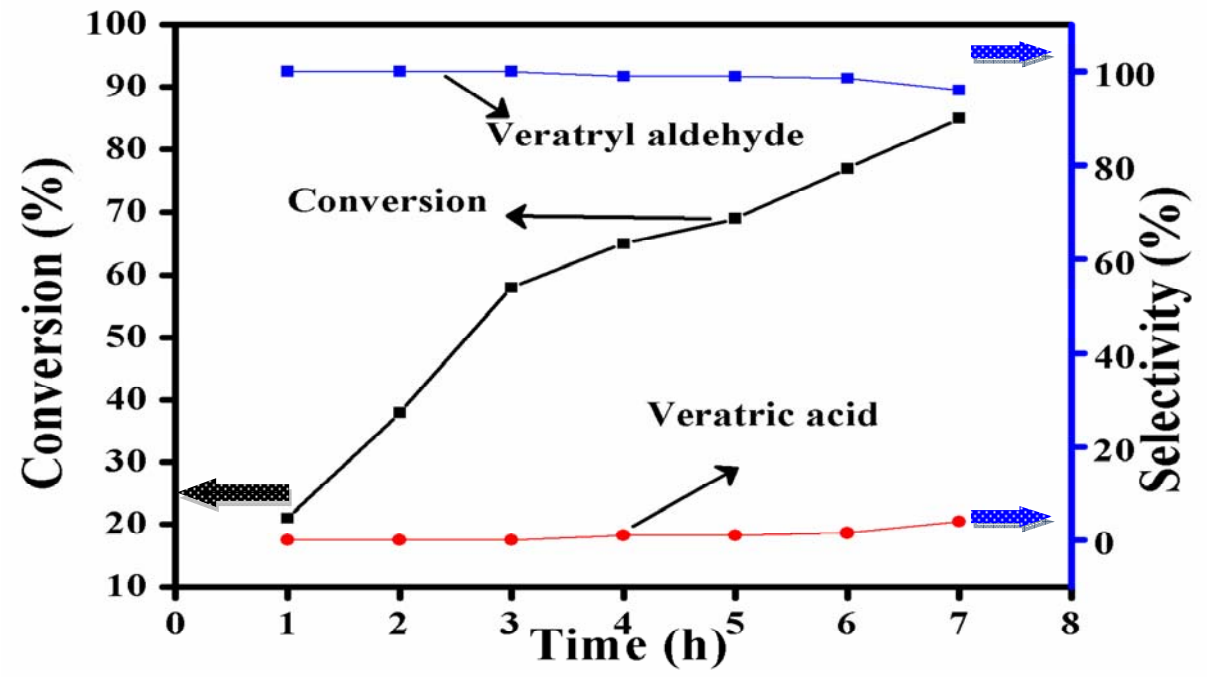

Figure 3.39. Conversion and product distribution with time for oxidation of veratryl alcohol over Co-3C-a catalyst

Reaction conditions: temperature, 413 K; oxygen pressure, 4 MPa; veratryl alcohol, 0.5 g (3 mmol); catalyst, 0.84 mmol; solvent water, 70 mL; agitation speed, 900 rpm; reaction time, 7 h.

3.3.4.3.3. Effect of pressure

In order to study the effect of partial oxygen pressure on conversion of veratryl alcohol and selectivity to veratryl aldehyde, oxidation experiments were carried out by varying the oxygen

pressure in the range of 0.68-4 MPa at 413 K and the results are shown in Figure 3.40. It was found that the conversion of veratryl alcohol increased from 37 to 85% with an increase in partial pressure of oxygen from 0.68 to 4 MPa, while selectivity to veratryl aldehyde remained almost constant (97%) [10]. The substantial increase in conversion was due to the higher oxygen solubilty at higher pressure [68].

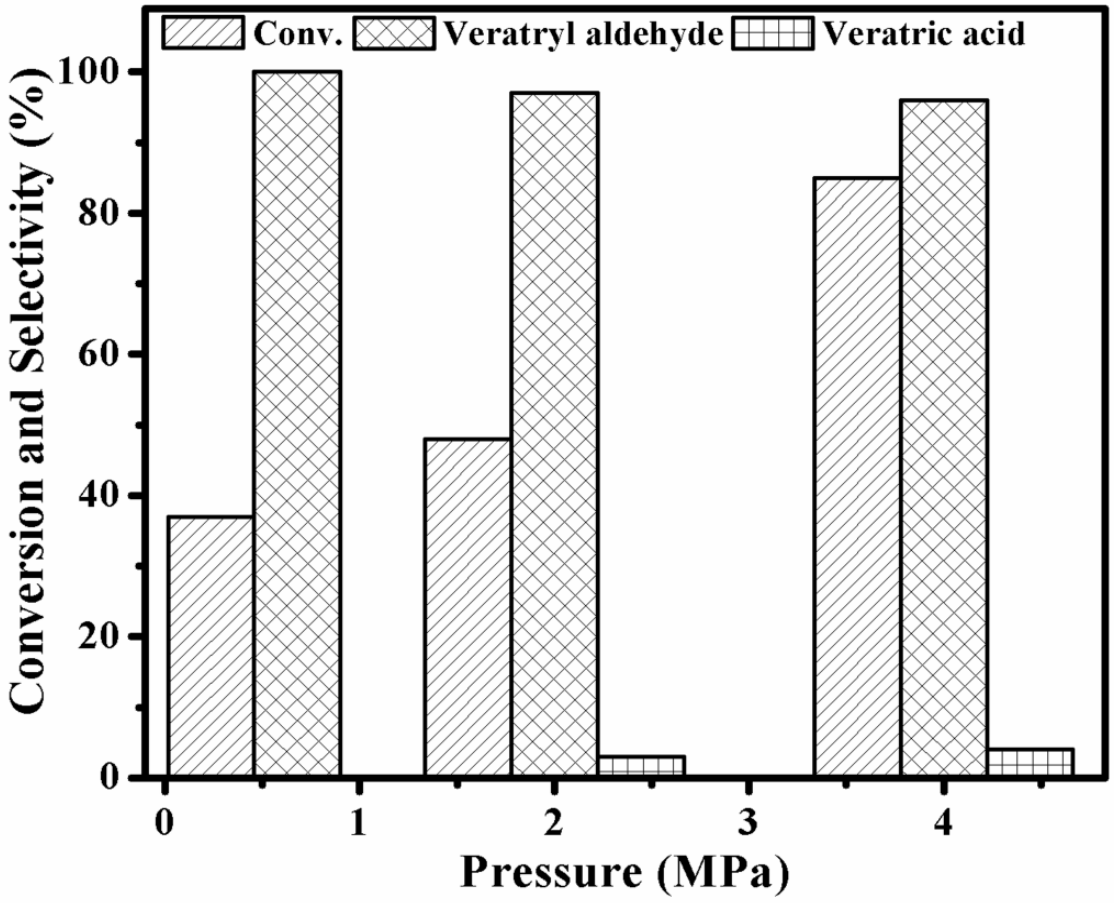

Figure 3.40. Influence of pressure on oxidation of veratryl alcohol using Co-3C-a catalyst

Reaction conditions: temperature, 413 K; veratryl alcohol, 0.5 g (3 mmol); catalyst, 0.2 g (0.84 mmol); solvent water, 70 mL; agitation speed, 900 rpm; reaction time, 7 h.

3.3.4.3.4. Effect of catalyst loading

Veratryl alcohol conversion increased from 22 to 85% (Table 3.17) with increase in amount of catalyst from 0.05 g to 0.2 g. However, the selectivity to veratryl aldehyde decreased by 4%. At higher catalyst loading, enhanced availability of active sites would facilitate the further oxidation of aldehyde to acid.

Table 3.16. Catalyst loading effect by using Co-3C-a

Entry	Catalyst loading (g)	Conversion (%)	Selectivity (%)	
			Veratryl aldehyde	Veratric acid
1	0.05	22	>99.9	<0.1
2	0.1	36	>99.9	<0.1
3	0.2	85	96	4

Reaction conditions: temperature, 413 K; oxygen pressure, 4 MPa; veratryl alcohol, 0.5 g (3 mmol); solvent water, 70 mL; agitation speed, 900 rpm; reaction time, 7 h.

3.3.4.3.5. Effect of solvent

Since the catalyst calcined at 573 K (Co-3C-a) showed the highest activity, the effect of various solvents on its performance was investigated and the results are shown in Table 3.12. The catalytic activity in different solvents was found to be in the following order: toluene > water > ethanol > methanol. The highest conversion of 75% was observed with 99% selectivity to veratryl aldehyde when non polar solvent such as toluene was used (Table 3.12, Entry 1). Among the polar solvents, highest conversion of 38% was observed in water (Table 3.12, Entry 2), however in case of methanol and ethanol, 21% and 29% conversions were observed respectively with complete selectivity to veratryl aldehyde in all the solvents (Table 3.12, Entries 3 and 4).

The highest catalytic activity in toluene solvent than that in polar solvents was due to the solubility of oxygen and non interaction of polar solvent with the intermediate state which is discussed in detailed in Section 3.3.4.3.5 [40, 60]. Thus, the preference of solvent allowed to achieve the desired catalytic activity.

Table 3.17. Activity of Co-3C-a catalyst in different solvents

Solvents	**Conversion (%)**	**Selectivity (%)**	
		Veratryl Aldehyde	**Veratric Acid**
Toluene	75	97.5	2.5
Water	38	>99.9	<0.1
Methanol	21	>99.9	<0.1
Ethanol	29	>99.9	<0.1

Reaction conditions: temperature, 413 K; oxygen pressure, 0.689 MPa; veratryl alcohol, 0.5 g (3 mmol); catalyst, 0.1 g (0.42 mmol); water, 70 mL; agitation speed, 900 rpm; reaction time, 7 h.

3.3.4.3.6. Catalyst recycles studies

In order to ensure that the catalytic activity of nano Co-3C-a spinel catalyst in water and toluene as solvents was constant during the run, we carried out catalyst recycle experiments. For this purpose, the catalyst afterr the first run was recovered by centrifugation. It was then washed with either by water or toluene and dired at 373 K for 2 h and reused for the subsequent run. It was found that in water as solvent, the catalyst showed almost the same selectivity with marginal decrease in conversion of veratryl alcohol even after the third recycle but in toluene after the first recycle, its activity decreased from 75 to 56% as shown in Figure 3.41. The marginal decrease in

conversion from 38 to 34% in water was due to the handling losses of the catalyst. However, these results were found to be in agreement with the CSC (cobalt surface composition) ratio found after first recycle in water ~1:2 which was the same as fresh catalyst (1:2) while in toluene it changed to ~1:4 confirmed by XPS examination. In order to know the stability during reaction, catalyst leaching test was also done after first recycle by ICP-OES and the results confirmed no leaching of the active metal function was observed in both the solvents (water and toluene) (Tables 3.13 and 3.14). These results estabilished that catalytic activity in water solvent was lower but catalyst was able to form redox couple in water while this was not possible in toluene. This clearly demonstrated that spinel type nano-structured Co-3C-a was truly a heterogeneous, highly efficient catalyst for aqueous phase oxidation.

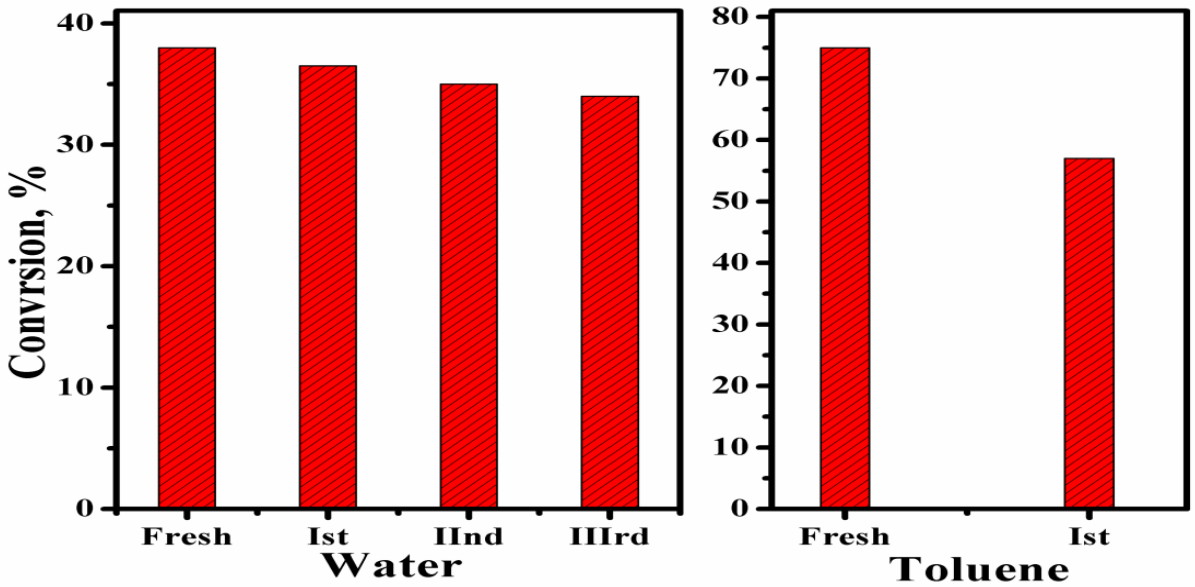

Figure 3.41. Recycle study of Co-3C-a catalyst in water and toluene solvents

Reaction conditions: temperature, 413 K; oxygen pressure, 0.689 MPa; veratryl alcohol, 0.5 g (3 mmol); catalyst, 0.1 g (0.42 mmol); solvent, 70 mL; agitation speed, 900 rpm; reaction time, 7 h.

3.3.4.4. Substrate screening

The oxidation of various phenolic and non phenolic substrates representing sub structure of lignin compounds were tested over active nano Co_3O_4 (Co-3C-a) catalyst (Table 3.18). Among phenolic compounds, di-substituted vanillin alcohol showed a maximum conversion of 86% with 81% and 11% selectivities to vanillin and vanillic acid respectively. With an increase in unsaturation, conversion dropped down to 61% for the coniferyl alcohol with 82% selectivity to coniferyl aldehyde. The substituents on the phenolic compounds showed a significant influence on the oxidation activity depending on their ability of electron donation. The planar benzyl alcohol showed only 17.4% conversion while for the mono-substituted phenolic compounds, 51.8% conversion of the *p*-hydroxy benzyl alcohol was obtained with 84% selectivity to *p*-hydroxy benzaldehyde. Similarly, 28% conversion of *p*-coumaryl alcohol was observed with 100% selectivity to *p*-coumaryl aldehyde. The tri-substituted phenolic compounds showed much higher activity, e.g. 77% conversion of the *p*-sinapyl alcohol was obtained with 78% selectivity to sinapyl aldehyde. Among the non-phenolic substrates, the veratryl alcohol showed highest conversion of 85% with 96% selectivity to veratryl aldehyde. On the other hand, mono-substituted methoxy groups such as *p*-anisic alcohol showed 55% conversion with 100% selectivity to *p*-anisaldehyde, while 3,4,5-tri methoxy benzyl alcohol showed higher conversion of 76.8% with 79% aldehyde selectivity. Highest conversion and selectivity of 90% to 4-hydroxy 3-methoxy alpha methyl benzylalcohol (4H3MAMBA) was obtained for the aromatic secondary alcohol viz. 1-(4-hydroxy-3-methoxyphenyl) ethanone. The activity of various sub structures of lignin compounds studied in this work was found in the following order of: secondary alcohol > di-substituted > tri-substituted > mono-substituted > non-substitution.

Table 3.18. Oxidation of non-phenolic and phenolic sub structure of lignin compounds catalysed by nano Co-3C-a spinel

Entry	Substrates	Conv. (%)	Selectivity (%)		
			Aldehyde	Acid	Other
1	vanillin alcohol	86.0	81	11	8
2	veratryl alcohol	85.0	96	4	0
3	*p*-sinapyl alcohol	77.0	78	10	12
4	3,4,5-tri-methoxy benzyl alcohol	76.8	79	21	0
5	*p*-anisic alcohol	55.0	>99.9	<0.1	0
6	coniferyl alcohol	61.0	82	18	0
7	*p*-hydroxy benzyl alcohol	51.8	84	16	0
8	*p*-coumaryl alcohol	28.0	>99.9	<0.1	0
9	4H3MAMBA	90.0	0	0	90[a]
10	benzyl alcohol	17.4	78	22	0

Reaction conditions: temperature, 413 K; oxygen pressure, 4 MPa; substrate, 3 mmol (0.5 g); water, 70 mL; catalyst loading, 0.84 mmol; reaction time, 7 h. Where; [a] = 1-(4-hydroxy-3-methoxyphenyl) ethanone.

3.3.4.5. Reaction mechanism

It is well known that the two oxidation states of Co^{2+} and Co^{3+} coexist in the spinel Co_3O_4 and a dynamic equilibrium is set up involving Co^{2+}, Co^{3+}, and the lattice oxygen (O_2^-) species under liquid phase oxidation conditions [14]. Oxidative dehydrogenation proceeds via approach of substrate (veratryl alcohol) towards the cobalt octahedral species having lattice oxide ion as shown in Scheme 3.3 [41, 69-71]. The adsorbed veratryl alcohol formed intermolecular bonding between cobalt(III) and oxygen while surface oxide ion formed intermolecular bonding with hydrogen of alcoholic group. Subsequently $Co^{III}OH$ species were formed due to abstraction of hydrogen by oxide ion [72]. Activated $Co^{III}OH$ species were capable of forming another intermolecular hydrogen bond and abstraction of an electron forms the major product veratryl aldehyde, Co(II) and water molecule [72]. The reduced Co(II) species get reoxidized using molecular oxygen to form again active $Co^{III}O^-$ species. The formation of veratric acid by further oxidation of veratryl aldehyde using molecular oxygen is also systematically shown in Scheme 3.3. However, the catalytic activity over nano Co-3C-a catalyst was found to depend on the reaction medium (Table 3.12). The lower catalytic activity in polar solvents might be due to an interaction of the solvent via intermolecular bonding with hydrogen and cobalt oxide ion either at the initial step or after the activation of reactant as shown in Scheme 3.3. Thus, active sites were blocked in presence of polar solvents resulting in lower catalytic activity. However, in case of the non polar (toluene) solvent, absence of any proton (hydrogen) does not form an intermolecular bond with cobalt oxide. As a result of this, maximum active sites were available leading to the higher conversion (75%). Similarly, the oxidative dehydrogenation of the other sub-structure lignin compounds also might proceed via similar reaction mechanism. In order to

investigate the role of organic and inorganic polar solvents in this oxidation reaction further studies are in progress.

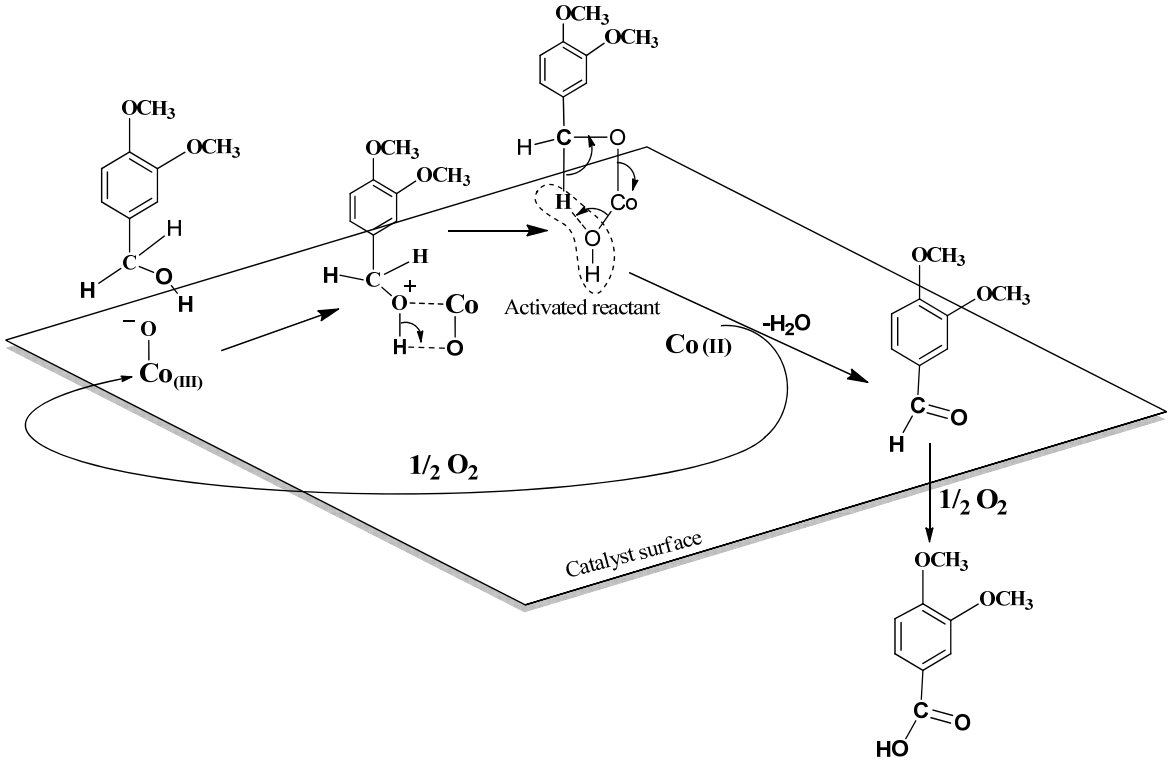

Scheme 3.3. Plausible catalytic path way for oxidation of veratryl alcohol

3.4. CONCLUSIONS

- Nano spinel Co_3O_4 catalyst (Co-3C-a) prepared by co-precipitation in a pH range of 7-8 and calcined at 573 K for 5 h time, showed the highest catalytic activity (38%), among the catalysts prepared by sol-gel, thermal decomposition and commercial Co_3O_4 samples. The highest activity of Co-3C-a catalyst was due to its rod-like morphology having particle size of 10-20 nm with mesoporous nature (pore size of 16.7 nm, pore volume of 1.3 cm^2/g) and surface area (110 m^2/g).

- The increase in calcination temperature from 573 to 873 K led to decrease in catalytic activity from 38% to 14.1%, mainly due to decrease in surface area from 110 to 24.5 m^2/g, change in morphology from mesoporous to microporous nature and increase in crystallite size from 12-38 to 20-70 nm.
- XRD patterns of samples prepared by various preparation methods and that of commercial Co_3O_4 exhibited the diffraction peaks at 2θ =19.2° (111), 31.2° (220), 36.84° (311), 44.84° (400), 55.65° (422), 59.42° (511) and 65.21° (422), which were attributed to the cubic spinel phase of Co_3O_4.
- The Co 2p XPS spectra of Co $2p_{3/2}$ peak at binding energies 779.4 and 781.9 eV which corresponded to Co^{2+} and Co^{3+} species. This evidenced the formation of spinel Co_3O_4 in all the samples.
- The surface composition from XPS examination established that there was participation of similar type of catalyst surface active species during reaction in polar and also in non polar solvents.
- Inter atomic bond distances between Co-O and Co-Co remained the same in case of fresh and used (Co-3C-a) catalyst in different solvents as observed from FT-EXAFS examination.
- FTIR of the prepared catalysts and commercial Co_3O_4 samples showed peaks at 568 and 660 cm^{-1} corresponding to Co^{3+} in octahedral and Co^{2+} in tetrahedral positions of Co_3O_4 spinel. The samples calcined at 573 K viz. Co-3C-e (sol-gel) and Co-3C-g (thermal decomposition, cobalt acetate) showed the presence of organic impurities, while this was not observed in case of co-precipitated and Co-3C-f (thermal decomposition, cobalt nitrate) catalysts. However,

used samples of (co-precipitated) catalysts showed the peaks same as those in the fresh samples indicating the stability of the catalyst under reaction conditions.

- Among various co-precipitated catalysts, only Co-3C-a (pH=8) and Co-3C-d (pH=14) showed uniform nano rod-like (10-20 nm) as well as elongated spherical (25-30 nm) morphology respectively.

- The highest redox ability of Co-3C-a was due to the presence of higher number of octahedral Co^{3+} and tetrahedral Co^{2+} species evident from XPS, FTIR, TPR, TPO and CV studies.

- The catalytic oxidation of veratryl alcohol to veratryl aldehyde in different solvents was found to be in the following order: toluene > water > ethanol > methanol.

- The optimum calcination time was 5 h, at 573 K for achieving the highest activity without active metal leaching.

- Activation energy calculated from the Arrhenius plot in water was found to be 42.46 kJ $mole^{-1}K^{-1}$.

- Catalyst reusability studies showed that nano Co-3C-a was truly a heterogeneous, highly efficient catalyst for aqueous phase oxidation of the C-OH at 413 K in water as a solvent.

- The activity of various sub-structure of lignin compounds studied in this work was found to be in the following order: secondary alcohol > di-substituted > tri-substituted > mono-substituted > non-substitution.

3.5. REFERENCES

1. F. Jin, H. Enomoto, *Bioresources* 4 (2009) 704.
2. J. Zakzeski, P. C. A. Bruijnincx, A. L. Jongerius, B. M. Weckhuysen, *Chem. Rev.* (2010) 3552.
3. J. Zakzeski, A. L. Jongerius, B. M. Weckhuysen, *Green Chem.* 12 (2010) 1225.
4. A. L. Gutman, G. Nisnevich, E. Shkolnik, B. Tishin, I. Zaltzman, US Patent 6,492,522 (2002).
5. C. Amen-Chen, H. Pakdel, C. Roy, *Bioresour. Technol.* 79 (2001) 277.
6. M. Y. Balakshin, E. A. Capanema, H. M. Chang, In Characterization of Lignocellulosic Materials, Hu T.Q. Ed.; Blackwell: Oxford, U.K., 2008, p 148.
7. F. Cui, D. Dolphin, *Biorg. Med. Chem,* 3 (1995) 471.
8. Z. Du, J. Ma, H. Ma, J. Gao, J. Xu, *Green Chem.* 12 (2010) 590.
9. J. Zakzeski, P. C. A. Bruijnincx, B. M. Weckhuysen, *Green Chem.* 13 (2011) 671.
10. V. R. Mate, M. Shirai, C. V. Rode, *Catal. Commun.* 33 (2013) 66.
11. V. S. Kshirsagar, S. Vijayanand, H. S. Potdar, P. A. Joy, K. R. Patil, C. V. Rode, *Chem. Lett.* 37 (2008) 310.
12. T. Li, S. G. Yang, L. S. Huang, B. X. Gu, Y. W. Du, *Nanotechnology* 15 (2004) 1479.
13. B. B. Lakshmi, C. J. Patrissi, C. R. Martin, *Chem. Mater.* 9 (1997) 2544.
14. G. X. Wang, X. P. Shen, J. Horvat, B. Wang, H. Liu, D. Wexler, J. Yao, *J. Phys. Chem. C* 113 (2009) 4357.
15. N. Du, H. Zhang, B. D. Chen, J. B. Wu, X. Y. Ma, Z. H. Liu, Y. Q. Zhang, D. R. Yang, X. H. Huang, J. P. Tu, *Adv. Mater*. 19 (2007) 4505.
16. Y. Chen, Y. Zhang, S. Fu, *Mater. Lett.* 61 (2007) 701.

17. L. Li, Y. Chu, Y. Liu, J. L. Song, D. Wang, X. W. Du, *Mater. Lett.* 62 (2008) 1507.

18. J. Jiu, Y. Ge, X. Li, L. Nie, *Mater. Lett.* 54 (2002) 260.

19. R. M. Wang, C. M. Liu, H. Z. Zhang, C. P. Chen, L. Guo, H. B. Xu, S. H. Yang, *Appl. Phys. Lett.* 85 (2004) 2080.

20. D. Y. Kim, S. H. Ju, H. Y. Koo, S. K. Hong, Y. C. Kang, *J. Alloys Compd.* 417 (2006) 254.

21. A. U. Mane, K. Shalini, A. Wohlfart, A. Devi, S. A. Shivashankar, *J. Cryst. Growth*. 240 (2002) 157.

22. D. Zou, C. Xu, H. Luo, L. Wang, T. Ying, *Mater. Lett.* 62 (2008) 1976.

23. S. W. Oh, H. J. Bang, Y. C. Bae, Y. K. Sun, *J. Power Sources.* 173 (2007) 502.

24. J. Ahmed, T. Ahmad, K. V. Ramanujachary, S. E. Lofland, A. K. Ganguli, *J. Colloid Interface Sci.* 321 (2008) 434.

25. A. S. Bhatt, D. K. Bhat, C. W. Tai, M. S. Santosh, *Mater. Chem. Phys.* 125 (2011) 347.

26. X. Wang, X. Y. Chen, L. S. Gao, H. G. Zheng, Z. Zhang, Y. T. Qian, *J. Phys. Chem. B.* 108 (2004) 16401.

27. M. A. Chougule, S. G. Pawar, P. R. Godse, R. D. Sakhare, S. Sen, V. B. Patil, *J. Mater. Sci. Mater. Electron.* 23 (2012) 772.

28. N. N. Binitha, P. V. Suraja, Z. Yaakob, M. R. Resmi, P. P. Silija, *J. Sol-Gel Sci. Technol.*53 (2010) 466.

29. L. Zhou, J. Xu, X. Li, F. Wang, *Chem. Phys. Mater.* 97 (2006) 137.

30. K. C. Patil, S. T. Aruna, S. Ekambaram, *Curr. Opin. Solid State Mater. Sci.* 2 (1997) 158.

31. H. Zhang, X. Chen, Z. Yang, L. Liu, Z. Li, T. Yu, Z. Zou, *Phys. D: Appl. Phys.* 40 (2007) 4129.

32. S. A. H. Tabrizi, E. T. Nassaj, *Science of Sintering* 42 (2010) 321.

33. X. Chen, J. P. Cheng, Q. L. Shou, F. Liu, X. B. Zhang, *CrystEngComm*. 14 (2012) 1271.

34. A. L. Ankudinov, B. Ravel, J. J. Rehr, S. D. Conradson, *Phys. Rev. B* (1998) 7565.

35. J. Yang, H. Liu, W. N. Martens, R. L. Frost, *J. Phys. Chem. C* 114 (2009) 111.

36. D. Patil, P. Patil, V. Subramanian, P. A. Joy, H. S. Potdar, *Talanta* 81 (2010) 37.

37. M. Kang, M. W. Song, C. H. Lee, *Appl. Catal. A: Gen.* 251 (2003) 143.

38. C. V. Rode, M. V. Sonar, J. M. Nadgeri, R. V. Chaudhari, *Org. Proc. Res. Dev.* 8 (2004) 873.

39. K. Sinko, G. Szabo, M. Zrinyi, *J. Nanosci. Nanotechnol.* 11 (2011) 4127.

40. Y. Chen, D. R. U. Knappe, M. A. Barlaz, *Environ. Sci. Technol.* 38 (2004) 3731.

41. A. Bielanski, J. Haber, *Cat. Rev. Sci. Eng.* 19 (1979) 1.

42. J. H. Park, C. H. Park, I. S. Nam, *Appl. Cat. A: Gen.* 277 (2004) 271.

43. A. Y. Khodakov, J. Lynch, D. Bazin, B. Rebours, N. Zanier, B. Moisson, P. Chaumette, *J. Catal.* 168 (1997) 16.

44. E. McCafferty, J. P. Wightman, *Surf. Interface Anal.* 26 (1998) 549.

45. D. Pyke, K. K. Mallick, R. Reynolds, A. K. Bhattacharya, *J. Mater. Chem.* 8 (1998) 1095.

46. J. F. Moulder, W. F. Stickle, P. E. Sobol, K. D. Bomben, Handbook of X-ray Photoelectron Spectroscopy, Published by: Physical Electronics Division, (1992-1995).

47. http://srdata.nist.gov/xps/Default.aspx

48. J. P. Bonnelle, J. G. A. D'huysser J. Electron. Spectrosc. Relat. Phenom. 7 (1975) 151.

49. C. Reichardt, Solvents and Solvent Effects in Organic Chemistry Wilay-VCH Pub Verlag GmbH & Co. KGaA, 1988.

50. E. A. Stern, M. Newville, B. Ravel, Y. Yacoby, D. Haskel, *Physica B* (1995) 117.

51. P. A. Chernavskii, A. Y. Khodakov, G. V. Pankina, J. S. Girardon, E. Quinet, *Appl. Catal. A: Gen.* 306 (2006) 108.

52. L. F. Liotta, G. D. Carlo, G. Pantaleo, A. M. Venezia, G. Deganello, *Appl. Catal. B: Env.* 66 (2006) 217.

53. J. Jansson, A. Palmqvist, E. Fridell, M. Skoglundh, L. Osterlund, P. Thormahlen, V. Langer, *J. Catal.* 211 (2002) 387.

54. K. Nakamoto, Infrared and Raman Spectroscopy of Inorganic and Coordination Compounds, Wiley: New York, 1978.

55. P. Zucca, F. Sollai, A. Garau, A. Rescigno, E. Sanjust, *J. Mol. Catal. A: Chem.* 306 (2009) 89.

56. B. Gillot, M. Laarj, P. Tailhades, A. Rousset, Mater. Chem. Phys. 19 (1988) 485.

57. W. L. Roth, *J. Ph vs. Chem. Solids.* 25 (1964) 1.

58. P. Dutta, M. S. Seehra, S. Thota, J. Kumar, *J. Phys. Condens. Matter.* 20 (2008) 015218.

59. Y. Lou, L. Wang, Y. Zhang, Z. Zhao, Z. Zhang, G. Lu, Y. Guo, *Catal. Today 175* (2011) 610.

60. Z. Nickolov, G. Georgiev, D. Stoilova, I. Ivanova, *J. Mol. Struct.* 354 (1995) 119.

61. A. M. Cao, J. S. Hu, H. P. Liang, W. G. Song, L. J. Wan, X. L. He, *J. Phys. Chem. B* 110 (2006) 15858.

62. K. Deshpande, A. Mukasyan, A. Varma, *Chem. Mater.* 16 (2004) 4896.

63. W. M. Keely, H. W. Maynor, *Journal of Chemical & Engineering Data* 8 (1963) 297.

64. T. Wanjun, C. Donghua, *Chem. Pap.* (2007) 329.

65. G. P. Glaspell, P. W. Jagodzinski, A. Manivannan, *J. Phys. Chem. B* 108 (2004) 9604.

66. R. W. Grimes, A. N. Fitch, *J. Mater. Chem.* 1 (1991) 461.

67. I. B. Chorkendorff, J. W. Niemantsverdriet, in Concepts of Modern Catalysis and Kinetics Wiley-VCH 2003.

68. V. S. Kshirsagar, J. M. Nadgeri, P. R. Tayade, C. V. Rode, *Appl. Catal. A: Gen.* 339 (2008) 28.

69. P. A. Rock, *Inorg. Chem.* 7 (1968) 837.

70. R. A. Sheldon, In Catalytic Oxidation: Principles and Applications, Eds.; R. A. Sheldon, `R. A. van Santen, World Scientific: Singapore, 1995, p 177.

71. G. Centi, F. Cavani, F. Trifiro, Fundamental and Applied catalysis Selective oxidation by heterogeneous catalysis Ed. M. V. Twigg, M. S. Spencer, Kluwer Academic/Plenum Publishers, New York, 2001, p. 218.

72. L. I. Simandi, Advances in catalytic activation of dioxygen by metal complexes, Kluwer Academic Publishers, The Netherlands, 2003, p.28.

Chapter 4

Zn and Al doped Co_3O_4 catalysts for oxidation of veratryl alcohol

4.1. INTRODUCTION

In continuation of our efforts on developing spinel type catalysts for oxidation we report here for the first time, Zn and Al doped Co_3O_4 catalysts for the liquid phase oxidation of veratryl alcohol. Both Zn and Al doped Co_3O_4 spinels are versatile oxides used in advanced applications such as high-performance anode material for lithium-ion batteries, solar selective absorbers, field emitters, gas sensors as well as in catalytic applications e.g. low temperature CO oxidation, hydrocarbon oxidation and Fischer-Tropsch synthesis [1-6]. Spinel oxides in nano forms are very interesting materials from catalysis point of view due to their different morphologies and non stoichiometric compositions, leading to the stabilization of high-spin configuration of the divalent cation which can result in higher catalytic activity for oxidation reactions. It is clear from the literature [7-11] that though, nano particle materials have been synthesized and characterized by various methods, a systematic investigation with the aim of their application as tailor made catalysts for liquid phase oxidation of veratryl alcohol is necessary.

In spinel oxides, A and B can occupy two different sites, tetrahedral and octahedral. Studies of such compounds are very important in solid-state chemistry for better understanding of structure and activity. In order to investigate the role of cations A and B in Co_3O_4 spinel, we doped it with Zn and Al in which Zn^{2+} occupies tetrahedral sites and Al^{3+} cation occupies octahedral sites. These Zn and Al doped Co_3O_4 spinels were prepared by a simple protocol without using any template, involving a simultaneous co-precipitation/digestion method. The different samples of the zinc doped Co_3O_4 were prepared by varying the zinc: cobalt (Zn:Co) compositions such as 1:1 (a), 1:2 (b) and 1:3 (c). Similarly, the Al doped Co_3O_4 samples were prepared by varying the cobalt: aluminium (Co:Al) compositions 1:2 (a), 1:1 (b) and 3:1 (c). These catalysts were

calcined at 573 and 873 K in air. Among the various compositions studied in this work ZC-3C-c and CA-3C-c showed the highest conversions of 24% and 26% respectively for the oxidation of veratryl alcohol to veratryl aldehyde. The catalytic activity and stability of these catalysts were found to be lower than that of pure nano Co_3O_4 (Co-3C-a, 38% conversion, Chapter 3) catalyst. In order to understand the roles of Zn and Al in the doped Co_3O_4, the prepared catalysts were thoroughly characterized by BET surface areas, powder X-ray diffraction (XRD), high-resolution transmission electron microscopy (HRTEM), X-ray photoelectron spectroscopy (XPS), FTIR, extended X-ray absorption fine structure spectroscopy (EXAFS) and temperature programmed reduction and temperature programmed oxidation (TPR/TPO).

4.2. RESULTS AND DISCUSSION

4.2.1. Zn doped Co_3O_4

4.2.1.1. BET surface area measurement

BET surface areas of Zn doped Co_3O_4 catalysts with ratios of Zn and Co as 1:1 (ZC-a), 1:2 (ZC-b) and 1:3 (ZC-c) calcined at 573 K and 873 K are presented in Table 4.1. The ZC-3C-a (Zn:Co, 1:1) catalyst showed surface area of the 75 m^2/g, while change in composition from 1:1 to 1:2 and 1:3 caused gradual increase in surface area to 81 and 86 m^2/g for ZC-3C-b and ZC-3C-c catalysts respectively. The increase in surface area with increase in cobalt content was due to decrease in crystallite/particle size as observed in the XRD and HRTEM characterization which is discussed later. While, increase in calcination temperature from 573 to 873 K caused significant decrease in surface area to 16.7, 18.3 and 19.2 m^2/g for ZC-6C-a, ZC-6C-b and ZC-6C-c catalysts respectively. This decrease in surface area by ~$1/4^{th}$ was due to the increase in crystallite size as observed in the XRD and HRTEM analysis discussed later.

Table 4.1. BET surface area of Zn doped Co_3O_4 samples

Entry	Catalysts	Zn:Co composition	Calcination temperature (K)	Specific Surface area (m^2/g)
1	ZC-3C-a	1:1	573	75.0
2	ZC-6C-a	1:1	873	16.7
3	ZC-3C-b	1:2	573	81.0
4	ZC-6C-b	1:2	873	18.3
5	ZC-3C-c	1:3	573	86.0
6	ZC-6C-c	1:3	873	19.2
7	Co-3C-a	NA	573	110.0

4.2.1.2. X-ray diffraction (XRD)

XRD patterns of Zn doped Co_3O_4 spinel samples with various compositions (Zn:Co from 1:1 to 1:3) calcined at 573 and 873 K are presented in Figure 4.1. All the samples exhibit the diffraction peaks at 2θ =18.2° (111), 31.7° (220), 36.17° (311), 44.84° (400), 55.85° (422), 59.16° (511) and 65.12° (422), which were attributed to the spinel phase of $ZnCo_2O_4$ (*), Co_3O_4 and ZnO (#) phases. It was observed that the samples calcined at 573 K showed weak crystalline reflections, due to which it was difficult to define maxima of the peaks and we could not assign the distinct phases of $ZnCo_2O_4$. While, the same sample after calcination at 873 K showed distinct phases of $ZnCo_2O_4$ and ZnO. The calculated lattice parameter for all the samples was found to be 8.101 Å that matched with the reported value for the spinel $ZnCo_2O_4$ and ZnO phases (JCPDS 81-2299 and 80-0075) respectively. With change in Zn:Co ratio from 1:1 to 1:3 and calcination at 573 K, slight decrease in peak broadening and increase in peak intensity was observed for the peaks at

2θ =31.7° (220), 36.17° (311), 44.84° (400), 55.85° (422), 59.16° (511) and 65.12° (422), indicating improvement in the crystallinity. The sample calcined at 873 K showed the peaks at 2θ =45.4° (211), 56.6° (221), 63.2° (311) and 69.5° (023) (Figure 4.1), which could be attributed to spinel phase of $ZnCo_2O_4$ (*) and additional peaks of ZnO_2 ($) phase (JCPDS 77-2414)**.** The gradual increase in intensity of the peaks at 2θ =45.4° (211), 56.6° (221), 63.2° (311) and 69.5° (023) (ZnO_2 phase) was observed for the change in composition of Zn:Co from 3:1 to 1:1, which is in accordance with increase in Zn compositions from 25% to 50%. Crystallite sizes of ZC-3C-a, ZC-6C-a, ZC-3C-b, ZC-6C-b, ZC-3C-c and ZC-6C-c samples were calculated using the Scherrer equation and were found to be in the range of 10-20, 40-65, 12-25, 45-70, 15-25 and 60-75 nm respectively. Thus, increase in crystallite size for the samples, ZC-6C-a, ZC-6C-b and ZC-6C-c was mainly due to the restructuring of the surface at 873 K [12, 13]. These results matched very well with the HRTEM results.

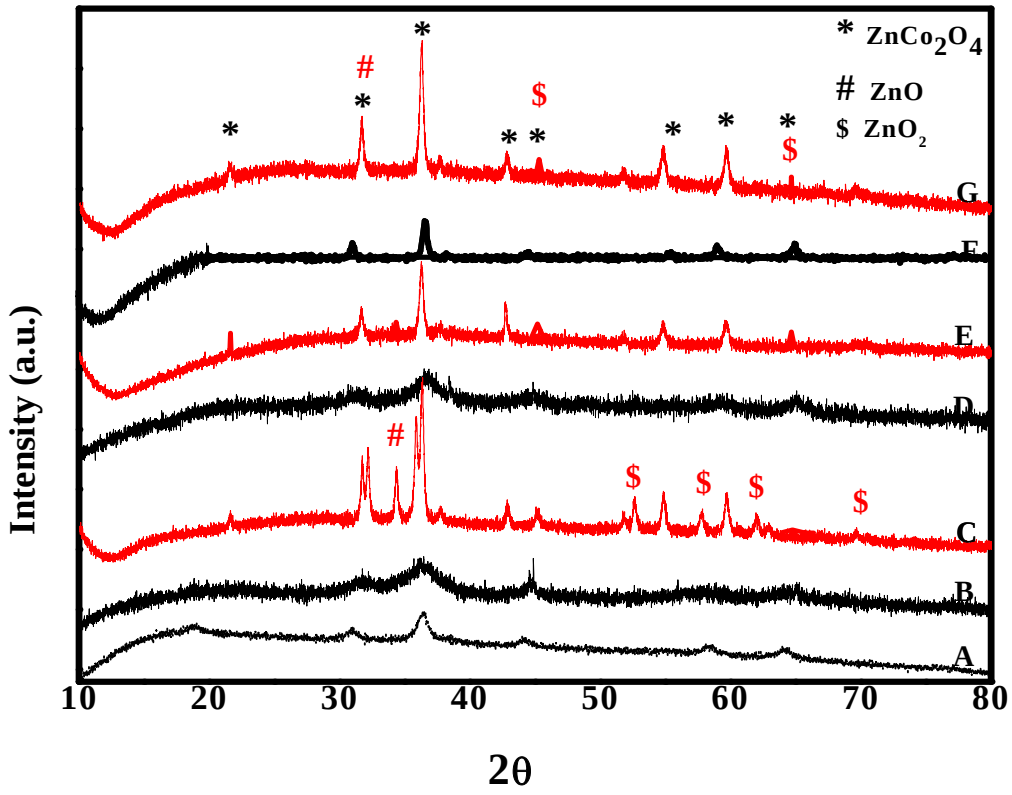

Figure 4.1. XRD of (A) Co-3C-a, (B) ZC-3C-a, (C) ZC-6C-a, (D) ZC-3C-b, (E) ZC-6C-b, (F) ZC-3C-c and G) ZC-6C-c samples

4.2.1.3. X-ray photoelectron spectroscopy (XPS)

In order to further establish the formation of $ZnCo_2O_4$ spinel, the samples of Zn doped Co_3O_4 with Zn:Co compositions 1:1, 1:2 and 1:3 (573 K) were characterized by XPS. The Co 2p and Zn 2p spectra of these samples are shown in Figures 4.2a, 4.2b and 4.3 respectively. The Co 2p spectra showed two peaks with binding energies at 779.8 and 795.0 eV, corresponding to Co $2p_{3/2}$ and Co $2p_{1/2}$ core level peaks [14, 15]. We observed a small increase in the binding energy of the Zn doped Co samples in comparision with the undoped one (779.3eV for Co $2p_{3/2}$ and 794.4 eV for Co $2p_{1/2}$). The Co $2p_{3/2}$ and Co $2p_{1/2}$ peaks separation value obtained was 15.2 eV, comparable to that observed for the Co_3O_4 spinel (Section 3.3.1.3). The Co $2p_{3/2}$ peak can be

deconvoluted into two peaks at binding energy of 779.8 and 781.9 eV, due to presence of Co^{3+} and Co^{2+} species (Figures 4.2b on the surface. A small hump observed at a binding energy of 788.5 eV was a characteristic satellite peak of Co^{3+} [5,16]. The Zn 2p spectra for all the samples showed two peaks with a binding energies at 1020.2 and 1043.8 eV, which were assigned to Zn $2p_{3/2}$ and Zn $2p_{1/2}$ levels with splitting value of 23.6 eV, confirming the presence of Zn^{2+} [17]. While, the binding energy of Zn^{2+} in ZnO is 1021.4 eV, the shift in binding energy of cobalt to higher value and for zinc to lower binding energy is due to the transfer of electrons from Zn 4s orbital to the unfilled Co 3d orbital [18].

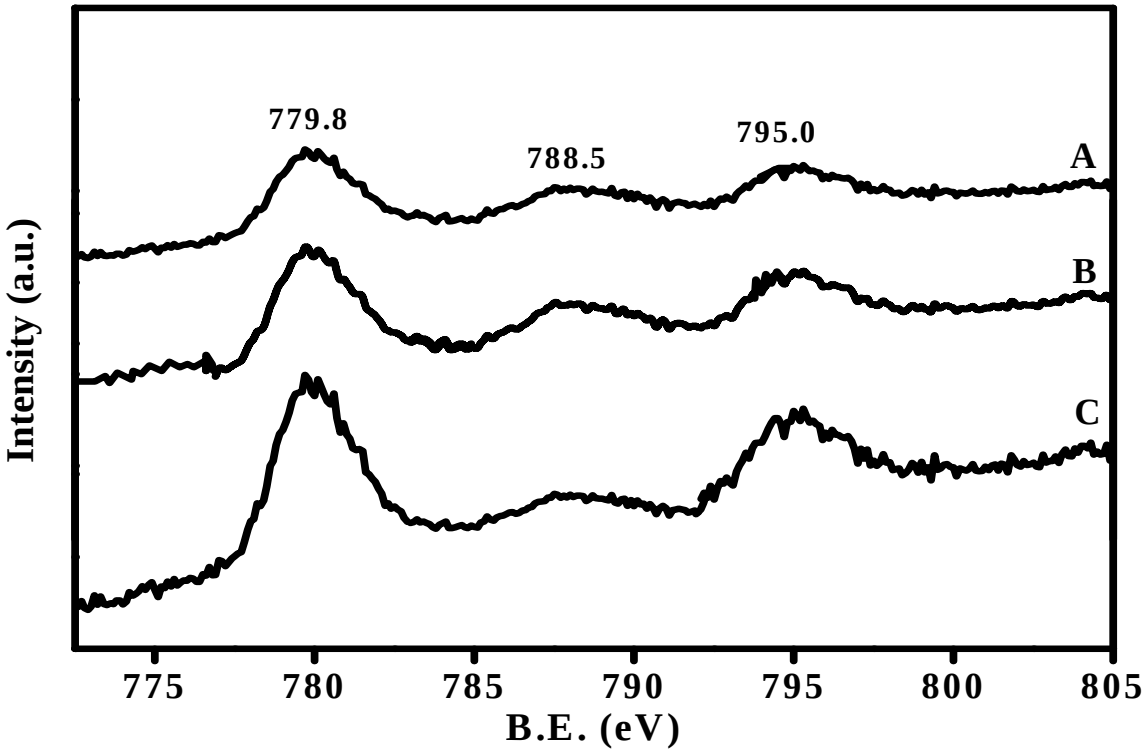

Figure 4.2a. XPS Co 2p spectra of (A) ZC-3C-a, (B) ZC-3C-b and (C) ZC-3C-c samples

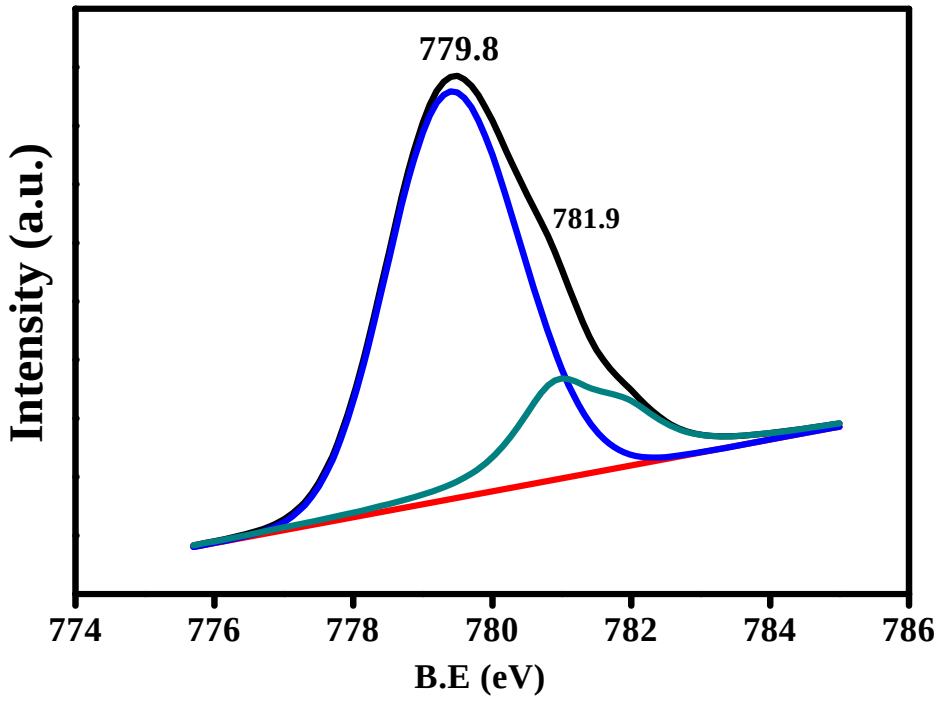

Figure 4.2b. Deconvolution spectra of Co $2p_{3/2}$

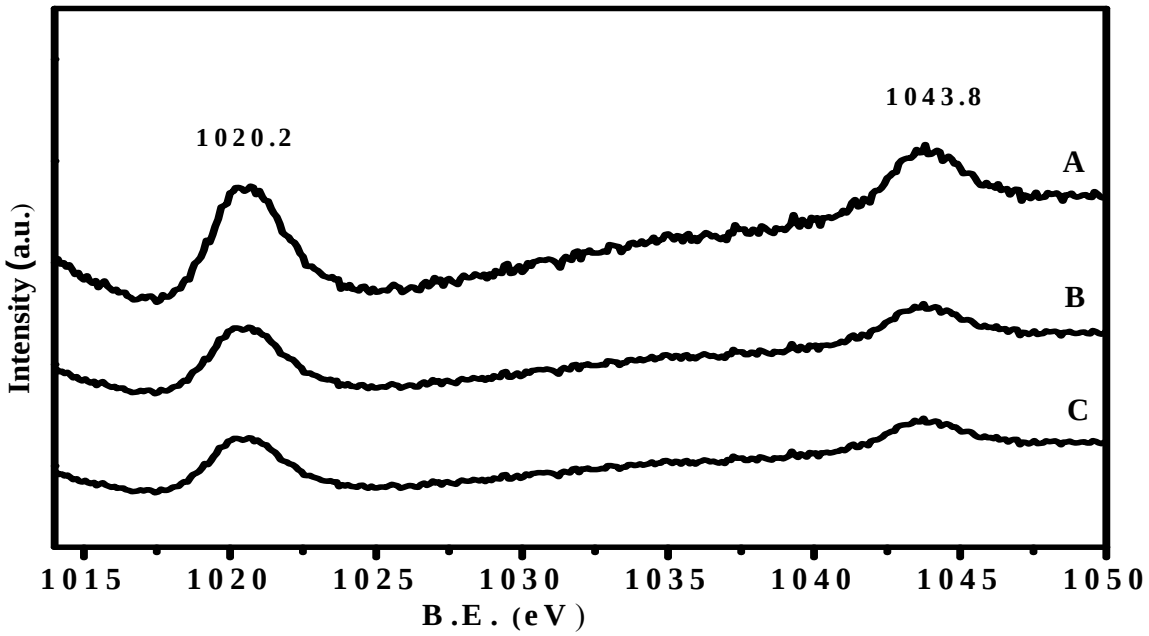

Figure 4.3. XPS Zn 2p spectra of (A) ZC-3C-a, (B) ZC-3C-b and (C) ZC-3C-c samples

4.2.1.4. Thermo gravimetric analysis (TG-DTA)

TG-DTA curves for the ZC-c (Zn:Co=1:3) are shown in Figure 4.4. The ZC-c sample showed the weight loss in two steps which is similar to the Co-a sample (Co_3O_4 prepared at pH 7-8, chapter 3, Section 3.3.1.5). The first continuous weight loss of 15% from room temperature to 520 K was due to the elimination of physically adsorbed/trapped water molecules [19]. While in the second step, 16.2% weight loss below temperature 680 K was due to the decomposition of carbonate anions and dehydroxylation [20]. However, continuous 4.3% weight loss observed with increase in temperature from 680 to 1100 K was also due to dehydroxylation (Table 4.2) [7]. Based on the observation that the major weight loss occurred below 620 K, higher than that observed at 553 K for the Co-a sample (Chapter 3), might be due to the influence of doping of Zn in Co_3O_4.

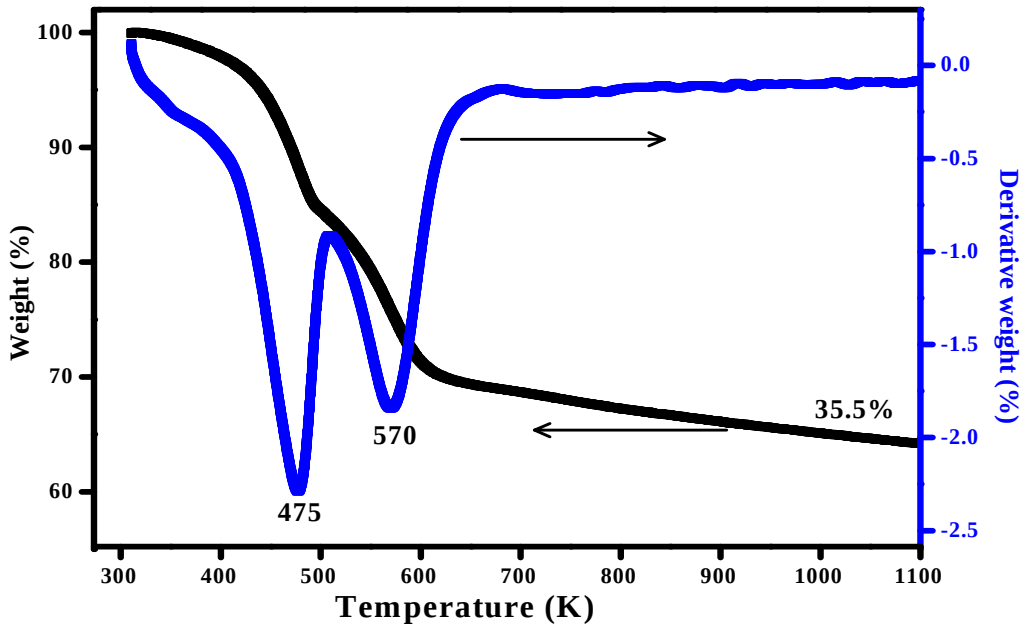

Figure 4.4. TG-DTA of ZC-3C-c sample

Table 4.2. Summary of thermogravimetric analysis

Sample	TG		DTA	Remarks
	Temperature range (K)	Weight loss (w/w. %)	Peak maximum (K)	
ZC-c	330-520	15.0	475	Loss of physically adsorbed/trapped water molecules.
	520-680	16.2	570	Decomposition of carbonate anions and dehydroxylation.
	680-1100	4.3	-	Dehydroxylation of surface hydroxyl group.

4.2.1.5. Fourier-transform infrared spectroscopy (FT-IR)

FT-IR spectra of Zn doped Co_3O_4 spinel with various compositions of Zn:Co (1:1, 1:2, and 1:3) are shown in Figure 4.5. The FT-IR spectra of ZC-c showed three bands at 564, 669 and 450 cm^{-1} and distinct bands at 1380 and 1499 cm^{-1} assigned to the stretching vibrations of metal-oxygen and metal-carbonate (CO_3^{2-}) bonds respectively (Figure 4.5, A) [21, 22]. The peak at 450 cm^{-1} was assigned to Zn^{2+} (ZnO) while the second peak at 567 cm^{-1} corresponds to Co^{3+} in an octahedral position and other peak at 666 cm^{-1} corresponds to the Co^{2+} in a tetrahedral position confirming the formation of ZnO and $ZnCo_2O_4$ spinel in the ZC-3C-a, ZC-3C-b and ZC-3C-c samples [22-24]. Samples calcined at 573 K showed increase in intensity of peaks at 564 and 669 cm^{-1} while diminished intensity was observed for peaks at 1380 and 1499 cm^{-1}. This was due to increase in cobalt loading by three times (from Zn:Co=1:1 to 1:3) and due to the decomposition of zinc cobalt hydroxy carbonate into ZnO, $ZnCo_2O_4$ and Co_3O_4 during the calcination process.

The presence of these phases was confirmed by XRD results (Section 4.2.1.2) [7, 25]. However, all the samples showed the presence of carbonate species even though calcination time kept was 5 h, this impurity found to decrease with an increase in cobalt composition from 1:1 to 1:3. The broad peaks at 3460 cm^{-1} and 1627 cm^{-1} were attributed to metal hydroxyl stretching vibrations observed in the ZC-c, ZC-3C-a, ZC-3C-b, ZC-3C-c samples [26, 27].

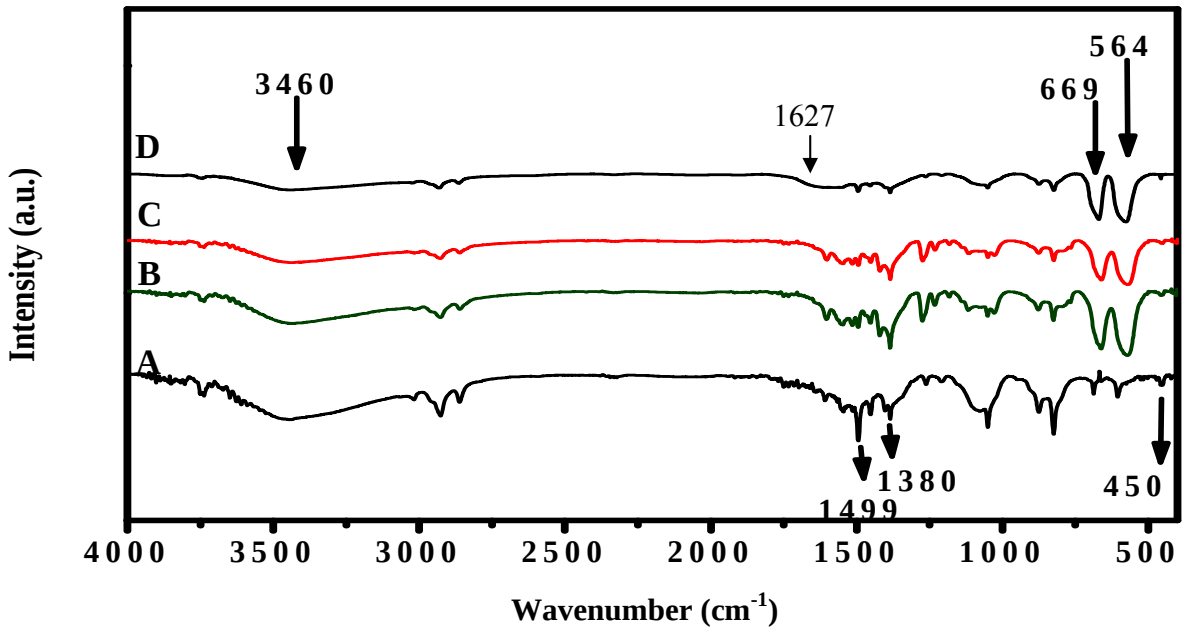

Figure 4.5. FTIR of (A) ZC-c, (B) ZC-3C-a, (C) ZC-3C-b and (D) ZC-3C-c samples

4.2.1.6. High resolution transmission electron microscopy

The morphologies of the zinc doped Co_3O_4 catalysts with different compositions of 1:1, 1:2 and 1:3 (ZC -a, ZC-b and ZC-c) and calcined at 573 and 873 K were examined by HR-TEM (Figure 4.6). The ZC-3C-a sample showed the aggregation of non uniform rod shaped and elongated spherical particles having the size in the range of 12-16 nm. With change in zinc to cobalt composition from 1:1 to 1:2, morphology of the particles remained almost the same, while in the sample with 1:3 ratio, the agglomeration of these particles formed slightly bigger particles (about

18 nm). However, with increase in calcination temperature from 573 to 873 K, increase in size of both rod shaped and elongated spherical particles was observed which was in the range of 38-59, 26-68 and 22-72 nm for ZC-6C-a, ZC-6C-b and ZC-6C-c samples respectively. The characteristic planes obtained from the SAED image and 'd' spacings of the fringe pattern (Figure 4.6, A-F) were found to be (311), (400), (422), (511), (620), (551) and (622) and was in good agreement with the XRD results.

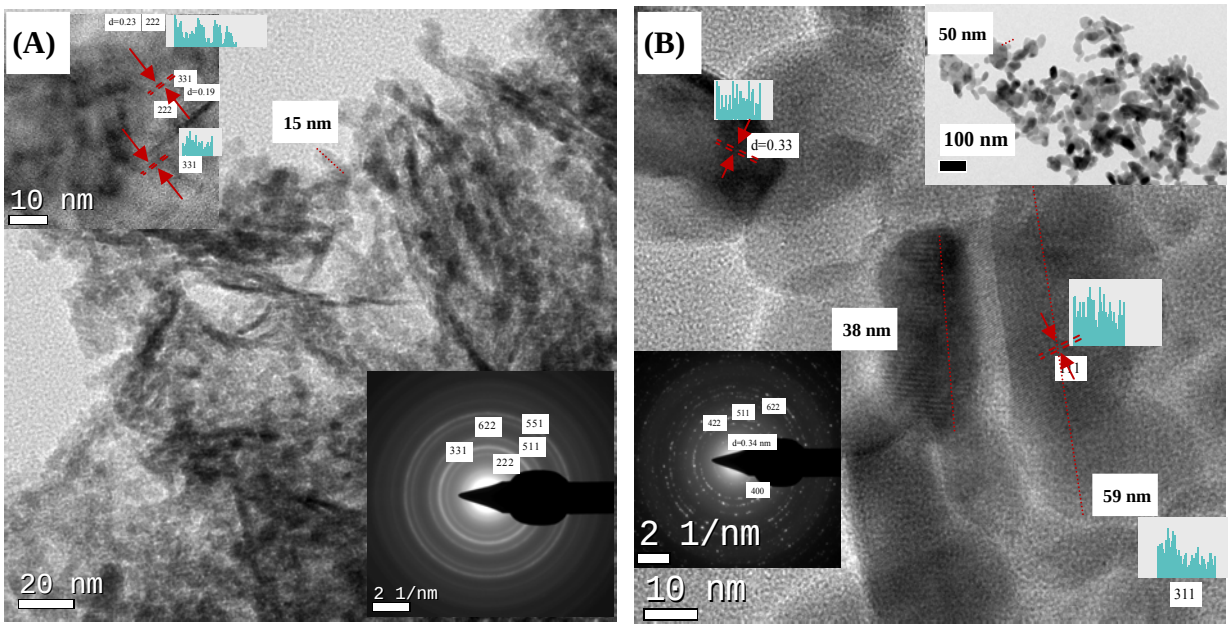

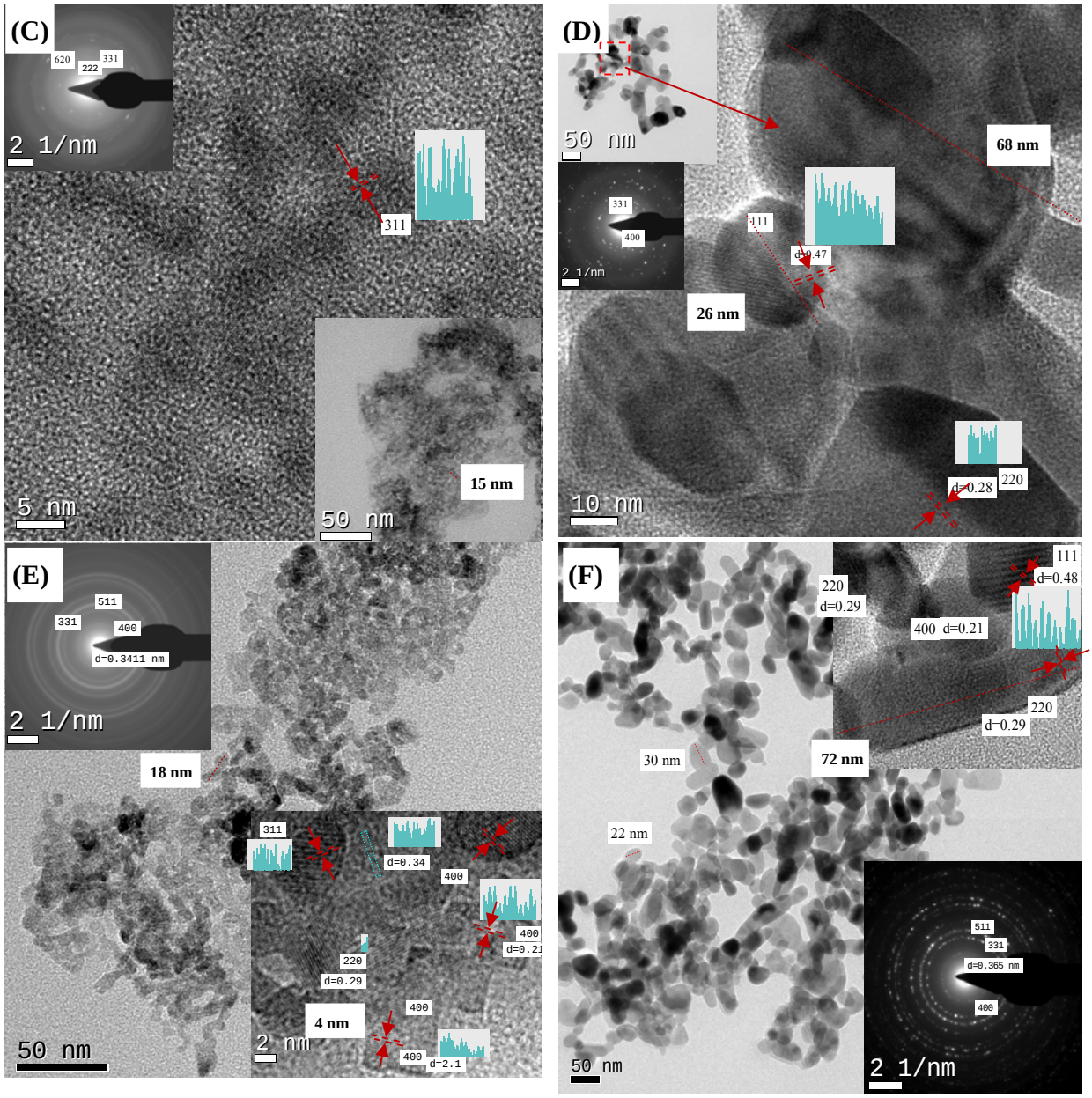

Figure 4.6. HRTEM of (A) ZC-3C-a, (B) ZC-6C-a, (C) ZC-3C-b, (D) ZC-6C-b, (E) ZC-3C-c and (F) ZC-6C-c samples

4.2.1.7. Energy dispersive X-ray (EDX)

The elemental compositions of the ZC-a, ZC-b and ZC-c samples obtained from EDX are shown in Figure 4.7. This confirmed the presence of the zinc, cobalt, oxygen, nitrogen and trace of

potassium elements present in all the samples. From the EDX examination zinc and cobalt compositions were found to be ~1:1, 1:2 and 1:3 for the ZC-a, ZC-b and ZC-c samples respectively (Table 4.3).

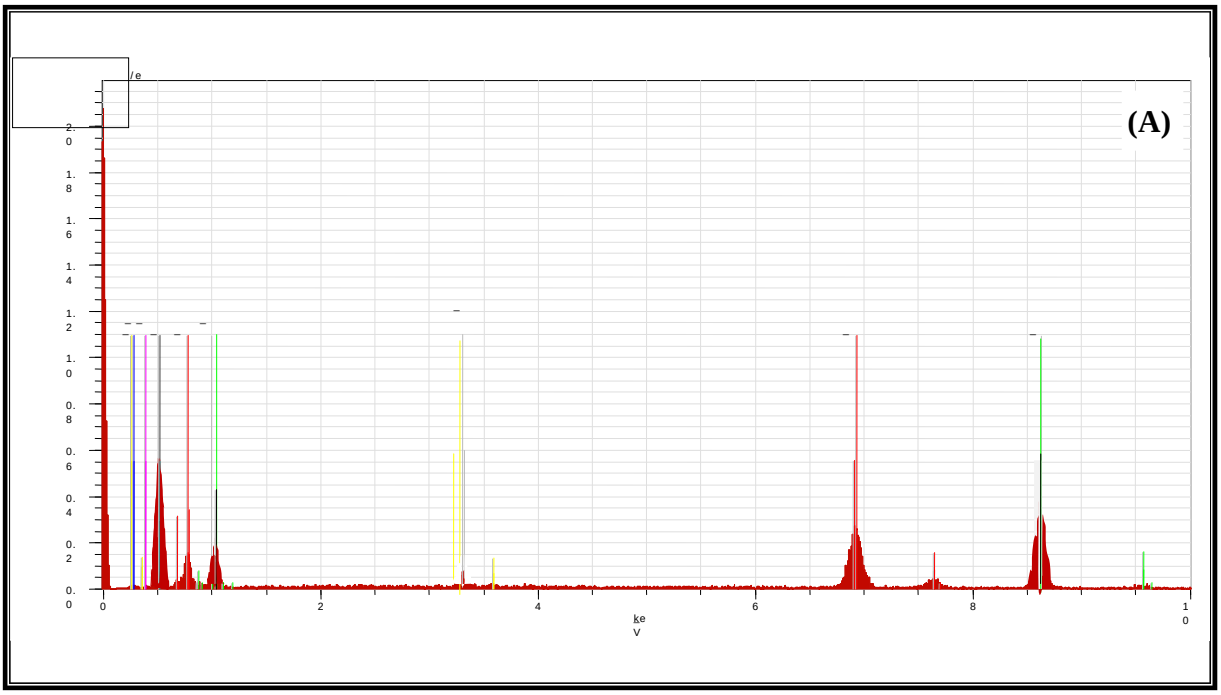

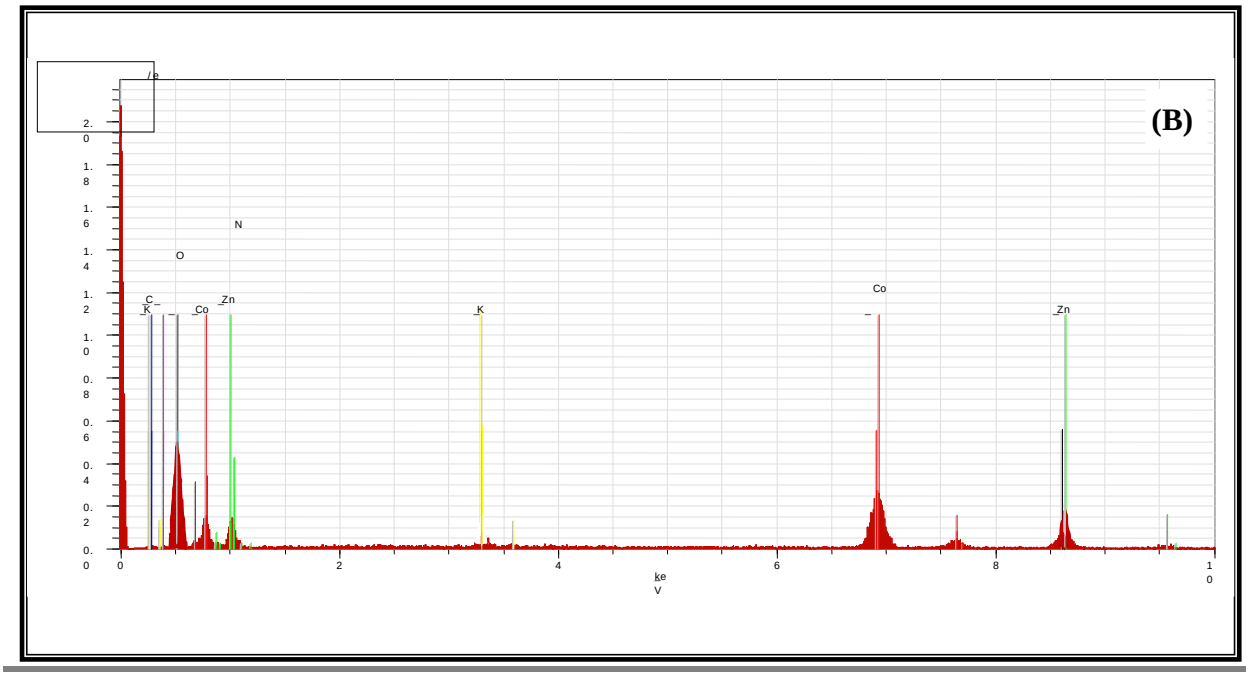

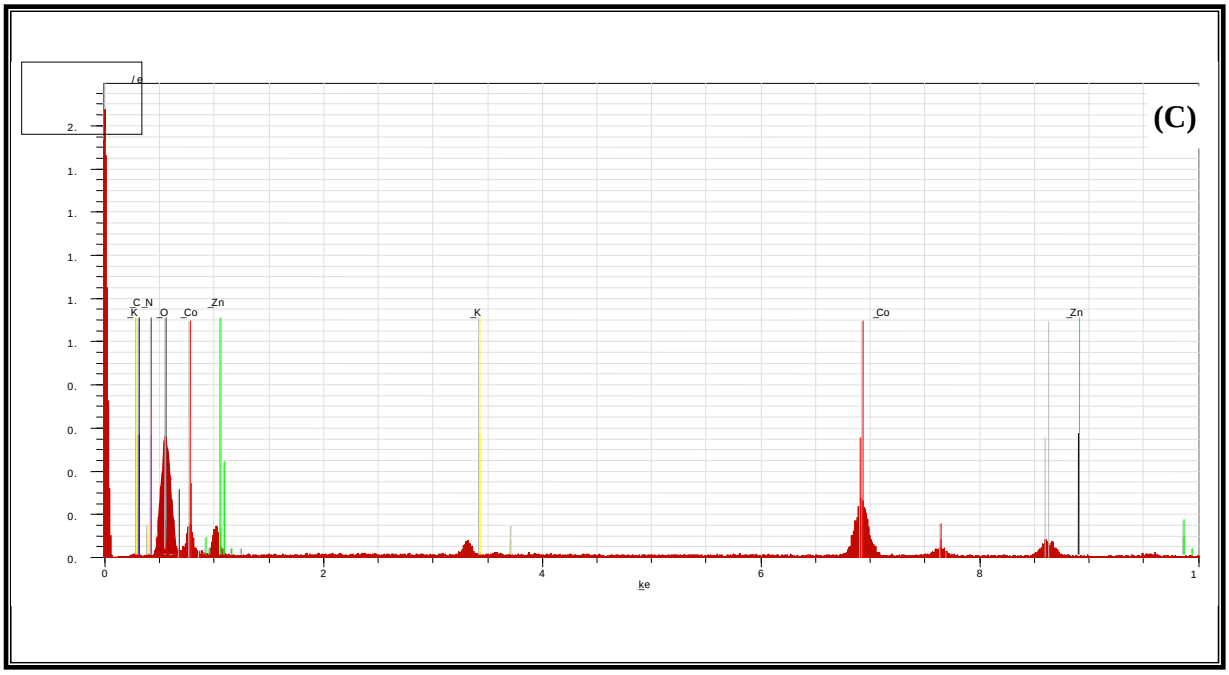

Figure 4.7. EDX of (A) ZC-a, (B) ZC-b and (C) ZC-c samples

Table 4.3. Atomic percentage of elements in the zinc doped Co_3O_4 samples

Entry	As-dried samples	Elemental compositions (Atom %)				
		Zn	Co	O	K	N
1	ZC-a	27.7	26.8	41.4	1.8	2.3
2	ZC-b	17.8	35.5	37.9	2.5	6.3
3	ZC-c	13.9	37.4	42.5	1.5	4.7

4.2.1.8. Temperature programmed reduction / Temperature programmed oxidation (TPR/TPO)

The reducibility of the ZC-3C-a, ZC-3C-b and ZC-3C-c catalysts was studied by H_2-TPR (Figure 4.8). The peak observed in the range of 450-550 K in all the samples was attributed to the reduction of trivalent cobalt oxide ($ZnCo_2O_4$) to divalent cobalt oxide (CoO). Another broad

peak in higher temperature range of 550-850 K in all the samples observed could be attributed to the reduction of divalent cobalt oxide (CoO) to metallic cobalt (Co^o) [23, 25, 28]. The slight increase in reduction temperature as indicated by a second peak at 550-850 K as compared to that observed in case of Co-3C-a catalyst (570-750 K) (Section 3.3.1.9), might be due to Zn doping in spinel Co_3O_4 [25, 29]. Interestingly, with increase in cobalt composition from 1:1 to 1:3 caused slight shift in thermal reducibility of the first peak to a lower temperature of 511 K which was almost equivalent to that in case of Co-3C-a (nano Co_3O_4) catalyst (Chapter 3). This was due to the proportional decrease in zinc composition by 50% to 25% resulted into the formation of higher spinel Co_3O_4 phase. With change in zinc and cobalt composition from 1:1 to 1:3 showed 229, 294 and 325 mmol of H_2 up take which was found to be ~50%, ~35% and 25% less than that for pure nano Co_3O_4 (Co-3C-a) spinel catalyst (Table 4.4). This indicates that Zn doping does not improve the reducibility of the Co_3O_4 spinel and it also confirmed that redox nature was purely dependent on population of both Co^{2+} & Co^{3+} species in Co_3O_4 spinel.

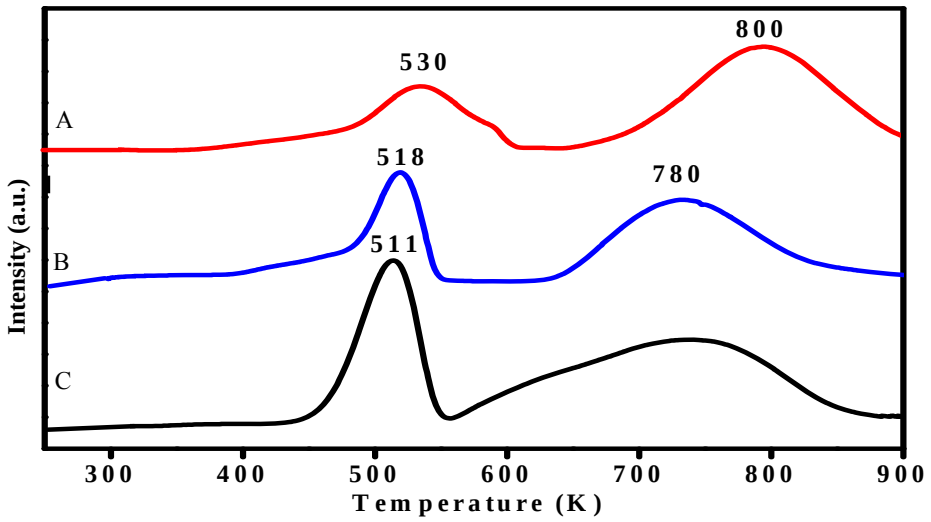

Figure 4.8. TPR of (A) ZC-3C-a, (B) ZC-3C-b and (C) ZC-3C-c samples

The oxidizability of pre-reduced ZC-3C-a, ZC-3C-b and ZC-3C-c samples was determined by TPO and the results are shown in Figure 4.9. The first peak in a range of 370-460 K in all the samples was attributed to the oxidation of metallic cobalt (Co^o) to divalent cobalt oxide (CoO). Second broad peak appearing in the range 450-630 K in all the samples indicates the oxidation of divalent cobalt oxide (CoO) to trivalent cobalt oxide (Co_3O_4/ Co_2O_3) [24, 26]. With change in zinc and cobalt composition from 1:1 to 1:3, there is a considerable shift of the first peak from 460 to 410 K and also of second peak from 570 to 510 K, similar observations were made in TPR studies. The shift of the peaks to lower temperature indicates the incorporation of zinc into the cobalt oxide frame work. The ZC-3C-a, ZC-3C-b and ZC-3C-c samples showed 11.2, 13.8 and 15.9 mmol of O_2 up take which was found to be ~50%, 35% and 25%, less than pure Co_3O_4 (Co-3C-a) spinel catalyst respectively (Table 4.4).

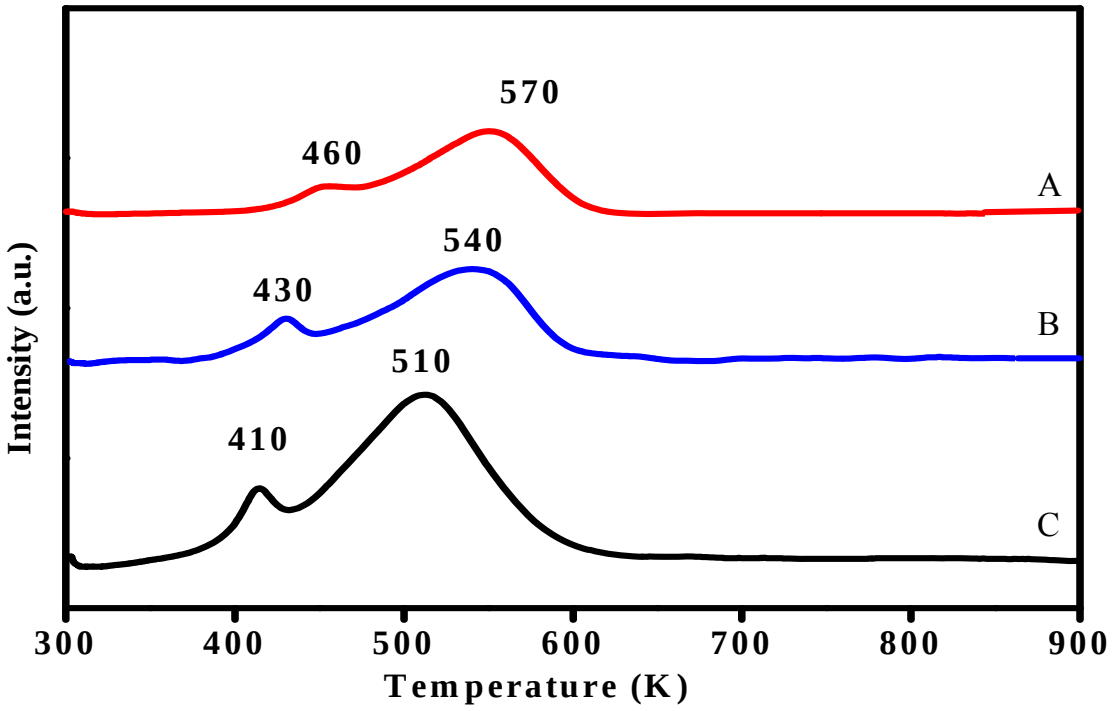

Figure 4.9. TPO of (A) ZC-3C-a, (B) ZC-3C-b and (C) ZC-3C-c samples

Table 4.4. TPR/TPO-H_2/O_2 uptake profiles of Zn doped Co_3O_4 catalysts

Catalysts	Calcination temperature (K)	H_2 (mmol)	O_2 (mmol)
ZC-3C-a	573	229	11.2
ZC-3C-b	573	294	13.8
ZC-3C-c	573	325	15.9
Co-3C-a	573	435	20.6

4.2.1.9. Fourier Transform Extended X-ray Absorption Fine Structure (FT-EXAFS)

FT-EXAFS characterization of all the Co catalysts was carried out in order to know the local environment viz. atomic intensity and bond distance of cobalt atom. Fourier transforms of k-weighted (Co k-space) EXAFS spectra of ZC-3C-c, ZC-6C-c and Co-3C-a samples was studied to understand the effect of Zn doping in spinel Co_3O_4 as shown in Figure 4.10. All the samples showed one peak at 1.52 Å corresponding to the Co-O bond and another peak at ~2.4 Å (split in to 2.45 Å and 3.04 Å) that could be assigned to either Co-Co and/or Co-O bonds, while the third peak at 4.6 Å was assigned to only Co-Co bond [20, 30, 31]. Thus, as a result of zinc doping in spinel Co_3O_4 increase in the inter atomic (Co-O) bond distance from 3.04 Å to 3.15 Å was observed in both ZC-3C-c and ZC-6C-c samples. However, the sample calcined at higher calcination temperature (873 K) showed additional peak at 1.03 Å. The increase in bond distance (from 3.04 to 3.15 Å) might be due to the formation of either ZnO or $ZnCo_2O_4$ spinel phases, while additional peak at 1.03 Å might be due to the formation of ZnO_2 phase in high temperature calcination as discussed in section 4.2.1.2**.** The above observation established that zinc doped Co_3O_4 is structurally different from the pure spinel Co_3O_4.

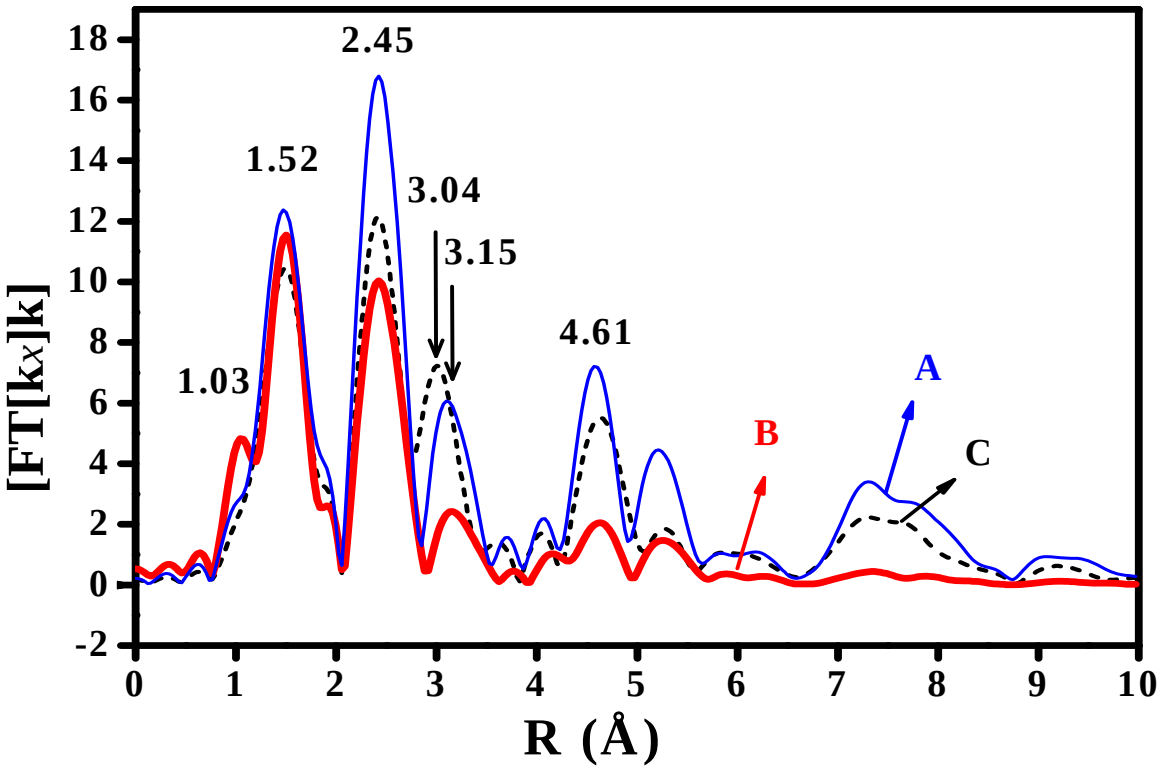

Figure 4.10. FTEXAFS of (A) ZC-3C-c, (B) ZC-6C-c and (C) Co-3C-a (Co_3O_4) samples

4.2.2. Al doped Co_3O_4

4.2.2.1. BET surface area measurement

BET surface areas of Al doped Co_3O_4 spinel catalysts with various Co:Al ratios 1:2 (CA-a), 1:1 (CA-b) and 3:1 (CA-c), calcined at 573 K and 873 K are presented in Table 4.5. The CA-3C-a catalyst showed 201 m^2/g surface area, while CA-3C-b and CA-3C-c catalysts showed surface area values of 167 and 123 m^2/g respectively. Above results indicate decrease in surface area with decrease in aluminum composition from 1:2 to 3:1 mainly due to increase in crystallite/particle size as observed in XRD and HRTEM. The parent Co_3O_4 sample showed surface area of 110 m^2/g, which is lower than that of Al doped Co_3O_4 samples, which indicates that Al doping in Co_3O_4 enhanced the surface area, due to decrease in crystallite/particle size

from 12-38 nm to 10-20 nm (XRD and HRTEM). Increase in calcination temperature from 573 to 873 K caused decrease in the surface area to 44.8, 37.2 and 27.4 m^2/g for CA-6C-a, CA-6C-b and CA-6C-c catalysts respectively. This substantial decrease in surface area by four times was due to the increase in crystallite size as observed in the XRD and HRTEM investigations discussed in the next sections.

Table 4.5. BET surface area of Al doped Co_3O_4 spinel samples

Entry	Catalysts	Co:Al ratio	Calcination temperature (K)	Specific Surface area (m^2/g)
1	CA-3C-a	1:2	573	201.0
2	CA-6C-a	1:2	873	44.8
3	CA-3C-b	1:1	573	167.0
4	CA-6C-b	1:1	873	37.2
5	CA-3C-c	3:1	573	123.0
6	CA-6C-c	3:1	873	27.4
7	Co-3C-a	NA	573	110.0

4.2.2.2. X-ray diffraction (XRD)

XRD patterns of Al doped Co_3O_4 spinel samples (with Co:Al composition as 1:2, 1:1 and 3:1) calcined at 573 and 873 K are presented in Figure 4.11. All the samples exhibited diffraction peaks at 2θ =19.08° (111), 31.28° (220), 36.97° (311), 44.97° (400), 59.45° (500) and 65.42° (422), which were attributed to the spinel phase of $CoAl_2O_4$. The calculated lattice parameter for all the samples was found to be 8.101 Å corresponding to the cubic type which is in good agreement with the reported value 8.106 Å for $CoAl_2O_4$ spinel (JCPDS =82-2252). With change in Co:Al ratio from 1:2 to 3:1, slight decrease in broadening and increase in intensity of peaks at 2θ =19.08° (111), 31.28° (220), 36.97° (311), 44.97° (400), 59.45° (500) and 65.42° (422), were

observed. This might be due to either decrease in Al composition or excess of aluminium present in amorphous phase. Increase in calcination temperature (from 573 to 873 K) led to gradual increase in intensity of peaks and the slight decrease in the width of peaks at 2θ =19.08° (111), 31.28° (220), 36.97° (311), 44.97° (400), 59.45° (500) and 65.42° (422) were observed. However, increase in cobalt loadings by three times might cause gradually increase in peak intensity of $CoAl_2O_4$ phase observed in CA-3C-c sample. In spite of increase in aluminium loading (from 3:1 to 1:2), samples did not show other phases of alumina as the excess of aluminium remained in the amorphous phase, while in case of zinc doped spinel Co_3O_4, different phases discussed were observed as in section 4.2.1.2. Crystallite sizes of CA-3C-a, CA-6C-a, CA-3C-b, CA-6C-b, CA-3C-c and CA-6C-c calculated using the Scherrer equation were found to be in the range of ~5-10, 15-35, 5-11, 30-35, 5-17 and 44-58 nm respectively. Thus, increase in crystallite size for samples CA-6C-a, CA-6C-b and CA-6C-c was mainly due to recrystallization of samples at 873 K [12]. The crystallite sizes of these samples matched very well with the HRTEM results.

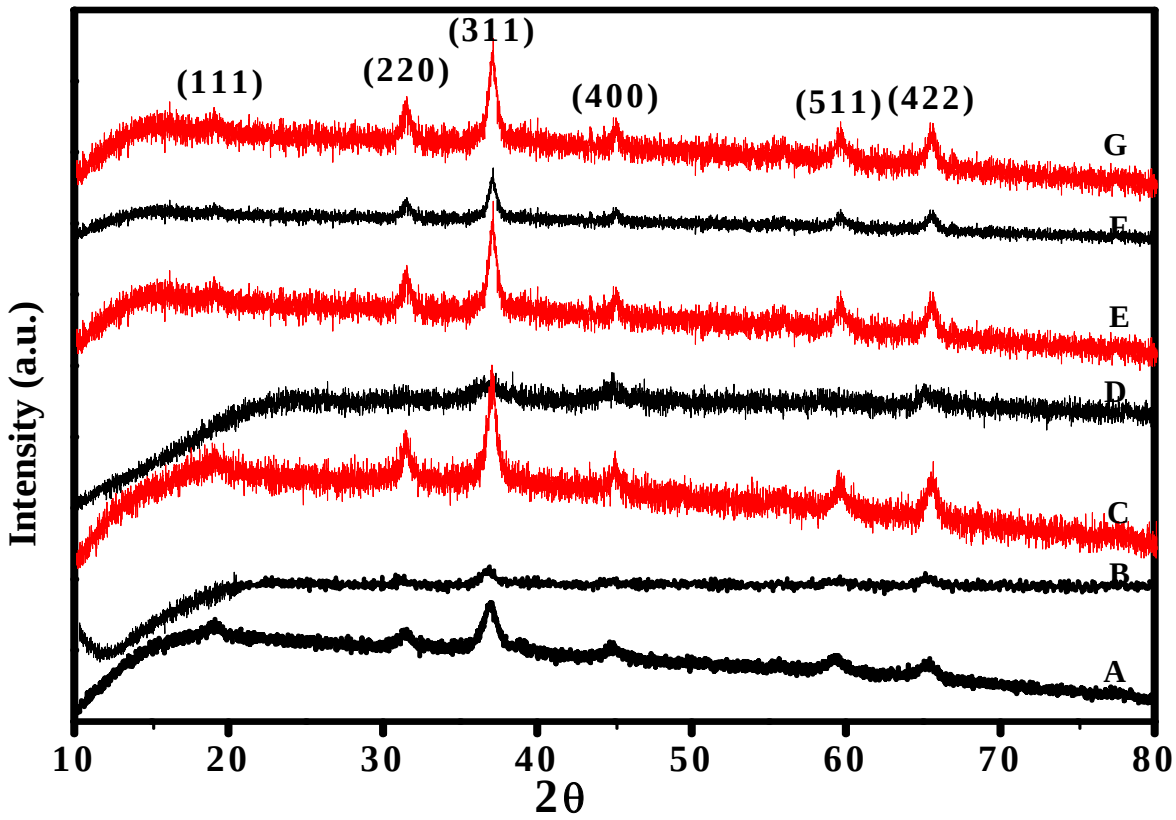

Figure 4.11. XRD of (A) Co-3C-a, (B) CA-3C-a, (C) CA-6C-a, (D) CA-3C-b, (E) CA-6C-b, (F) CA-3C-c, and (G) CA-6C-c samples

4.2.2.3. X-ray photoelectron spectroscopy (XPS)

In order to further establish the formation of $CoAl_2O_4$ spinel, the samples of Al doped Co_3O_4 having Co:Al compositions as 1:2, 1:1 and 3:1 (calcined at 573 K) were charaterized by XPS. The Co 2p and Al 2p spectra of these samples are shown in Figures 4.12a, 4.12b and 4.13. The Co 2p spectra showed two peaks with binding energy values of 779.4 and 795.2 eV, corresponding to Co $2p_{3/2}$ and Co $2p_{1/2}$ core level peaks respectively [14, 15]. The Co $2p_{3/2}$ spectrum after deconvoluation was split into two peaks at binding energies of 778.9 and 780.9 eV. The first peak corresponds to Co^{3+} and the second peak corresponds to Co^{2+} and has binding energy similar to that of $CoAl_2O_4$ [32]. Co $2p_{3/2}$ - Co $2p_{1/2}$ peak separation value obtained was

15.8 eV [33]. Two satellite peaks, one strong and another weak were observed with binding energies of 801.5 and 786.8 eV respectevely, which was characteristic feature of the tetrahedal cobalt (Co^{2+}) in presence of aluminium environment [33]. The Al spectra of the all the samples showed a peak at binding energies of 73.6 eV, which was assigned to Al $2p_{3/2}$, confirming the presence of Al in the octahedral (Al^{+3}) state [34]. Thus, XPS results in combination with XRD data confirmed the formation of $CoAl_2O_4$ along with Co_3O_4 spinel.

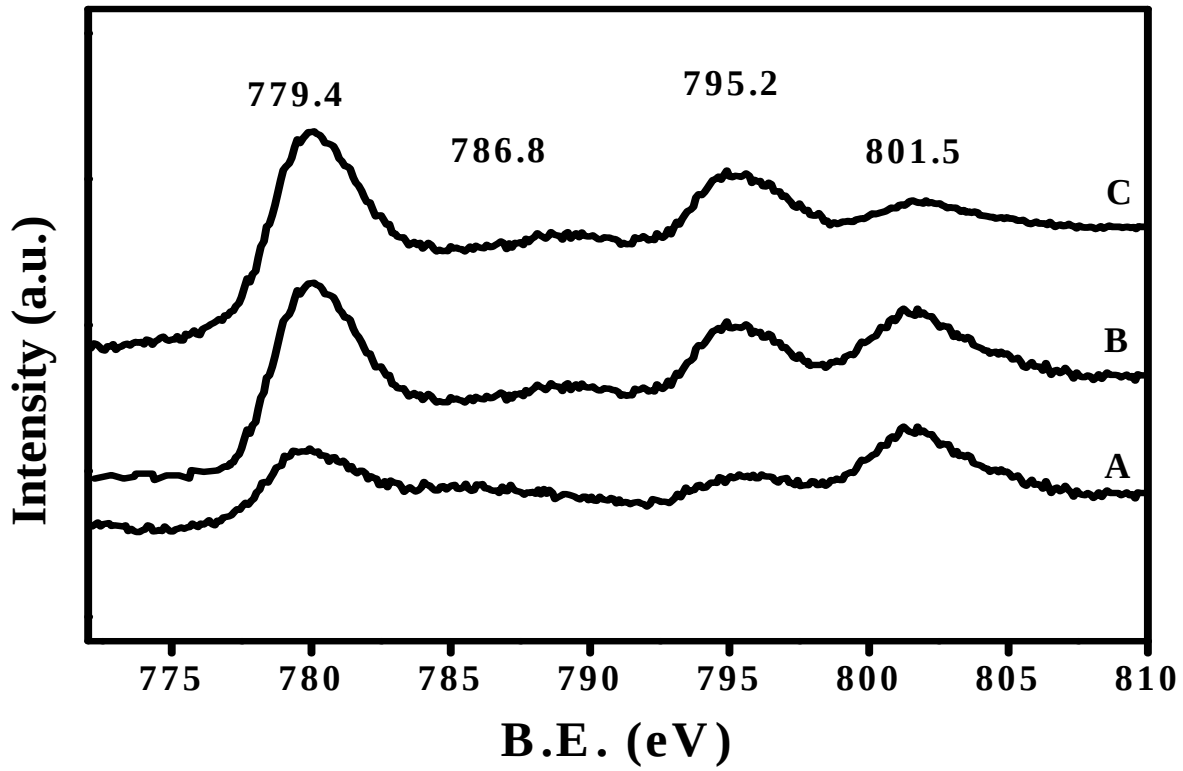

Figure 4.12a. XPS Co 2p spectra of (A) CA-3C-a, (B) CA-3C-b and (C) CA-3C-c samples

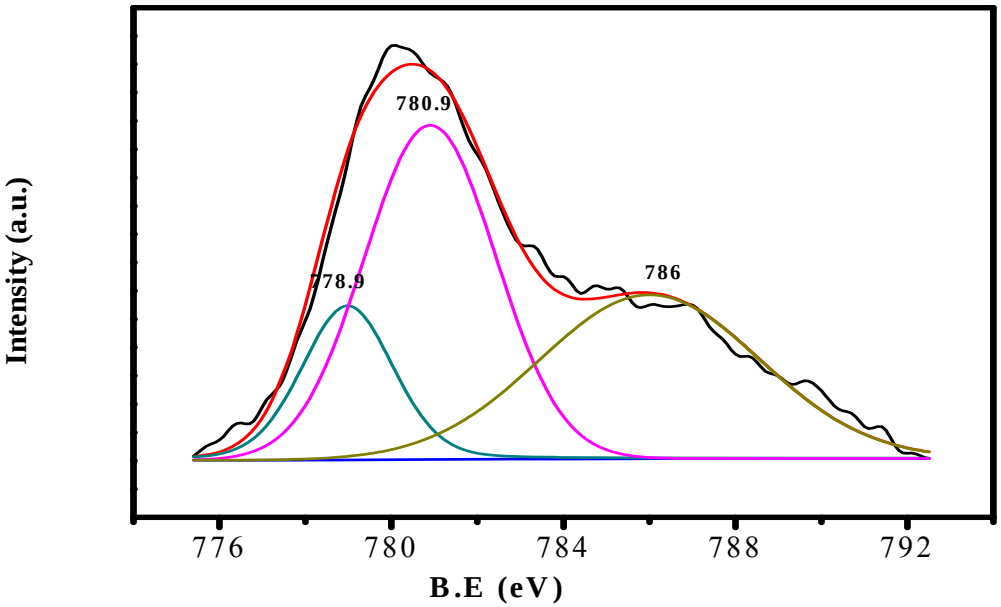

Figure 4.12b. Deconvolution spectra of Co $2p_{3/2}$

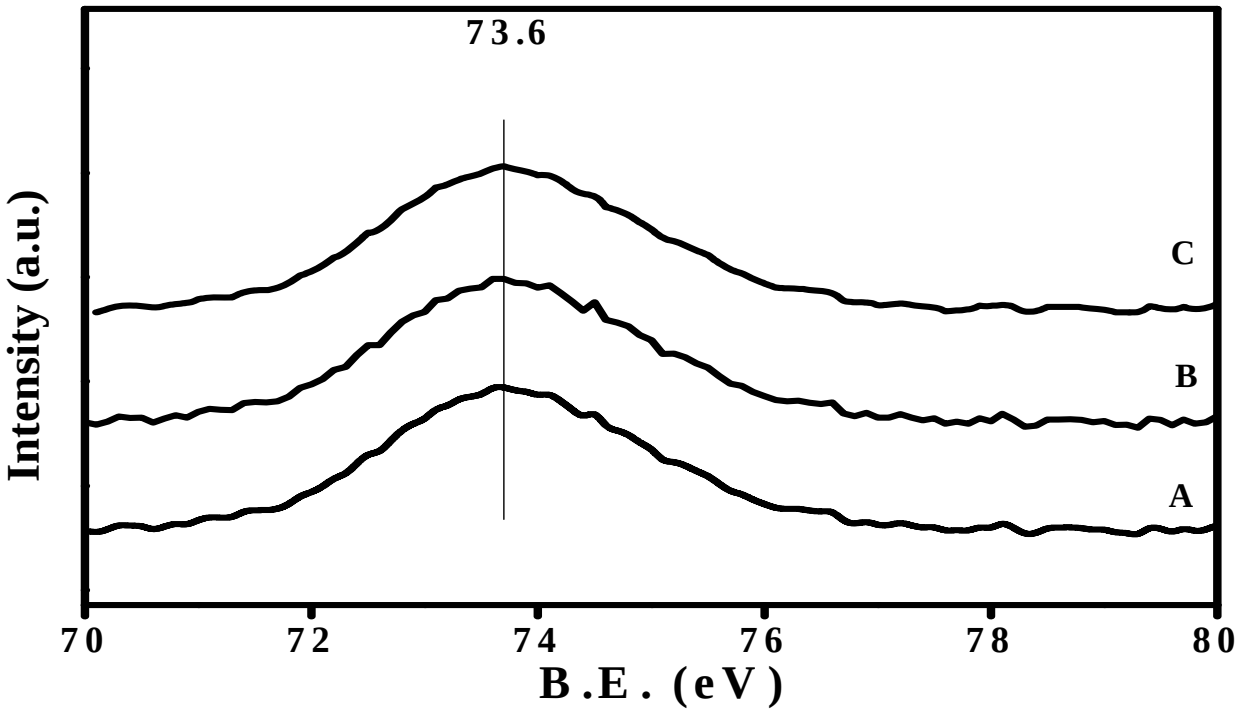

Figure 4.13. XPS Al 2p spectra of (A) CA-3C-a, (B) CA-3C-b and (C) CA-3C-c samples

4.2.2.4. Thermo gravimetric analysis (TGA)

TG-DTA profile of the as-prepared CA-c (Co:Al ratio 3:1) sample is shown in Figure 4.14. The CA-c sample showed weight loss in three steps which is different than the TG profile of Co-a and ZC-a samples (prepared at pH 7-8) where both showed a weight loss in two steps (Sections 3.3.1.5 and 4.2.1.4). The first continuous 15% weight loss from room temperature to 458 K was observed due to loss of physically adsorbed water molecules [19]. In the second step, 13% weight loss at 523 K was observed due to the decomposition of carbonate anions [18], while in the third step, 8.7% weight loss at 643 K was due to dehydroxylation (Table 4.6) [7, 20]. The major weight loss occurred below 643 K, which was much higher than that observed for the Co-a sample (48.4% at 553 K) (Section 3.3.1.5), might be due to aluminium doping in Co_3O_4 causing aggregation of particles as observed in HRTEM (Section 4.2.2.6).

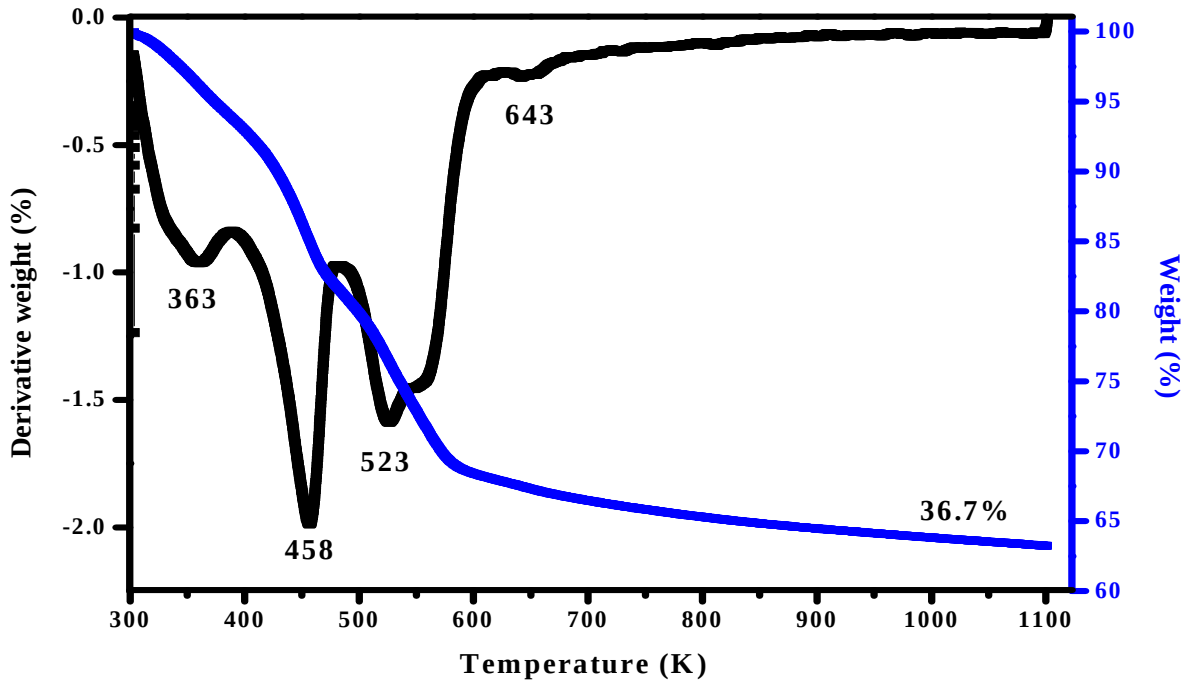

Figure 4.14. TG-DTA of CA-3C-c sample

Table 4.6. Summary of thermogravimetric analysis

Sample	TG		DTA	Remarks
	Temperature range (K)	Weight loss (w/w. %)	Peak maximum (K)	
CA-c	300-490	15.0	458	Loss of physically adsorbed water molecules.
	490-620	13.0	523	Decomposition of carbonate anions and dehydroxylation.
	630-1100	8.7	643	Dehydroxylation of surface hydroxyl group.

4.2.2.5. Fourier-Transform infrared spectroscopy (FT-IR)

FT-IR spectra of CA-3C-a, CA-3C-b, CA-3C-c and CA-c samples are shown in Figure 4.15. The FT-IR spectra of CA-c sample showed three bands at 569, 668 and 438 cm^{-1} and a distinct band at 1370 cm^{-1} which could be assigned to stretching vibrations of metal-oxygen bonds and metal-carbonate (CO_3^{2-}) bonds respectively (Figure 4.15, A) [21, 22]. After calcination at 573 K, CA-a, CA-b and CA-c samples showed an increase in intensity of the peaks at 564 and 669 cm^{-1} and a diminishing intensity of the peak at 1370 cm^{-1}, indicating the decomposition of aluminium cobalt hydroxy carbonate in to $CoAl_2O_4$ spinel which was also confirmed by XRD [7, 25, 35]. The peak at 438 cm^{-1} was assigned to Al^{3+} (Al_2O_3) [36], while the second peak 569 cm^{-1} corresponds to Co^{3+} in an octahedral position while the other peak at 668 cm^{-1} corresponds to the Co^{2+} in a tetrahedral position confirming the formation of $CoAl_2O_4$ spinel in CA-3C-a, CA-3C-b and CA-3C-c samples [37-39]. However, with decrease in aluminium composition from 1:2 to 3:1 led to gradual increase in intensity of the peaks at 668 and 569 cm^{-1}. CA-3C-a and CA-3C-b samples calcined at 573 K showed the presence of some sort of carbonate (1370 cm^{-1}) even after

calcination time of 5 h, while CA-3C-c sample did not show any carbonate species formation. The broad peaks at 3478 cm^{-1} and 1637 cm^{-1} were attributed to metal hydroxyl stretching vibrations observed in all the samples [26, 27, 40].

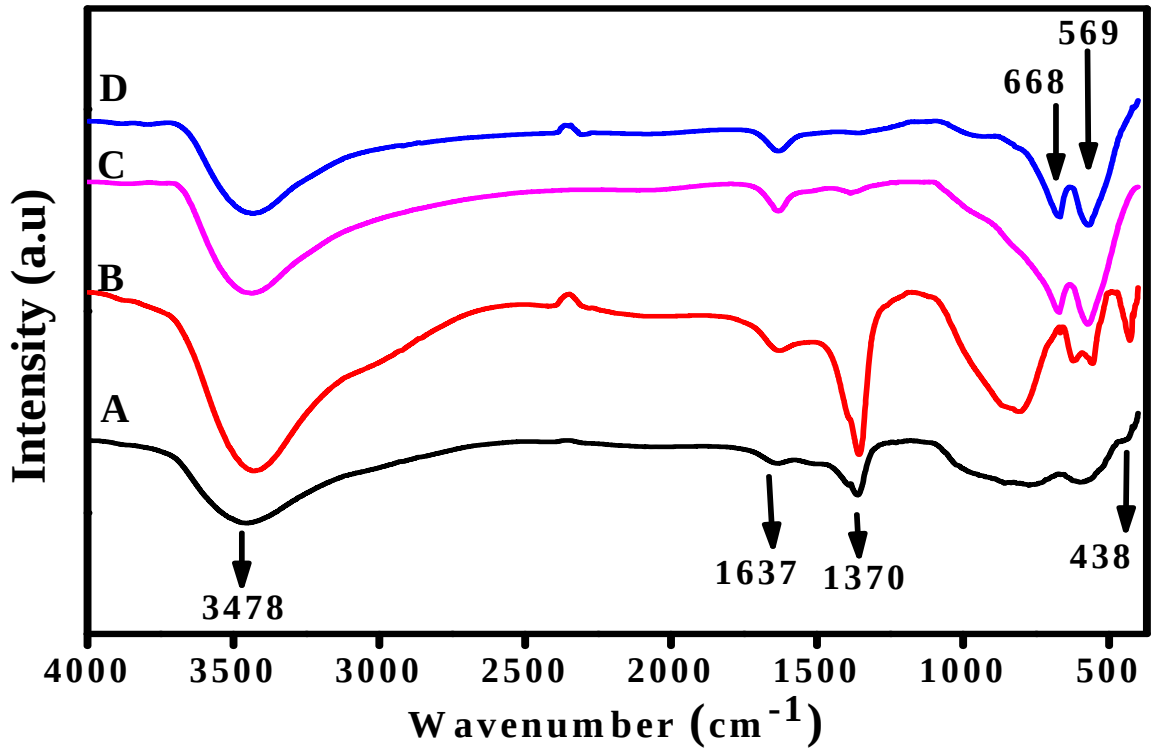

Figure 4.15. FTIR of (A) CA-c, (B) CA-3C-a, (C) CA-3C-b and (D) CA-3C-c samples

4.2.2.6. High resolution transmission electron microscopy

The morphologies of the aluminium doped Co_3O_4 catalysts with different compositions (1:2, 1:1 and 3:1) calcined at temperature 573 and 873 K were studied by HR-TEM (Figure 4.16). The CA-3C-a sample showed the aggregation of both rod and elongated spherical shaped particles (5 nm) to form uniform laterally aggregated porous structure with average particle size in the range of 100-110 nm. With change in aluminium to cobalt ratio from 1:2 to 1:1, aggregation of particles occurred to form particles with an average size in the range of 90-99 nm, while further

change in ratio to 3:1 caused slight restriction of the agglomeration of these particles to give the average particle size range of 60-75 nm. Lattice fringes of these samples were not clearly visible, due to the amorphous nature of these samples, which was also confirmed by XRD results. However with increase in calcination temperature from 573 to 873 K, increase in size of both rod shape and elongated spherical particles was observed in the range of 25-27, 30-35 and 50-60 nm was observed for CA-6C-a, CA-6C-b and CA-6C-c samples respectively, which was in good agreement with the XRD results. The characteristic planes obtained from the SAED image (Figure 4.16, A-F) were (311), (400), (422) and (511), matched with the XRD data confirming the $CoAl_2O_4$ in all the samples.

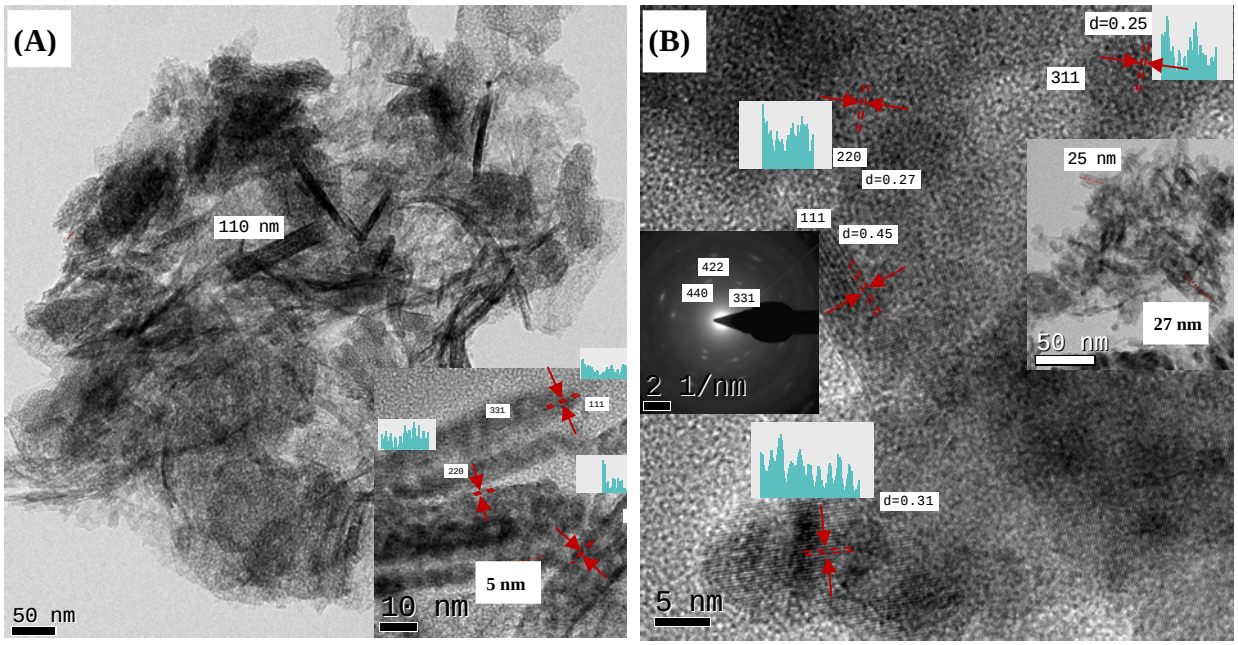

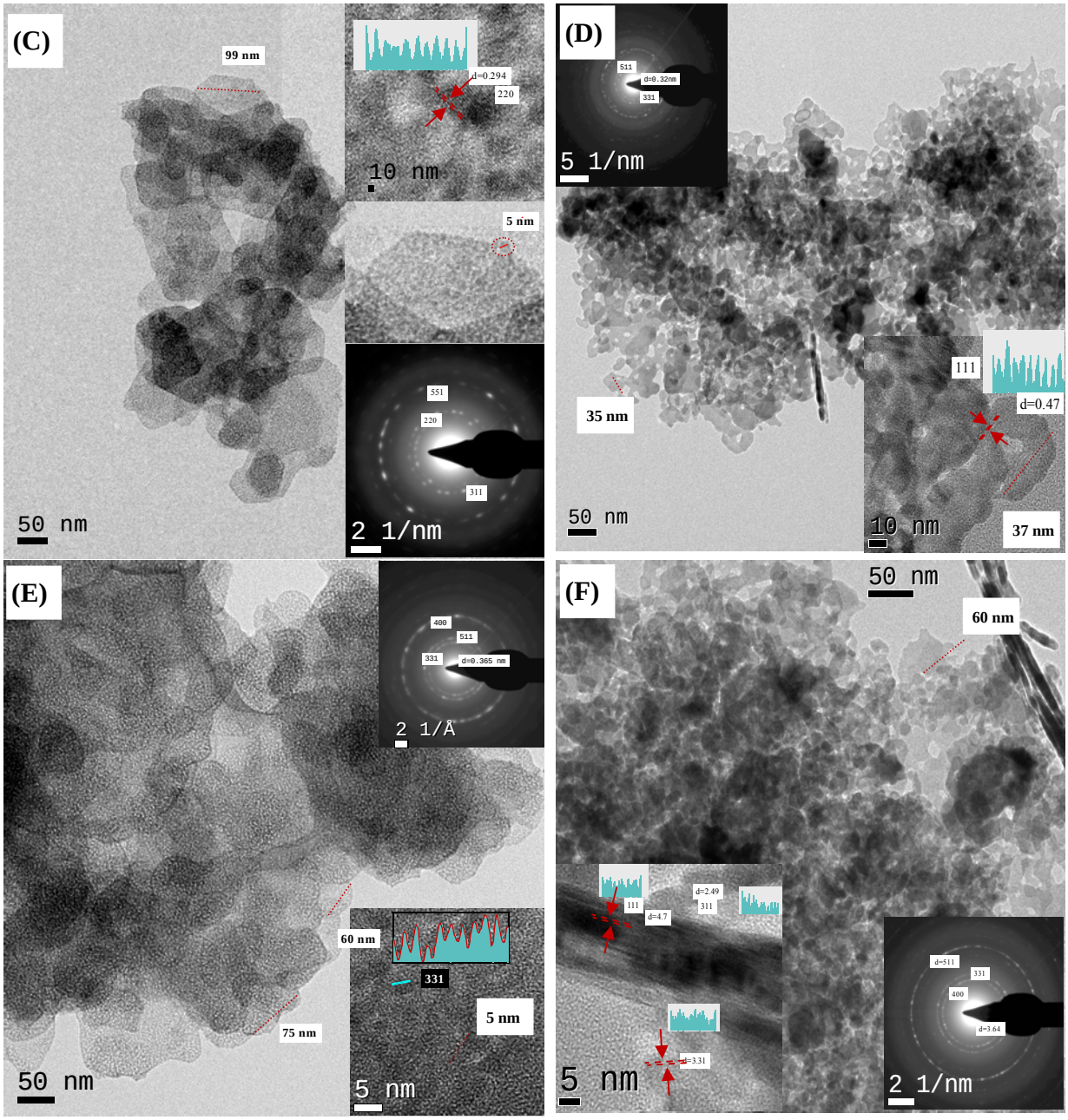

Figure 4.16. HRTEM of (A) CA-3C-a, (B) CA-6C-a, (C) CA-3C-b, (D) CA-6C-b, (E) CA-3C-c and (F) CA-6C-c samples

4.2.2.7. Energy dispersive X-ray (EDX)

The elemental composition of the CA-a, CA-b and CA-c samples were studied by EDX (Figure 4.17, A-C). These samples showed the presence of cobalt, aluminium, oxygen, nitrogen and absence of any residual potassium (used in to preparation protocol). From EDX studies, cobalt and aluminium compositions were found to be ~1:2, 1:1 and 3:1 ratio for CA-a, CA-b and CA-c samples respectively (Table 4.7). Thus these elemental compositions are in accordance with the nominal compositions (1:2, 1:1 and 3:1) used for the preparation.

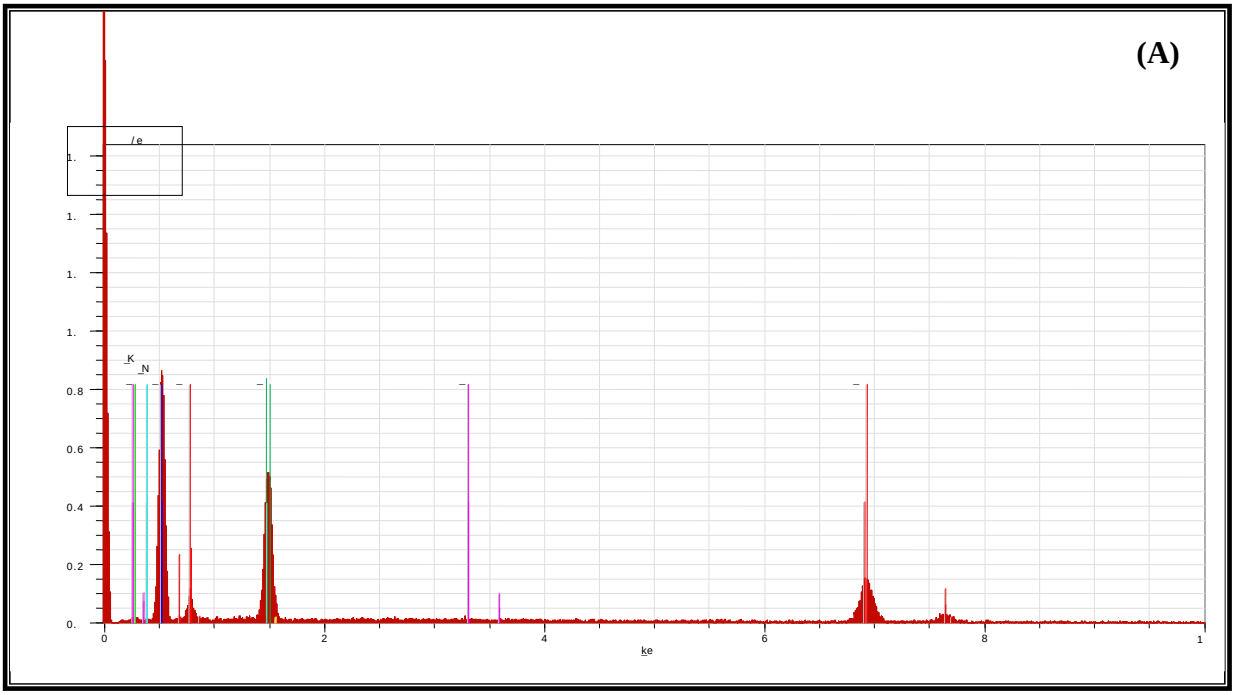

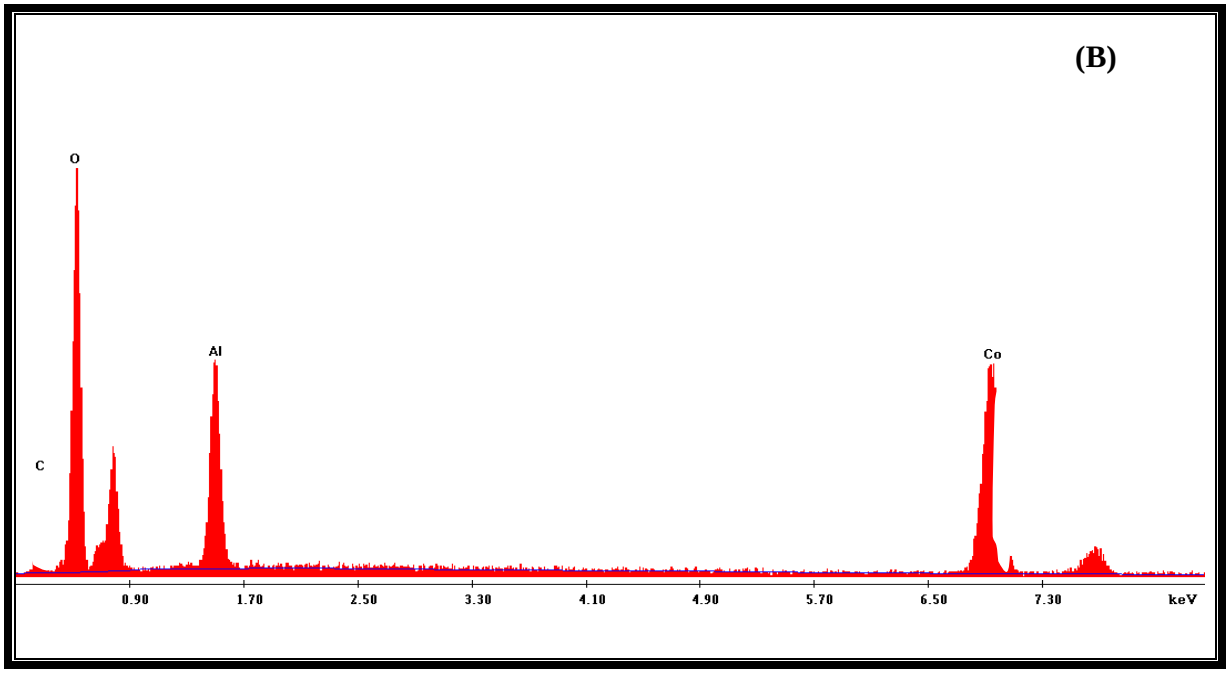

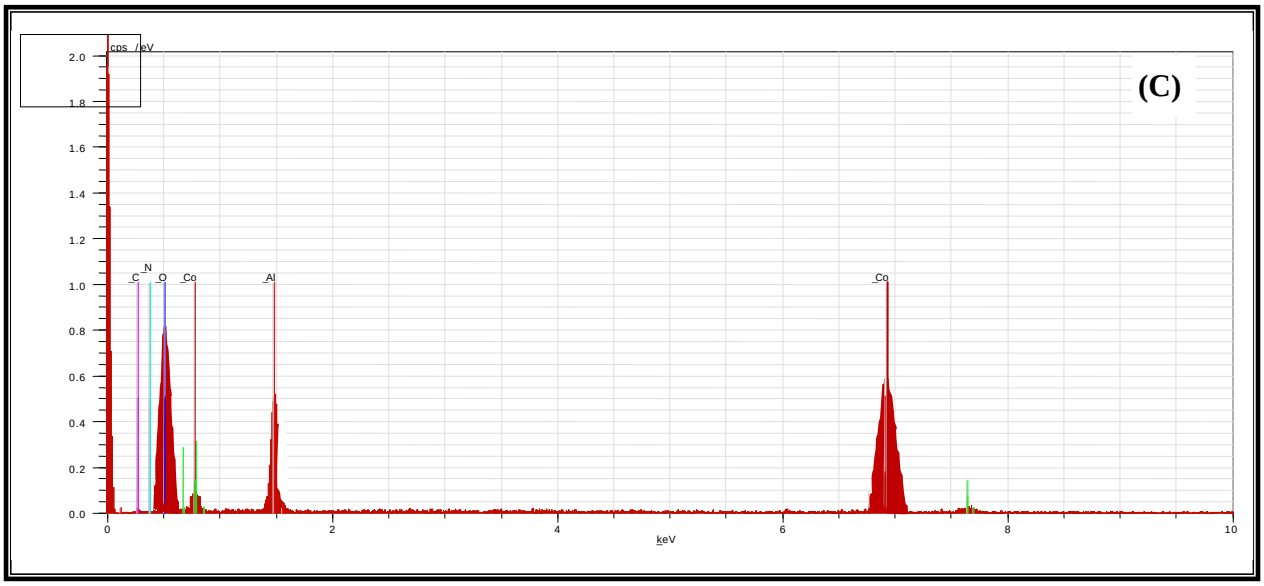

Figure 4.17. EDX of (A) CA-a, (B) CA-b and (C) Co-c samples

Table 4.7. EDX results showing atomic percentage in the aluminium doped Co_3O_4 catalysts

Entry	Samples	Co:Al ratio	Elemental compositions (Atom %)				
			Co	Al	O	K	N
1	CA-a	1:2	17.8	35.5	43.2	<0.1	<0.1
2	CA-b	1:1	28.2	23.9	47.7	<0.1	<0.1
3	CA-c	3:1	39.1	11.0	49.4	<0.1	0.4

4.2.2.8. Fourier-Transform Extended X-ray absorption for fine structure (FT-EXAFS)

FT-EXAFS of CA-3C-c and CA-6C-c samples was studied to understand the effect of Al doping on the electronic environment, bond distance, co-ordination number of Co in various samples and the spectra are shown in Figure 4.18. All the samples showed the first peak at 1.52 Å corresponding to Co-O bond and a second peak at ~2.4 Å (split in to 2.45 Å and 3.04 Å) assigned to both Co-Co and Co-O bonds. While, a third peak at 4.6 Å was assigned to Co-Co bond [20, 30, 31]. With aluminium doping in spinel Co_3O_4 caused a decrease in inter atomic (Co-O) bond distance from 3.04 Å to 3.02 and 2.99 Å observed for CA-3C-c and CA-6C-c samples respectively [41]. However, the sample calcined at higher temperature (873 K) showed an additional peak at 1.03 Å. This might be due to the interaction of aluminium with cobalt in spinel, decreasing metal to metal bond distance. The above observation and XRD results support the formation of $CoAl_2O_4$ spinel.

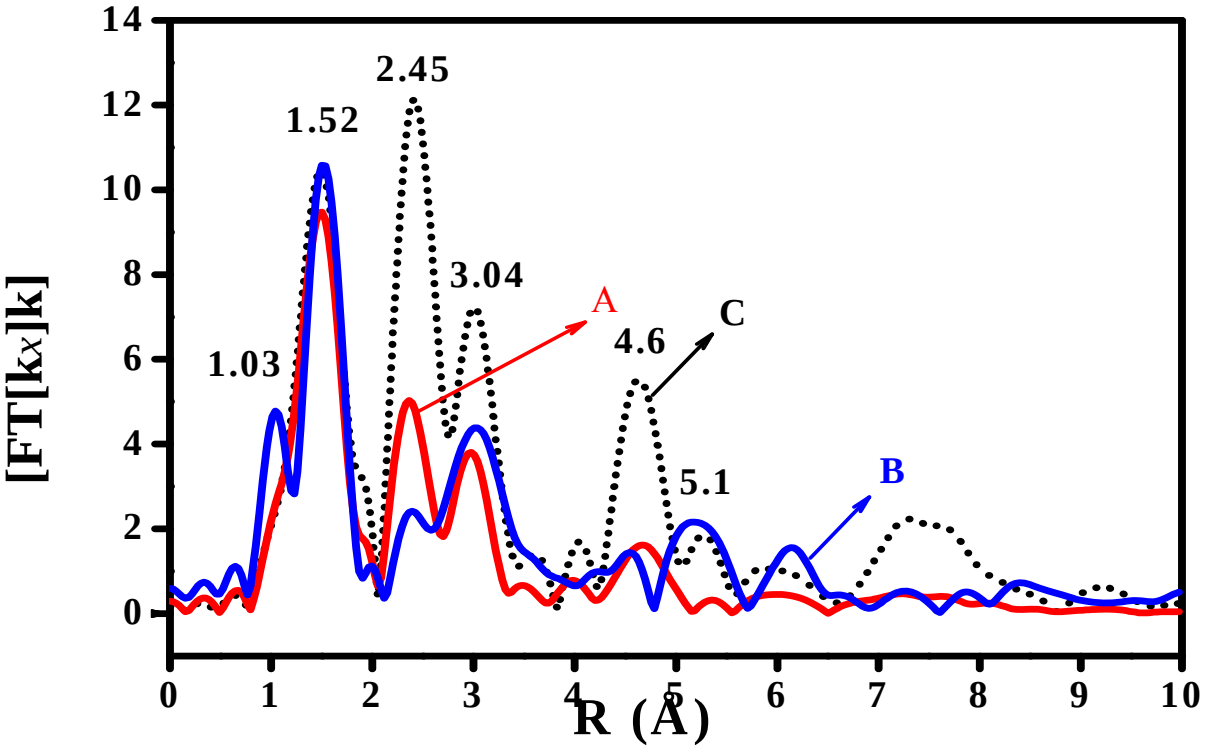

Figure 4.18. FT-EXAFS of (A) CA-3C-a, (B) CA-6C-a and (C) Co-3C-a (Co_3O_4) samples

4.2.2.9. Temperature programmed reduction / Temperature programmed oxidation (TPR/TPO)

The reducibility of the CA-3C-a, CA-3C-b and CA-3C-c catalysts was studied by H_2-TPR technique (Figure 4.19). All the samples showed a single less intense and broad reduction peak in the range of 350-640 K. This broad peak can be split into two peaks, first peak observed in the range of 350-520 K while second in the range of 520-640 K attributable to sequential reduction of Co^{3+} to Co^{2+} and Co^{2+} to Co^{o} respectively [23, 25, 28]. The single broad and less intense reduction peak observed in case of all Al doped Co_3O_4 might be due to interaction of cobalt with the aluminium. Jansson *et al.* stated similar type of observation [42]. With change in aluminium and cobalt composition from 1:2 to 3:1 showed 224, 297 and 341 mmol of H_2 up take which was

found to be ~65%, 50% and 25% lower than the pure Co_3O_4 (Co-3C-a) spinel catalyst (Table 4.8). These results conclude that Al doping does not improve the reducibility of $CoAl_2O_4$ spinel and it is purely depend on cobalt composition.

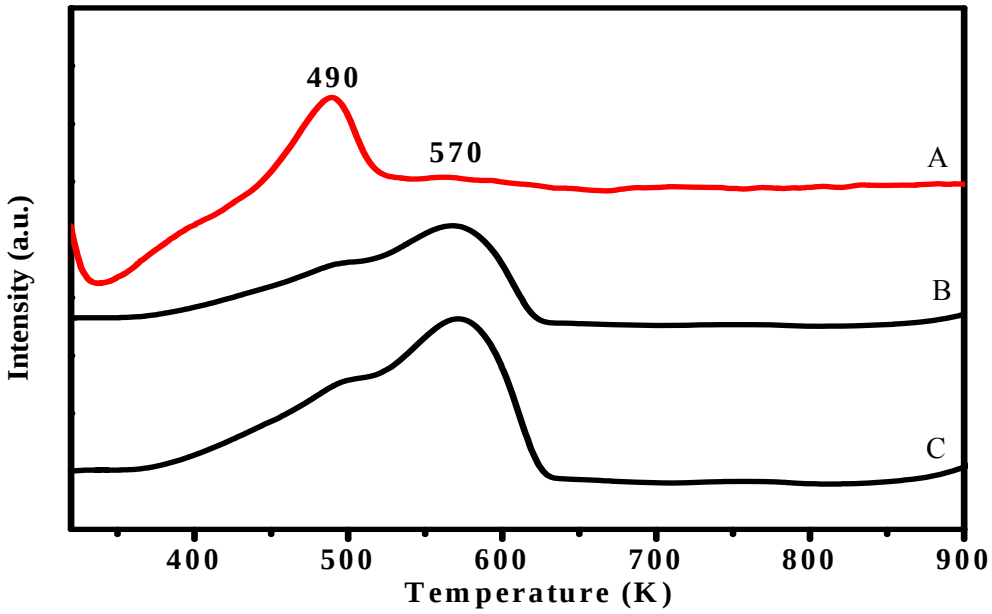

Figure 4.19. TPR of (A) CA-3C-a, (B) CA-3C-b and (C) CA-3C-c samples

The oxidizability of pre-reduced CA-3C-a, CA-3C-b and CA-3C-c catalysts was studied by TPO as shown in Figure 4.20. All the samples showed two broad oxidation peaks. The first peak observed in the range of 350-520 K while second in the range of 520-650 K attributed to the sequential oxidation of Co^o to Co^{2+} and Co^{2+} to Co^{3+}respectively [24, 26]. The increase in intensity of reduction peak observed with increase in cobalt loading form 1:2 to 3:1. The CA-3C-a, CA-3C-b and CA-3C-c samples showed 11.1, 14.2 and 16.7 mmol of O_2 up take which was found to be ~47.2%, 31.0% and 18.9% lesser than Co-3C-a (pure Co_3O_4) sample.

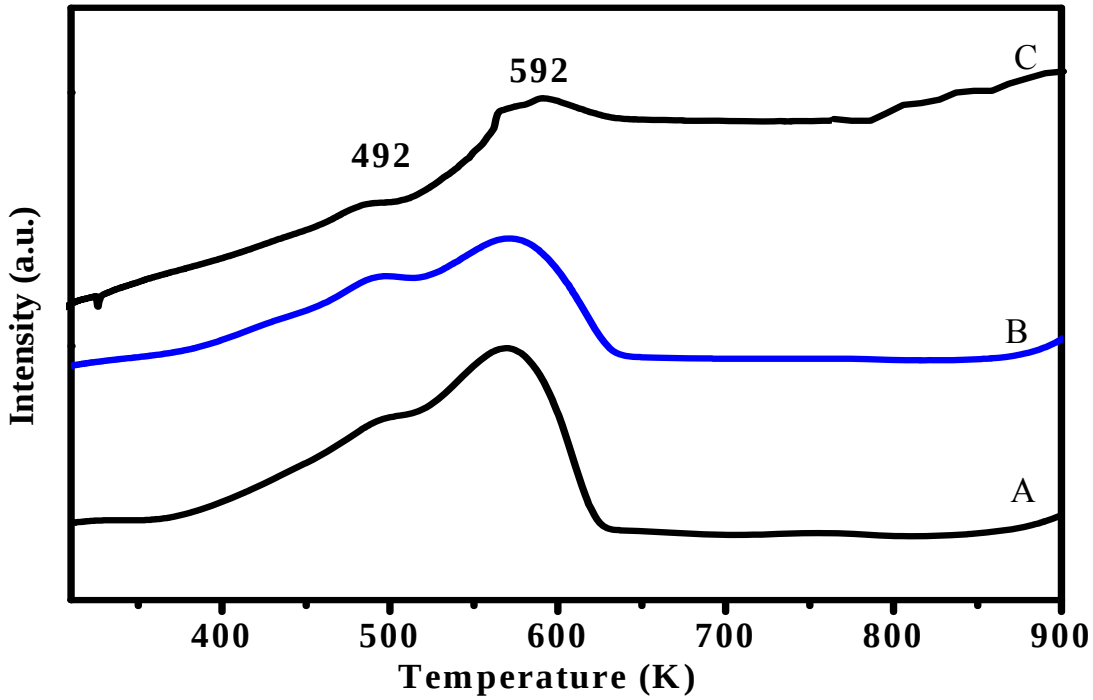

Figure 4.20. TPO of (A) CA-3C-a, (B) CA-3C-b and (C) CA-3C-c samples

Table 4.8. TPR/TPO-H_2/O_2 uptake profiles of Al doped Co_3O_4 catalysts

Catalysts	Co:Al ratio	Calcination temperature (K)	H_2 (mmol)	O_2 (mmol)
CA-3C-a	1:2	573	224	11.1
CA-3C-b	1:1	573	297	14.2
CA-3C-c	3:1	573	341	16.7
Co-3C-a	NA	573	435	20.6

4.2.3. Activity measurement

4.2.3.1. Catalyst screening

A comparative study of activity results of both the Zn and Al doped spinel Co_3O_4 samples calcined at temperatures 573 and 873 K are presented in Table 4.9. Among the Zn and Al doped Co_3O_4 catalysts, ZC-3C-c and CA-3C-c samples showed the highest conversion of 24% and 26% respectively, with complete selectivity to veratryl aldehyde (Table 4.9, Entries 5 and 11). In Zn:Co catalysts, with change in Zn:Co composition from 1:1 to 1:3 catalytic activity increased by 1.5 times mainly due to increase in cobalt composition from 50% to 75%, which was in accordance with increase in redox ability by ~45% as confirmed by TPR and TPO studies. While, in case of Al doped Co_3O_4 spinel catalysts with change in Co:Al composition from 1:2 to 3:1, catalytic activity increased by more than two times mainly due to decrease in cobalt composition from ~33% to 75%, although the redox ability increased by 50% as confirmed by TPR and TPO analysis. CA-3C-c having the higher surface area of 123 m^2/g showed lower catalytic activity of 26% conversion than that of Co-3C-a catalyst with a lower surface area of 110 m^2/g giving 38% conversion which indiactes that the activity mainly depends on the redox ability of the catalyst. Interestingly, for equal compositions of both Zn and Al with Co (1:1) equal catalytic activities with conversions of 16% and 15.5% were observed for ZC-3C-b and CA-3C-b samples respectively. While, calcination at higher temperature of 873 K caused decrease in conversion from 50 to 30%, due to larger crystallite size (from 10-20 nm to 40-65 and from 5-10 to 15-35) and lowering in redox ability of these samples as evidenced by XRD, HRTEM, TPR and TPO examinations (Table 4.9) [13, 43]. The stability of these catalysts increased with increase in cobalt composition and calcination temperature as confirmed by the leaching test and ICP-OES analysis (Table 4.9). Above observations estabilished that doping of

Zn and Al in spinel Co_3O_4 was not found to significantly infulence the catalytic activity which was dependant upon the dynamic equilibirum between Co^{2+} and Co^{3+} surface species.

Table 4.9. Catalytic activity of Zn and Al doped Co_3O_4 catalysts for liquid phase oxidation of veratryl alcohol to veratryl aldehyde

Entry	Catalysts	Ratio	Surface area, (m^2/g)	Conversion, (%)	Selectivity, (%)	Leaching, (ppm)	
					Veratryl Aldehyde	Cobalt	Zinc/Aluminium
1	ZC-3C-a	1:1	75.0	16.0	100	1.78	**5.85**
2	ZC-6C-a	1:1	12.5	4.8	100	0.54	**ND**
3	ZC-3C-b	1:2	81.0	21.0	100	1.55	**3.54**
4	ZC-6C-b	1:2	19.2	8.0	100	0.68	**ND**
5	**ZC-3C-c**	**1:3**	**86.0**	**24.0**	**100**	**1.29**	**1.18**
6	ZC-6C-c	1:3	31.8	12.4	100	0.71	**ND**
7	CA-3C-a	1:2	201.0	12.0	100	4.27	**8.12**
8	CA-6C-a	1:2	112.0	5.0	100	1.52	**2.14**
9	CA-3C-b	1:1	167.0	15.5	100	8.54	**15.77**
10	CA-6C-b	1:1	85.8	8.4	100	1.14	**1.57**
11	**CA-3C-c**	**3:1**	**123.0**	**26.0**	**100**	**2.19**	**5.28**
12	CA-6C-c	3:1	69.5	13.2	100	0.95	**ND**
13	Co-3C-a	-	110.0	38.0	100	0.11	-

Reaction conditions: temperature, 413 K; oxygen pressure, 0.689 MPa; veratryl alcohol, 0.5 g (3 mmol); catalyst, 0.1 g ; water, 70 mL; total volume, 70.6 mL; agitation speed, 900 rpm; reaction time, 7 h.

4.3. CONCLUSIONS

- The mixed oxide spinel of Co_3O_4 were prepared by simple co-precipitation digestion method and doping divalent Zn (Zn^{2+}) and trivalent Al (Al^{3+}) species respectively.
- In Zn doped Co_3O_4 catalysts, compositions of Zn:Co were ~1:1, 1:2 and 1:3 as confirmed by EDX analysis were in accordance with those of nominal values. Among these, ZC-3C-c (1:3) showed the highest 24% conversion for veratryl alcohol and complete selectivity to veratryl aldehyde.
- Similarly, in case of the Al doped Co_3O_4 various compositions of Co:Al prepared were ~1:1, 1:2, 1:3 and were also established by EDX analysis. Among these, ZC-3C-c (1:3) sample showed the highest 26% conversion for veratryl alcohol and complete selectivity to veratryl aldehyde.
- Change in Zn:Co composition from 1:1 to 1:3 caused mainly increase in distribution of the surface active Co^{2+} & Co^{3+} species which resulted in the increase in redox ability as confirmed by FTIR, XPS, TPR and TPO studies. This enhancement in the redox ability was responsible for the increase in the catalytic activity up to the 1.5 times (from 16% to 24%) for liquid phase oxidation of veratryl alcohol to veratryl aldehyde.
- The lower redox ability and catalytic activity of all the Zn and Al doped Co_3O_4 samples than that of the pure spinel Co_3O_4 (38% conversion) samples, indicate that Zn as well as Al did not form any redox couples between Co and only the redox couple between Co^{3+} and Co^{2+} is responsible for the liquid phase oxidation of veratryl alcohol.

4.4. REFERENCES

1. W. Luo, X. L. Hu, Y. M. Sun, Y. H. Huang, *J. Mater. Chem.* 22 (2012) 8916.
2. Y. Z. Wang, Y. X. Zhao, C. G. Gao, D. S. Liu, *Catal. Lett.* 116 (2007) 136.
3. E. V. Steen, H. Schlz, *Appl. Catal. A Gen.* 186 (1999) 309.
4. Y. Yu, F. Yung, *J. Catal.* 33 (1974) 108.
5. S. Vijayanand, P. A. Joy, H. S. Potdar, D. Patil, P. Patil, *Sensors and Actuators B: Chemical* 152 (2011) 121.
6. N. W. Zhang, C. J. Huang, X. Q. Zhu, J. D. Xu, W. Z. Weng, H. L. Wan, *Chemistry – An Asian Journal* 7 (2012) 1895.
7. D. Patil, P. Patil, V. Subramanian, P. A. Joy, H. S. Potdar, *Talanta* 81 (2010) 37.
8. V. S. Kshirsagar, S. Vijayanand, H. S. Potdar, P. A. Joy, K. R. Patil, C. V. Rode, *Chem. Lett.* 37 (2008) 310.
9. V. S. Kshirsagar, J. M. Nadgeri, P. R. Tayade, C. V. Rode, *Appl. Catal. A: Gen.* 339 (2008) 28.
10. G. Xanthopoulou, G. Vekinis, *Appl. Catal. A: Gen.* (2000) 227.
11. R. T. Kumar, N. C. S. Selvam, T. Adinaveen, L. J. Kennedy, J. J. Vijaya, *Reac. Kinet. Mech. Cat.*106 (2012) 379.
12. J. Yang, H. Liu, W. N. Martens, R. L. Frost, *J. Phys. Chem. C*. 114 (2009) 111.
13. V. R. Mate, M. Shirai, C. V. Rode, *Catal. Commun.* 33 (2013) 66.
14. C. V. Chenck, J. G. Dillard, J. W. Murray, *J. Colloid Interf. Sci*. 95 (1983) 398.
15. M. Oku, Y. Sato, *Appl. Surf. Sci.* 55 (1992) 37.
16. T. J. Chuang, C. R. Brundle, D. W. Rice, Surf. Sci. 59 (1976) 413.
17. I. Grohmann, B. Peplinski, W. Unger, *Surf. Interface Anal.* 19 (1992) 591.

18. X. Wang, J. Xu, B. Zhang, H. Yu, J. Wang, X. Zhang, J. Yu, Q. Li, Adv. Mater. 18 (2006) 2476.

19. J. Yang, H. Liu, W. N. Martens, R. L. Frost, *J. Phys. Chem. C* 114 (2009) 111.

20. A. L. Ankudinov, B. Ravel, J. J. Rehr, S. D. Conradson, *Phys. Rev. B* (1998) 7565.

21. R. Das, S. Ray, *J. Phys. D: Appl. Phys.* 36 (2003) 152.

22. Y. He, B. Yang, G. Cheng, *Catal. Today.* 98 (2004) 595.

23. P. A. Chernavskii, A. Y. Khodakov, G. V. Pankina, J. S. Girardon, E. Quinet, *Appl. Catal. A: Gen.* 306 (2006) 108.

24. L. F. Liotta, G. D. Carlo, G. Pantaleo, A. M. Venezia, G. Deganello, *Appl. Catal. B: Env.* 66 (2006) 217.

25. D. G. Klissurski, E. L. Uzunova, *J. Mater. Sci. Lett.* 9 (1990) 576.

26. J. Jansson, A. Palmqvist, E. Fridell, M. Skoglundh, L. O sterlund, P. Thormahlen, V. Langer, *J. Catal.* 211 (2002) 387.

27. K. Nakamoto, Infrared and Raman Spectroscopy of Inorganic and Coordination Compounds, Wiley: New York, 1978.

28. P. Zucca, F. Sollai, A. Garau, A. Rescigno, E. Sanjust, *J. Mol. Catal. A: Chem.* 306 (2009) 89.

29. D. Klissurski, E. Uzunova, K. Ivanov, *Catal. Lett.* 15 (1992) 385.

30. A. Y. Khodakov, J. Lynch, D. Bazin, B. Rebours, N. Zanier, B. Moisson, P. Chaumette, *J. Catal.* 168 (1997) 16.

31. E. A. Stern, M. Newville, B. Ravel, Y. Yacoby, D. Haskel, *Physica B* (1995) 117.

32. M. Meng, Pei-yan Lin,Yi-lu Fu, Catal. Lett. 48 (1997) 213

33. S. Salem, S. H. Jazayeri, F. Bondioli, A. Allahverdi, M. Shirvani, *Journal of Ceramic Processing Research* 12 (2011) 677.

34. T. A. Patterson, J. C. Carver, D. E. Leyden, D. M. Hercules, *J. Phys. Chem.* 80 (1976) 1700.

35. M. Zayat, D. Levy, *Chem. Mater.* 12 (2000) 2763.

36. A. Vazquez, T. Lopez, R. Gomez, Bokhimi, A. Morales, O. Novaro, *J. Solid State Chem.* 128 (1997) 161.

37. W. Y. Li, L. N. Xu, *J. Che. Adv. Funct. Mater.* 15 (2005) 851.

38. T. Li, S. G. Yang, L. S. Huang, B. X. Gu, Y. W. Du, *Nanotechnology* 15 (2004) 1479.

39. B. B. Lakshmi, C. J. Patrissi, C. R. Martin, *Chem. Mater.* 9 (1997) 2544.

40. K. Nakamoto, Infrared and Raman Spectroscopy of Inorganic and Coordination Compounds, Wiley: New York, 1978.

41. E. Burattini, G. Dalba, A. Kuzmin, A. Lusis, G. Mariotto, *J. Purans, phys. stat. sol. A.* 129 (1992) K61.

42. J. Jansson, *J. Catal.* 194 (2000) 55.

43. I. B. Chorkendorff, J. W. Niemantsverdriet, in Concepts of Modern Catalysis and Kinetics Wiley-VCH 2003.

Chapter 5

Metal aluminosilicate catalysts for oxidation of veratryl alcohol

5.1. INTRODUCTION

Mesoporous aluminosilicates have attracted much attention in recent years because of their prospective applications in heterogeneous catalysis [1-5], separation processes [6], biology [7], pharmaceuticals [8] and environmental monitoring [9]. Industrial applications of pure silica are hardly possible hence, special attention has been devoted for developing meso structured aluminosilicates with high aluminum content to impart stability to them due to tetrahedral aluminum [1]. There are a number of successful approaches to introduce an heteroatom (such as Co, Mn, Fe, Na, Cu, etc.) into mesoporous aluminosilicates materials [10-16]. Some of these involves, (i) direct-synthesis under microwave-hydrothermal conditions [17], (ii) use of strong acidic media [18, 19], (iii) template-assisted method [19, 20], (iv) hydrothermal method [21] and (v) co-precipitation method [22]. However, major challenge is still the synthesis of mesoporous aluminosilicates with the lowest possible Si:Al (1:10) ratio that is with the highest aluminium content. Herein, using an inexpensive and simple *in-situ* co-precipitation method [2, 22-25], metal containing (cobalt, iron, copper and manganese) mesoporous aluminosilicate catalysts is reported.

Recently, we have reported cobalt containing aluminosilicate (cobalt-saponite having Si:Al ratio ~8:1) as solid catalysts for side chain oxidation of phenol derivative such as *p*-cresol [22]. This catalyst (15% cobalt aluminosilicate) when tested for liquid phase oxidation of veratryl alcohol (non-planar bulkier molecule), did not show any activity. The poor activity of this catalyst was due to limited pore size (micropores with pore diameter ~1.17 nm) and restricted mobility of substrate in a two dimensional (2D) layered saponite clay. Considering this limitation, silica alumina (Si:Al) ratio was changed from 10:1 to 1:10 to obtain mesoporous aluminosilicate with a

pore diameter of ~4.04 nm which showed an excellent activity for oxidation of veratryl alcohol to veratryl aldehyde. Veratryl alcohol oxidation is an industrially important reaction as the end product veratryl aldehyde finds wide range commercial applications in food and pharmaceutical industries [26].

Cobalt aluminosilicate catalysts with varied Si:Al ratio and cobalt compositions were prepared by a simple protocol, these were then characterized by various techniques such as N_2 adsorption-desorption isotherm, BET surface area, XRD, XPS, FTIR, TG-DTA, SEM-EDX, TEM, DRUV-vis, TPR, TPO, CV and EXAFS . Among various compositions, 15% cobalt aluminosilicate (Si:Al 1:10) calcined at 573 K (CSA-4) showed an excellent activity and selectivity (86% conversion and 94% selectivity to veratryl aldehyde) for the liquid phase oxidation of veratryl alcohol. Effects of various reaction parameters such as catalyst loading, temperature, oxygen partial pressure on the conversion and selectivity pattern were also investigated. The stability of the catalyst was confirmed by the catalyst recycle experiments.

5.2. RESULTS AND DISCUSSION

5.2.1. N_2 adsorption isotherm

The textural properties of the 15% cobalt aluminosilicate having various silica alumina (Si:Al) ratios as 10:1 (CSA-1), 1:1 (CSA-2), 1:5 (CSA-3), 1:10 (CSA-4) and of the calcined sample of CSA-4 at two different temperatures, 573 K and 773 K (CSA-4-3C, CSA-4-5C respectively) determined by nitrogen adsorption-desorption measurements, are shown in Figure 5.1(a-f). All the samples showed type IV isotherm (Figure 5.1, a-f) [27-30]. The hysteresis feature of the as synthesized cobalt aluminosilicates (CSA-1, CSA-2 and CSA-3) at the relative pressure (p/p_0) of 0.4-0.9 were classified as the type H3 loop, while in case of CSA-4 sample, the hysteresis at the

relative pressure of 0.1-0.9 was classified as the type H4 loop [28, 31]. The type H3 loop, was observed with aggregates of plate-like particles giving rise to narrow slit shaped pores (diameter ~1.17 and ~3.40 nm). Similarly, the type H4 loop is often associated with uniform two parallel plates. In case of CSA-4 sample, the type IV isotherm was indicative of both meso and microporous nature with pore diameters of 4.04 and 2.0 nm (Figures 5.1 and 5.2). The gradual increase in pore diameter from 1.17 to 2.0 nm and 3.40 to 4.04 nm was observed with increase in aluminium content (Si:Al from 10:1 to 1:10) [32].On the other hand, (CSA-4) calcined at temperatures 573 K and 773 K (CSA-4-3C and CSA-4-5C) showed hysteresis at the relative pressures of 0.1-0.9 and 0.4-0.9 respectively and were classified as the H2 type loop (Figure 5.3). The type H2 loop is a mixture of pores with micro and meso dimensions [28]. The calcination at higher temperature (773 K) caused shift in hysteresis feature from relative pressure 0.1-0.9 to 0.4-0.9. This might be due to dehydroxylation resulting in either disruption or collapse of mesopores and resulting into the formation of microporous (pore size from 4.10 to ~2.0) materials. A sharp decrease in surface area from 232.8 to 6.1 m^2/g and increase in pore diameter from 1.17 nm to 4.04 nm was observed on changing the composition from 10:1 to 1:10 (Table 5.1) (Figure 5.2). Similar results was reported in the literature for Si-MMS, Si-MCM-41, Al-MCM and Al-MMS materials [33]. The significant decrease in surface area was due to increase in aluminium composition which caused hydrophilicity (weight loss increased from 26.1% to 77.5%) as observed in TG-DTA analysis. However, in case of CSA-4 sample calcined at 573 K, increase in surface area from 6.1 to 113.4 m^2/g was observed as a result of dehydration or decomposition of water (weight loss 77.5%) present in the mesopores (pore diameter 4.04 nm) as observed in TG-DTA and FTIR analysis (Table 5.1) (Figure 5.3). Further increase in calcination temperature (773 K) caused decrease in surface area from 113.4 to 96.3 m^2/g due to restructuring

which induces disappearance of spaces between cobalt aluminosilicate as observed in TEM studies discussed later (sections 5.2.5 and 5.2.8). From the pore size distribution curve, it was found that all the samples showed a bimodal pore distribution as determined by using the Barrett-Joyner-Halenda (BJH) method with smaller pores in the region of ~1.5-2.0 nm and larger pores ranging from ~3.8-4.1 nm (Table 5.1).

Thus, above observations established that the textural properties of the material can be varied from microporous (~2.0 nm) to mesoporous (~4.1 nm) by changing the Si:Al ratio (from 10:1 to 1:10) and calcination at 573 K.

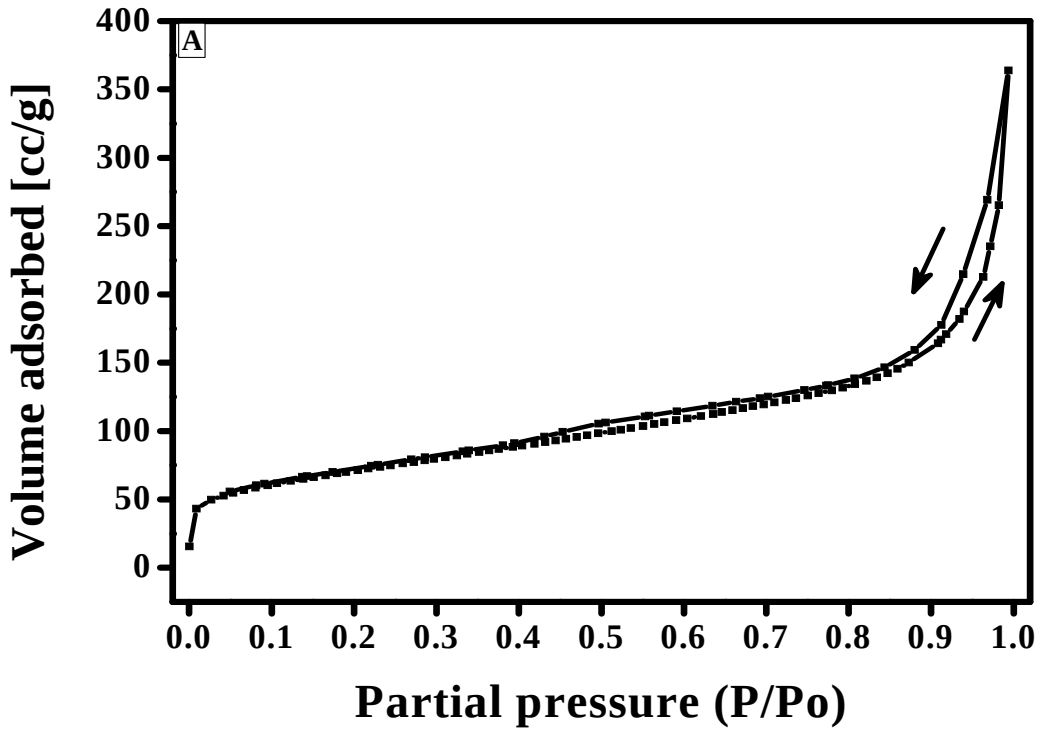

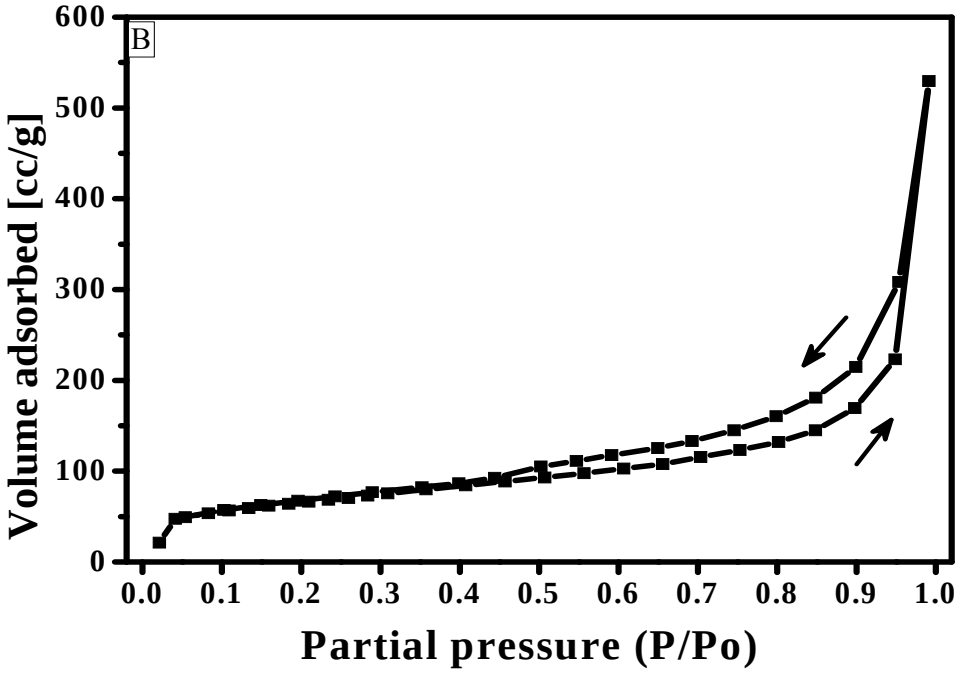
B
Volume adsorbed [cc/g]
0
100
200
300
400
500
600
0.0
0.1
0.2
0.3
0.4
0.5
0.6
0.7
0.8
0.9
1.0
Partial pressure (P/Po)

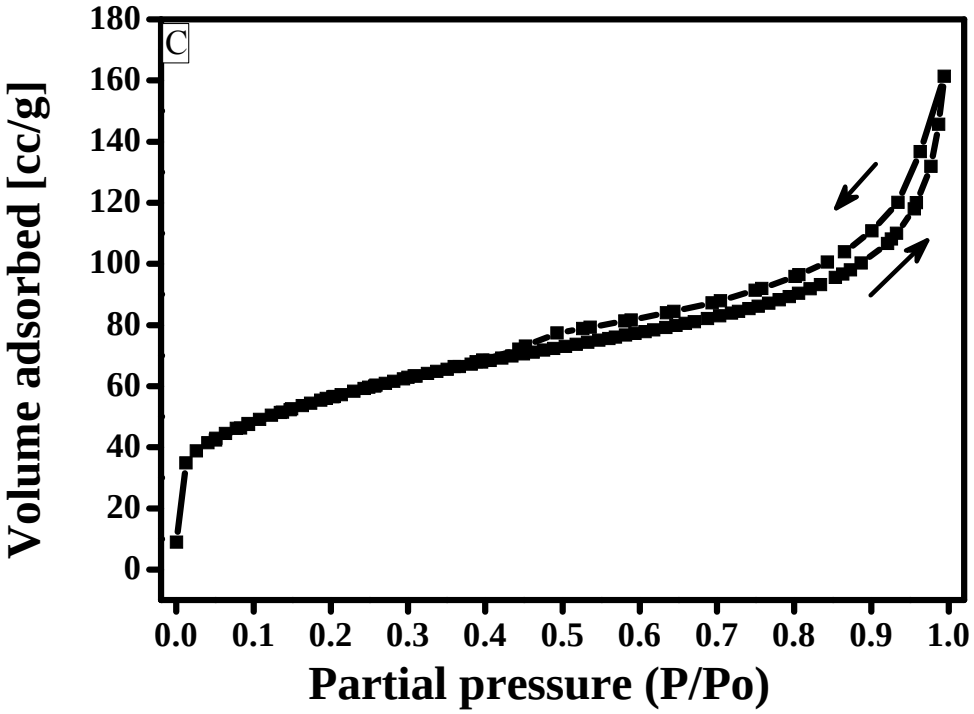
C
Volume adsorbed [cc/g]
0
20
40
60
80
100
120
140
160
180
0.0
0.1
0.2
0.3
0.4
0.5
0.6
0.7
0.8
0.9
1.0
Partial pressure (P/Po)

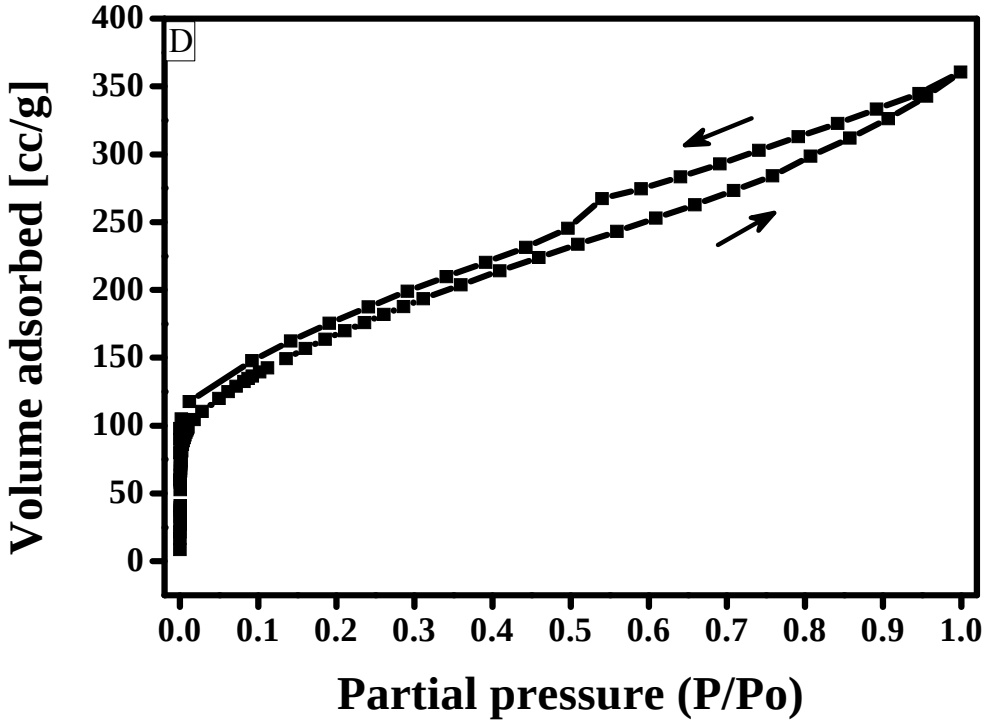
D
Volume adsorbed [cc/g]
400
350
300
250
200
150
100
50
0
0.0
0.1
0.2
0.3
0.4
0.5
0.6
0.7
0.8
0.9
1.0
Partial pressure (P/Po)

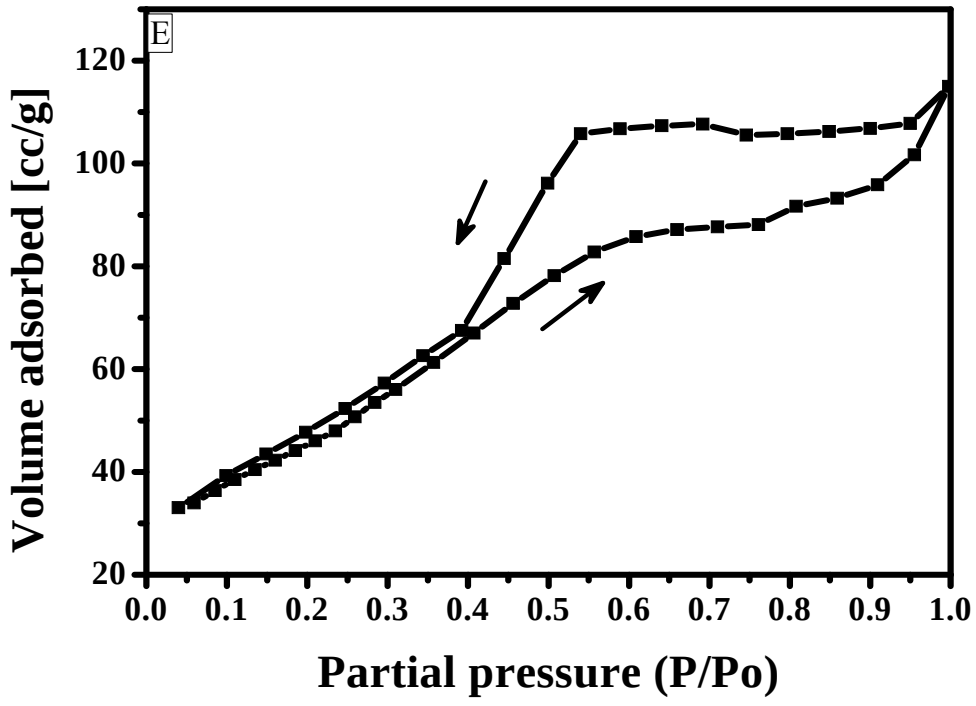
E
Volume adsorbed [cc/g]
120
100
80
60
40
20
0.0
0.1
0.2
0.3
0.4
0.5
0.6
0.7
0.8
0.9
1.0
Partial pressure (P/Po)

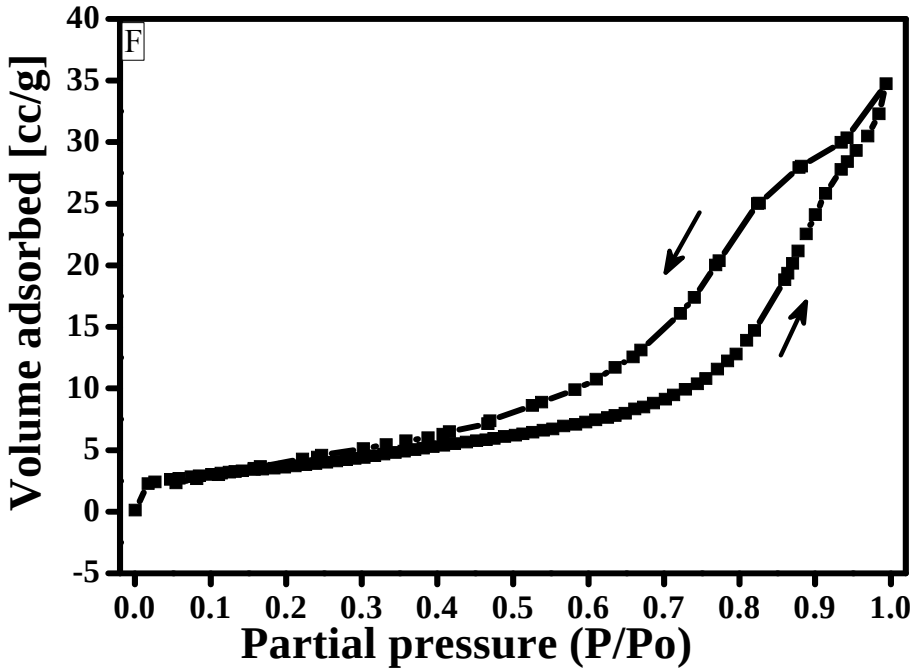

Figure 5.1. Adsorption isotherm of (A) CSA-1, (B) CSA-2, (C) CSA-3, (D) CSA-4, (E) CSA-4-3C and (F) CSA-4-5C samples

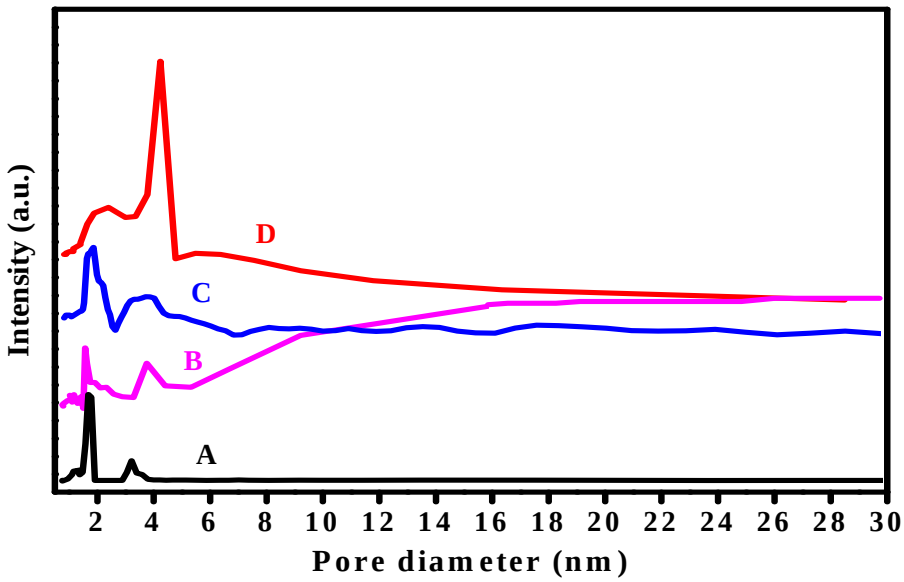

Figure 5.2. Pore size distribution of (A) CSA-1, (B) CSA-2, (C) CSA-3 and (D) CSA-4 samples

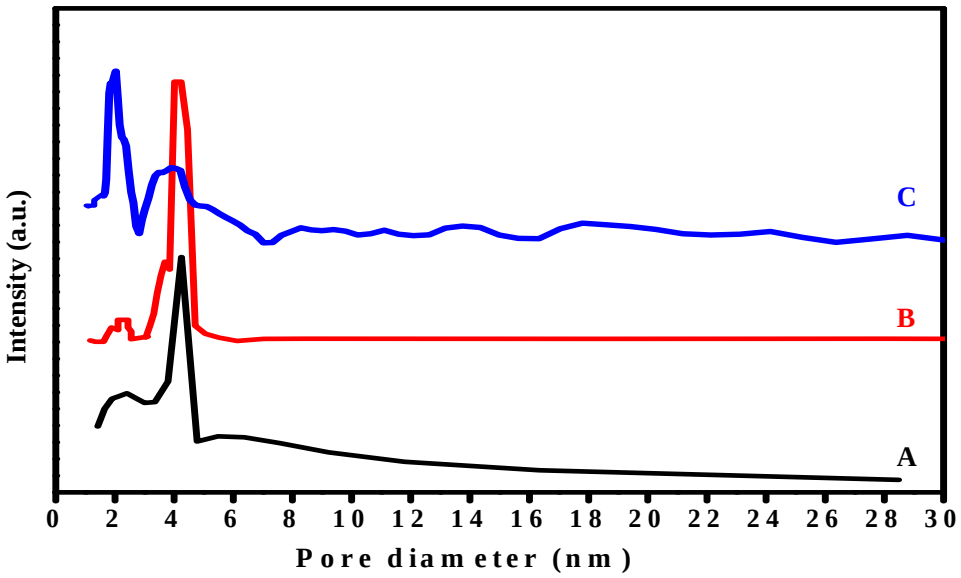

Figure 5.3. Pore size distribution of (A) CSA-4, (B) CSA-4-3C and (C) CSA-4-5C samples

Table 5.1. Textural properties of cobalt catalysts prepared with at different silica alumina (Si:Al) ratios and calcination temperatures

Catalysts	Si:Al ratio	Calcination temperature (K)	Surface area (m^2/g)	Pore size, BJH_{DES} (nm)	Pore volume, BJH_{DES} (cm^3/g)
CSA-1	10:1	423	232.8	1.17	0.17
CSA-2	1:1	423	134.3	2.81	0.29
CSA-3	1:5	423	13.3	3.40	0.48
CSA-4	1:10	423	6.1	4.04	0.50
CSA-4-3C	1:10	573	113.4	4.10	0.79
CSA-4-5C	1:10	773	96.3	3.98	0.58

5.2.2. X-ray diffraction (XRD)

Powder X-ray diffraction patterns of 15% cobalt aluminosilicate samples with different Si:Al ratios, calcined at 573 K and 773 K at different calcination times are shown in Figures 5.4 (a), (b) and (c) respectively. Intense peaks in case of CSA-1, CSA-2 and CSA-3 samples observed at

2θ=12.2° (110), 19° (101), 23.5° (300), 32.1°, 37.3°, 48.3° and 60.2° (060) could be assigned to smectite phase. These peaks became broader and less intense with change in silica alumina ratio from 10:1 to 1:5 (Figure 5.4, a). This might be due to increase in aluminium content causing slight change in layered morphology to amorphous nature [34]. This indicates the formation of saponite clay especially smectite type with a tri-octahedral structure and divalent cobalt being inserted in tetrahedral positions within the layer; replacing sodium to some extent. The peaks at 2θ=31.1°, 37.3°, 48.3° and 62.2° (060) confirmed that material with mixed phases was formed [2]. However, further change in silica: alumina ratio to 1:10 (CSA-4) caused disappearance of the peaks at 2θ=12.2° (110), 19° (101), 23.5° (300), 32.1°, 37.3°, 48.3° and 60.2° (060) and formation of new peaks at 2θ=29.6° (321), 31.2° (321), 38.2° (216) and 48.7° (611), which correspond to the garnet (spinel) phase of aluminosilicate (JCPDS =86-0657). The higher proportion of aluminum insertion in case of CSA-4 (Si:Al 1:10) sample indicated the formation of either pillaring or disruption of layer morphology as observed in nitrogen adsorption-desorption isotherm discussed in the Section 5.2.2. Also, there was little or no ordered stacking of the layers, as evidenced by the absence of a reflection at 2θ=60.2° (060).

Increase in calcination temperature from 573 to 773 K (CSA-4) caused gradual increase in intensities and the slight decrease in widths of the peaks at 2θ=29.6° (321), 31.2° (321), 38.2° (216) and 48.7° (611) (Figure 5.4(b)). These samples did not show any shift in peak position or additional peaks after calcination indicating that there was no delamination and the sample (CAS-4) was highly stable having amorphous nature, even after calcination (Figure 5.4(b)). Further, CSA-4 sample was calcined at 573 K with increase in calcination time from 1 to 6 h (Figure 5.4(c)). With increase in calcination time from 1 to 6 h, increase in intensity of peaks at

2θ=29.6° (321), 31.2° (321), 38.2° (216) and 48.7° (611) was observed. Above observations established the fact that increase in aluminium content, calcination temperature and time facilitated the increase in garnet phase of spinel cobalt aluminosilicate.

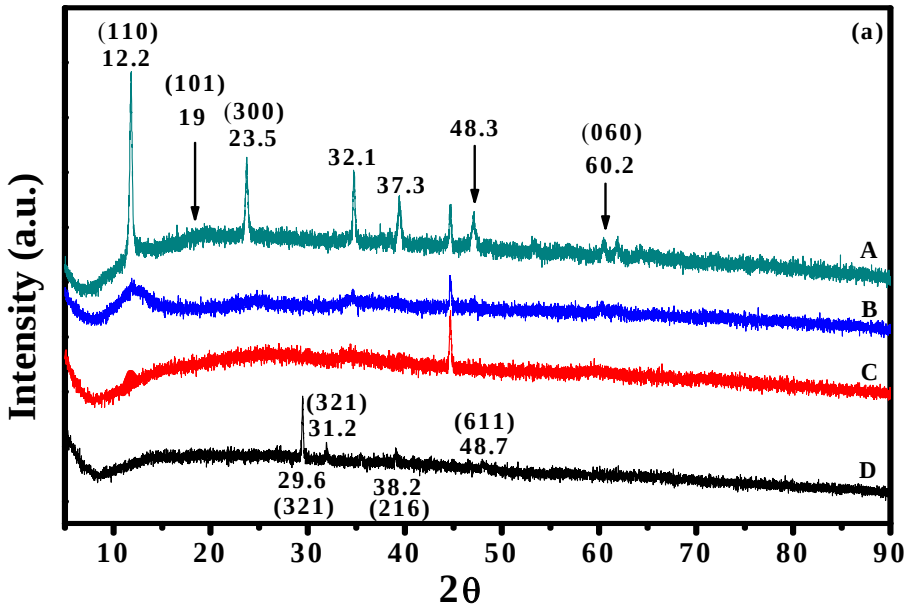

Figure 5.4 (a). XRD patterns of (A) CSA-1, (B) CSA-2, (C) CSA-3 and (D) CSA-4 samples

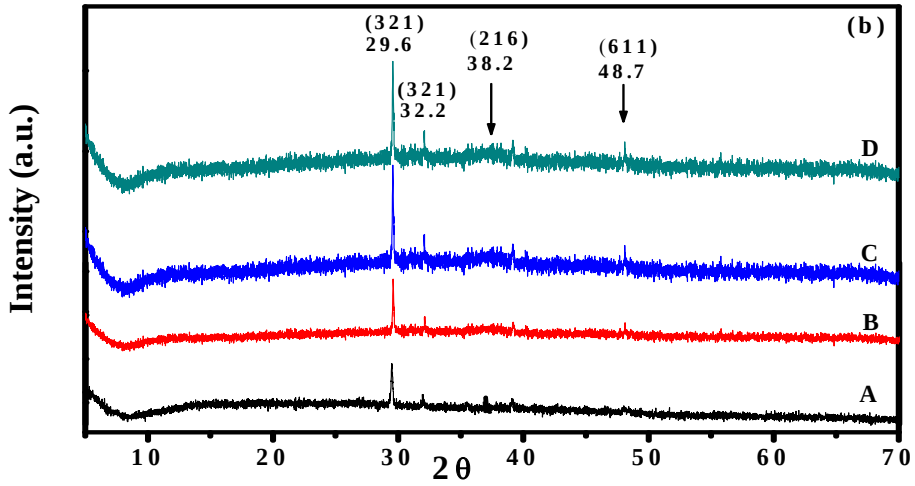

Figure 5.4(b). XRD patterns of (A) CSA-4, (B) CSA-4-3C, (C) CSA-4-4C and (D) CSA-4-5C samples

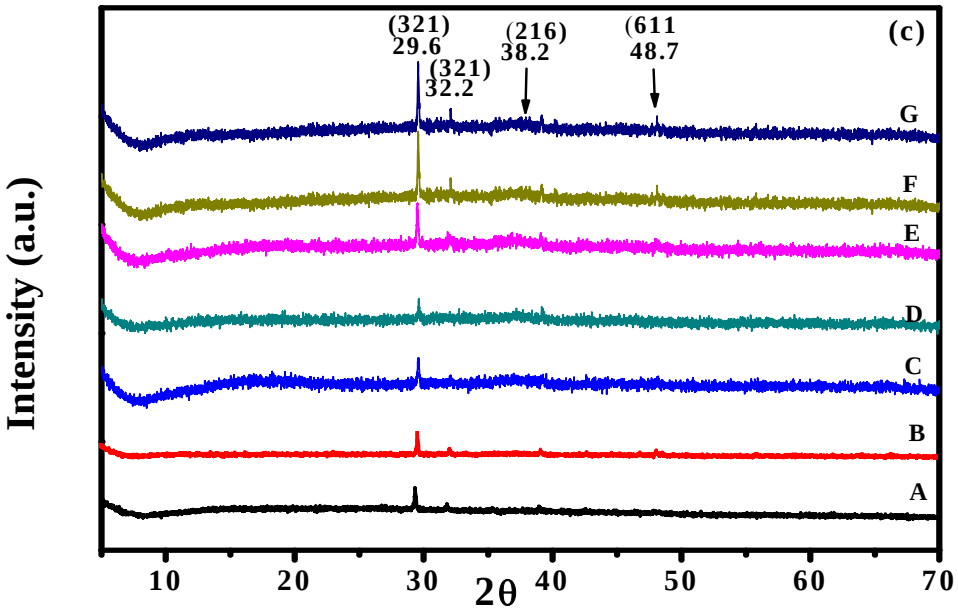

Figure 5.4 (c). XRD patterns of (A) CSA-4, (B) CSA-4-3C-1h, (C) CSA-4-3C-2h, (D) CSA-4-3C-3h, (E) CSA-4-3C-4h, (F) CSA-4-3C-5h and (G) CSA-4-3C-6h samples

5.2.3. X-ray photoelectron spectroscopy (XPS)

The Co 2p XPS spectra of 15% cobalt aluminosilicates as a function of silica alumina ratio (10:1, 1:1, 1:5 and 1:10) are shown in Figure 5.5. CSA-2, CSA-3 and CSA-4 samples show contain the Co $2p_{3/2}$ and Co $2p_{1/2}$ core level peaks at binding energies of 780.1 and 795.4 eV having difference of 15.3 eV which is almost equivalent in all samples except CSA-1 (13.9 eV). The increase in aluminium content caused gradual increase of peak intensities at binding energies of 780.1, 795.4 and 801.6 eV, which might be due to the change in layered morphology of clay to disordered layer morphology of aluminosilicate which is in accordance with XRD as discussed in Section 5.2.2 [35, 36]. Co $2p_{3/2}$ peaks observed at binding energies of 780 eV was very close to those reported for Co^{2+} as well as Co^{2+} exchanged NaY and for highly dispersed cobalt species

in Co-ZSM-5 indicating that cobalt was coordinated to lattice oxygen probably associated with aluminum and silanol groups [35, 36]. In addition to these spin-orbital peaks, the satellite peak for Co $2p_{3/2}$ was also observed at 786.2 eV, confirming that maximum species were in cobalt (II) state [37, 38].

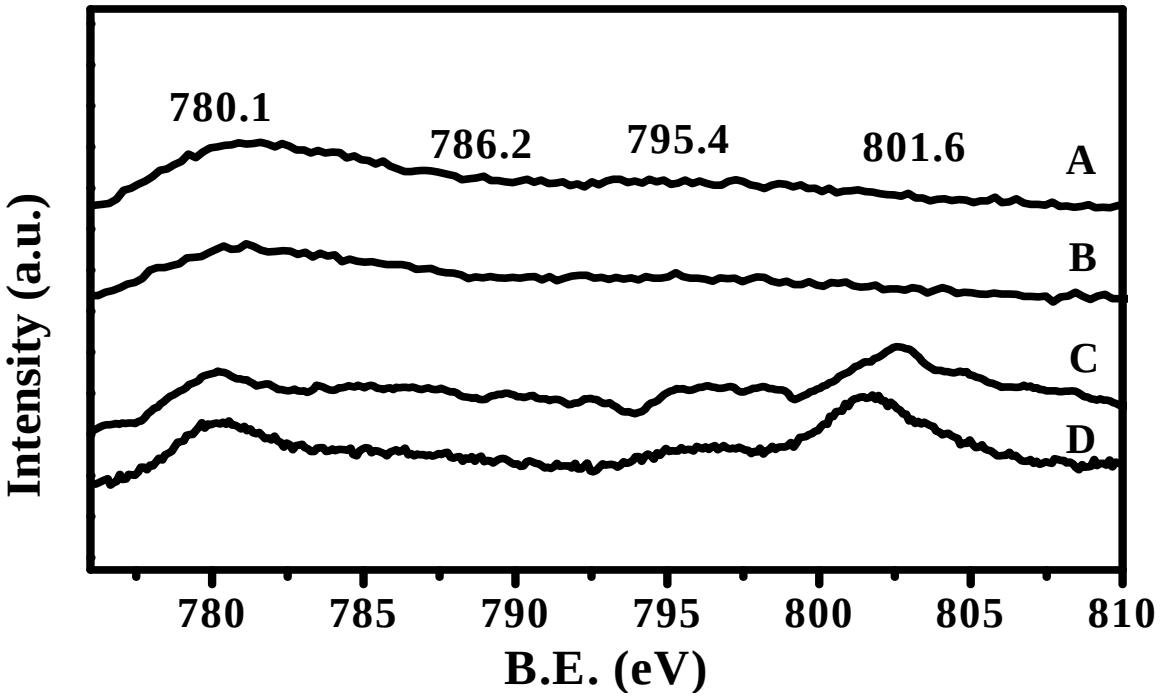

Figure 5.5. XPS of (A) CSA-1, (B) CSA-2, (C) CSA-3 and (D) CSA-4 samples

5.2.4. Diffuse reflectance UV-visible spectroscopy

DRUV-Visible spectra recorded for samples with varying Si:Al ratios, calcined at 573 and 773 K and with different cobalt loadings (5%, 15% and 30%) are shown in Figures 5.6(a), (b) and (c). The samples with Si:Al-10:1 (CSA-1) and Si:Al-1:2 (CSA-2) ratios showed a band at 242 nm. With further increase in aluminium content (Si:Al-1:1), CSA-3 sample showed a shift of 242 nm band to 263 nm and finally for Si:Al-1:10, CSA-4 showed two bands at 263 nm and 305 nm associated with oxygen to cobalt charge transfer (CT) transition assigned to tetrahedral Co^{2+}

species (Figure 5.6, a) [39]. Among all the samples, CSA-4 sample showed relatively stronger bands at 522 and 625 nm. A band at 522 nm suggests the presence of an extra lattice Co(II) in octahedral symmetry [40], whereas band at 625 nm was assigned for charge transfer (CT) transition band between oxygen to cobalt assigned to octahedral Co^{3+} species [41]. The intensities of all bands in case of CSA-1, CSA-2 and CSA-3 samples were relatively lower than those for the CSA-4 sample. This might be due to the incorporation of most of the cobalt into aluminosilicate (clay) lattice and not present on the surface as also observed in XPS studies discussed in Section 5.2.4.

The CSA-4 sample calcined at 573 K showed a slight increase in band intensities at 263, 305, 522 and 625 nm (Figure 5.6, b). This might be due to ~70% weight loss below 573 K (observed in TG-DTA) which caused opening of the mesopores (4.04 nm) of cobalt aluminosilicates and calcination in air causing oxidation of some of Co^{2+} species to Co^{3+} [40], as evidenced by FTIR, XPS, TPR and TPO studies. However, further increase in calcination temperature from 573 to 673 and 773 K, caused increase in intensities of bands at 263, 305, 522, 625 nm and an additional band appeared at 380 nm (Figure 5.6, b). Thus, the interaction of cobalt either with aluminium or with silica due to dehydroxylation of surface hydroxyl group at higher temperature, caused disruption/collapse of cobalt aluminosilicate structure which was also evidenced by nitrogen adsorption-desorption isotherm, surface area, pore size distribution and pore volume studies. In case of CSA-4 sample calcined at 573 K, slight increase in intensity of a peak at 625 nm indicated that tetrahedral Co^{2+} in the framework of the aluminosilicates was interconverted to Co^{3+} upon oxidation.

The cobalt loading in aluminosilicates (Si:Al; 1:10) was varied in the range of 5% to 30% (Figure 5.6, c). The intensities of bands at 263, 305, 522 and 625 nm increased with increase in

cobalt loading from 5% to 30%. As a result of increase in cobalt loading, distribution of both cobalt Co^{2+} and Co^{3+} species also increased [42-44].

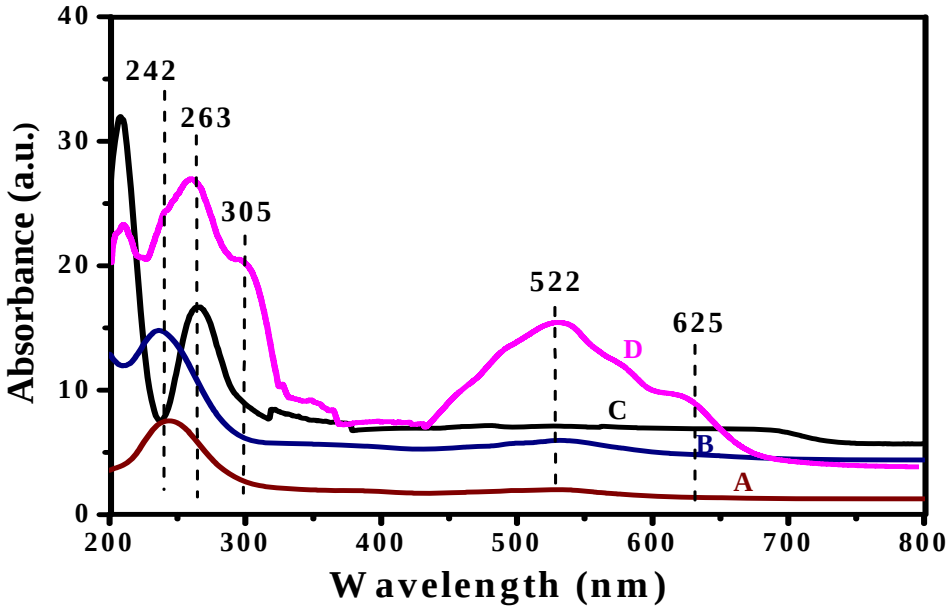

Figure 5.6(a). DRUV-vis spectra of (A) CSA-1, (B) CSA-2, (C) CSA-3 and (D) CSA-4 samples

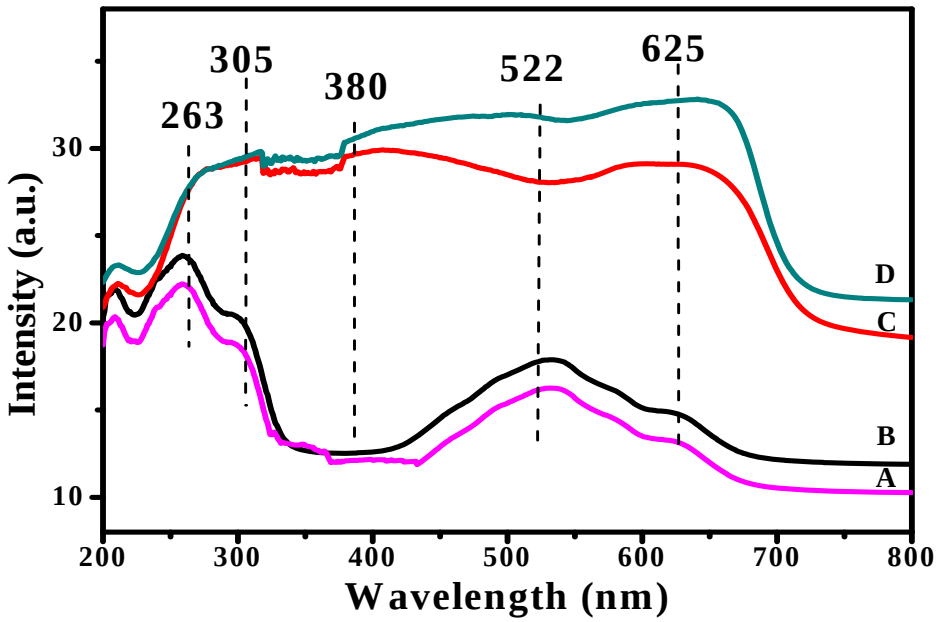

Figure 5.6(b). DRUV-vis spectra of (A) CSA-4, (B) CSA-4-3C, (C) CSA-4-4C and (D) CSA-4-5C samples

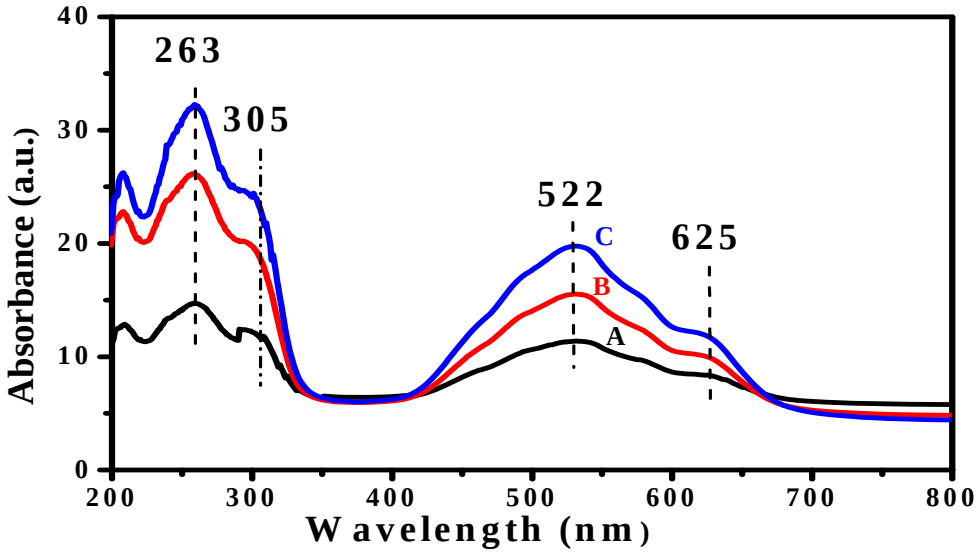

Figure 5.6(c). DRUV-vis spectra of (A) 5%, (B) 15% and (C) 30% cobalt loading on SA-4 (Si:Al-1:10) samples

5.2.5. Thermo gravimetric analysis (TGA)

TG-DTA of 15% cobalt aluminosilicates with different Si:Al ratios (from 10:1 to 1:10) is shown in Figure 5.7. With change in Si:Al ratio from 10:1 to 1:10, the total increase in weight loss was observed from 26.19% to 77.5% (Table 5.2). An appreciable weight loss of 20%, 15%, 27% and 57% was observed below 453 K, in case of CSA-1, CSA-2, CSA-3 and CSA-4 samples respectively, due to the loss of water absorbed and coordinated to and/or present in the meso-/micro pores [45]. The gradual increase in percentage weight loss due to increase in aluminium content, resulted into change in cobalt aluminosilicate property from hydrophobic to hydrophilic [45]. The second weight loss of 2.1%, 9.1%, 12% and 27% in case of all samples below 573 K was due to decomposition and dehydroxylation of carbonate (reaction product of urea), trace of acetate from cobalt acetate, undissolved nitrate and hydroxyl group which were confirmed from FTIR examination. The continuous percentage weight loss of 4.1%, 7.1%, 7.6% and 7.5% above

573 K was due to the dehydroxylation of surface Si-OH or cobalt acetate present/trapped in meso pores of the sample. Among all the samples, CSA-1 showed weight loss in a single step, while remaining all showed the weight loss in three steps. This might be due to the disorder in layered morphology as well as increase in pore diameter from 1.17 nm to 4.04 nm as observed in nitrogen adsorption-desorption isotherm and XRD analysis. The increase in disorder in morphology leads to difficulty in the removal/escape of water molecules trapped in layer or meso-/micro pores which require higher temperature [46, 47]. However, the presence of interlayer water and swelling properties of the clay clearly demonstrate that the material is not talc [48, 49].

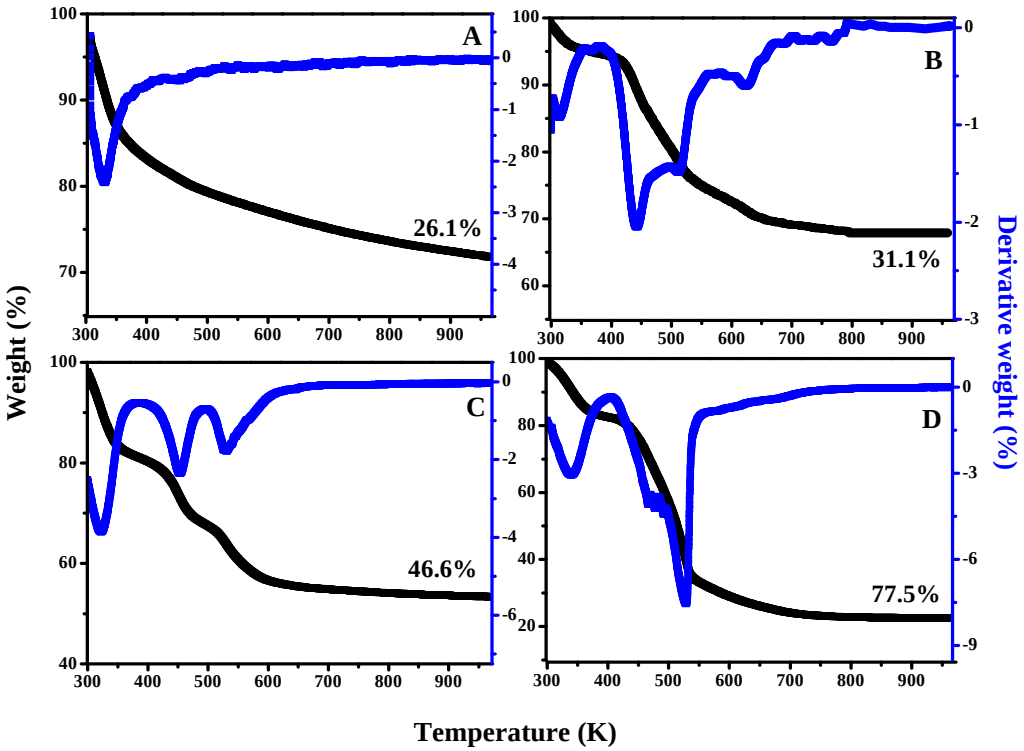

Figure 5.7. TG-DTA of (A) CSA-1, (B) CSA-2, (C) CSA-3 and (D) CSA-4 samples

Table 5.2. Summary of thermogravimetric analysis

Catalysts →	**CSA-1**	**CSA-2**	**CSA-3**	**CSA-4**	**Remarks**
Temperature range (K) ↓	**Percentage weight loss**				
300-370	15.0	5.0	18.0	16.0	Loss of physically adsorbed water molecules.
373-473	5.0	10.0	9.0	41.0	Loss of physically adsorbed/trapped water molecules.
473-573	2.1	9.1	12.0	13.0	Decomposition of carbonate anions, acetate and nitrate.
573-873	4.1	7.1	7.6	7.5	Dehydroxylation of surface hydroxyl group.
Total	26.2	31.2	46.6	77.5	

5.2.6. Fourier-transform infrared spectroscopy (FTIR)

The FTIR spectrum of 15% cobalt aluminosilicate samples having different Si:Al ratios and CSA-4 sample calcined at 573 and 773 K are shown in Figure 5.8. The very strong and relatively sharp peaks at 1005, 1386 and 1648 cm^{-1}, were due to carbonate (product of urea), trace of acetate from cobalt acetate, undissolved nitrate and hydroxyl group present in CSA-1, CSA-2, CSA-3 and CSA-4 samples (Figure 5.8, A-D). Three small and broad peaks at 468, 620 and 780 cm^{-1} observed in all the samples were due to Si-O/Al-O and Co-O vibrations [50]. The two broad and intense bands at 3345 cm^{-1} were attributable to structural *ν*(OH) and a broader band at 3605 cm^{-1} to the *ν*(OH) of interlayer water. The intensities of these bands gradually increased with increase in aluminium content (from 10:1 to 1:10), confirming the shift in nature of samples from hydrophobic to hydrophilic which was also evidenced in TG-DTA analysis. However due to calcination at 573 K and 773 K, the peaks at 3605, 3345, 1648, 1386 and 1005 cm^{-1} disappeared

(Figure 5.8, E-F). This was mainly due to the decomposition and dehydroxylation of water, carbonate, acetate, nitrate and hydroxyl molecules present before calcination in the CSA-4 sample. Also, two low intensity peaks appeared at 676 and 546 cm^{-1} assigned to Co^{2+} in a tetrahedral and Co^{3+} in octahedral positions observed in CSA-4-3C and CSA-4-5C samples [51, 52]. This might be due to calcination at 573 and 773 K converting some of the Co^{+2} in to Co^{3+}, which was also confirmed from DR-UV, XPS, CV, TPR and TPO studies.

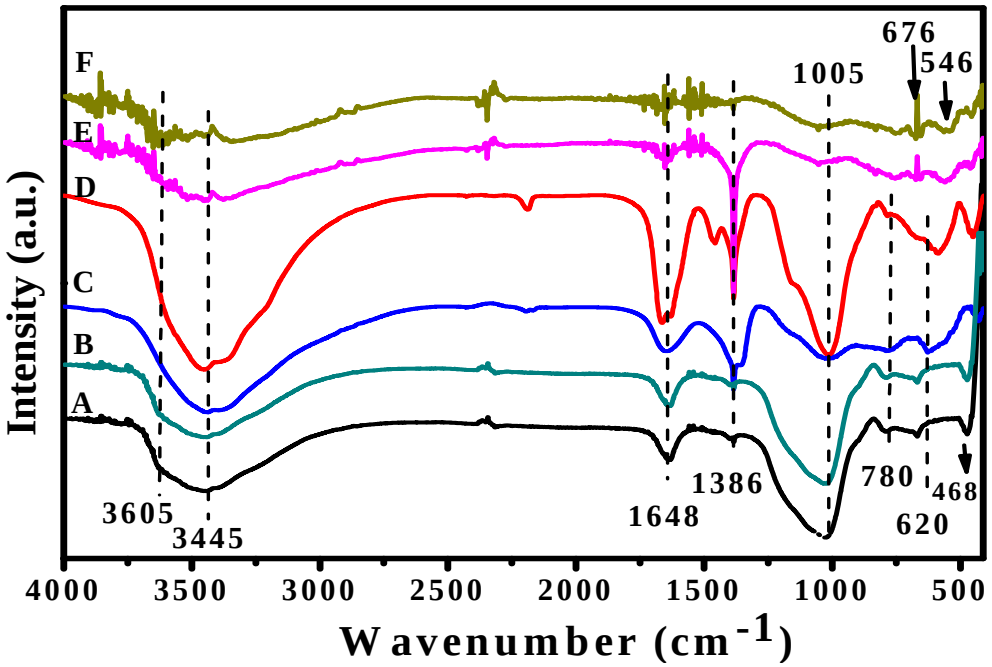

Figure 5.8. FTIR spectra of (A) CSA-1, (B) CSA-2, (C) CSA-3, (D) CSA-4, (E) CSA-4-3C and (F) CSA-4-5C samples

5.2.7. Scanning electron microscope (SEM) and Energy dispersive X-ray (EDX)

SEM spectra of 15% cobalt aluminosilicate samples having different Si:Al ratios are shown in Figure 5.9. The average size of particles was found to be ~10-25, 10-28, 20-40 and 30-60 μm in

case of CSA-1, CSA-2, CSA-3 and CSA-4 samples respectively. The gradual increase in the particle size was in order with the increase in aluminium content due to the hydrophilicity which caused the particles to come closer and remain intact. The particles showed the aggregates formed by packing of sheets thus demonstrating that the synthesis method can lead to the formation of materials with layered morphology.

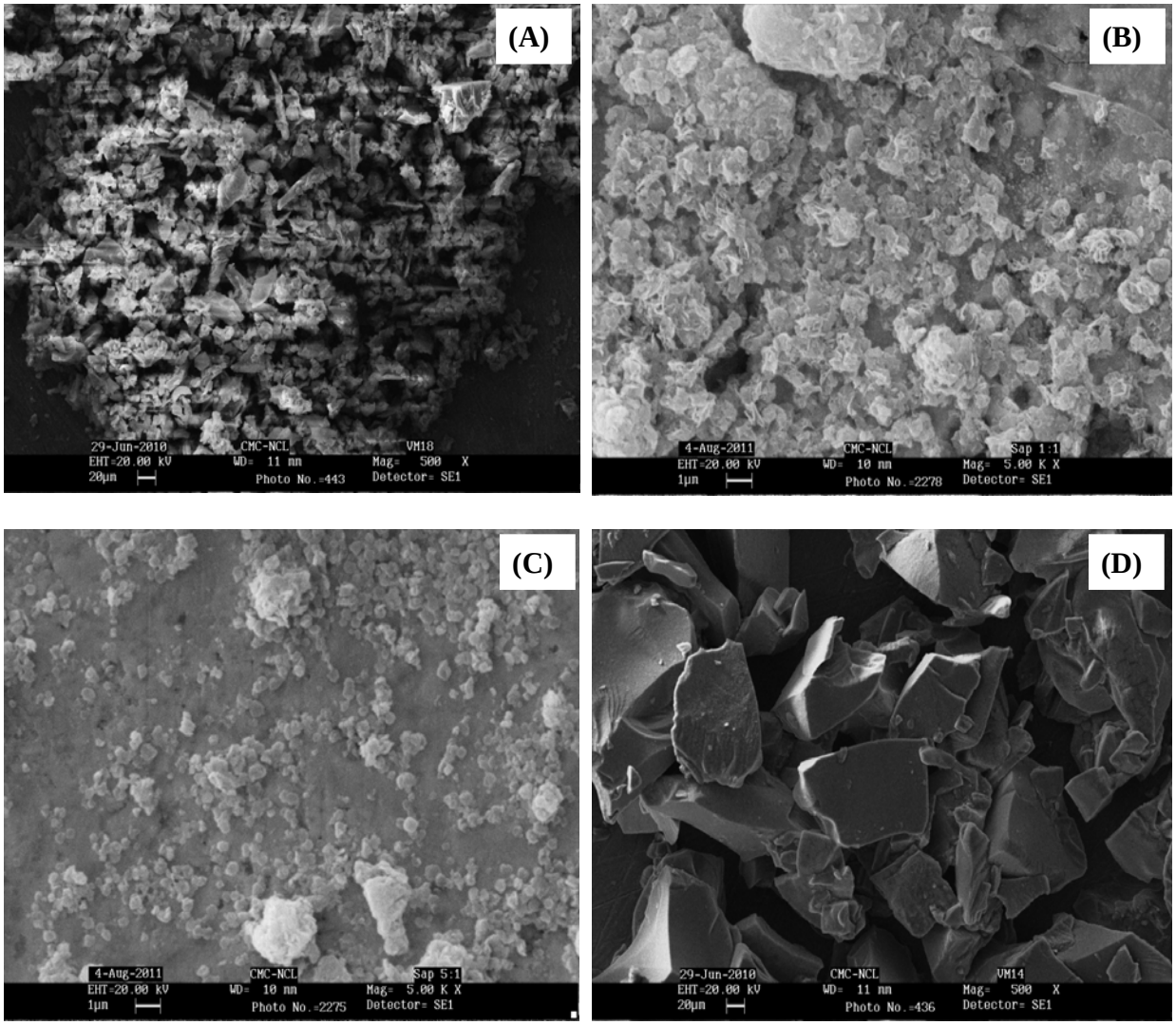

Figure 5.9. SEM spectra of (A) CSA-1, (B) CSA-2, (C) CSA-3 and (D) CSA-4 samples

The elemental composition of cobalt aluminosilicates samples having different Si:Al ratios and cobalt loadings (5% to 30%) Si:Al were determined by EDX, as shown in Figure 5.10. CSA-1, CSA-2, CSA-3 and CSA-4 samples showed the presence of cobalt, aluminium, silicon, sodium, oxygen, nitrogen and traces of carbon. The calculated (especially silicon and aluminium) elemental ratio of Si:Al in weight percentages were found to be about ~1:10, 1:1, 1:5 and 1:10 which were in excellent agreement with the theoretical percentages (Table 5.3). The percentage of cobalt loading in case of CSA-1, CSA-2, CSA-3 and CSA-4 samples found to be in the range of 14.2 to 15.2% closely matching with the theoretical cobalt loading of ~15%, (Table 5.3). The cobalt loadings in case of 5%, 15% and 30% samples were found to be 3.1%, 15.2% and 18.5% of cobalt respectively (Table 5.3). The lower percentage found in case of both 5% and 30% samples might be because some of the cobalt was incorporated within aluminosilicates layer and/or leached out.

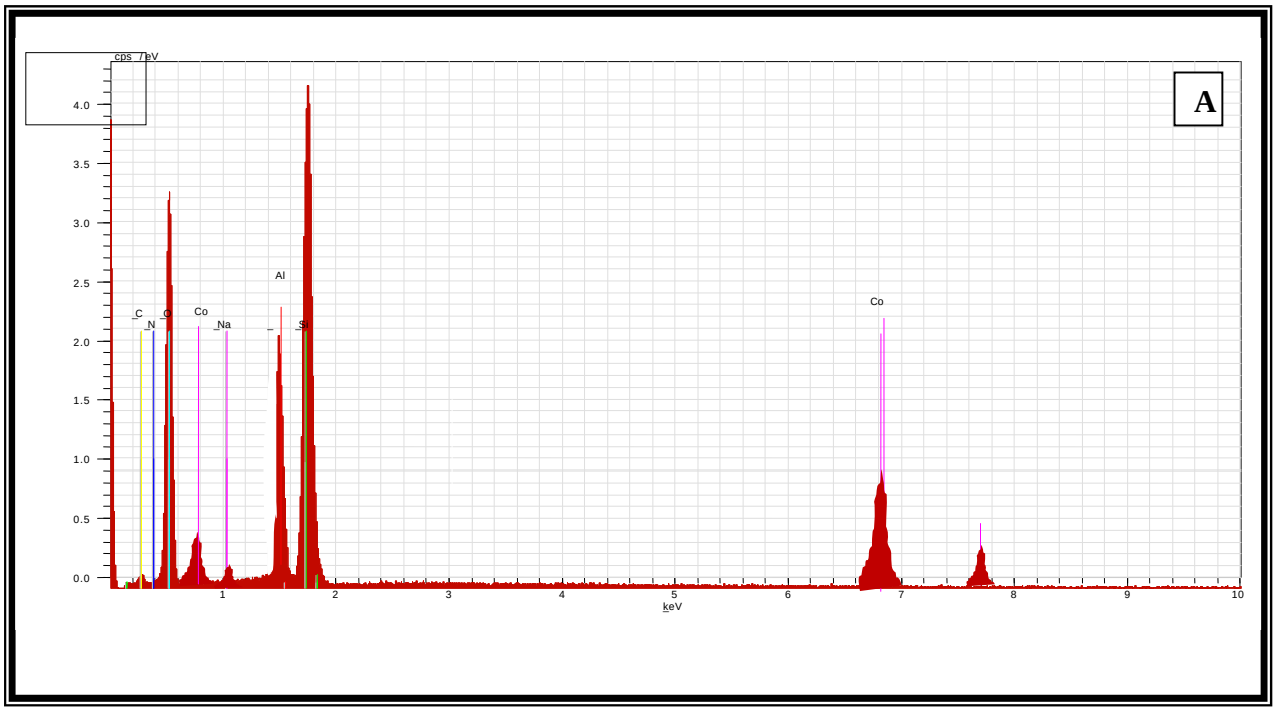

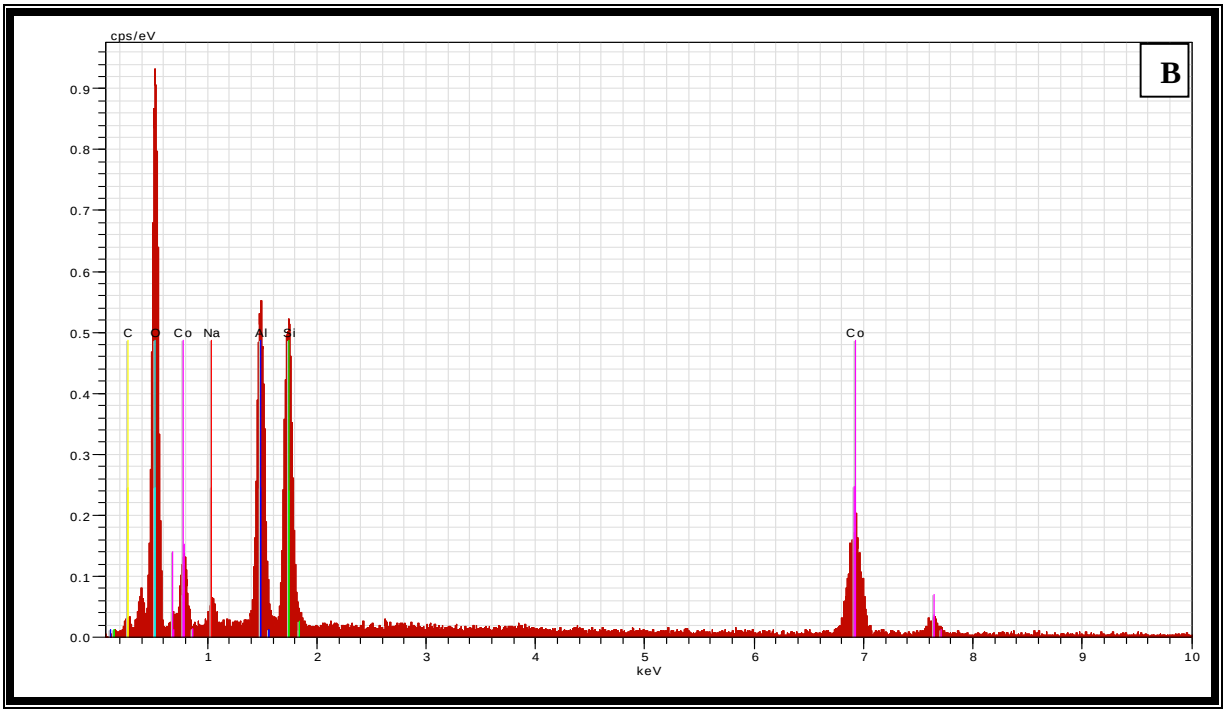
cps/eV
B
C
O
Co
Na
Al
Si
Co
keV

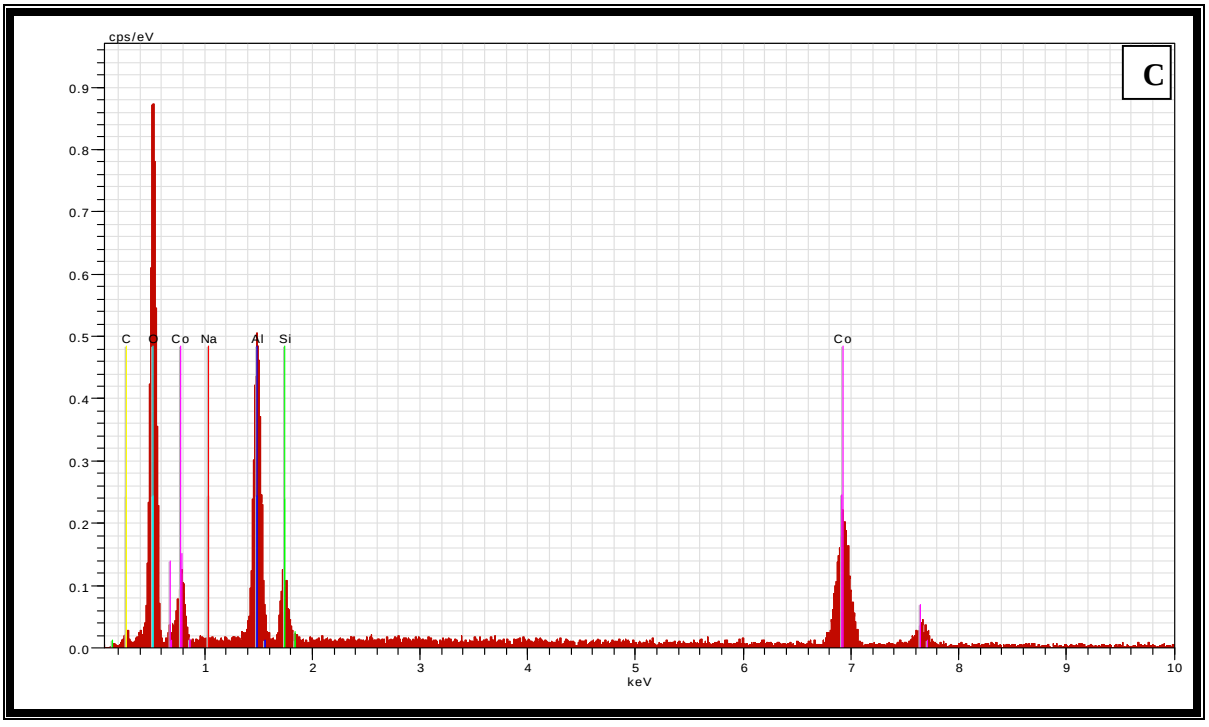
cps/eV
C
C
O
Co
Na
Al
Si
Co
keV

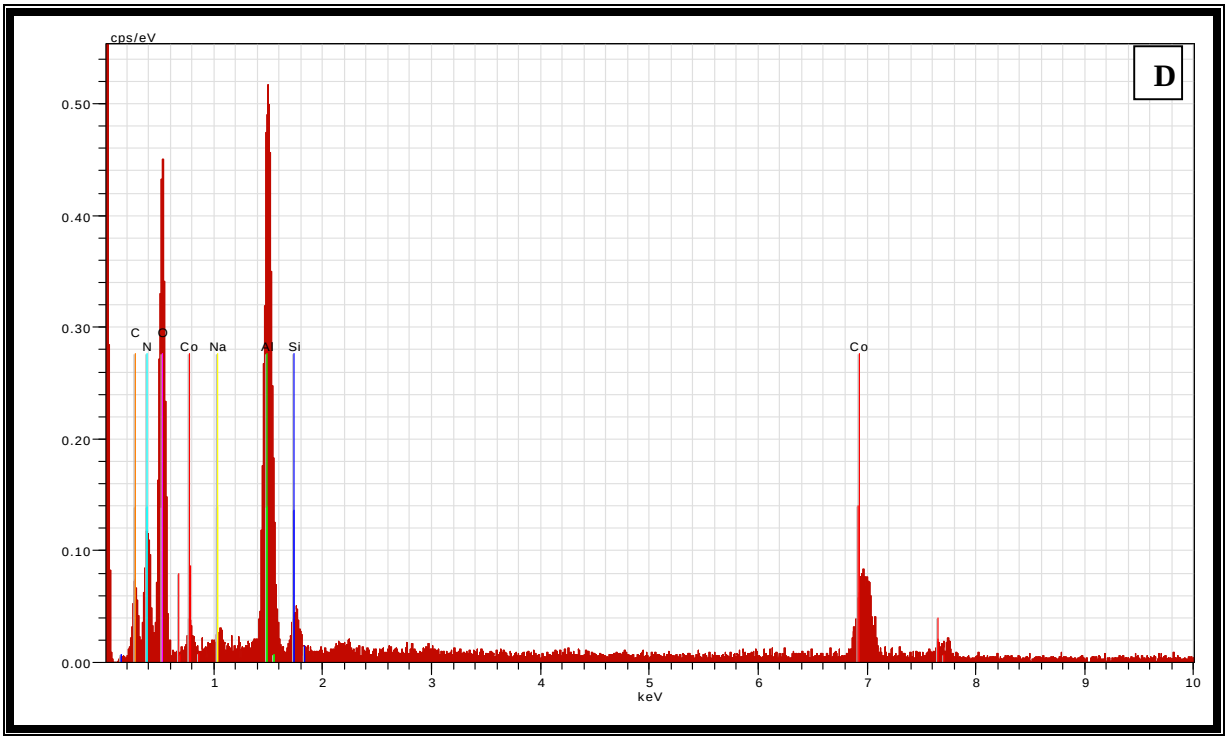
D
cps/eV
0.50
0.40
0.30
0.20
0.10
0.00
C
N
O
Co
Na
Al
Si
Co
1
2
3
4
5
6
7
8
9
10
keV

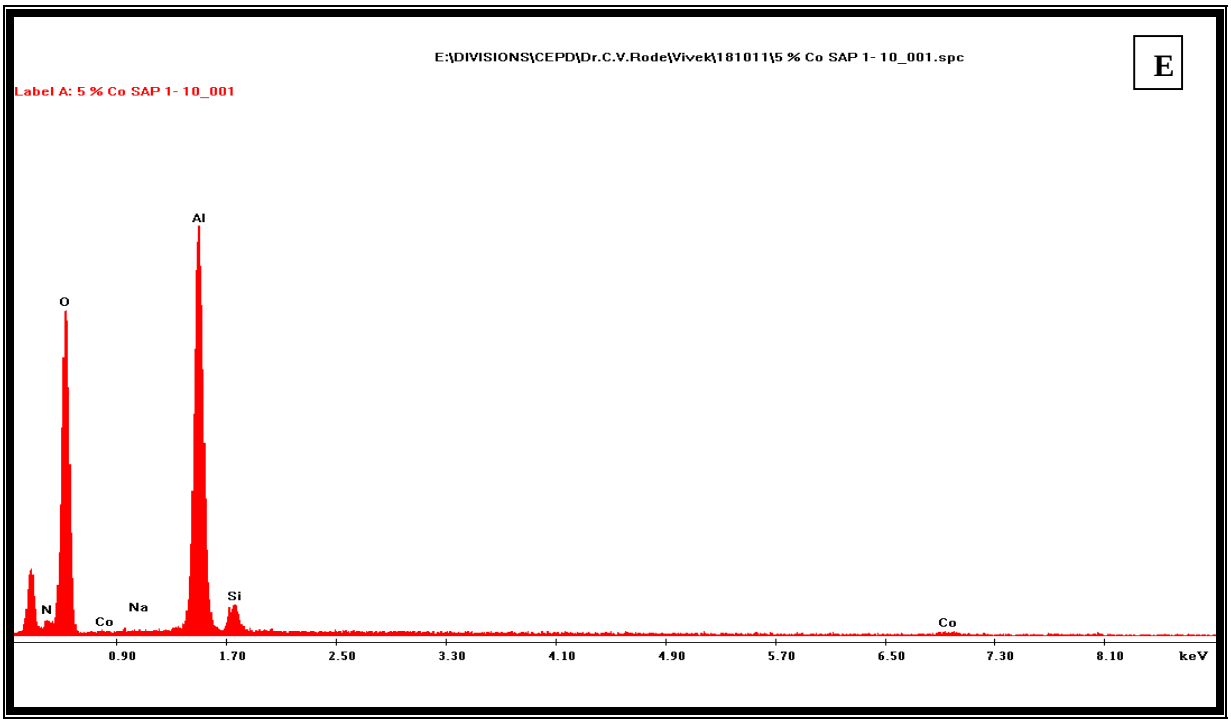
E
E:\DIVISIONS\CEPD\Dr.C.V.Rode\Vivek\181011\5 % Co SAP 1- 10_001.spc
Label A: 5 % Co SAP 1- 10_001
Al
O
N
Co
Na
Si
Co
0.90
1.70
2.50
3.30
4.10
4.90
5.70
6.50
7.30
8.10
keV

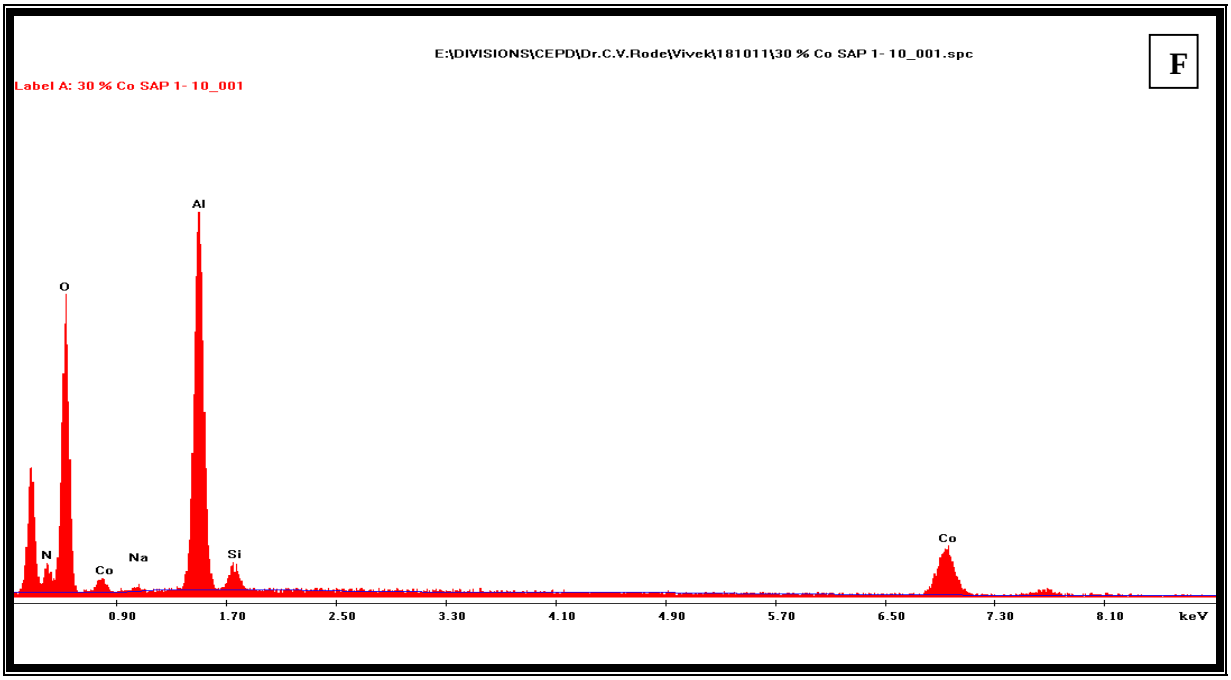

Figure 5.10. EDAX of (A) 15% CSA-1, (B) 15% CSA-2, (C) 15% CSA-3, (D) 15% CSA-4, (E) 5% CSA-4 and (F) 30% CSA-4 samples

Table 5.3. Elemental compositions of cobalt aluminosilicate catalysts

Catalysts	Atom, (weight %)						
	Co	**O**	**Si**	**Al**	**Na**	**N**	**C**
15% CSA-1	14.9	40.0	32.0	3.5	4.5	1.2	5.8
15% CSA-2	14.3	62.0	9.0	10.0	3.0	2.0	4.0
15% CSA-3	14.2	62.0	3.0	15.0	1.0	3.0	2.0
15% CSA-4	15.2	26.8	3.2	32.9	2.0	14.0	7.0
5% CSA-4	3.1	33.9	3.8	45.2	1.1	2.1	9.8
30% CSA-4	18.5	29.0	3.2	37.0	1.5	4.6	6.2

5.2.8. Transmission electron microscopy

In order to know the effect of calcination temperature (573 and 773 K) on layered morphology of CSA-4 sample, characterization by TEM was studied (Figure 5.11). The sample calcined at 573 K (CSA-4-3C) showed the opening of mesopores (pore diameter 4.10 nm) while sample calcined at higher temperature of 773 K (CSA-4-5C) showed that the sheet morphology was significantly hampered due to the disappearance of interparticle spaces and decrease in pore size from 4.10 nm to ~2.0 nm (peak intensity at 2.0 nm is higher than the of 3.98 nm peak) as observed in the pore size distributions (Section 5.2.1). The significant increase in surface area in case of CSA-4-3C (calcination at 573 K) sample by seventeen times (from 6.1 to 113.5 m^2/g). This might be due to a weight loss of ~70% (dehydration and decomposition) below 573 K resulting into the opening of the pores. However, in case of CSA-4-5C sample calcined at 773 K caused dehydroxylation which significantly resulted into disruption of layered structure and pores opening which is observed in TG-DTA, surface area, pore size distribution and DRUV examinations.

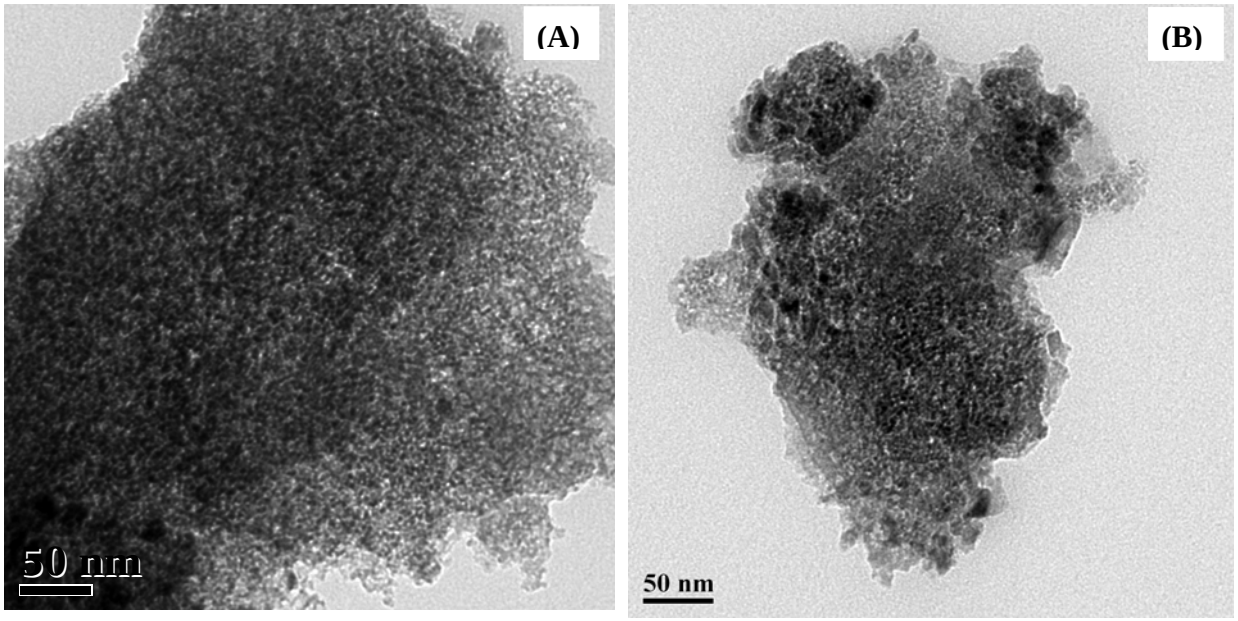

Figure 5.11. TEM of (A) CSA-4-3C and (B) CSA-4-5C samples

5.2.9. Temperature programmed reduction / Temperature programmed oxidation (TPR/TPO)

TPR experiments were carried out in order to study the change in redox behavior of cobalt aluminosilicate having different Si/Al ratios and effect of calcination temperatures (573 and 773 K) on CSA-4 samples (Figure 5.12). Broad and less intense peaks appeared in the range of 373-873 K, while intensity of characteristics Co^{2+}/Co^{3+} reduction peak was too low in case of CSA-1, CSA-2, CSA-3 and CSA-4 samples. The broad and less intense reduction peaks might be due to the ~26.2%, 31.2%, 46.6% and 77.5% weight loss as a result of loss of water, acetate, carbonate of urea which were present in interlayer/mesopores. CSA-4 sample calcined at 573 and 773 K showed an intense single peak in the range of 470-673 K assigned to the sequential reduction of (Co^{3+}) trivalent cobalt oxide to (Co^{2+}) divalent cobalt oxide (CoO) and further reduction to metallic cobalt (Co^{o}) [53-55]. The calcination caused dehydration and decomposition of molecules (water, acetate, carbonate of urea) resulting in to opening of interlayer and meso pores

causing significant increase in cobalt active species as evidenced by nitrogen adsorption-desorption isotherm, surface area, XPS, TEM, FTIR and DRUV studies.

The change in Si:Al composition from 10:1 to 1:10 showed slight increase in H_2 up take (2.1, 2.3, 2.7 and 3.3 mmol) (Table 5.4), which was found to be very less (435.0 mmol) than that observed for pure spinel Co_3O_4 (Co-3C-a) catalyst. However, CSA-4 sample calcined at 573 and 773 K showed 1.5 and 1.2 times higher H_2 up take (681.4 and 527 mmol) respectively, than spinel Co_3O_4 catalyst. This remarkable enhancement in H_2 up take was due to distribution of 15% cobalt (Co^{2+}/Co^{3+}) species over aluminosilicate surface and within the meso pores.

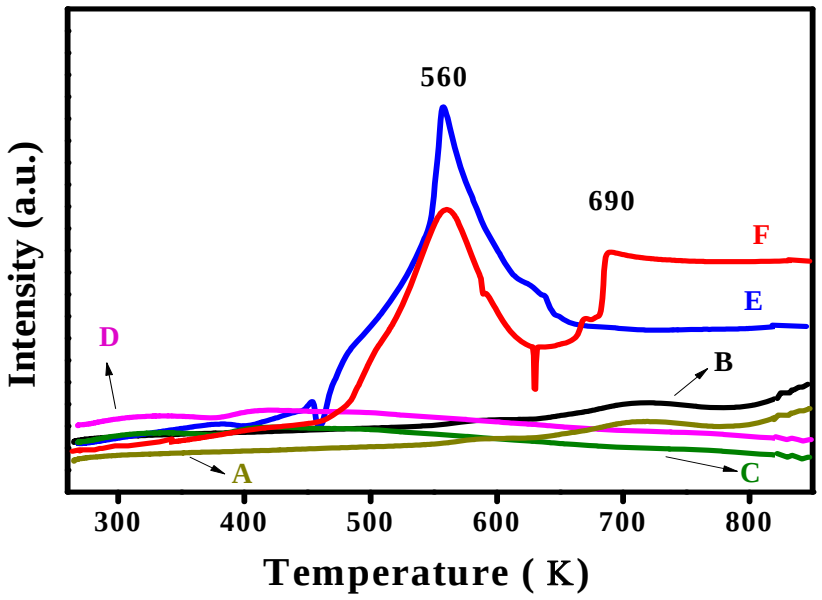

Figure 5.12. TPR of (A) CSA-1, (B) CSA-2, (C) CSA-3, (D) CSA-4, (E) CSA-4-3C and (F) CSA-4-5C samples

The ability of oxidation of pre-reduced cobalt aluminosilicate catalysts having different Si:Al ratio (10:1 to 1:10) and CSA-4 samples calcined at 573 and 773 K, was calculated by using TPO analysis as shown in Figure 5.13. The broad and less intense peak in the range of 450-550 K in

all the samples was attributed to sequential oxidation of metallic cobalt oxide (Co^o) to divalent cobalt oxide (CoO) and finally to trivalent cobalt oxide (Co_3O_4) [52, 56]. With change in Si:Al ratio (from 10:1 to 1:10) and calcination temperature (CSA-4-3C and CSA-4-5C), slight increase in peak intensity was observed.

As much as about twice increase in O_2 up take (from 7.8 to 14.6 mmol) was observed with change in Si:Al from 10:1 to 1:10, while both these values were lower than that for the spinel Co_3O_4 (20.6 mmol) sample (Table 5.4). However, with increase in calcination temperature to 573 and 773 K, there was a significant increase in O_2 up take by 2 times and 1.5 times respectively, compared to spinel Co_3O_4 catalyst.

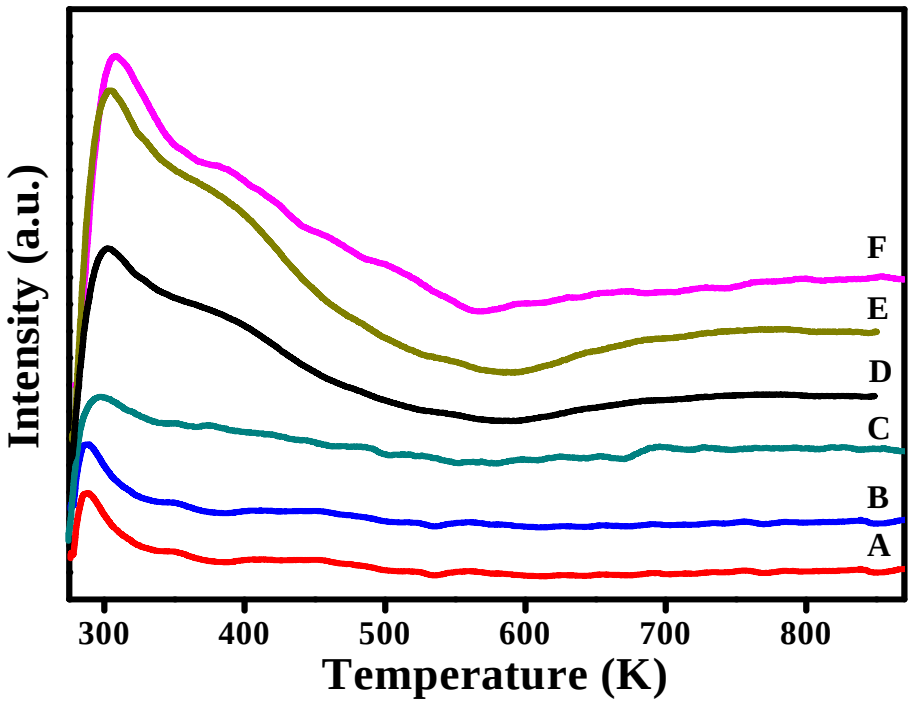

Figure 5.13. TPO of (A) CSA-1, (B) CSA-2, (C) CSA-3, (D) CSA-4, (E) CSA-4-3C and (F) CSA-4-5C samples

Table 5.4. TPR/TPO-H_2/O_2 uptake profile of cobalt aluminosilicate catalysts with different Si:Al ratio and calcined samples of CSA-4 at 573 and 773 K

Catalysts	Si:Al ratio	Calcination temperature (K)	H_2 (mmol)	O_2 (mmol)
CSA-1	10:1	423	2.1	7.8
CSA-2	1:1	423	2.3	8.2
CSA-3	1:5	423	2.7	10.8
CSA-4	1:10	423	3.3	14.6
CSA-4-3C	1:10	573	1781.4	43.5
CSA-4-5C	1:10	773	1027.3	31.9
Co-3C-a	NA	573	435.0	20.6

Where; NA is not applicable

5.2.10. Cyclic voltammogram (CV)

The redox potential profiles of the cobalt aluminosilicate catalysts with various Si:Al ratios were obtained by cyclic voltammogram (Figure 5.14). All the samples showed broad oxidation and reduction peaks. The cathodic peak in the lower potential region (0.41 V) could be assigned to the oxidation of Co^{2+} to Co^{3+}. Similarly, the anodic peak present at higher potential (0.5 V) could be assigned to the reduction of Co^{3+} to Co^{2+}. The anodic and cathodic peak intensities gradually increased from CSA-1 to CSA-4 samples. This was due to the gradual increase in number of surface active tetrahedral (Co^{3+}) and octahedral (Co^{3+}) species as a result of enhancement in the redox potential, indicating that among the prepared catalysts, higher oxidizing ability of CSA-4 catalyst was due to its enhanced redox potential.

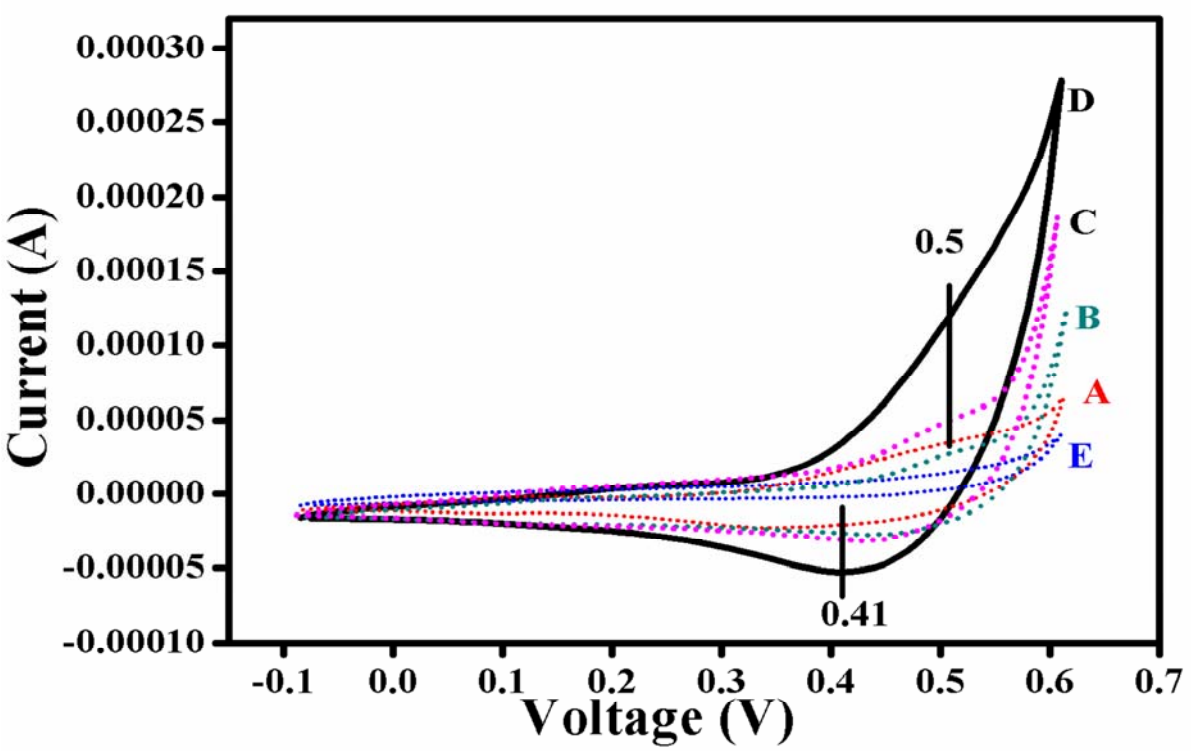

Figure 5.14. CV of (A) CSA-1, (B) CSA-2, (C) CSA-3, (D) CSA-4 and (E) Si:Al-4 samples

5.2.11. Fourier Transform Extended X-ray Absorption Fine Structure (EXAFS)

FT-EXAFS was studied to understand the cobalt interaction with aluminosilicate (CSA-4) and the effect of calcination temperature (573 and 773 K) on the bond distance and environment around Co (Figure 5.15). The peaks appearing at 1.46, 2.45 and 3.04 Å were assigned to Co-O, Co-Co and Co-O bond distances respectively (Figure 5.15, A) [57, 58]. These observed bond distances were almost identical to those observed for the spinel Co_3O_4 however, the peak showed lower intensities (Figure 5.15, D). This might be due to incorporation of cobalt in the aluminosilicate environment. The CSA-4 sample calcined at higher 573 and 773 K caused increase in bond distances by 0.6, 0.26 and 0.27 Å assigned to Co-O, Co-Co and Co-O bonds respectively, while new additional peak at 1.1 Å for the Co-O bond was observed in CSA-4-3C

and CSA-4-5C samples (Figure 5.15, B and C). The calcination at higher temperature resulted in dehydration, decomposition and most importantly, dehydroxylation of silanol and cobalt hydroxyl groups, due to which recombination of all bonds resulted in to shift in peaks from 1.46, 2.45, 3.04 Å to 1.52, 2.71, 3.31 Å respectively. The new Co-O bond at 1.1 Å confirmed that Co-O bond was affected due to interaction of Co-O in the interlayer more with tetrahedral than the octahedral layer (Figure 5.15, B and C) [59]. The slight decrease in peak intensity and change in bond distance for Co-O in case of calcined catalyst suggested that the peaks at 1.1 and 1.6 Å were due to the tetrahedral Co-O binding with octahedral layers of the silanol and aluminium respectively. The slight change in inter atomic M-O bond distance was due to the release of water molecules from inter layers of clay resulted in an increase in pillaring by 0.2 Å of cobalt cation. The decrease in intensity of Co-O at 2.71 Å suggested the formation of Al_2O_3CoO as well as spinel SiO_4Co (garnet phase). There was also a possibility of the formation of slight spinel Co_3O_4 which can coordinate with either the octahedral or the tetrahedral layer via oxygen which is in accordance with XRD, DRUV, FTIR, XPS, TPR, TPO and CV results [60, 61].

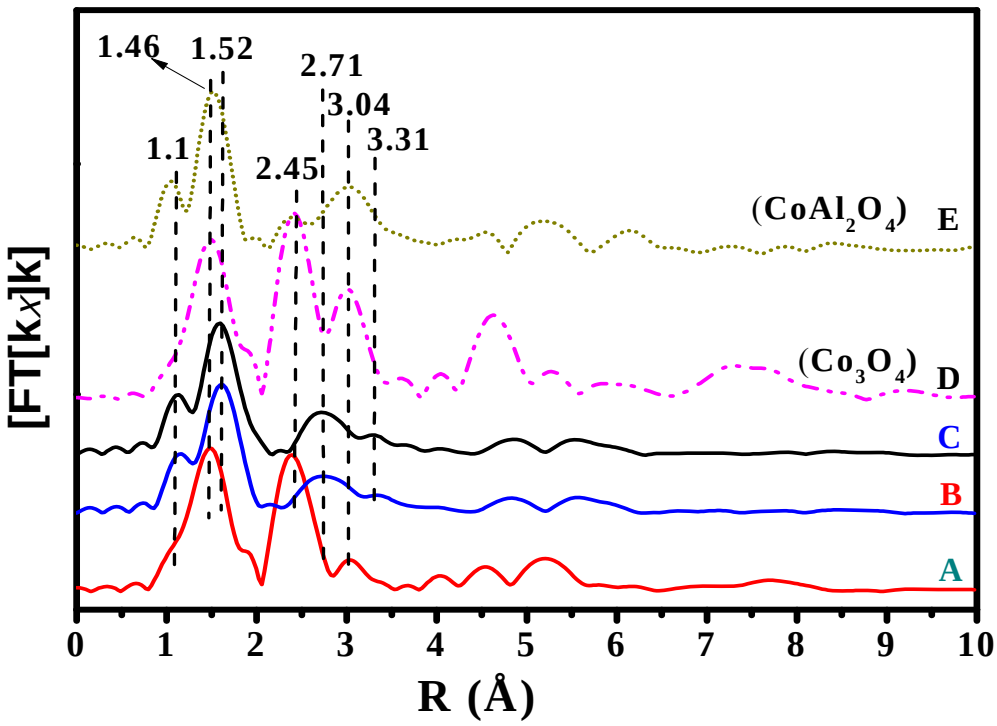

Figure 5.15. FT-EXAFS of (A) CSA-4, (B) CSA-4-3C, (C) CSA-4-5C, (D) Co-3C-a (Co_3O_4) and (E) CA-6C ($CoAl_2O_4$) samples

5.3. ACTIVITY MEASUREMENT

In our previous studies, it was found that cobalt aluminosilicate (especially saponite clay) was highly active for catalytic oxidation of *p*-cresol under mild reaction conditions [22]. Therefore as a continuation of this work, CSA-1 (cobalt aluminosilicate with Si:Al ratio 10:1) was evaluated for the liquid phase oxidation of veratryl alcohol (Scheme 5.1). However, CSA-1 did not show any activity for this reaction (Table 5.5, next section) due to its layered morphology (with restricted space mobility to two dimension) with small pore diameter (1.17 nm) and most of the surface active sites were trapped inside the layers. Veratryl alcohol having non-planar geometry with a larger size (9.2151 Å) than *p*-cresol (7.5454 Å) [Figure 5.16, A and B] [62-64] was rather difficult to diffuse through the pores (with 11.7 Å diameter) to access the cobalt active species

present inside. Considering this, cobalt aluminosilicates with different silica alumina ratios were prepared in order to get aluminosilicates with large pores so as to enable the substrate having non-planer geometry like veratryl alcohol can easily diffuse to interact with the active species. Vienna *ab-initio* Simulation Package (VASP) was used for the optimization of the structures [Figure 5.16, A and B] [62-64].

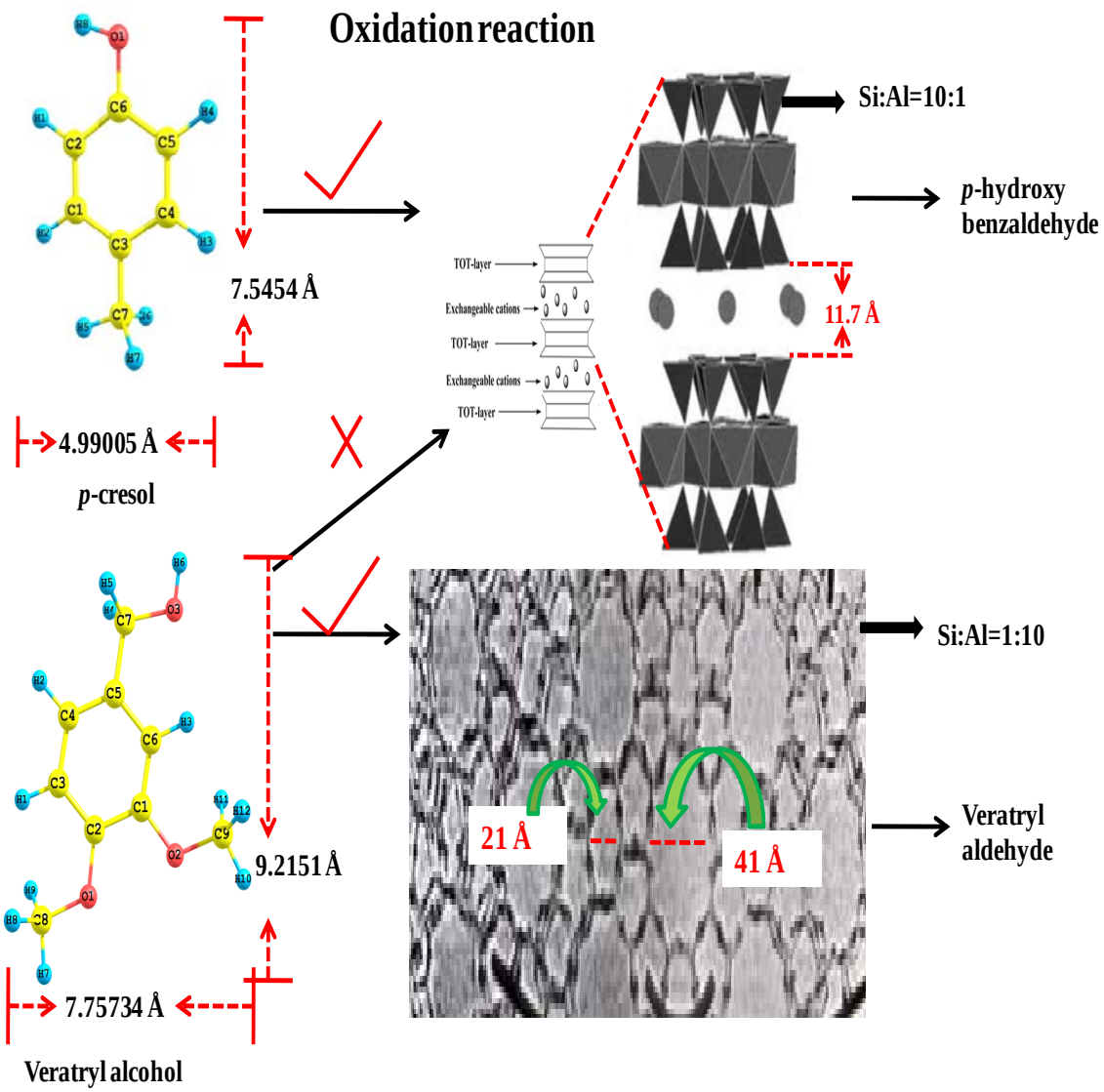

Scheme 5.1. Pictorial representation of oxidation reaction over the cobalt aluminosilicate Catalysts

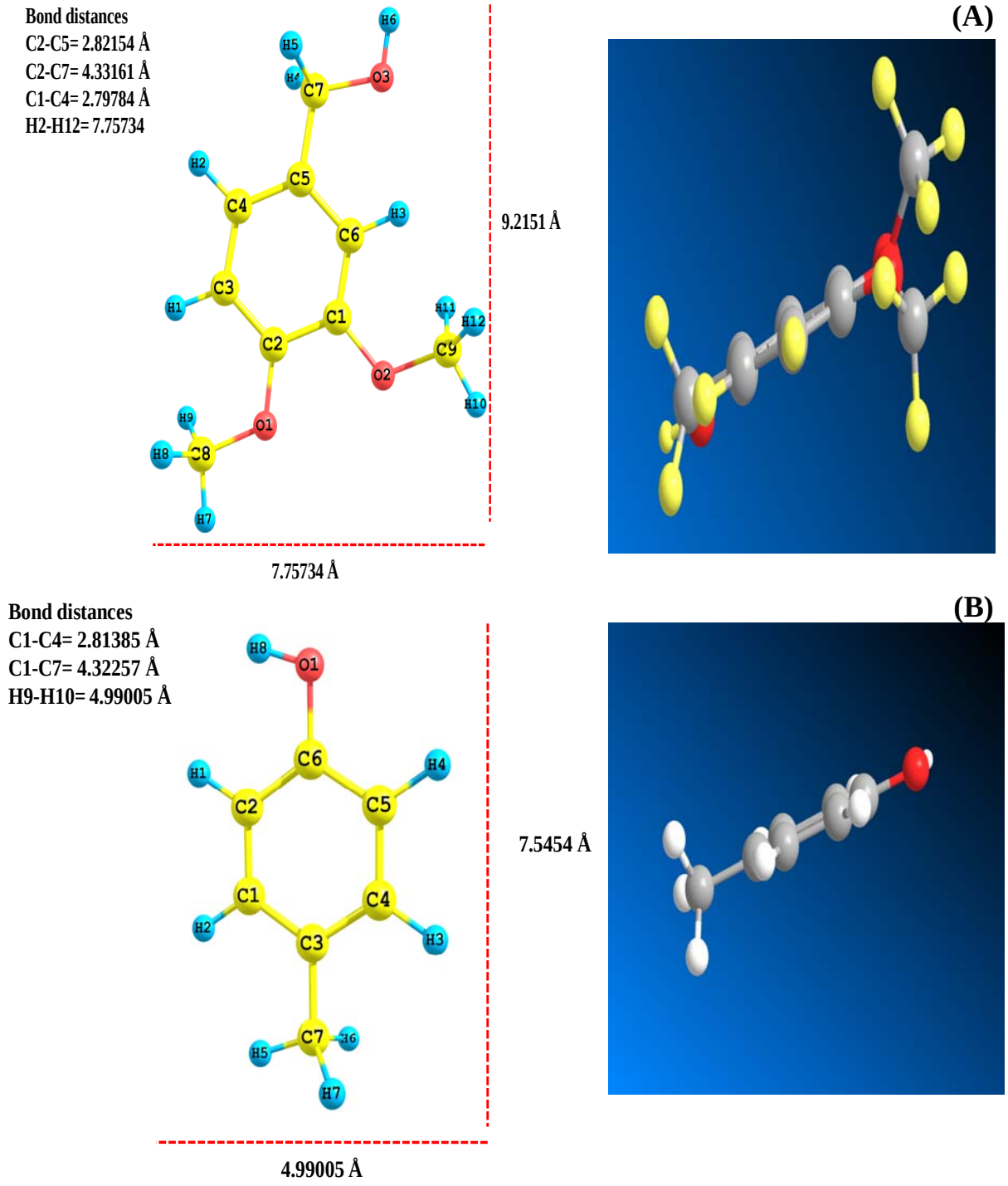

Figure 5.16. Three dimensional (3D) representations of (A) veratryl alcohol and (B) *p*-cresol molecules

5.3.1. Catalyst screening

The liquid phase oxidation of veratryl alcohol was carried out by using cobalt aluminosilicate catalysts with various Si:Al ratios (from 10:1 to 1:10). Based on the highest activity of the CSA-4 (having Si:Al ratio 1:10), other transition elements such as Cu, Mn and Fe were also used to prepare the corresponding metal aluminosilicate keeping Si:Al ratio constant at 1:10. The catalytic performance of these prepared catalysts is discussed in the following sections.

5.3.1.1. Effect of different transition elements

Various transition metal (such as Co, Cu, Fe and Mn) incorporated aluminosilicate with a constant Si:Al ratio of 1:10 were screened for the liquid phase oxidation of veratryl alcohol and results are shown in Table 5.5. Cobalt [43, 65], copper [66], iron [67] and manganese [68] were of particular interest since, these have long been known to reversibly bind and activate dioxygen forming mononuclear superoxo species responsible for catalytic oxidation of phenolic substrates [69]. Inspite of having almost equivalent surface areas (CSA-4, CuSA-4, FeSA-4 and MnSA-4); CSA-4 catalyst showed the highest activity among all the catalysts. The higher activity of the cobalt aluminosilicate than that of copper, iron and manganese catalysts was because of highly efficient redox system of cobalt ($Co^{2+} \leftrightarrow Co^{3+}$) responsible for the oxidation. The catalytic oxidation of veratryl alcohol to veratryl aldehyde over different catalysts was found to be in the following order: cobalt > iron > manganese > copper.

Table 5.5. Comparative catalytic activity and stability results of various metals aluminosilicate with Si:Al ratio 1:10

Catalysts	Elements	Surface area (m^2/g)	Conversion (%)	Selectivity (%)		Leaching of metal (ppm)
				Veratryl aldehyde	Veratric acid	
CSA-4	Cobalt	6.1	24.4	< 99.9	>0.1	ND
CuSA-4	Copper	5.4	15.7	< 99.9	>0.1	ND
FeSA-4	Iron	6.0	23.7	< 99.9	>0.1	ND
MnSA-4	Manganese	5.8	19.8	< 99.9	>0.1	ND

Reaction conditions: temperature, 413 K; oxygen pressure, 2.01 MPa; veratryl alcohol, 0.5 g (3 mmol); catalyst, 0.3 g; solvent toluene, 70 mL; NaOH, 1.0 g (24 mmol); agitation speed, 900 rpm; reaction time, 5 h. *ND: not detected

5.3.1.2. Effect of cobalt loading

The effect of cobalt loading (5-30%) in aluminosilicate (CSA-4) for the liquid phase oxidation of veratryl alcohol was studied and the results are shown in Figure 5.17. For this purpose, cobalt aluminosilicate catalysts were prepared with varying cobalt percentage from 5 to 30% and were evaluated for the oxidation of veratryl alcohol at 413 K and 2.01 MPa O_2 pressure conditions. It was observed that the conversion of veratryl alcohol increased with increase in Co loading from 5 to 15% and then remained constant up to 30% of Co loading. Hence, further work on the effects of various reaction parameters on conversion of veratryl alcohol and product selectivities was carried out over 15% cobalt aluminosilicate (CSA-4) catalyst. In each experiment, the final sample was analyzed by HPLC to calculate the conversion and product selectivities.

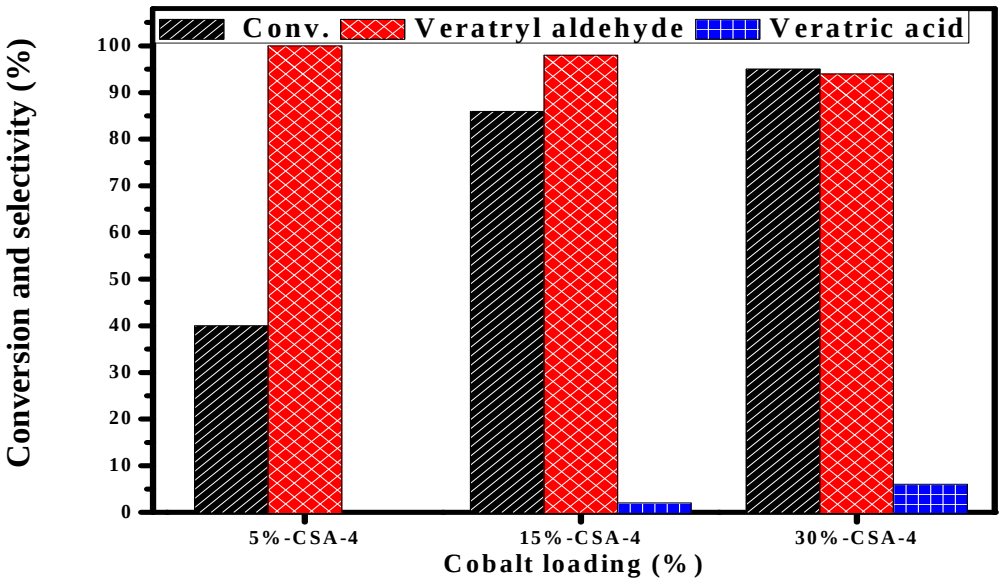

Figure 5.17. Effect of cobalt loading in aluminosilicate on catalytic oxidation of veratryl alcohol Reaction conditions: temperature, 413 K; oxygen pressure, 2.01 MPa; veratryl alcohol, 0.5 g (3 mmol); catalyst, 0.3 g; solvent toluene, 70 mL; NaOH, 1.0 g (24 mmol); a gitation speed, 900 rpm; reaction time, 5 h.

5.3.1.3. Effect of Si:Al ratio on activity

The results of Si:Al ratio on activity of alumina silicate for the liquid phase oxidation of veratryl alcohol to veratryl aldehyde are shown in the Table 5.6. For this purpose, cobalt (15%) aluminosilicate samples were prepared with varying Si:Al ratios in the range of 10:1 to 1:10. Among the prepared catalysts, highest catalytic activity was shown by CSA-4 sample (24.4% conversion and complete selectivity to veratryl aldehyde). The increase in conversion by six times (from 4.0% to 24.4%) due to gradual increase in pore diameter from 1.17 nm to 4.04 nm and increase in surface active cobalt Co^{2+}/Co^{3+} species resulted in enhancement of the formation of a redox couple on the surface as was observed in XPS, FTIR, TPR, TPO and CV analysis. Thus highest activity for the bulkier non-planar veratryl aldehyde molecule over CSA-4 catalyst

(inspite of having lower surface area 6.1 m^2/g) was due to mesopores with diameter 41 Å (4.10 nm) which allowed easy diffusion and adsorption via pore resulting into highest activity.

Table 5.6. Catalytic activity of 15% cobalt loading in aluminosilicate having different Si:Al ratio

Catalysts	Si:Al ratio	Surface area (m^2/g)	Conversion (%)	Selectivity (%)	
				Veratryl aldehyde	Veratric acid
CSA-1	10:1	232.8	4.0	> 99.9	<0.1
CSA-2	1:1	120.0	7.6	>99.9	<0.1
CSA-3	1:5	13.3	15.8	>99.9	<0.1
CSA-4	1:10	6.1	24.4	>99.9	<0.1

Reaction conditions: temperature, 413 K; oxygen pressure, 2.01 MPa; veratryl alcohol, 0.5 g (3 mmol); catalyst, 0.3 g; solvent toluene, 70 mL; NaOH, 1.0 g (24 mmol); agitation speed, 900 rpm; reaction time, 5 h.

5.3.2. Effect of catalyst pretreatment conditions

5.3.2.1 Effect of calcination temperature

Various samples of CSA-4 catalyst were prepared and calcined in a temperature range of 573-773 K. As can be seen from the Table 5.7, it was observed that the conversion increased more than three times (from 24.4 to 86%) with increase in calcination temperature from 423 to 573 K. However, the selectivity to veratryl aldehyde decreased from 99.9% to 94%, due to further oxidation of veratryl aldehyde to veratric acid. The increase in conversion by more than three times was due to increase in surface area by 18 times from 6.1 to 113.5 m^2/g which eventually caused a significant increase in cobalt (Co^{2+} and Co^{3+}) active species. The significant increase in active species in case of a sample calcined at 573 K was due to dehydration and decomposition

of water molecules and other starting precursors present in the mesopores (diameter 4.04 nm) and on the surface, as evidenced by various characterization results discussed in previous sections. However, with increase in calcination temperature from 573 to 673 and 773 K, marginal decrease in activity was observed (from 86% to 80.7% and 78.9% respectively). The increase in calcination temperature from 573 K to 673 K caused dehydroxylation of surface hydroxyl group causing disruption of surface morphology, slight decrease in pore diameter from 4.10 nm to 3.98 and slight decrease in surface area from 113.5 to 102.2 and 96.2 m^2/g resulted in decrease in number of active sites as well as it retarded diffusion of the substrate through the micropores.

Table 5.7. Effect of calcination temperature on catalytic activity

Catalysts	Calcination temperature (K)	Surface area (m^2/g)	Conversion (%)	Selectivity (%)	
				Veratryl aldehyde	Veratric acid
CSA-4	423	6.1	24.4	< 99.9	>0.1
CSA-4-3C	573	113.5	86.0	94.0	6.0
CSA-4-4C	673	102.2	80.7	93.0	7.0
CSA-4-5C	773	96.2	78.9	94.0	6.0

Reaction conditions: temperature, 413 K; oxygen pressure, 2.01 MPa; veratryl alcohol, 0.5 g (3 mmol); catalyst, 0.3 g; solvent toluene, 70 mL; NaOH, 1.0 g (24 mmol); agitation speed, 900 rpm; reaction time, 5 h.

5.3.2.2. Effect of calcination time

The calcination times was varied from 1 to 6 h for the CSA-4 sample at constant calcination temperature (573 K). The catalytic activity of these catalysts prepared with different calcination time was evaluated in toluene and the activity was found to be increase by about three times, with increase in calcination time from 1 to 6 h (Table 5.8). Enhancement in the catalytic activity was due to increase in active sites resulted from increase in surface area by nine times (from 12.6 to 114.2 m^2/g) for the increase in calcination time from 1 to 6 h. The increase in calcination time facilitates the removal of water and other starting precursors trapped in the inter layers and mesopores of the catalyst, leading to significant increase in cobalt active species (Co^{2+} and Co^{3+}). The optimum calcination time was found to be 5 h required to remove these molecules from CSA-4 catalyst, beyond which (6 h) both surface area and catalytic activity were found to be constant.

Table 5.8. Effect of calcination time on catalytic performance

Catalysts	Calcination Time, (h)	Surface area, (m^2/g)	Conversion, (%)	Selectivity, (%)	
				Veratryl aldehyde	Veratric acid
CSA-4-3C	1	12.6	31.3	98.0	2.0
CSA-4-3C	2	26.5	45.4	97.5	2.5
CSA-4-3C	3	57.3	48.9	97.0	3.0
CSA-4-3C	4	99.3	61.7	93.0	7.0
CSA-4-3C	5	113.5	86.0	94.0	6.0
CSA-4-3C	6	114.2	86.6	94.0	6.0

Reaction conditions: temperature, 413 K; oxygen pressure, 2.01 MPa; veratryl alcohol, 0.5 g (3 mmol); catalyst, 0.3 g; solvent toluene, 70 mL; NaOH, 1.0 g (24 mmol); agitation speed, 900 rpm; reaction time, 5 h.

5.3.3. Optimization of reaction conditions

Among the prepared catalysts, CSA-4-3C (cobalt aluminosilicate with Si:Al 1:10 and calcined at 573 K) was found to exhibit the highest activity for liquid phase oxidation of veratryl alcohol. Further catalyst development as well as optimization of reaction conditions using active CSA-4-3C catalyst is discussed in the following sections.

5.3.3.1. Effect of NaOH concentration

Although, veratryl alcohol is a dimethoxy aryl alcohol, we expected that NaOH would play a role similar to that in case of phenolic –OH. Hence effect of NaOH concentration on the veratryl alcohol conversion and oxidation product selectivities was studied and the results are shown in Figure 5.18. It is known that oxidation of phenolic (such as *p*-cresol) compounds proceeds only after the conversion of –OH group in to its sodium salt [3]. The conversion of veratryl alcohol increased from 35 to 90% with increase in NaOH concentration from 3 to 30 mmol while the selectivity to veratryl aldehyde decreased from 100 to 93% and that for veratric acid increased from 0 to 7%. Beyond 24 mmol of NaOH concentration, conversion of veratryl alcohol marginally increased from 86 to 90%. With further increase in NaOH concentration to 30 mmol, conversion of veratryl alcohol was almost constant. A blank run (without NaOH) showed 20% conversion with complete selectivity to veratryl aldehyde. Only with increase in NaOH concentration conversion of veratryl alcohol increased while veratryl aldehyde to veratric acid remained almost same. However, more detailed investigation is necessary to study the exact role of NaOH in enhancing the catalytic activity especially, when non phenolic compound was used.

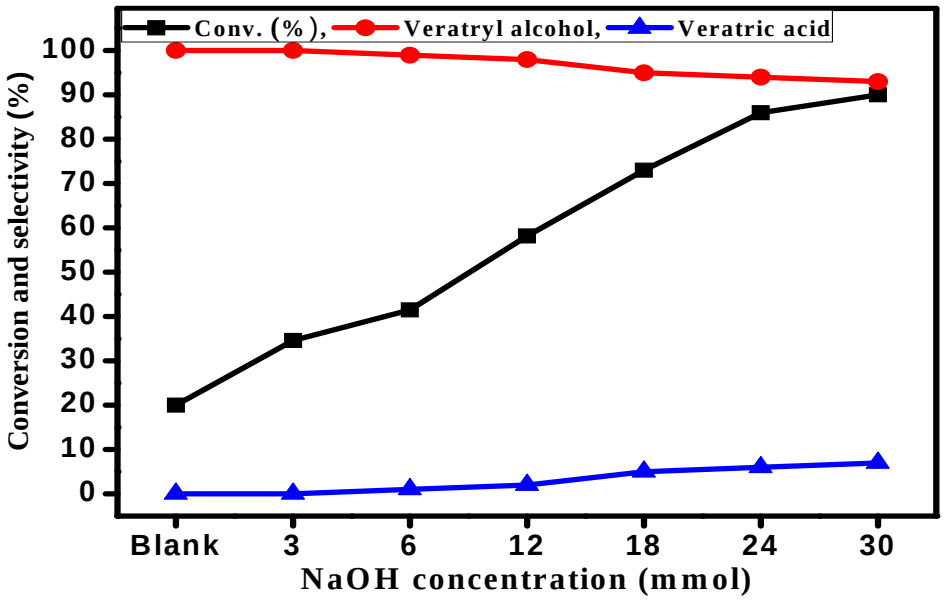

Figure 5.18. Effect of NaOH concentration on oxidation of veratryl alcohol on CSA-4-3C catalyst

Reaction conditions: temperature, 413 K; oxygen pressure, 2.01 MPa; veratryl alcohol, 0.5 g (3 mmol); catalyst, 0.3 g; solvent toluene, 70 mL; agitation speed, 900 rpm; reaction time, 5 h.

5.3.3.2. Effect of temperature

The effect of temperature on veratryl alcohol conversion and selectivity was studied in the temperature range of 393 to 433 K and the results are presented in Figure 5.19. The conversion of veratryl alcohol increased from 44 to 96% with increase in temperature from 393 to 433 K. The selectivity to veratryl aldehyde decreased gradually (100 to 80%) giving veratric acid with increase in temperature. This clearly indicated that veratryl aldehyde was the first intermediate formed in veratryl alcohol oxidation, while the reaction pathway was found to be similar with the reaction with nano Co-3C-a (Co_3O_4) spinel catalyst (Scheme 3.1, Chapter 3). The rate of oxidation increased with increase in temperature, and the activation energy evaluated from the Arrhenius plot was 26.76 $KJmole^{-1}K^{-1}$ (Figure 5.20).

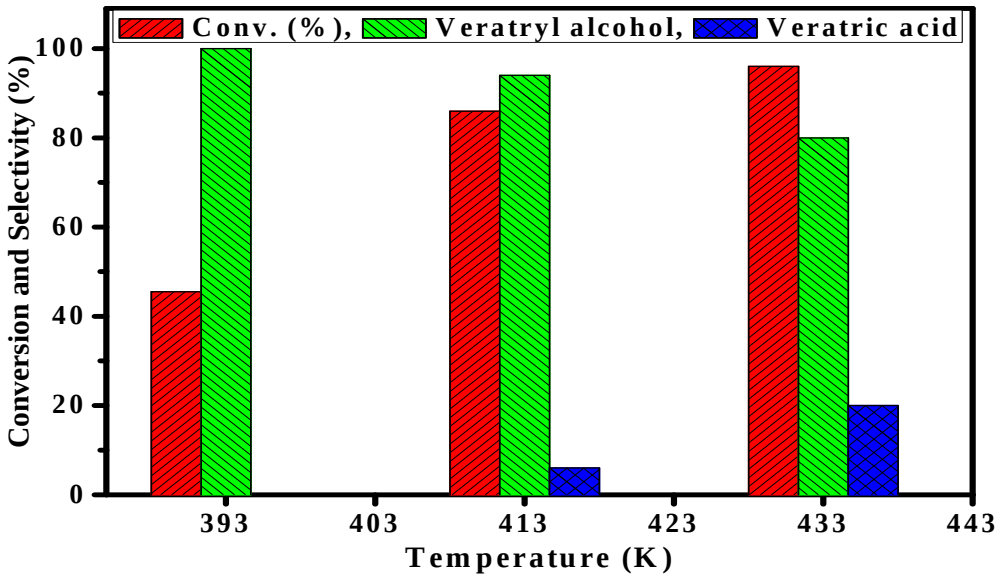

Figure 5.19. Effect of reaction temperature on conversion and selectivity

Reaction conditions: oxygen pressure, 2.01 MPa; veratryl alcohol, 0.5 g (3 mmol); catalyst, 0.3g; solvent toluene, 70 mL; NaOH, 1.0 g (24 mmol); agitation speed, 900 rpm; reaction time, 5 h.

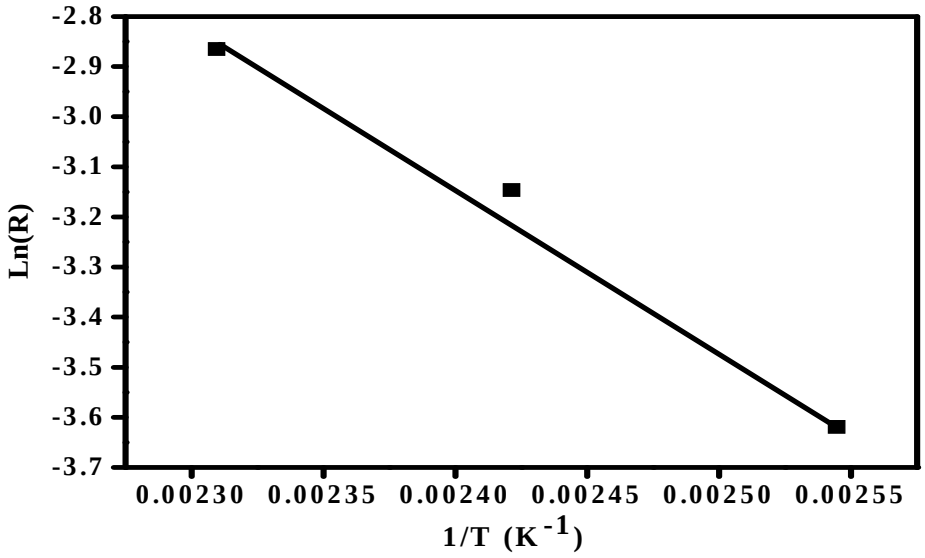

Figure 5.20. Arrhenius plot

5.3.3.3. Effect of pressure

In order to study the effect of partial oxygen pressure on conversion of veratry alcohol and selectivity to veratryl aldehyde, oxidation experiments were carried out by varying the oxygen pressure in the range of 0.68-4 MPa at 413 K and the results are shown in Figure 5.21. It was found that the conversion of veratryl alcohol increased from 46 to 95% as the oxygen pressure increased from 0.68 to 4.13 MPa. However, the selectivity to veratryl aldehyde decreased from 98 to 86% due to its further conversion to veratric acid at higher concentration of oxygen. The substantial increase in conversion was due to the higher oxygen solubilty at higher pressures [70].

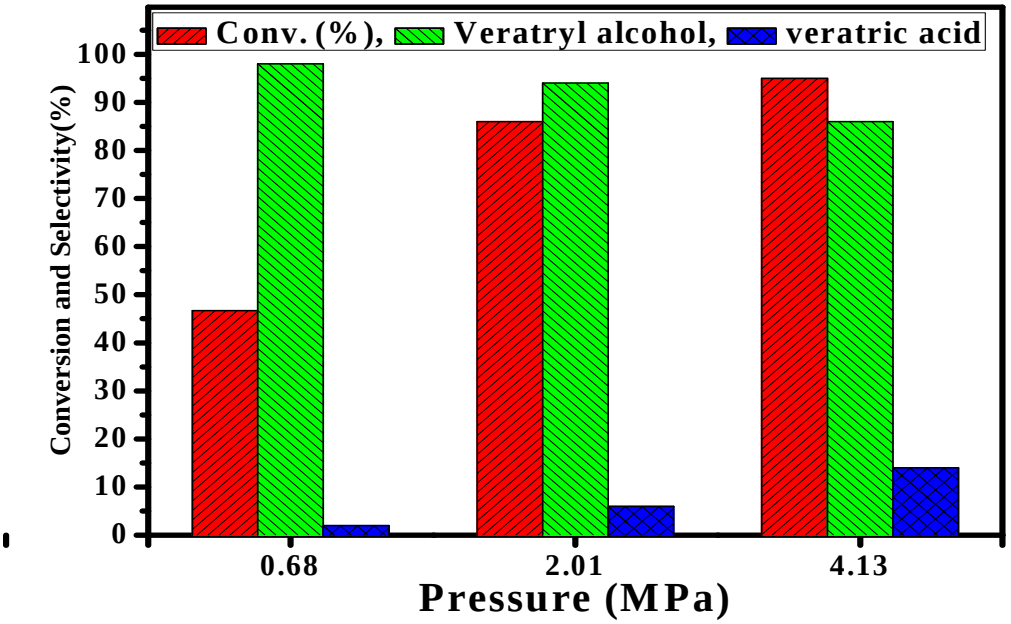

Figure 5.21. Effect of pressure on catalytic activity

Reaction conditions: temperature, 413 K; veratryl alcohol, 0.5 g (3 mmol); catalyst, 0.3 g; solvent toluene, 70 mL; NaOH, 1.0 g (24 mmol); agitation speed, 900 rpm; reaction time, 5 h.

5.3.3.4. Effect of catalyst loading

Effect of catalyst loading in the range of 0.1 to 0.3 g on veratryl alcohol conversion and product selectivity was also studied and the results are presented in Figure 5.22. The veratryl alcohol conversion increased from 27 to 86% with increase in catalyst loading from 0.1 to 0.3 g. This is obvious since with increase in catalyst concentration; the number of active cobalt sites also increased which facilitated the conversion of veratryl alcohol to veratryl aldehyde. However, the selectivity for veratryl aldehyde decreased from 100 to 94% as the catalyst concentration increased from 0.1 to 0.3 g due to its further conversion to veratric acid.

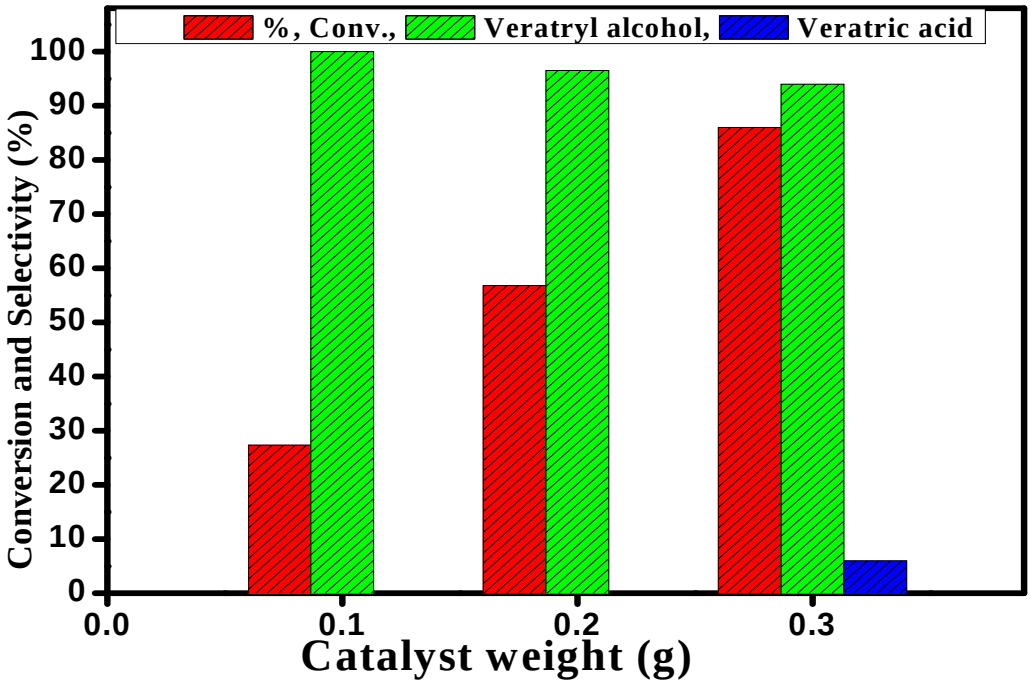

Figure 5.22. Result of catalyst loading on liquid phase oxidation of the veratryl alcohol

Reaction conditions: temperature, 413 K; oxygen pressure, 2.01 MPa; veratryl alcohol, 0.5 g (3 mmol); solvent toluene, 70 mL; NaOH, 1.0 g (24 mmol); agitation speed, 900 rpm; reaction time, 5 h.

5.3.3.5. Solvent screening

The oxidation of veratryl alcohol was also investigated in various solvents and the results are shown in Table 5.9. The CSA-4-3C catalyst was found to be active only in non polar toluene solvent while it was inactive in all polar solvents. This order of activity was not consistent with the order of polarity of the solvents [71], and it was rather dependent on the hydrophilic property of the catalyst which in polar solvents cause the blockage of active species significantly as evidenced by TG-DTA, SEM, TEM, TPR and TPO characterizations discussed in earlier sections. Thus, the choice of solvent was critical in order to achieve the optimum activity.

Table 5.9. Solvent effect on catalytic performance of CSA-4-3C sample

Solvents	**Conversion (%)**	**Selectivity (%)**	
		Veratryl aldehyde	**Veratric acid**
Water	<0.1	99	1
Methanol	<0.1	99	1
Ethanol	<0.1	99	1
n-propanol	<0.1	99	1
Toluene	86.0	94.0	6.0

Reaction conditions: temperature, 413 K; oxygen pressure, 2.01 MPa; veratryl alcohol, 0.5 g (3 mmol); catalyst, 0.3 g; solvent, 70 mL; NaOH, 1.0 g (24 mmol); agitation speed, 900 rpm; reaction time, 5 h.

5.3.3.6. Reusability and stability experiment

In order to ensure that the activity of CSA-4-3C catalyst was constant during the run, catalyst recycle experiments were carried out, in which the catalyst was found to retain its original activity and selectivity even after the fifth recycle (Figure 5.23). The stability of the CSA-4-3C

catalyst under the reaction conditions was also confirmed by conducting leaching test. For this purpose, the oxidation experiment was interrupted after (3 h) a partial conversion of ~ 57% and the catalyst was removed by filtration and the reaction was further continued without the catalyst. As can be seen from Figure 5.24, the conversion of veratryl alcohol remained constant at ~ 57% after continuing the reaction without the catalyst. Thus above results indicated true heterogeneous nature of our catalyst.

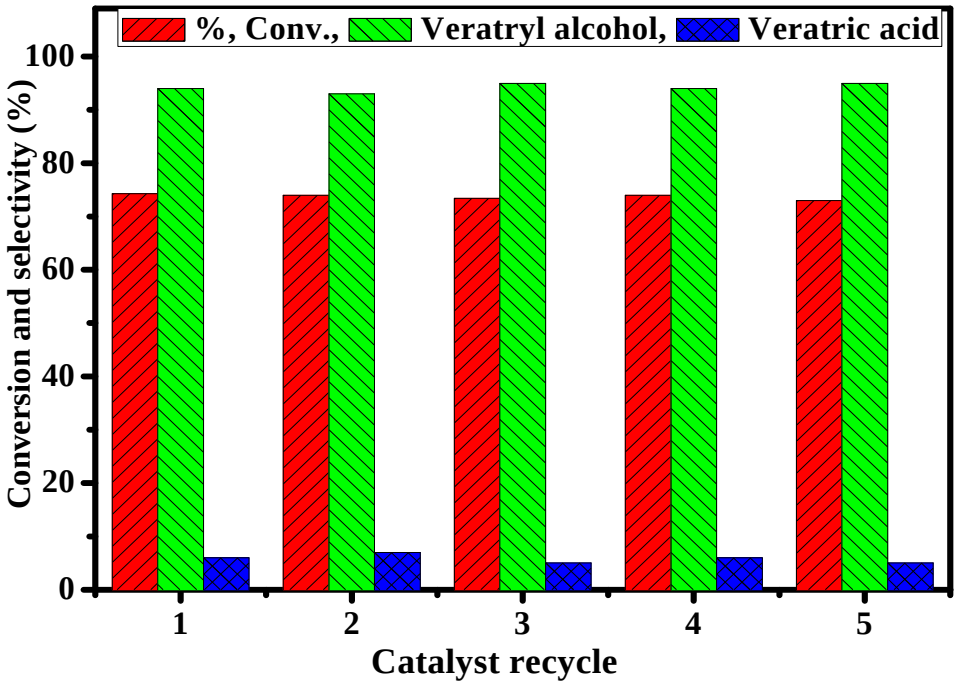

Figure 5.23. Catalyst recycle study

Reaction conditions: temperature, 413 K; oxygen pressure, 2.01 MPa; catalyst, CSA-4-3C; veratryl alcohol, 0.5 g (3 mmol); catalyst, 0.3 g; solvent toluene, 70 mL; NaOH, 1.0 g (24 mmol); agitation speed, 900 rpm; reaction time, 5 h.

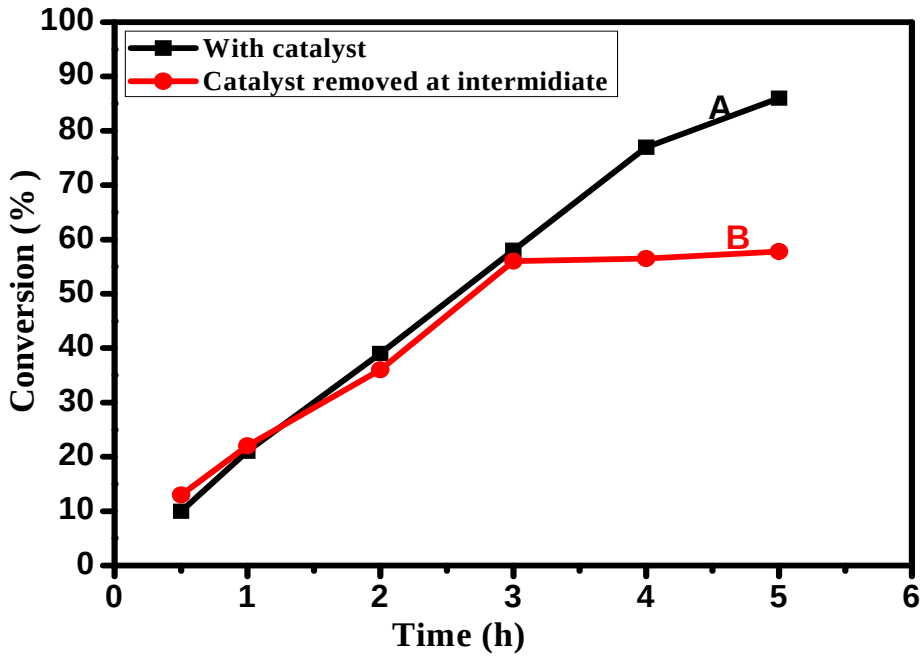

Figure 5.24. Leaching test for the CSA-4-3C catalyst during oxidation of veratryl alcohol

Reaction conditions: temperature, 413 K; oxygen pressure, 2.01 MPa; veratryl alcohol, 0.5 g (3 mmol); catalyst, 0.3 g; solvent toluene, 70 mL; NaOH, 1.0 g (24 mmol); agitation speed, 900 rpm; reaction time, 5 h.

5.4. CONCLUSIONS

- The cobalt aluminosilicates catalysts with various Si:Al ratios were prepared by simple co-precipitation method.
- The change in Si:Al ratio from 10:1 to 1:10 caused change in the physico-chemical properties as well as change from hydrophobic to hydrophilic nature which was confirmed by various characterization techniques. The pore diameter changed from 1.17 nm to 4.04 nm with increase in pore diameter from 1.17 to 4.04 nm and enhancement in the redox ability due to increase in distribution of surface active Co^{2+}/Co^{3+} species. The catalytic

oxidation of veratryl alcohol to veratryl aldehyde over different catalysts (aluminosilicates with Si:Al 1:10 ratios) was found to be in the following order: cobalt > iron > manganese > copper.

- Among the prepared catalysts, aluminosilicates with Si:Al 1:10 ratio having 15% cobalt loading showed the highest conversion of 86% for the oxidation of veratryl alcohol with a selectivity 94% to veratryl aldehyde and 6% veratric acid.
- Increase in Si:Al ratio from 10:1 to 1:10 caused increase in pore diameter from 1.17 to 4.04 nm leading to activity enhancement by six times (from 4% to 24 %) for veratryl alcohol oxidation.
- Activation energy for oxidation of veratryl alcohol over CSA-4-3C catalyst found to be 26.7 $KJmole^{-1}K^{-1}$.

5.5. REFERENCES

1. A. Corma, *Chem. Rev.* 97 (1997) 2373.
2. A. C. Garade, N. S. Biradar, S. M. Joshi, V. S. Kshirsagar, R. K. Jha, C. V. Rode, *Appli. Clay Sci.* 53 (2011) 157.
3. V. S. Kshirsagar, A. C. Garade, R. B. Mane, K. R. Patil, A. Yamaguchi, M. Shirai, C. V. Rode, *Appl. Catal. A: Gen.* 370 (2009) 16.
4. A. C. Garade, V. R. Mate, C. V. Rode, *Appli. Clay Sci.* 43 (2009) 113.
5. Z. T. Zhang, Y. Han, F. S. Xiao, S. L. Qiu, L. Zhu, R. W. Wang, Y. Yu, Z. Zhang, B. S. Zou, Y. Q. Wang, H. P. Sun, D. Y. Zhao, Y. Wei, *J. Am. Chem. Soc.* 123 (2001) 5014.
6. H. Yang, A. Kuperman, N. Coombs, S. Mamicheafara, G. A. Ozin, *Nature* 379 (1996) 703.
7. Y. Wang, F. Caruso, *Chem. Commun.* 13 (2004) 1528.
8. C. Y. Lai, B. G. Trewyn, D. M. Jeftinija, K. Jeftimija, S. Xu, V. S. Y. Lin, *J. Am. Chem. Soc.* 125 (2003) 4451.
9. R. M. Krishna, A. M. Prakash, L. Kevan, *J. Phys. Chem. B* 104 (2000) 1796.
10. A. Szegedi, M. Hegedus, J. L. Margitfalvi, I. Kiricsi, *Chem. Commun.* 11 (2005) 1441.
11. R. Mokaya, *Angew. Chem.* 111 (1999) 3079.
12. R. Mokaya, *Angew. Chem. Int. Ed.* 38 (1999) 2930.
13. R. Ryoo, S. Jun, J. M. Kim, M. J. Kim, *Chem. Commun.* 22 (1997) 2225.
14. Z. Luan, M. Hartmann, D. Zhao, W. Zhou, L. Kevan, *Chem. Mater.* 11 (1999) 1621.
15. S. Sumiya, Y. Oumi, T. Uozumi, T. Sano, *J. Mater. Chem.* 11 (2001) 1111.
16. M. Morey, S. O'Brien, S. Schwarz, G. D. Stucky, *Chem. Mater.* 12 (2000) 898.

17. B. L. Newalkar, J. Olanrewaju, S. Komarneni, *Chem. Mater.* 13 (2001) 552.

18. Y. Han, F. S. Xiao, S. Wu, Y. Sun, X. Meng, D. Li, S. Lin, *J. Phys. Chem. B.* 105 (2001) 7963.

19. Y. Liu, T. J. Pinnavaia, *Chem. Mater.* 14 (2002) 3.

20. W. Li, S. Huang, S. Liu, M. O. Coppens, *Langmuir* 21 (2005) 2078.

21. Y. Li, J. Shi, H. Chen, Z. Hua, L. Zhang, M. Ruan, J. Yan, D. Yan, *Microporous Mesoporous Mater.* 60 (2003) 51.

22. V. S. Kshirsagar, A. C. Garade, K. R. Patil, M. Shirai, C. V. Rode, *Top. Catal.* 52 (2009) 784.

23. D. J. Yang, Y. Xu, S. R. Zh, J. L. Zh, J. P. Li, D. Wu, Y. H. Sun, *Chem. Lett.* 34 (2005) 1138.

24. D. J. Yang, Y. Xu, D. Wu, Y. H. Sun, *J. Phys. Chem. C* 111 (2007) 999.

25. C. V. Rode, A. C. Garade, R. C. Chikate, *Catal. Surv. Asia* 13 (2009) 205.

26. A. L. Gutman, G. Nisnevich, E. Shkolnik, B. Tishin, I. Zaltzman, US Patent, 6,492,522 (2002).

27. Z. Zhang, Y. Han, F. S. Xiao, S. Qiu, L. Zhu, R. Wang, Y. Yu, Z. Zhang, B. Zou, Y. Wang, H. Sun, D. Zhao, Y. Wei, *J. Am. Chem. Soc.* 123 (2001) 5014.

28. K. S. W. Sing, D. H. Everett, R. A. W. Haul, L. Moscou, R. A. Pierotti, J. Rouquerol, *Pure & Appl. Chem.* 57 (1985) 603.

29. J. Weitkamp, M. Hunger, U. Rymsa, *Microporous Mesoporous Mater.* 48 (2001) 255.

30. E. Masika, R. Mokaya, *Chem. Mater.* 23 (2013) 2491.

31. J. C. Groen, L. A. Peffer, J. P. Ramirez, *Microporous Mesoporous Mater.* 60 (2003) 1.

32. H. Shao, T. J. Pinnavaia, *Microporous Mesoporous Mater.* 133 (2010) 10.

33. E. M. Serwicka, R. Mokaya, J. Połtowicz, W. Jones, *ChemPhysChem*. 3 (2002) 892.

34. M. M. Duane, C. R. Robert, II Ed. ed., Oxford university press, 1997.

35. R. S. da Cruz, A. J. S. Mascarenhas, H. M. C. Andrade, *Appl. Catal. B: Envi.* 18 (1998) 223.

36. J. M. Stencel, V. U. S. Rao, J. R. Diehl, K. H. Rhee, A. G. Dhere, R. J. DeAngelis, *J. Catal.* 84 (1983) 109.

37. Y. Chen, D. R. U. Knappe, M. A. Barlaz, *Environ. Sci. Technol.* 38 (2004) 3731.

38. G. Fierro, M. A. Eberhardt, M. Houalla, D. M. Hercules, W. K. Hall, *J. Phys. Chem.* 100 (1996) 8468.

39. J. Janas, T. Machej, J. Gurgul, R. P. Socha, M. Che, S. Dzwigaj, *Appl. Catal. B: Envi.* 75 (2007) 239.

40. M. Mhamdi, E. Marceau, S. Khaddar-Zine, A. Ghorbel, M. Che, Y. B. Taarit, F. Villain, *Catal. Lett.* 98 (2004) 135.

41. B. M. Weckhuysen, A. A. Verberckmoes, M. G. Uytterhoeven, F. E. Mabbs, D. Collison, E. de Boer, R. A. Schoonheydt, *J. Phys. Chem. B* 104 (2000) 37.

42. S. L. Suib, *Chem. Rev.* 93 (1993) 803.

43. V. S. Kshirsagar, A. C. Garade, K. R. Patil, R. K. Jha, C. V. Rode, *Ind. Eng. Chem. Res.* 48 (2009) 9423.

44. V. S. Kshirsagar, A. C. Garade, K. R. Patil, M. Shirai, C. V. Rode, *Top. Catal.* 52 (2009) 784.

45. L. Xu, S. Wu, J. Guan, Y. Ma, K. Song, H. Xu, C. Xu, Z. Wang, Q. Kan, *Catal. Commun.* 9 (2008) 1970.

46. J. A. Cecilia, C. G. Sancho, F. Franco, *Microporous Mesoporous Mater*. 176 (2013) 95.

47. M. F. Brigatti, L. Poppi, *Clays Clay Miner.* 33 (1985) 128.

48. J. C. Davidtz, P. F. Low, *Clays Clay Miner.* 8 (1970) 325.

49. E. J. M. Hensen, B. Smit, *J. Phys. Chem. B* 106 (2002) 12664.

50. H. W. van der MAREL, H. Beutelspacher, Atlas of infrared spectroscopy of clay minerals and their admixtures, Amsterdam, 1974.

51. P. A. Chernavskii, A. Y. Khodakov, G. V. Pankina, J. S. Girardon, E. Quinet, *Appl. Catal. A: Gen.* 306 (2006) 108.

52. L. F. Liotta, G. D. Carlo, G. Pantaleo, A. M. Venezia, G. Deganello, *Appl. Catal. B: Env.* 66 (2006) 217.

53. X. Xie, W. Shen, *Nanoscale* 1 (2009) 50.

54. V. R. Mate, M. Shirai, C. V. Rode, *Catal. Commun.* 33 (2013) 66.

55. P. A. Chernavskii, A. Y. Khodakov, G. V. Pankina, J. S. Girardon, E. Quinet, *Appl. Catal. A: Gen.* 306 (2006) 108.

56. J. Jansson, A. Palmqvist, E. Fridell, M. Skoglundh, L. O sterlund, P. Thormahlen, V. Langer, *J. Catal.* 211 (2002) 387.

57. E. A. Stern, M. Newville, B. Ravel, Y. Yacoby, D. Haskel, *Physica B* (1995) 117.

58. A. L. Ankudinov, B. Ravel, J. J. Rehr, S. D. Conradson, *Phys. Rev. B* (1998) 7565.

59. R. G. Leliveld, T. G. Ros, A. J. van Dillen, J. W. Geus, D. C. Koningsberger, *J. Catal.* 185 (1999) 513.

60. E. Burattini, G. Dalba, A. Kuzmin, A. Lusis, G. Mariotto, *J. Purans, Phys. Stat. Sol.* 129 (1992) K61.

61. E. Burattini, J. Purans, A. Kuzmin, *Jap. J. Appl. Phys.* 32 (1993) 655.

62. G. Kresse, J. Furthmuller, *J. Comp. Mater. Sci.* 6 (1996) 15.

63. G. Kresse, J. Furthmuller, *Phys. Rev. B.* 54(16) (1996) 11169.

64. G. Kresse, J. Hafner, *Phys. Rev. B.* 47(1) (1993) 558.

65. R. A. Sheldon, J. Kochi, Metal-catalyzed oxidations of organic compounds, Academic Press (1981) 72.

66. A. Santos, P. Yustos, A. Quintanilla, F. Garcia-Ochoa, *Top. Catal*. 33 (2005) 181.

67. A. C. Garade, M. Bharadwaj, S. V. Bhagwat, A. A. Athawale, C. V. Rode, *Catal. Commun.* 10 (2009) 485.

68. M. A. Wolfovich, R. Jothiramalingam, M. V. Landau, M. Herskowitz, B. Viswanathan, T. K. Varadarajan, *Appl. Catal. B: Envi.* 59 (2005) 91.

69. Martell, (Eds. Martell, A.; Sawyer, D.), in Oxygen complexes and oxygen activation by transition metals, Plenum Press (1987).

70. V. S. Kshirsagar, J. M. Nadgeri, P. R. Tayade, C. V. Rode, *Appl. Catal. A: Gen.* 339 (2008) 28.

71. C. Reichardt, Solvents and Solvent Effects in Organic Chemistry Wilay-VCH Pub Verlag GmbH & Co. KGaA, 1988.

Chapter 6

Summary and conclusions

6.1. SUMMARY AND CONCLUSIONS

In this thesis, a detailed study on preparation of three types of heterogeneous cobalt based catalytic systems viz. nano Co_3O_4, Zn and Al doped Co_3O_4 and cobalt aluminosilicates, their characterization and evaluation for oxidation of various important lignin derived phenolic and non-phenolic sub-structured compounds was carried out. The summary and main conclusions of this work are given below.

1. Spinel Co_3O_4 was prepared by three different methods, (i) co-precipitation (ii) sol-gel and (iii) thermal decomposition. All the preparation methods are studied in this work gave the formation of cubic type of Co_3O_4 spinel. The highest surface area (110 m^2/g) with lowest crystallite size (10-20 nm) and controlled rod –like morphology could be achieved for Co_3O_4 prepared by only co-precipitation method. All these characteristics of the co-precipitated (pH= 7-8) nano Co_3O_4 spinel catalyst led to its highest activity (38% conversion) for the liquid phase oxidation of veratryl alcohol to veratryl aldehyde.
2. The increase in calcination temperature from 573-873 K of the co-precipitated Co_3O_4, led to significant decrease in its oxidation activity due to change in meso to micro porous nature, decrease in surface area and increase in crystallite size.
3. The highest redox ability of the most active Co_3O_4 was due to the presence of higher number of Co^{3+} in an octahedral position and Co^{2+} in tetrahedral position as evidenced by XPS, FT-IR, TPR, TPO and CV studies.
4. The mixed oxides of spinel Co_3O_4 were prepared by doping Zn^{2+} and Al^{3+}.

5. With increase in cobalt in Zn:Co composition from 1:1 to 1:3, caused increase in distribution of surface active Co^{2+} and Co^{3+} subsequently, leading to enhancement in its oxidation ability for conversion of veratryl alcohol to veratryl aldehyde.
6. In case of Al doped Co_3O_4, 1:3 ratio of Co:Al showed the best activity. However both Zn:Co (1:3) and Co:Al (3:1) showed lower activity than the pure spinel Co_3O_4, indicating Zn as well as Al did not participate in the formation of any type of redox system with Co.
7. The third type of catalyst was developed by *in-situ* preparation of cobalt aluminosilicate with silica alumina ratio varied as 10:1, 1:1, 1:5 and 1:10. The change in Si:Al ratio from 10:1 to 1:10 transformed pore size from micro (~2.0 nm) to meso (~5.2 nm) and led to increase in disorder in layered morphology. Among these catalysts, CSA-4-3C (15% Co with Si:Al ratio 1:10) showed the highest activity for the oxidation of veratryl alcohol with 86% conversion and 96% selectivity to veratryl aldehyde.

6.2. LIST OF PUBLICATIONS

Research papers published in peer reviewed journals

1. Heterogeneous Co_3O_4 catalyst for selective aqueous oxidation of veratryl alcohol using molecular oxygen, **V. R. Mate**, M. Shirai, C. V. Rode, *Catal. Commun.*, 13 (2013) 66-69.
2. Selectivity tailoring in liquid phase oxidation over MWNT-Mn_3O_4 nanocomposite catalysts, M. Biswal, V. V. Dhas, **V. R. Mate**, A. Banerjee, P. Pachfule, K. L. Agrawal, S. B. Ogale, C. V. Rode *J. Phys. Chem. C*, 115 (2011) 15440–15448.
3. Montmorillonite for selective hydroxyalkylation of *p*-cresol, A. C. Garade, **V. R. Mate**, C. V. Rode, *Applied Clay Science*, 43 (2009) 113–117.
4. Cobalt aluminosilicate catalysts: Preparation, characterization and catalytic performance for liquid phase oxidation veratryl oxidation, **V. R. Mate,** A. Jha, A. C. Garade, K. R. Patil, A. Yamaguchi, M. Shirai, C.V. Rode, *communicated.*
5. Facile synthesis of nano spinel Co_3O_4 catalyst for liquid phase oxidation of veratryl alcohol **V. R. Mate**, A. Jha, H. S. Potdar, K. R. Patil, R. Pant, M.Shirai, A. Yamaguchi, C. V. Rode, *communicated.*

b) Presentations in national/international symposia

1. "Spinel Co_3O_4 catalyzed oxidation of lignin model compounds." Entitled poster was presented in National Chemical Laboratory, Pune (*INDIA*)-411008 on *the Science Day* on 26/02/2012. **V. R. Mate**, C. V. Rode.
2. "Spinel Co_3O_4 catalyzed oxidation of lignin model compounds." Entitled poster was presented in National Seminar on "*Recent Advances in Synthetic Chemistry and*

Nanomaterials" (*RASCN*-2012) organized by Kolhapur university (*INDIA*) in January 2012. **V. R. Mate**, C. V. Rode.

3. "Liquid phase oxidation of veratryl alcohol over nano structured spinel type catalyst." Entitled poster was presented in National Chemical Laboratory, Pune (*INDIA*)-411008 on *the Science Day* on 26/02/2011. **V. R. Mate**, C. V. Rode.
4. "Liquid phase atmospheric air oxidation of *p*-cresol catalyzed by heterogeneous Co (II) complexes." Entitled poster was presented in National Chemical Laboratory, Pune (*INDIA*)-411008 on *the Science Day* on 26/02/2008. V. S. Kshirsagar, **V. R. Mate**, C. V. Rode.
5. Participated in 19th *National symposium on catalysis* (CATSYMP-19) on "Catalysis for Sustainable Energy and Chemicals." organized by National Chemical Laboratory (*INDIA*) in January 2009.
6. "Liquid phase air oxidation of *p*-cresol over Co-saponite catalyst." poster presented in Pre-ICC2008 International Symposium organized by *The Catalysis Society of Japan, KYOTO (JAPAN).* V. S. Kshirsagar, **V. R. Mate**, M. Shirai, C. V. Rode.
7. "Production of Platform Chemicals from Biomass: Sustainable Processed using Cobalt Containing Mesoporous Catalysts." Entitled poster was presented at *International Workshop on Process Intensification* (*IWPI 2011*) *(JAPAN).* C. V. Rode, **V. R. Mate**, M. Shirai.
8. "Nanostructured Co_3O_4 Catalyst for Selectivity Tuning in Liquid Phase Oxidation of Phenol Derivatives." poster presented in *International Conference on Advanced Catalytic Science and Technology* (TOCAT6/APCAT5-2010) (*Sapporo JAPAN*). C. V. Rode*, **V. R. Mate**, R. B. Mane, V. S. Kshirsagar.